ISBN 978-91-628-7069-0
LUNFD6/(NFFL-7225)2007

Forward Jet Production in ep-collisions at HERA

Thesis submitted for the degree of
Doctor of Philosophy
by

Albert Knutsson

LUND
UNIVERSITY

DEPARTMENT OF EXPERIMENTAL HIGH ENERGY PHYSICS
LUND, 2007

Organization **LUND UNIVERSITY** Department of Physics Lund University Box 118 SE-221 00 Lund SWEDEN		**Document name** **DOCTORAL DISSERTATION** **Date of issue** February, 2007 **CODEN** LUNFD6/(NFFL-7225)2007
Author(s) Albert Knutsson		**Sponsoring organization**
Title and subtitle Forward Jet Production in ep-collisions at HERA		
Abstract		
Key words: Jets, Forward Jets, Parton Dynamics, low-x, HERA, H1		
Classification system and/or index terms (if any)		
Supplementary bibliographical information:		**Language** English
ISSN and key title:		**ISBN** 978-91-628-7069-0
Recipient's notes	**Number of pages** 180	**Price**
	Security classification	

Distribution by (name and address)
Albert Knutsson, Department of Physics
Box 118, SE-221 00 Lund, SWEDEN
I, the undersigned, being the copyright owner of the above-mentioned dissertation, hereby grant to all reference sources permission to publish and disseminate the abstract of the above-mentioned dissertation.

Signature  **Date** 9/2, 2007

Contents

To my parents,
Karin and Folke

General Introduction

My research deals with the inner structure of the proton and the dynamics of the constituents of the proton, called partons.

The earliest model for describing the substructure of the proton is the **Quark-Parton-Model** (QPM), which considered the proton to consist of 3 quarks moving freely within the proton and sharing the total momentum of the proton. In this picture Deep Inelastic Scattering (DIS) is considered to be elastic scattering against one of the three quarks inside the proton. In order for these proton constituents to build up the total charge of the proton it was assumed that they themselves have charges which are multiples of $\pm 1/3e$. Although the last statement is true, the QPM turns out to be a naive model. From experiments in the late 60s and early 70s it was found that these quarks carried less than half of the total proton momentum. The solution to this problem was provided by the quantum field theory describing the strong force, Quantum Chromo Dynamics (QCD). According to QCD the strong force is mediated by gluons, which consequently also carry some momentum. Through quantum fluctuations the gluons may split up into quark-anti quark pairs, which recombine. These quark-anti quark pairs are called sea quarks. The three original quarks exist permanently in the proton and are called valence quarks since they carry the quantum numbers of the proton.

Today, the dynamics of the partons can be described to some extent by QCD in combination with phenomological models. Electrons[1], which are believed to be elementary particles without any internal structure, can be used to probe the inner structure of the proton and thus the theoretical description by the models can be tested. In hard collisions between electrons and protons, DIS, the structure of the proton can be resolved by the virtual photon exchanged between the electron and the proton in the reaction.

A special kind of DIS is called diffractive scattering. In this class of events an object with no color (the charge of the strong force) is exchanged in the interaction between the exchanged virtual photon and the proton. As a consequence the proton may remain intact and will, in the kinematic region studied, be scattered at very small angle. Although inclusive diffractive data are well described by certain models for the exchanged colorless object the description of the parton dynamics in diffractive scattering is not settled.

From the collision experiments at HERA in Hamburg a better knowledge of the proton structure has been gained and as a consequence also a deeper insight into QCD. The research presented in this thesis is performed with data collected by the H1 detector, and

[1] In this thesis "electrons" refers to both electrons and positrons. For the measurement presented here, the sign of the charge of the lepton is of no consequence.

the aim has been to test the underlying parton dynamics in the proton (part 1) and study diffractive scattering (part 2).

The most relevant and highly cited measurements at HERA concerns the structure function of the proton, F_2. However, this measurement does not adress the issue of details in QCD, such as evolution equations and the ordering of emissions in the parton shower. This is something that is adressed in the forward jet and the diffractive forward jet analyses presented here. Choosen are two interessting QCD areas which can make an important experimental impact.

Since HERA is closing down in 2007, these measurements may be among of the last on the specific topic, even though there are more data left to be analysed. The non-diffractive forward jet measurement was published in [1].

Part 1

Forward Jet Production in Deep Inelastic Scattering

Chapter 1

Introduction to Forward Jet Production in Deep Inelastic Scattering

In certain kinematic regions of high energy collisions between electrons and protons a parton (i.e. a quark or gluon) in the proton can induce a cascade of QCD radiation, consisting of several subsequent parton emissions, before an interaction with the virtual photon eventually takes place (see Fig. 1.1). It is of fundamental interest to understand the dynamics of the partons involved.

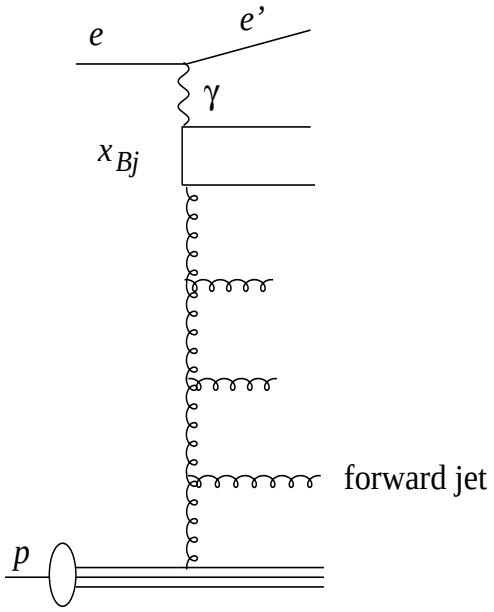

Figure 1.1: *Schematic diagram of ep scattering with a forward jet.*

Emitted partons will fragment and hadronize into collimated flows of particles, so-called jets, and if such a particle flow occurs close to the proton remnant it is referred to as a forward jet. The forward jet will lie well away in rapidity from the photon end of the reaction.

Thus, at one end of the QCD cascade we have the exchanged virtual photon, whose kinematics can be well measured by tagging the scattered electron, and in the other part of the QCD cascade we have the forward jet. By applying kinematic cuts to this kind of events it is possible to study the parton dynamics in different kinematic regions.

The first part of this thesis discusses the production of forward jets in normal DIS events.

An introduction on the basic theory of deep inelastic scattering is given, including the kinematics of DIS, a description of simple (lower order) *ep*-reactions, with very few partons in the final state, and more complex (higher order) *ep*-reactions, in which several partons are produced in the reaction. The concept of evolution equations, which provide an approximate method for calculating higher order *ep*-reactions, is also covered. The main goal of the work, described in part 1, of this thesis has been to find evidence for so called BFKL dynamics.

In the measurement various constraints are applied, which suppress contributions to the parton evolution described by the conventional equations (DGLAP) and enhance the sensitivity to other parton dynamics. In inclusive forward jet production this is achieved by requiring that the transverse momentum squared of the forward jet and the photon virtuality are of similar order.

Chapter 3 summarizes the various event generators, which have been used to simulate the *ep*-reactions for this analysis. The evolution equations are implemented in so-called Monte Carlo (MC) programs, in which statistical methods are used to generate the *ep*-events. Also programs for analytical calculations of the *ep*-cross sections are described in this chapter. In chapter 4 the HERA-facility and the H1-detector are described. Chapter 5 treats the event selection, in which kinematic restrictions are used to select clean and interesting events for the analysis. Special attention is given to the selection of forward jets in the events. The investigations of detector effects are presented in chapter 6. This chapter also includes a study of the systematic errors and the calculation of correction factors used to correct for detector effects. Finally, chapter 7 presents the results and chapter 8 gives the conclusions.

Compared to earlier measurements of particle production in the forward region at H1 [2, 3], the measurements presented in this thesis involve higher statistic, which allows for a more detailed study. A triple differential cross-section measurement gives a higher precision, and also events where two jets with high transverse momentum in addition to the forward jet are selected, referred to as the 2+forward measurement. This measurement has never been done within H1 before.

Chapter 2

Deep Inelastic Scattering and QCD

In this chapter the fundamental features of DIS are defined and explained. Concepts and models needed to describe the proton and the full *ep*-reaction are presented [4–6].

2.1 DIS Kinematics

In the basic DIS reaction, i.e. to the lowest order in the strong coupling constant, α_s, the exchanged virtual photon hits one of the partons inside the proton without any further interactions involved. The process, which in fact is independent of α_s, is referred to as the Born level reaction and is illustrated in Fig. 2.1 as a Feynman diagram with the incoming particles (e, p), the exchanged photon (γ), the scattered electron (e') and the four-momenta of these particles (k_e, k'_e, q and k_p respectively). In cases where very high momenta are transferred from the electron to the proton the process can also occur via the exchange of an electroweak vector boson, Z^0 or $W^{\pm}$. Events where a photon or a Z^0-boson have been exchanged are called neutral current events whereas the exchange of a W-boson gives a charged current event. However, since this analysis is restricted to a kinematic region of lower momentum transfers ($\lesssim$ 10GeV) only the photon exchange has to be considered. The high energy transferred by the exchanged photon makes the struck quark change its direction of flight. A DIS interaction can be characterised by two variables. The following variables, defined below and also denoted in the figure, are frequently used to describe the kinematics of an *ep*-reaction:

- The virtuality of the exchanged photon, Q^2, is defined as the squared negative four-momentum transferred from the electron to the photon

$$Q^2 \equiv -q^2 = -(k_e - k'_e)^2. \tag{2.1}$$

- The square of the total center of mass energy, s, and the square of the hadronic center of mass energy, W^2, are given by

$$s \equiv (k_e + k_p)^2 \approx 2k_e k_p \tag{2.2}$$

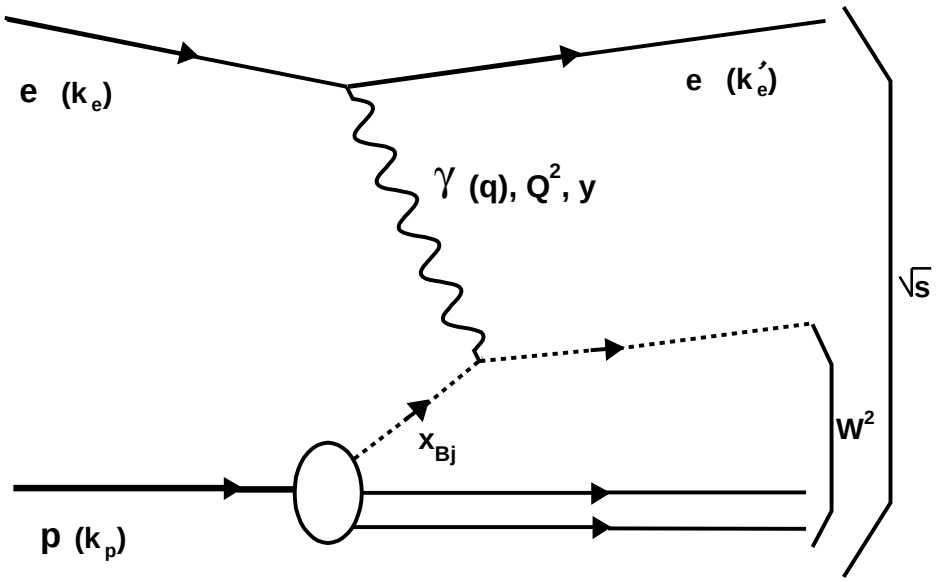

Figure 2.1: *Schematic illustration of the lowest order DIS reaction.*

$$W^2 \equiv (q + k_p)^2 \approx 2qk_p - Q^2 \tag{2.3}$$

where the electron and proton mass have been neglected in the approximate expressions.

- The Bjorken scaling variable, x_{Bj}, is defined as

$$x_{Bj} \equiv \frac{Q^2}{2qk_p} \approx \frac{Q^2}{Q^2 + W^2} \tag{2.4}$$

and in the lowest order α_S DIS reaction can be interpreted as the momentum fraction of the proton carried by the struck quark in the infinite momentum frame, see Fig. 2.1.

- The inelasticity variable y is defined as the scaled photon energy

$$y \equiv \frac{k_p q}{k_p k_e} \approx \frac{Q^2 + W^2}{s} \tag{2.5}$$

2.2 The DIS Cross-Section

In DIS processes the exchanged virtual photon scatters against one of the quarks inside the proton with a probability that can be formulated analytically and expressed in terms of a partonic cross-section. However, the total DIS cross-section also involves the probability that the interacting quark i carries a certain fraction x of the proton's longitudinal momentum, which is expressed by the parton density function $f_i(x, \mu^2)$. The full interpretation of the parton density function, is that it gives the probability of finding a parton carrying a fraction x of the proton momentum if the proton is observed with a resolution given by

μ^2, called the scale of the process. The total ep-cross-section, σ_{ep}, can thus be formulated as a convolution of the partonic cross section, σ_{ei} and the parton density function (PDF):

$$\sigma_{ep} = \sum_i (f_i \otimes \sigma_{ei}) \tag{2.6}$$

where i denotes the different partons in the proton. This approach of calculating the DIS cross-section is called **factorization**, since the hadronic cross-section is factorized into a pertubative and a non-pertubative part. That means that a separation of dynamics associated with short and long range parts of the interaction is possible. The PDF corresponds to a part of the cross-section which is not pertubatively calculable, but has to be measured from experiments by making fits to the data.

2.2.1 Factorization and Renormalization Scales

The partonic cross-section calculations can suffer from divergences arising from the presence of soft or collinear radiations, but since the ep-cross-section is expressed as a convolution of the electron-parton cross-section and the parton density function, this can be technically avoided by letting the radiation be absorbed into the PDF. The **factorization scale**, $\mu_F = \mu$, determines at which point, the transverse soft radiation is considered to belong to the hadronic structure (the PDF), with respect to, for example, the virtuality (if Q^2 is used as factorization scale of the event). The PDF is thus defined at a certain factorization scale.

The **renormalization scale**, μ_r, determines the strength of the running strong coupling constant, α_s, by

$$\alpha_s = \frac{12\pi}{(33 - 2N_f) \ln \frac{\mu_r^2}{\Lambda^2}} \tag{2.7}$$

where Λ is the QCD scale which depends on the number of quark flavours, N_f. This is the one loop expression, i.e. the lowest order expression. The choice of renormalization scale is of importance for the cross-section calculations since the strong coupling constant is used as the expansion parameter in the pertubative calculations.

The choices of renormalization and factorization scales used in this analysis are listed in chapter 3.

2.2.2 The Structure Function

Considering the fact that photons couple differently to particles with different electric charges, the structure function, $F_2(x_{Bj}, Q^2)$, of the proton can be defined as:

$$F_2(x_{Bj}, Q^2) = x_{Bj} \sum_i C_i^2 f_i(x_{Bj}, Q^2) \tag{2.8}$$

where C_i is the electric charge of a quark with flavour i and the sum is over all possible quark flavours. This is the definition of F_2 in the so-called DIS scheme.

The total cross-section for DIS can be written in terms of the variables in section 2.1 and two structure functions, $F_1(x_{Bj}, Q^2)$ and $F_2(x_{Bj}, Q^2)$:

$$\frac{d^2\sigma}{dx_{Bj}dQ^2} = \frac{4\pi\alpha^2}{x_{Bj}Q^4}\Big\{(1-y)F_2(x_{Bj}, Q^2) - y^2 x_{Bj} F_1(x_{Bj}, Q^2)\Big\} \tag{2.9}$$

where α is the electromagnetic coupling constant. The structure functions F_1 and F_2 can be related through the longitudinal structure function $F_L = F_2 - 2x_{Bj}F_1$, where F_L describes the structure of the proton as measured by longitudinally polarized photons.[1] Since real (massless) photons can not be longitudinally polarized there is no such contribution to so-called photoproduction processes where $Q^2 = 0$. In DIS where the exchanged photons are virtual (massive) the influence of longitudinally polarized photons could in principle be taken into account, although in most cases it is very small. The DIS cross-section can be rewritten as

$$\frac{d^2\sigma}{dx_{Bj}dQ^2} = \frac{2\pi\alpha^2}{x_{Bj}Q^4}\Big\{[1+(1-y)^2]F_2(x_{Bj}, Q^2) - y^2 F_L(x_{Bj}, Q^2)\Big\} \tag{2.10}$$

where $F_2(x_{Bj}, Q^2)$ and $F_L(x_{Bj}, Q^2)$ now parameterize the structure of the proton.

At high virtualities the weak boson exchange is important. In this case two more structure functions are introduced. F_2^Z, defined in the same way as F_2, but for Z instead of photon exchange, and $F_3^{\gamma Z}$, which describes the interference between the photon and the Z. This analysis is performed in the low Q^2 range where the Z exchange is not important.

2.2.3 Bjorken Scaling and Scaling Violation

The proton structure function F_2 is measured as a function of two independent Lorenz invariant variables, most often Q^2 and x_{Bj}. At large x_{Bj} ($x_{Bj} \gtrsim 0.1$) the valence quarks are strongly dominating the proton structure. In this region the structure function turns out to be independent of Q^2 for fixed x_{Bj} as can be seen in Fig. 2.2, where the measured F_2 is shown [7] as a function of Q^2 for different fixed x_{Bj}. This phenomenon is called Bjorken scaling and is expected to happen if the valence quarks are point like particles. For smaller x_{Bj}, scaling violation is clearly visible, in the sense that the structure function becomes dependent on both x_{Bj} and Q^2. The explanation is that the sea quarks are dominating at small x_{Bj} and with increasing resolution of the exchanged photon (increasing Q^2) more of the low-momentum sea-quarks can be probed.

Another observation from Fig. 2.2 is that F_2 rises as x_{Bj} gets smaller, meaning that the parton (gluon) density in the proton increases. It is however expected, that when the parton density in the proton becomes very high the partons will start interacting and recombine, which leads to saturation of the parton density.

One of the main purposes of the H1 experiment has been to measure the structure functions with the highest possible accuracy. So far no evidence for a flattening out of F_2 is seen.

[1] In the QPM model F_L=0 since spin $\frac{1}{2}$ particles without transverse momenta can not interact with longitudinally polarized photons.

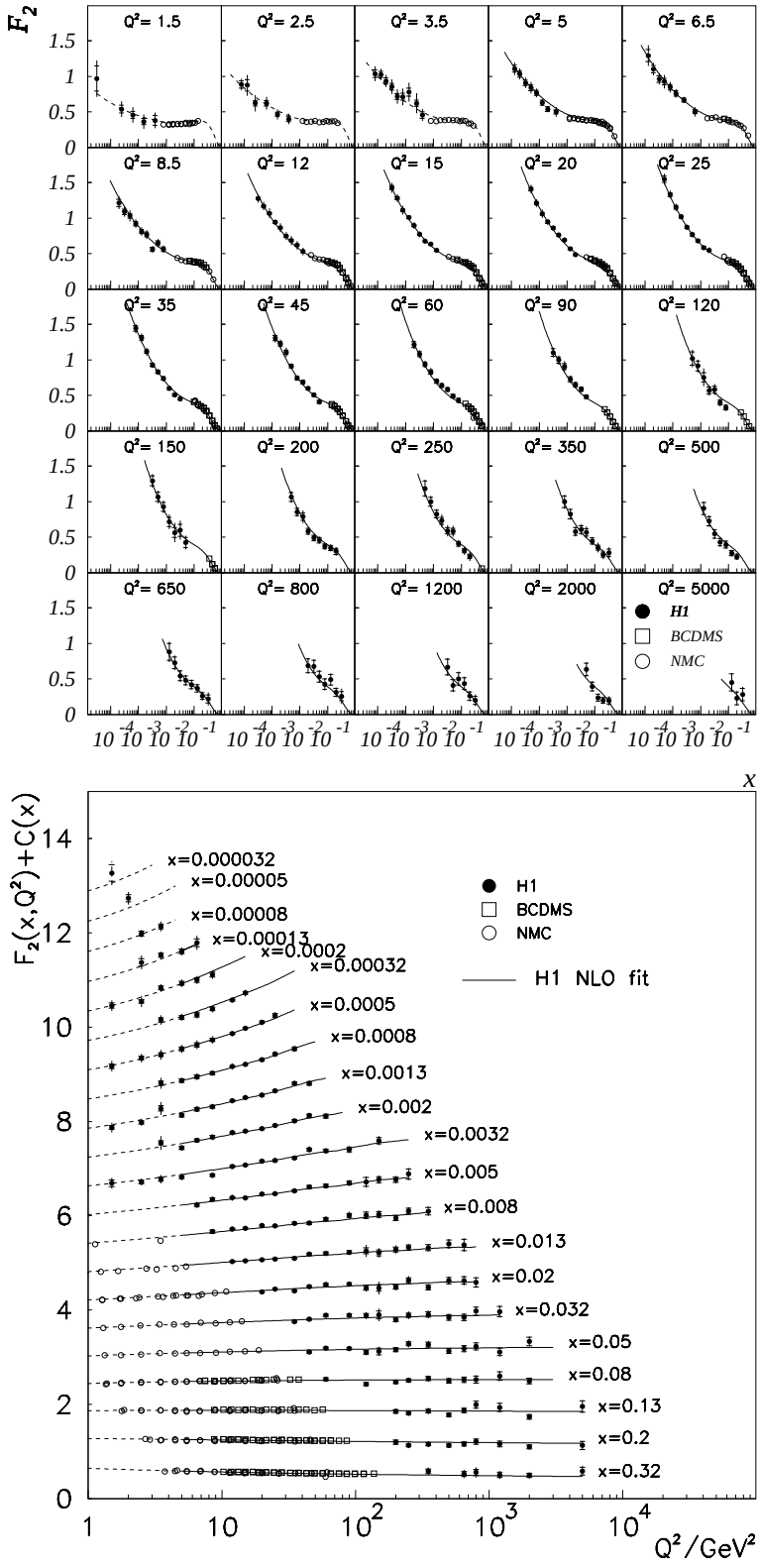

Figure 2.2: *The structure function, $F_2(x_{Bj}, Q^2)$, as a function of x_{Bj} (top) and Q^2 (bottom), respectively. [7].*

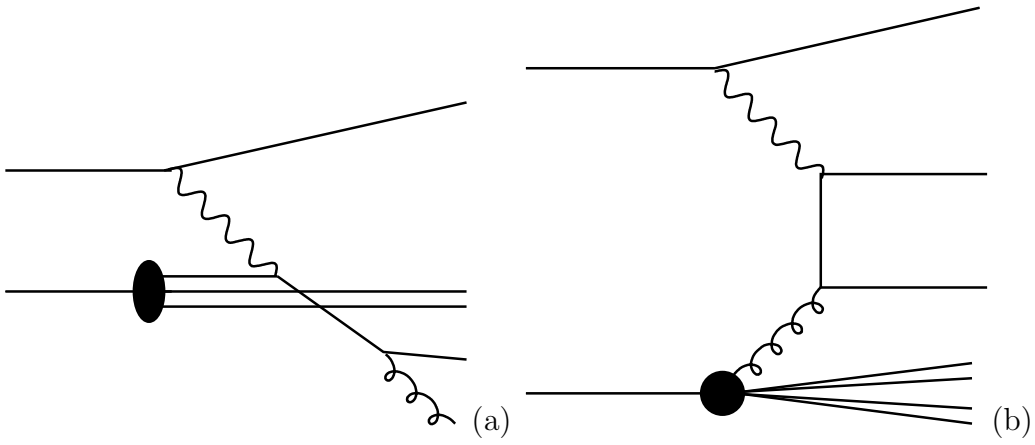

Figure 2.3: *The possible first order α_s reactions, QCD compton (QCDC) (a) and boson gluon fusion (BGF) (b).*

2.3 QCD Calculations

The simple QPM was formulated before the era of QCD. In order to describe the structure of the proton at low x_{Bj} where the parton density is high one has to take the strong force, interacting between the partons into account. The fact that a valence quark may emit a gluon, which in turn may emit another gluon or fluctuate into a sea quark pair, and so on, means the interaction may take place with a quark which is a product of a long chain of splittings into gluons and sea quark pairs. To calculate the cross-sections one uses pertubative QCD calculations where the strong coupling constant α_s is used as the expansion parameter. The powers of α_s in the expansion corresponds to the number of gluon vertices taken into account in the reactions.

2.3.1 Zeroth and First Order α_s Reactions

The number of possible reactions, is strongly limited for the zeroth and the first order α_s reactions, which makes the partonic cross-sections for these reactions calculable from first principle pertubative methods. For the zeroth order (independent of α_s) reaction, where the virtual photon is directly exchanged between the electron and a valence quark, only the Born level Feynman diagram, shown in Fig. 2.1, contributes. A first order ($O(\alpha_S)$) reaction means that there is one strong vertex in the reaction, giving two possible Feynman graphs, QCD Compton scattering (QCDC), as in Fig 2.3a, and boson-gluon fusion (BGF), as in Fig 2.3b. In QCDC a gluon is radiated from the scattered quark. The reaction is similar to QED Compton scattering, but with a quark-gluon vertex instead of an electron-photon vertex. In BGF the photon interacts with a quark (anti quark) created from a gluon, which has split up into a quark-antiquark pair. The photon-quark vertex is called the hard scattering vertex and the quark system attached to this is referred to as the quark-box or the matrix element (ME), simply because this subsystem can be calculated by exact pertubative matrix element calculations.

2.3.2 Higher Order Reactions - Parton Dynamics

Evolution Equations

Exact calculations of higher order interactions become increasingly complicated and more approximate pertubative methods called **evolution equations**, have to be used. So far, exact pertubative calculations have been performed up to order α_s^2 reactions [8, 9].

Additional initial state gluon radiation can be described by so-called parton ladders as sketched in Fig. 2.4 where x_i denotes the fraction of the proton momentum carried by parton i and k_i^2 is the virtuality of that parton, whereas $p_{t,j}$ is the transverse momentum of the emitted parton j.

The pertubative expansion in α_s contains x and Q^2 dependent terms such as $\alpha_s^m(\ln\frac{1}{x})^n$ and $\alpha_s^m(\ln Q^2)^n$, which obviously are important in different kinematic regions of x and Q^2. Three different evolution schemes, called DGLAP [10–13], BFKL [14–16] and CCFM [17–21], which treat these terms differently, are presented here. The evolution equations resum the terms in the pertubative expansion, which means that the important terms for that scheme are rearranged in order of magnitude. Frequently the resummation is approximated further by using the leading log approximation (LLA), such that the resummation only includes single logarithmic terms.

The basic concept of a parton evolution equation is that a propagating parton splits up into a pair, with a new propagator and an emitted parton. The probability for this to happen is given by a so-called splitting function. The probability of having a propagator of a certain momentum is given by the parton density function. The possible splittings are $g \to gg$, $q \to qg$ and $g \to qq$. The initial parton density function distribution is defined at a certain (low) scale and can then be evolved to any scale through the evolution equations. The relevant scale parameter is the one providing the hardest scale in the interaction. It may be Q^2 or p_t^2 of the scattered parton or a combination of these two.

A forward evolution scheme means that the evolution starts at the proton end of the ladder. For technical reasons concerning energy and momentum conservation, backward evolution is often performed.

DGLAP

The DGLAP [10–13] (Dokshitzer-Gribov-Lipatov-Altarelli-Parisi) evolution scheme uses the LLA to resum terms of the type $\alpha_s^m \ln Q^2$. Thus, the DGLAP kinematics should be most predictive when $Q^2 >> 1$, and where x_{Bj} is large enough such that the terms proportional to $\ln\frac{1}{x}$ can be neglected. The DGLAP equation can be written as

$$\frac{d}{d\ln Q^2} f_i(x, Q^2) = \frac{\alpha_s Q^2}{2\pi} \sum_j \int_x^1 \frac{dx'}{x'} f_i(x', Q^2) P_{ij}(\frac{x}{x'}) \tag{2.11}$$

where the probability density P_{ij} is the splitting kernel giving the probability for the mother parton i to radiate a parton j. At small enough x_{Bj} the gluon content dominates the proton and one may restrict oneself to considering gluon splittings alone. The gg splitting function can be written

$$P_{gg}(z) = 6\big(\frac{1-z}{z} + \frac{z}{1-z} + z(1-z)\big) \tag{2.12}$$

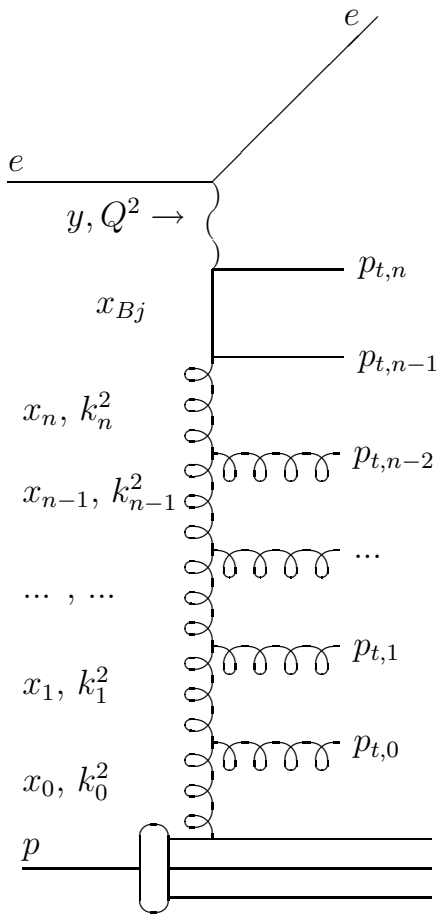

Figure 2.4: *Diagram of a higher order DIS process approximated with a so-called parton ladder. The vertex where the photon couples to the quark is referred to as the hard subprocess or the hard scattering vertex. The variables describing the ladder are the fractional momentum of the proton carried by the propagating parton i, x_i, the virtuality of that parton, k_i^2, and the the transverse momentum of the emitted partons, $p_{t,j}$.*

and can be interpreted as the probability density function for finding a daughter gluon, carrying a momentum fraction z, inside the mother gluon. Since the parton density function and the splitting functions are different for different types of parton, there obviously are several DGLAP equations.

The DGLAP evolution scheme corresponds to a strong ordering in the virtuality, k, of the propagating partons in the parton ladder,

$$Q^2 \gg k_i^2 \gg k_{i-1}^2 \gg ... \gg k_0^2, \tag{2.13}$$

where the subscript of k refers to the order in which the gluon is emitted, as shown in Fig. 2.4. A consequence of the strong ordering in virtuality is that the virtualities of all propagating partons are small compared to the hard scale, Q^2, and they can therefore be treated as massless. Although the DGLAP equation does not consider the terms in $\ln(1/x)$ there has to be at least a weak ordering in x whatever evolution equation is used, since a daughter parton has to carry a smaller fraction of the proton momentum than its mother parton

$$x_i < x_{i-1} < ... < x_0 \tag{2.14}$$

.

The DGLAP evolution is most often used toghether with the *collinear approximation* where the propagating partons are all assumed to travel in the same direction as the incoming proton. The consequence is that the calculations can be simplified since the transverse momenta of the partons can be neglected.

BFKL

In the BFKL [14–16] (Balitsky-Fadin-Kuraev-Lipatov) evolution scheme, terms like $\alpha_s^m(\ln Q^2)^n$ are neglected and instead an LLA is made in terms of $\alpha_s^m \ln \frac{1}{x}$. This evolution scheme is thus expected to be valid for smaller x_{Bj}, where $\ln Q^2 < \ln \frac{1}{x}$. The BFKL evolution uses strong ordering in the fractional momentum, x, carried by the propagating partons,

$$x_i \ll x_{i-1} \ll ... \ll x_0, \tag{2.15}$$

and no ordering of the parton virtualities is required. Instead they follow a random walk behavior in virtuality. It is therefore possible that the evolution diffuses into the infra-red region with $k_i^2 < Q_0^2$, where Q_0^2 is the starting scale of the evolution. In this region the pertubative physics is not valid (due to the fact that α_s will be large and not useful as an expansion parameter).

Another consequence of non-ordering in the parton virtualities is that the partons can have high virtual masses and the matrix element has to be taken off mass shell. Furthermore, the transverse momenta of the emitted partons can no longer be neglected. Therefore the partons can not be treated as collinear and the evolution and the PDFs must depend on the transverse momentum of the propagating partons. In the BFKL scheme k_t-factorization is used, meaning that the cross-section is factorized into terms depending on k_t.

The BFKL equation has a form similar to the DGLAP equation but, due to the possible high virtual masses of the propagating gluons it is expressed in terms of the unintegrated gluon density, $A(x, k_t^2)$, which can be related to the normal integrated gluon density,

$f_{gluon}(x, Q^2)$, by

$$xf_{gluon}(x, Q^2) \approx \int_0^{Q^2} \frac{dk_t^2}{k_t^2} A(x, k_t^2) \tag{2.16}$$

The BFKL equation is given by

$$\frac{dA(x, k_t)}{d\log(1/x)} = \int dk`t^2 A(x, k`_t^2) K(k_t^2, k`_t^2) \tag{2.17}$$

where $K(k_t^2, k`_t^2)$ is the BFKL splitting function.

CCFM

The CCFM [17–21] (Catani-Ciafaloni-Fiorani-Marchesini) equation resums leading log terms in both $\ln Q^2$ and $\ln \frac{1}{x}$, and offers a bridge between the DGLAP and the BFKL equations. In the CCFM model coherence effects are taken into account by angular ordering,

$$\theta_j > \theta_{j-1} > ... > \theta_0, \tag{2.18}$$

where j denotes the emitted partons as in Fig. 2.4.

The CCFM equation can be used with different splitting functions in the unintegrated gluon density. In this thesis the unintegrated PDFs J2003-set1 and J2003-set2 [17–20] are used, of which the first one uses the original CCFM splitting function

$$P_g g(z_i, q_i^2, k_t^2) = \alpha_s(q_i^2(1-z_i)^2)\frac{1}{1-z_i} + \alpha_s(k_{ti}^2)\frac{1}{z_i}\Delta_{ns}(z_i, q_i^2, k_{ti}^2) \tag{2.19}$$

where Δ_{ns} is the non-Sudakov form factor taking care of the Reggeization of the gluon vertex, meaning that all higher order corrections of the gluon vertex are taken into account.

While the J2003-set1 splitting function includes only singular terms, the J2003-set2 splitting function also involves non-singular terms

$$\begin{aligned} P_g g(z_i, q_i^2, k_t^2) &= \alpha_s(q_i^2(1-z_i)^2)(\frac{1-z_i}{z_i} + \frac{z_i(1-z_i)}{2})\Delta_{ns}(z_i, q_i^2, k_{ti}^2) + \\ &+\alpha_s(\frac{z_i}{1-z_i}+)z_i(1-z_i)\Delta_{ns}(z_i, q_i^2, k_{ti}^2) \end{aligned} \tag{2.20}$$

Like BFKL, CCFM evolution has to be used with k_t-factorization.

The kinematic regions for the different approaches are shown schematically in Fig. 2.5. For very small values of Q^2 the strong coupling constant becomes large and the pertubative calculations break down. For very low x the parton density becomes very high and one may reach a region where saturation effects are expected to be visible.

The Color Dipole Model

The Colour Dipole Model [22–24] (CDM) is an alternative model for calculating higher order QCD emissions which is not based on standard evolution equations. In this model, an initial quark-anti quark pair is spanned by a color dipole and the probability that this

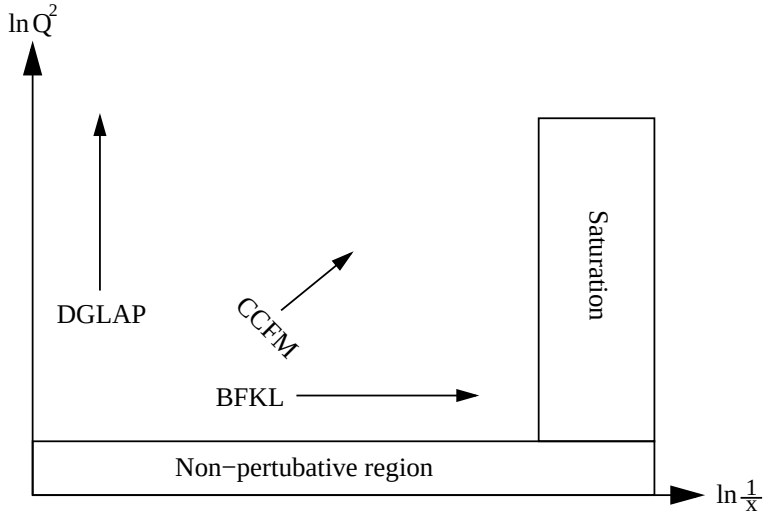

Figure 2.5: *Different kinematical regions sketched in the* $\ln Q^2$-$\ln \frac{1}{x}$ *phase space.*

dipole will emit a gluon is calculated. This is illustrated in Fig. 2.6a). New dipoles are spanned between the quarks and the radiated gluons such that an avalanche of radiated gluons are produced. In this scheme the dipoles are radiating gluons independently of one another. CDM was originally constructed for $e^+e^- \to qq$, but in ep-collisions the struck quark and the proton remnant spans the first dipole. Therefore CDM can only calculate QCDC and higher order processes, not BGF processes. The latter have to be included in the matrix element.

Contrary to the evolution equations, where initial state radiation and final state radiation are generated separately, all emissions in CDM are treated as final state dipole radiation. Since there is no k_t-ordering of the emitted partons, the CDM gives BFKL like parton emissions [25–27].

The phase space available for gluon emission as calculated in CDM is indicated in Fig. 2.6b) where the logarithm of the transverse momentum squared of the emitted gluon is drawn versus its pseudo rapidity, $\eta = -\ln\tan(\theta/2)$. Emissions are possible inside the triangle, limited by the available dipole energy W. The thick line indicates a reduction of phase space due to the spatial extension of the proton.

2.4 Jet Physics

Experimentally a jet is a flow of hadrons collimated in solid angle. Section 2.4.1 describe how the partons are converted into hadrons according to the Lund string model [28, 29]. In section 2.4.2 it is discussed how the jet properties can be reconstructed by using a so-called jet algorithm, which in this case is a clustering algorithm.

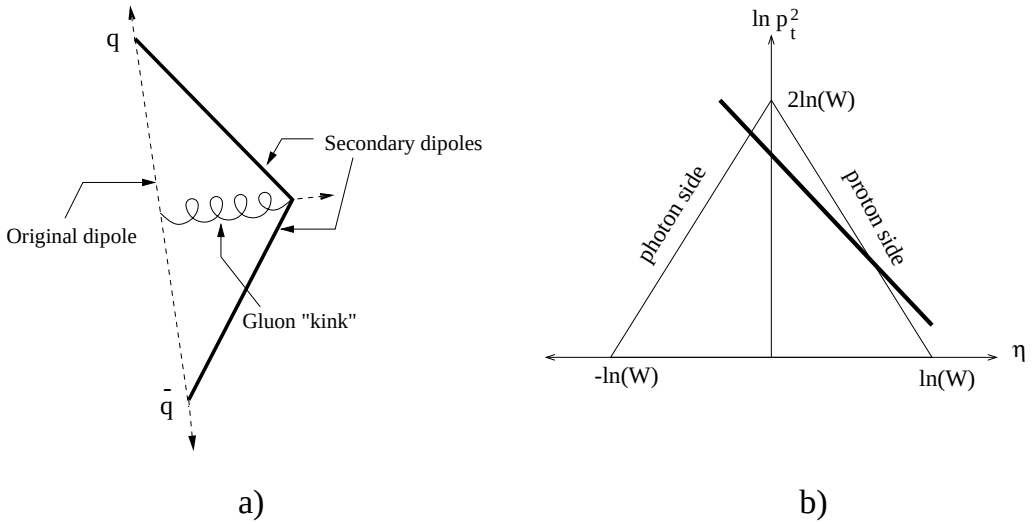

Figure 2.6: *In a) the basic principle of the CDM is sketched. In b) the η-p_t^2 (pseudo rapidity-transverse momentum) phase space for radiation in the CDM is drawn. The thick line indicates the part of phase space which is excluded due to the extended nature of the proton.*

2.4.1 Hadronization

Hadronization processes are responsible for the conversion of the color-charged particle into colorless hadrons. These processes cannot be calculated from perturbation theory but have to be described by phenomenological models. The Lund string model [28, 29] is such a model.

In the Lund string model, two color charged objects are bound together by a color string with the string constant κ [GeV/fm]. As the two particles move apart the color string is stretched out causing the energy in the string to increase. When enough energy is stored in the string it can break and new quarks are produced. In order to conserve quantum numbers the created particles must be either a quark-anti quark pair or a diquark-anti diquark pair. Each of the newly created quarks connects to the old quarks with the remaining parts of the color string.

To create a quark with mass, m_q, and transverse momentum, p_t, in the string, the energy $m_t = \kappa\Delta l$ is taken from a piece of string, Δl, where $m_t^2 = m_q^2 + p_t^2$. Thus, the two quarks produced can not be created in the same point but have to be created at a distance $2\Delta l$ from each other. Theoretically the production of new quarks can be formulated as a tunneling process where the tunneling probability, i.e. the probability for creation of new quarks, is proportional to $e^{-\frac{\pi}{\kappa}m_t}$.

The quark-antiquark pairs and the diquark-anti-diquark pairs created in the Lund hadronization process combine into colorless mesons and baryons, respectively, which are observed in nature.

2.4.2 Jet Reconstruction

In the string picture a jet is not a well defined object. The colour string connects the initially scattered quarks. Therefore, the particles created in the break-up of the string, can not unambiguously be associated to one or the other of the scattered quarks. Jets are usually defined by a clustering algorithm, which merges particles into jets according to a scheme taking angle and momentum of the particles into consideration.

The inclusive k_t-algorithm [30,31] has turned out to perform well in reconstructing jets with respect to partons created in the matrix element and showers [32], and is therefore used in the forward jet analysis.

The Inclusive k_t Algorithm

In the inclusive k_t algorithm all final state particles, i, are initially defined as proto-jets with transverse momentum $p_{t,i}$, azimuthal angle ϕ_i and pseudo rapidity $\eta_i = -\ln\tan(\theta_i/2)$. The algorithm proceeds according to the following recipe:

1. For each proto-jet, i, the distance $d_{ip} = p_{t_i}^2$ to the proton remnant in 3-momentum space is calculated.
2. For each pair of proto-jets, (i,j), the distance $d_{ij} = \min(p_{ti}^2, p_{tj}^2)R_{ij}^2$ is calculated, where R_{ij} is the distance in η-ϕ space, i.e. $R_{ij}^2 = \Delta\eta_{ij}^2 + \Delta\phi_{ij}^2$.
3. If $d_{ij} < d_{ip}$ the two proto-jets, (i,j), are merged into a new proto-jet, else the proto-jet i is removed from the proto-jet list and added to the lists of true jets. In both cases i and j are removed from the proto-jet list.
4. 1-3 is repeated until no more proto-jets remain.

Proto-jets are merged according to the p_t-weighting scheme:

$$p_{tij} = p_{ti} + p_{tj} \tag{2.21}$$

$$\eta_{ij} = \frac{p_{ti}\eta_i + p_{tj}\eta_j}{p_{tij}} \tag{2.22}$$

$$\phi_{ij} = \frac{p_{ti}\phi_i + p_{tj}\phi_j}{p_{tij}} \tag{2.23}$$

where the left hand sides are the properties of the new proto-jet or a final jet.

2.5 Photon Structure

The virtual photon exchanged in DIS can fluctuate into a quark-anti quark pair. The quarks may radiate gluons which in turn fluctuate into new quark-anti quark pairs. This results in a complex system of quarks and gluons, and hadronic properties can thus be ascribed to photon. In this case, the photon is no longer considered point-like, but hadron like. The reactions involving point-like and hadron-like photons are often described as "direct" and "resolved", respectively.

It is possible to define a structure function, F_2^γ for the photon

$$F_2^\gamma = \sum C_q^2 x f_q^\gamma(x, Q^2) \tag{2.24}$$

where f_q, as before, is the quark density for a quark of type q, and C_q is the charge. Just like the process on the proton side, higher order reactions have to be calculated by evolution equations and matched to the ME. In resolved DIS the hard scattering process can have one parton ladder on the photon side and one parton ladder on the proton side.

The resolved photon can be treated as interacting as a bound vector meson state ($\gamma \to V$) (the VMD state) or as decoupled partons ($\gamma \to q\bar{q}$) (the anamolous state). The former state is important for $Q^2 \lesssim 1$ GeV, since most resonances have masses below 1 GeV. The two models parameterize the γPDF differently.

The importance of the resolved photon contribution is determined by Q^2 and some scale, μ^2, close to the target region. In the same way as Q^2 determines how well the structure of the proton is resolved in direct DIS, the scale μ^2 compared to Q^2 determines how much the structure of the photon is resolved. If $\mu^2 \gg Q^2$ the importance of the resolved photons is larger since the structure of the photon can be resolved. $\mu^2 \ll Q^2$ corresponds to direct DIS. This has an direct impact on the measurement of the forward jet cross-section, for which it is shown that for forward jets with $p_t^2 \gg Q^2$ the resolved process is most prominent.

2.6 Photoproduction

Photoproduction events are events where $Q^2 \approx 0$, the photon is quasi-real and the electon is scattered through very small angles and will not be seen by the detector. The photoproduction processes involves physics which are not considered in this analysis. These events are excluded by imposing a cut on the minimum value of Q^2 of 5 GeV.

2.7 Reference Frames

The Laboratory Frame

In the laboratory frame, the detector is at rest and the electron and the proton are collinear with the z-axis, but have opposite directions of motion. At HERA, the electron and proton energy are 27.5 and 920 GeV, respectively. Before 1999, the proton energy was 820 GeV.

The Hadronic Center of Mass (HCM) Frame

In the hadronic center of mass frame the positive z-axis is defined by the virtual photon, and the rest frame of the photon-proton system is defined by

$$\bar{k_p} + \bar{q} = 0 \tag{2.25}$$

which means that the incoming proton and the exchanged photon are collinear. As a consequence, if one neglects the intrinsic momentum of the scattered quark, the proton and the quark is scattered back to back for QPM processes.

The Breit Frame

The Breit frame is also called "the brick wall" frame, due to the fact that in this frame the scattered quark direction is reversed when hit by the photon. As in the HCM the virtual photon and the incoming proton are collinear, but in the Breit frame the quark absorbs the photon and does not lose any energy in the scattering, i.e.

$$\begin{aligned} p_{\text{incoming quark}} &= xP = (Q/2, 0, 0, -Q/2) \\ p_{\text{scattered quark}} &= xP = (Q/2, 0, 0, Q/2) \end{aligned}$$

where the exchanged photon defines the positive z-axis. The jet created from the scattered quark in the QPM events thus has $p_t = 0$ GeV.

Chapter 3

Event Generation

In this chapter the computer programs used to calculate or simulate electron-proton scattering are presented. Two types of programs have been used, programs which calculate cross-sections on the parton level, i.e. the partons are not hadronized, by fixed order matrix element calculations, and event generators which simulate the full events including hadronization. Both programs are based on Monte Carlo methods. Also presented are the scales and PDFs that have been used in the different QCD programs. A new tuning of the parameters of the ARIADNE [33] program is presented.

3.1 Simulation Programs and Fixed Order Calculations

So-called Monte Carlo (MC) programs based on random number generation are used to simulate various physics processes for comparisons to experimental data. The MC programs used for event generation of DIS processes include one part for exact pertubative calculations of the matrix element and one for generating higher order emissions according to one of the evolution schemes described in section 2.3.2. The starting point is a parton density distribution defined at some small scale Q^2 (about 1 GeV) at which the perturbative theory is still expected to be valid. By performing the parton evolution the PDF can be calculated at an arbitrarily high scale which is given by the factorization scale. The factorization scale is normally defined as the hardest scale of the scattering process and can for example be Q^2, the transverse momentum of a jet or something else. For each event the parton evolution is performed up to the value of the hard scale and the corresponding PDF gives the probability for a parton with a specific x-value to be emitted at each splitting. In a final step the emitted partons undergo the hadronization process. For technical reasons it is more effective to generate the parton ladder in a so-called backward evolution. In this case the evolution is performed from the hard scattering vertex towards the proton side of the reaction.

Few Monte Carlo program provide a full event simulation on their own. Several programs have been developed, each handling a different step in the reaction chain. Here follows a list including a brief description of the programs used for this analysis.

RAPGAP [34] uses leading order (LO) matrix element calculations matched to LO DGLAP parton showers. In RAPGAP there the possibility to calculate a contribution from a resolved photon component also exists. In this case there is an additional DGLAP chain evolved towards the hard scattering vertex on the photon side in the reaction.

CASCADE [35–37] models the parton evolution according to the CCFM formalism. It assumes that gluons highly dominate the cross-section and takes no quarks into consideration, either in the parton density function, given by an unintegrated gluon density function, or in the parton radiation, which is governed by the gluon splitting function only. The CASCADE program is thus constructed to describe the low x region.

Two different versions of the unintegrated gluon density were used, J2003 set-1 and set-2. The difference between these two sets is that in set-1 only singular terms were included in the splitting function, whereas set-2 also takes the non-singular terms into account. The unintegrated gluon densities have been determined from fits to the $F_2(x, Q^2)$ data obtained by H1 and ZEUS in 1994 and 1996/97 [38].

In **ARIADNE** [33] the lowest order reaction and BGF is calculated by LO ME, while QCDC and higher order reactions are simulated by using the color dipole model. In addition, QED radiation can be added to the event simulation by using **HERACLES** [39] program, which is interfaced to ARIADNE via the **DJANGO** [40] program.

In this analysis HERACLES has only been used for generating events to be run through the detector simulation. These events are used to estimate detector effects and QED effects. This will be further discussed in section 6. Events with QED radiation included are referred to as radiative events.

The generators above are used together with **JETSET/PYTHIA** [41, 42] which performs the fragmentation according to the Lund string model.

DISENT [8, 43] and **NLOJET++** [9] provide perturbative cross-section calculations at next-to-leading-order (NLO). The former for di-jet events and the latter for 3-jet events. For the di-jet case this means that there is a third parton in addition to the two quarks at the hard scattering vertex. This can either occur as a real emission, as shown in Fig. 3.1a), or as a so-called virtual correction, like in Fig. 3.1b). The 3-jet case has an additional real emission compared to the di-jet situation as illustrated in Fig. 3.1c) and d). Calculations at NNLO accuracy would involve one more parton which can also be either a real emission or a virtual correction. At the moment no NNLO calculations exist [44, 45].

DISENT is based on perturbative NLO di-jet calculations, i.e. α_s^2-calculations without parton showers and hadronization. For comparisons with experimental data hadronization effects have to be taken into account by using correction factors. These can be estimated as the ratio between the cross-sections on the hadron level and the parton level, which can be obtained from simulations by other event generators. In this analysis the calculations from DISENT are corrected for hadronization effects by using CASCADE together with the KMR PDF [46]. This PDF takes only the hard scattering vertex and one additional emission into account and should therefore be suitable for estimating corrections of NLO di-jet calculations. The hadronization effects are typically not larger than 10%. The renomalization scale (μ_r^2) in DISENT is given by the average p_t^2 of the di-jets from the

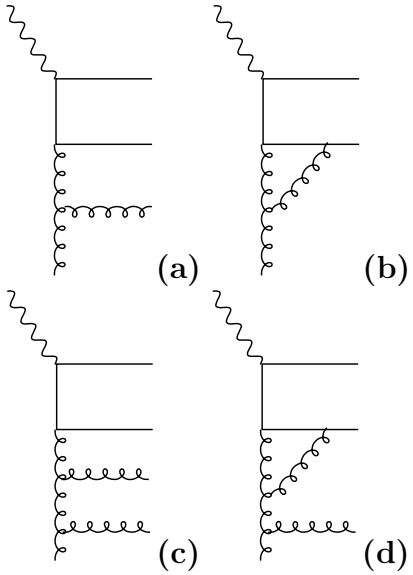

Figure 3.1: *Example of diagrams contributing to NLO di-jet (a, b) and the NLO 3-jet (c, d) cross-sections calculations.*

matrix element ($\langle p^2_{t,\text{di-jets}} \rangle$), while the factorisation scale (μ_f^2) is given by the average p_t^2 of all forward jets in the selected sample.[1]

NLOJET++ provides perturbative calculations for 3-jet calculations in DIS at NLO accuracy, i.e. α_s^3-calculations without parton showers and hadronization. Although NLOJET++ can calculate ME for final states with 4 partons it is worth noting that it cannot perform calculations with NNLO accuracy since important terms are missing in the calculations. The NLOJET++ calculations are corrected to the hadron level using CASCADE together with the unintegrated gluon density J2003 set-2 [38]. The hadronisation effects for the "2+forward jet" cross-sections vary between 30% and 50%. In NLOJET++, where the factorisation scale can be defined for each event, μ_r^2 and μ_f^2 are set to the average p_t^2 of the forward jet and the two hardest jets in the event.

The uncertainty in the NLO calculations, originating from the PDF uncertainty, has been estimated by using the CTEQ eigenvector sets according to [47]. In practice this means calculating the cross-section, σ, several times using N different PDFs, $S_i^{\pm}$. The uncertainty in the cross-section, $\delta\sigma$, is then obtained by using the formula

$$\delta\sigma = \frac{1}{2}\left(\sum_{i=1}^{N} (\sigma(S_i^+) - \sigma(S_i^-))^2 \right)^{\frac{1}{2}} \tag{3.1}$$

The set of eigenvector PDFs, $S_i^{\pm}$, are obtained by statistical methods [47, 48] which will not be further discussed in this thesis. The + and − notation corresponds to the result obtained from positive and negative shift of free parameters in the calculation.

The scale uncertainty for the fixed order calculations is estimated by simultaneously changing the renormalisation and factorisation scales (μ_r^2, μ_f^2) by a factor of 4 up and 1/4

[1] For the triple differential forward jet cross-section, $d^3\sigma/dx_{Bj}dQ^2dp^2_{t,\text{ jet}}$, this means different factorisation scales for the three different $p_{t,\text{ jet}}$ bins.

down. In CASCADE the renormalisation scale (μ_r^2) is changed by the same factors and in each case the unintegrated gluon density is adjusted such that the prediction of CASCADE describes the inclusive F_2 data [49, 50]. The forward jet cross-section is then calculated to estimate the upper and lower limit of the scale uncertainty. The resulting uncertainty in the forward jet cross-sections obtained from CASCADE is less than 10% at the smallest x_{Bj} and decreases for higher x_{Bj}.

In table 3.1 the scales and the parametrization of the parton densities used for the different programs are summarized.

	CASCADE	RG-DIR/RES	DISENT	NLOJET++
μ_r^2	$\hat{s} + \langle p^2_{t,\text{di-jets}} \rangle$	$Q^2 + \langle p^2_{t,\text{di-jets}} \rangle$	$\langle p^2_{t,\text{di-jets}} \rangle$	$(p^2_{t,\text{jet1}} + p^2_{t,\text{jet2}} + p^2_{t,\text{fwdjet}})/3$
μ_f^2	$\hat{s} + Q_t^2$	$Q^2 + \langle p^2_{t,\text{di-jets}} \rangle$	$\langle p^2_{t,\text{fwdjet}} \rangle$	$(p^2_{t,\text{jet1}} + p^2_{t,\text{jet2}} + p^2_{t,\text{fwdjet}})/3$
proton PDF	J2003 set-1 & 2	CTEQ6L [47]	CTEQ6M	CTEQ6M
photon PDF	-	SaS1D [51] (RES only)	-	-

Table 3.1: *The renormalisation (μ_r^2) and factorisation (μ_f^2) scales, and the parton density functions used in the different programs. The average squared transverse momentum of the forward jet, $\langle p^2_{t,fwdjet} \rangle$, is 45 GeV^2 for the single differential forward jet cross-section, and 24, 55 and 183 GeV^2 for the three different p_t^2-bins in the triple differential cross-sections. The average p_t^2 of the di-jets from the matrix element ($p^2_{t,di\text{-}jets}$) is calculated event by event.*

3.2 A New Tuning of ARIADNE

ARIADNE with the parton density function parameterized according to CTEQ6L has been tuned to fit a set of data. ARIADNE uses a large number of free parameters. In order do minimize the uncertainty of theoretical prediction a tuning is necessary. The tuning made in this thesis, follows the recipe in [52], in which ARIADNE was tuned with the GRV94 PDF. The following 3 data sets have been used for the tuning:

- The pseudo rapidity spectra in the center-of-mass system for charged particles with $p_t > 1$ GeV and for charged particles in the full p_t range. DIS events in the range $5 < Q^2 < 50$ GeV^2 were used in this measurement [53].
- The inclusive transverse energy flow for DIS events, $1/N dE_T^* d\eta^*$, in bins of x_{Bj} and Q^2. The measurements were made for $2.5 < Q^2 < 100$ GeV^2 [54].
- The di-jet cross-section as a function of the average transverse energy of the di-jets, E_T, and the pseudo rapidity of the most forward jet of the di-jets. The jets were reconstructed from DIS events within the range $10 < Q^2 < 70$ GeV^2, using the inclusive k_t algorithm in the Breit frame [55].

Statistical and systematic errors in each measurement were taken into consideration, but no correlation effects between the errors were included.

The average reduced χ^2 was calculated for different combinations of values of the following four parameters:

- PARA(10) : This parameter determines the dimensionality of the proton remnant, which specifies the energy available for radiation. The phenomenon is referred to as soft suppression. In principle this parameter gives the position of the thick line in Fig. 2.6b) defining the phase space region available for emissions in CDM. This parameter should be around 1.0 and not larger than 2.0.

- PARA(15) : This parameter determines the soft suppression for the struck quark.

- PARA(25) : A parameter that governs the probability of having emissions outside the soft suppression cutoff, i.e. in the part of the phase space above the line in Fig. 2.6b).

- PARA(27) : The square of this parameter is the mean value of the primordial p_t^2 for the struck quark in the DIS process.

In table 3.2-3.4 the calculated average reduced χ^2 for the different combinations of values of the tuned parameters are summarised. Two combinations of parameters give the same lowest value of χ^2 but one of them (PARA(10)=1.5, PARA(15)=1.3, PARA(25)=1.8, PARA(27)=0.9) deviates most from the default values. Therefore the other combination of values (PARA(10)=1.2, PARA(15)=1.0, PARA(25)=1.2, PARA(27)=0.9) is chosen for the new tuning. In table 3.5 the new and old parameters are summarized. Finally, in Fig. 3.2 the forward jet cross-section is calculated by ARIADNE using the CTEQ6L+old tuning, the GRV94+new tuning and the CTEQ6L+new tuning, respectively. As can be seen the CTEQ6L+new tuning gives results similar to the GRV94+old tuning, while the CTEQ6L+old tuning, which is the tuning made for the GRV94, does not.

PARA(10)	PARA(15)	PARA(25)	PARA(27)	Average χ^2
1.0	0.7	1.2	0.6	4.12
			0.8	4.29
			0.9	4.39
		1.5	0.6	4.81
			0.8	5.48
			0.9	5.80
		1.8	0.6	6.32
			0.8	7.27
			0.9	7.54
	1.0	1.2	0.6	3.76
			0.8	3.70
			0.9	3.79
		1.5	0.6	4.16
			0.8	4.56
			0.9	4.68
		1.8	0.6	5.31
			0.8	5.73
			0.9	5.94
	1.3	1.2	0.6	3.80
			0.8	3.40
			0.9	3.34
		1.5	0.6	4.02
			0.8	3.95
			0.9	3.98
		1.8	0.6	4.63
			0.8	4.82
			0.9	5.15

Table 3.2: *The values of χ^2 resulting from the fit of free parameters within ARIADNE to experimental data.*

PARA(10)	PARA(15)	PARA(25)	PARA(27)	Average χ^2
1.2	0.7	1.2	0.6	4.02
			0.8	3.46
			0.9	3.39
		1.5	0.6	3.99
			0.8	3.90
			0.9	4.05
		1.8	0.6	4.61
			0.8	4.92
			0.9	5.16
	1.0	1.2	0.6	4.37
			0.8	3.36
			0.9	3.27
		1.5	0.6	3.85
			0.8	3.60
			0.9	3.60
		1.8	0.6	4.13
			0.8	4.28
			0.9	4.44
	1.3	1.2	0.6	4.88
			0.8	3.78
			0.9	3.41
		1.5	0.6	3.83
			0.8	3.43
			0.9	3.34
		1.8	0.6	3.92
			0.8	3.80
			0.9	3.88

Table 3.3: *The values of χ^2 resulting from the fit of free parameters within ARIADNE to experimental data.*

PARA(10)	PARA(15)	PARA(25)	PARA(27)	Average χ^2
1.5	0.7	1.2	0.6	7.19
			0.8	4.68
			0.9	4.24
		1.5	0.6	4.83
			0.8	3.56
			0.9	3.31
		1.8	0.6	3.98
			0.8	3.62
			0.9	3.58
	1.0	1.2	0.6	8.23
			0.8	5.62
			0.9	4.81
		1.5	0.6	5.21
			0.8	3.89
			0.9	3.38
		1.8	0.6	4.00
			0.8	3.43
			0.9	3.43
	1.3	1.2	0.6	8.86
			0.8	6.59
			0.9	5.42
		1.5	0.6	5.80
			0.8	4.08
			0.9	3.63
		1.8	0.6	4.31
			0.8	3.35
			0.9	3.27

Table 3.4: *The values of χ^2 resulting from the fit of free parameters within ARIADNE to experimental data.*

Parameter	New tuning	Old tuning	Default
PARA(10)	1.2	1.2	1.0
PARA(15)	1.0	1.0	1.0
PARA(25)	1.2	1.5	2.0
PARA(27)	0.9	0.6	0.6

Table 3.5: *The default values of the tuned parameters in ARIADNE compared to those obtained from the old and new tunings.*

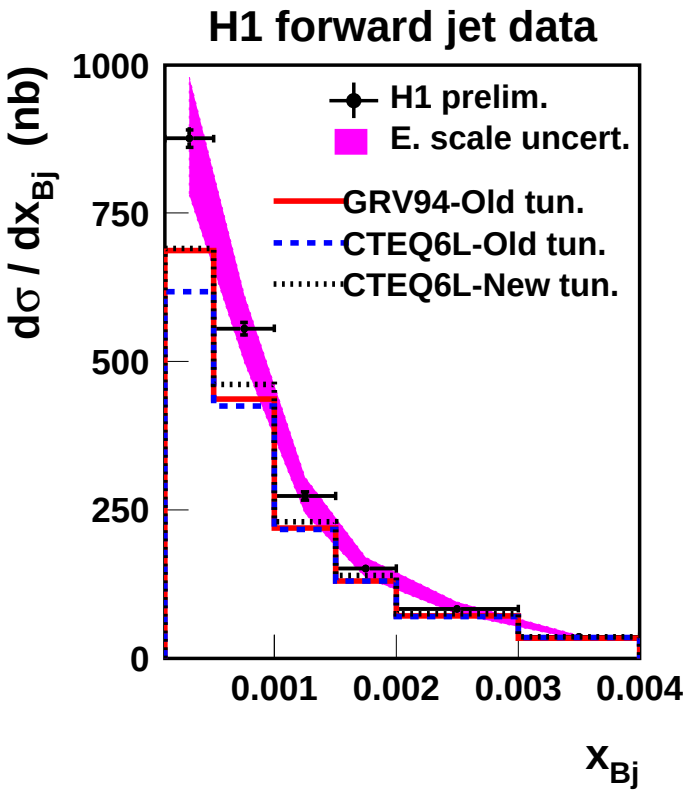

Figure 3.2: *Cross-sections for experimental forward jet data, with the statistical error and the scale uncertainty (shaded band) of the measurement. The lines show the cross-sections calculated with ARIADNE using GRV94+old tuning (full line), CTEQ6L+old tuning (dashed line) and CTEQ6L+new tuning (dotted line).*

Chapter 4

DESY - The HERA-ring and the H1-detector

The only high energy physics electron-proton collider in the world is situated at the research laboratory Deutsches Elektronen Synchrotron (DESY) in Hamburg, Germany. As the name indicates the laboratory was originally built up around an electron synchrotron, but since 1959, when the facility was founded, many upgrades have been made and new accelerators have been constructed. Since 1992 high energy physics research at DESY has been largely focused on the electron-proton collider HERA. In order to feed this machine with high energy electrons (positrons) and protons several preaccelerators are needed. The tunnel in which the original electron synchrotron was placed now houses two new accelerators, one for electrons (DESY II) and one for protons (DESY III). The final acceleration of the electrons and the protons takes place in HERA itself. The electrons and protons are injected into HERA in opposite directions, and are collided in two interaction points surrounded by the H1 and ZEUS detectors, respectively. In addition there are two fixed target detectors of which the HERMES detector only uses the polarized electron beam to study the spin structure of (fixed target) protons, whereas the HERA-B detector has measured collisions of the protons with a fixed target to investigate CP-violation and B-physics. HERA-B stopped taking data in 2003. The other experiments will continue until the year 2007 when HERA will stop running.

4.1 The HERA-ring

When the electrons and protons are injected into the HERA-ring they have been accelerated in several steps from the initial linear machines to the PETRA ring, which is the final preaccelerator in the chain and is used for both electrons and protons. PETRA delivers electrons of 14 GeV into HERA, while the protons are injected at 40 GeV. In HERA the electrons obtain a final energy of 27.5 GeV and the protons a final energy of 820 GeV. In 1998/99 an upgrade of the HERA-ring led to an increase of the proton energy to 920 GeV. An overview of the accelerator system can be seen in Fig. 4.1.

The particles are accelerated in bunches with a bunch crossing frequency of about 10 MHz. In a normal run the initial electric beam current is measured to be of the order of

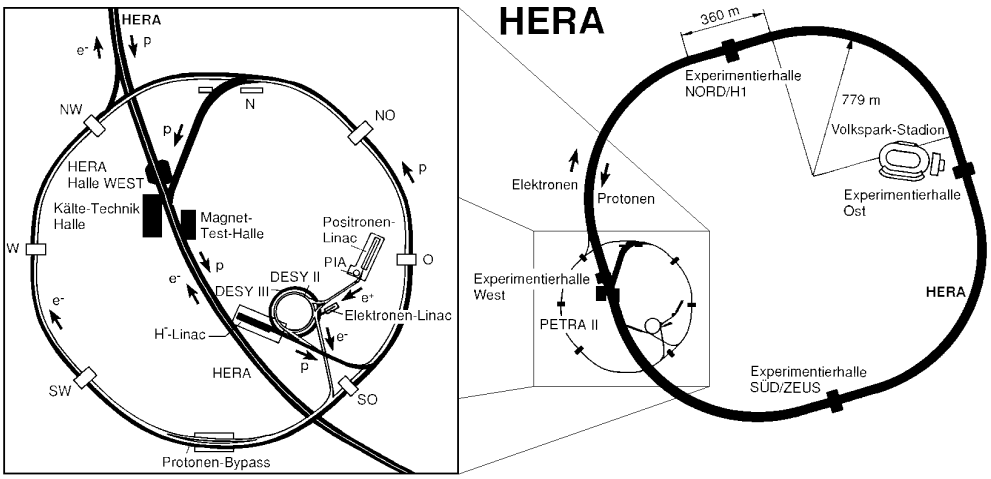

Figure 4.1: *Overview of the DESY accelerator system.*

~ 40 mA for the electrons and ~ 100 mA for the protons. This means that each electron and proton bunch contains about $2 \cdot 10^{10}$ and $6 \cdot 10^{10}$ particles, respectively.

4.2 The H1-detector

Since the final energy of the protons is much higher than the final energy of the electrons, a collision between them results in a particle flow, which is highest along the direction of the incoming proton, referred to as the **forward direction**. This has been taken into account in the construction of the detector, such that it is more densely instrumented in the forward region than in the backward region. The backward region of the detector is constructed such that the precision in the measurement of the scattered electron is high, which allows a very accurate determination of the event kinematics. Fig. 4.2 shows a cross-section of the H1 detector. In the figure the electrons enter from the left and the protons from the right. Closest to the collision vertex is the tracking system, which in turn is surrounded by the calorimetric system. For the central and forward regions a Liquid Argon calorimeter is used and in the backward region the so-called SPAghetti CALorimeter (SPACAL) has been installed. Outside the calorimeter system are the superconducting coil and the muon system.

The H1 Coordinate System

The coordinate system of H1 is defined such that the incoming protons move parellell to the positive z-axis, the y-axis is vertical, pointing upwards in the detector, and the x-axis is pointing towards the center of the HERA ring. Thus, the polar angle $\theta = 0^o$ coincides with the incoming proton direction and $\theta = 180^o$ is equivalent to the incoming electron direction. The azimuthal angle is denoted by ϕ.

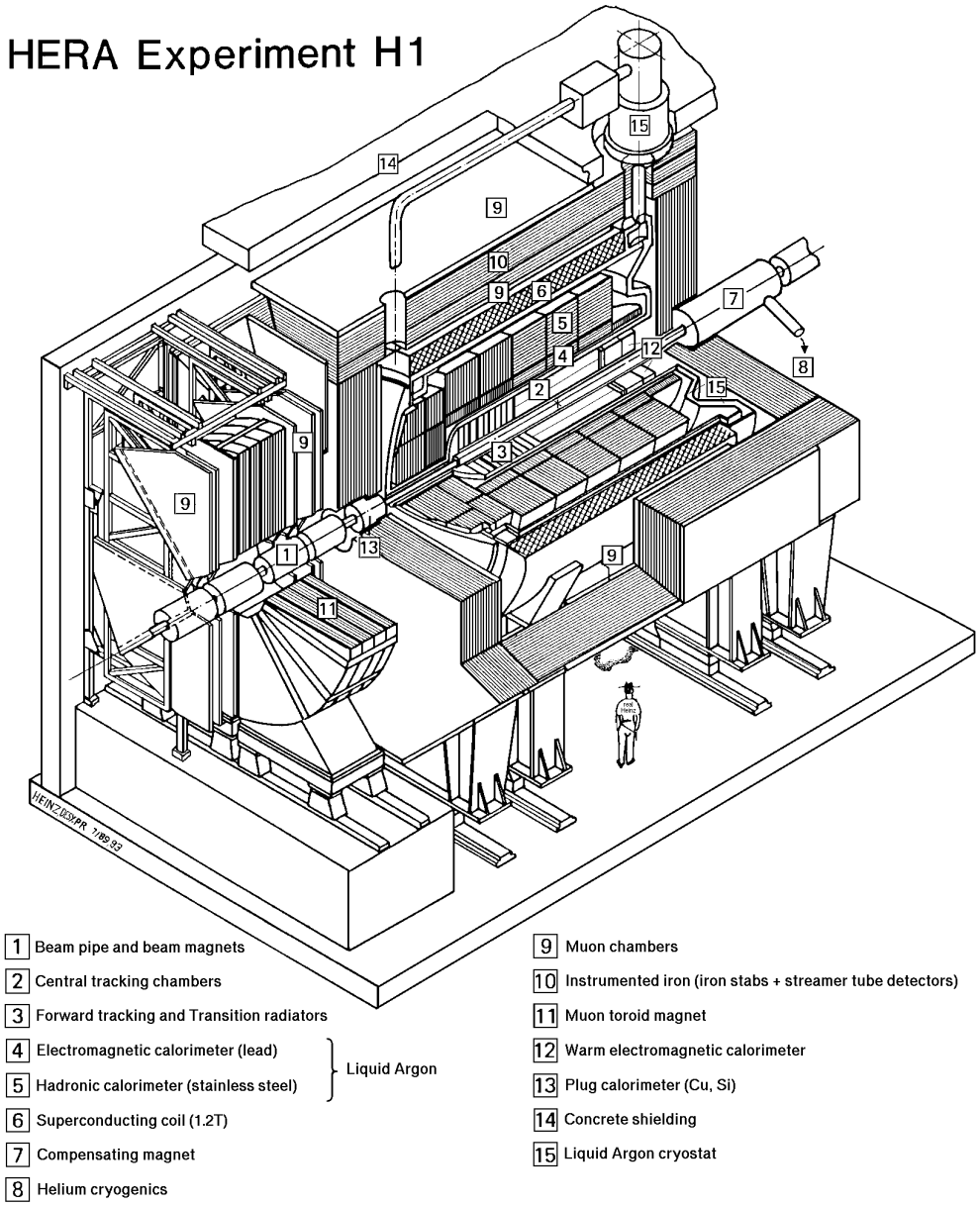

Figure 4.2: *Schematic cross-section of the H1 detector.*

Since the particle density at small angles, i.e. in the forward region, is large, the quantity rapidity, y, is often used. Rapidity is defined as:

$$y = \frac{1}{2} \ln \frac{E + p_z}{E - p_z} \tag{4.1}$$

where E is the energy of the particle and p_z its longitudinal momentum. Normally the particles are not identified, which means that their masses are not known. However, since their momenta in these collisions are much higher than their masses it is a good approximation to assume them to be massless. The rapidity is then approximated with pseudo-rapidity, η.

$$\eta = -\ln \tan \frac{\theta}{2} \tag{4.2}$$

where θ is the polar angle of the object. The shape of the distribution of y and η are Lorentz invariant under longitudinal boosts, so are (pseudo-) rapidity differences.

4.2.1 The Tracking System

The tracking system in the H1-detector is positioned closest to the interaction vertex. As can be seen in Fig. 4.3 the tracking system consists of central and forward tracking detectors as well as a drift chamber in the backward region. The momenta of charged particles are measured through their bending in a magnetic field of 1.15 T, which is generated by a super conducting coil positioned outside the calorimetric system, with the iron return yoke positioned outside the coil.

The main parts of the **central tracking system**, shown in Fig. 4.3, are two concentric drift chambers (CJC1 and CJC2) with wires strung parallel to the beam direction giving a precise reconstruction of the particle trajectory in $r - \phi$ space. The longitudinal track coordinates in these chambers are provided by the charge division method, i.e. from a comparison of the pulse heights of the signal at the two ends of the signal wire. This gives the z-coordinates with an accuracy of about 1% of the wire length. Inside CJC1 and sandwiched between CJC1 and CJC2 is a combination of one proportional chamber and one additional drift chamber. The drift chamber has wires strung perpendicular to the beam direction in order to improve the measurement of the polar angle of the track. The proportional chambers provide a fast trigger signal of an event. The momentum resolution and the angular resolution of tracks in the central tracking detector is $\sigma_p/p^2 \approx 3{\cdot}10^{-3}\text{GeV}^{-1}$ and $\sigma_\theta \approx 1$mrad, respectively. The central tracking system covers the angular range $15^o < \theta < 165^o$.

The **backward drift chamber** (BDC) has its drift cells organized in an octagonal pattern providing accurate position measurements in the radial drift direction, and thus good resolution in the polar angle of the particle trajectories. This drift chamber covers the angular range $153^o < \theta < 177.5^o$ and can measure the angle of a particle with an accuracy of $\Delta\theta < 0.5$ mrad.

For various technical reasons the **forward tracking detector** (FTD) could not be used for the analysis of the data collected in 1997. However, the current forward tracking detector consists of three modules, each consisting of two different drift chambers denoted by P and Q, respectively, in Fig. 4.3. The Q chambers have wires at $+30^o$ and $+90^o$ and

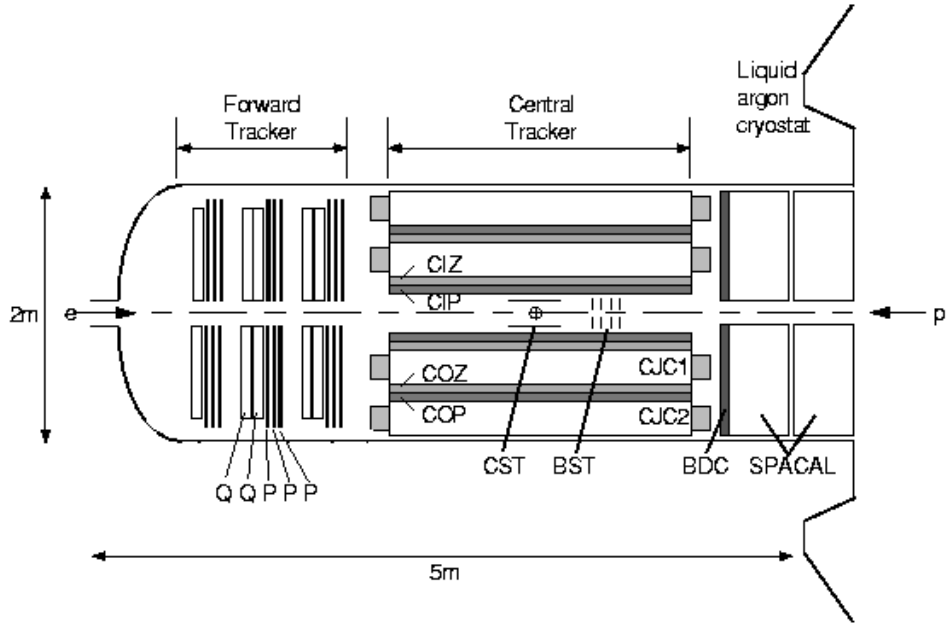

Figure 4.3: *Side view of the tracking system in the H1 detector, divided into a forward, a central and a backward tracking system (BST, BDC). In the figure is the backward calorimetric system, the SPACAL, also shown.*

the P chambers have wires at 0^o, $+60^o$ and -60^o. In contrast to the central drift chambers the wires in the forward drift chambers are only read out in one end of the wire and thus only the drift coordinate can be measured. However, by combining the information from wire planes of different directions a space point can be obtained. The forward tracking detector covers the angular range between $5^o < \theta < 25^o$.

4.2.2 Calorimetry

The Liquid Argon and the SPACAL calorimeters are both positioned inside the solenoid to reduce the amount of dead material that can cause interactions of the measured particles. Both calorimeters contain a hadronic part and an electromagnetic part.

The **Liquid Argon (LAr) calorimeter**, shown in Fig. 4.4, covers the central and the forward region of the H1-detector, corresponding to the angular range $4^o < \theta < 153^o$. The active material in the calorimeter is liquid argon and the absorbing material in the electromagnetic part is lead, while the absorbing material in the hadronic part is stainless steel. The shower created by the interactions of an incoming particle with the absorber material produces ionization in the liquid argon. To achieve a good spatial resolution the ionization is collected on small pads on an electronic board. The LAr calorimeter is subdivided into eight concentric wheels with an orientation of the absorber plates such that the impact angle is always larger than 45^o. The electromagnetic part of the LAr-calorimeter is placed closest to the beampipe. The energy resolution of the electromagnetic showers

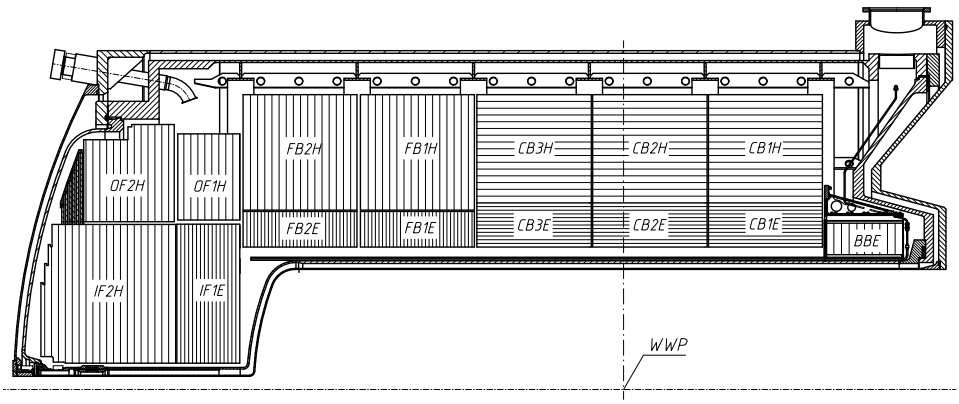

Figure 4.4: *Side view of one half of the LAr-calorimeter. The interaction vertex is denoted WWP.*

varies between 10-13% over the various modules with a constant term $< 1\%$ whereas the resolution of the hadronic showers is $\sigma/E \approx 0.5/\sqrt{E}$ with a constant term of $< 2\%$.

The **SPACAL** (SPAghetti CALorimeter), seen in Fig. 4.3 and Fig. 4.5 covers the backward region, corresponding to the angular range $154^o < \theta < 177.8^o$. The absorbing material in the SPACAL is lead for both the electromagnetic and the hadronic part. The shower particles created in the lead produce light in scintillating fibers, which are longitudinally oriented and bundled behind the calorimeter cell to connect to a light mixer. The light is collected by a photomultiplier at the end of the cell. Fig. 4.5 shows a radial cross-section of the SPACAL. Here the 60 so-called supermodules are seen, each consisting of 8 submodules which in turn consists of 52 lead plates with grooves holding the scintillating fibers. Since each submodule bundles the scintillating fibers into two bundles each supermodule is 16-channeled. The electromagnetic and the hadronic parts differ by the size of the calorimetric cells, the thickness of the absorbers and the diameter of the scintillating fibers, which is a consequence of the the different nature of hadronic and electromagnetic interactions. The main purpose of the SPACAL is to measure the scattered electron with high accuracy. The coverage of the SPACAL in polar angle corresponds to the detection of scattered electrons in the region of momentum transfer squared (c.f. Eq. 4.5), $1 < Q^2 \lesssim 100$ GeV^2. The energy resolution in the SPACAL is $7\%/\sqrt{(E)} \oplus 1\%$.

4.2.3 Luminosity Measurement

The total integrated luminosity, L, collected by the detector is defined as:

$$L = \frac{N}{\sigma} \tag{4.3}$$

where N is the number of detected events and σ is the cross-section for a certain reaction. To measure the luminosity in the H1 detector the Bethe-Heitler process $ep \to ep\gamma$ is used. This is a simple bremsstrahlung process and the theoretical cross-section of this reaction is well known. The event rate of the process can be accurately measured by tagging

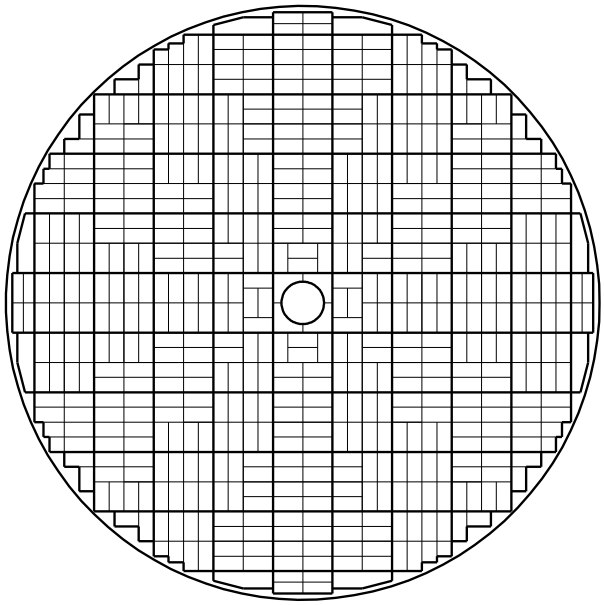

Figure 4.5: *Radial cross-section of the SPACAL. The thin lines mark individual submodules each consisting of 52 lead plates with scintillating fibers put into grooves. The thicker lines indicate the supermodules in which 8 submodules have been clustered together into a common read-out system.*

the electron and the radiated photon in coincidence. In H1 this is done with detectors positioned at -33.5m and -102.9m from the interaction vertex.

The total integrated luminosity in 1997 was measured as 13.72 pb^{-1}, which can be compared to the luminosities of 0.85 and 66.9 pb^{-1}, collected in 1994 and 2000, respectively.

4.2.4 The Trigger System

Due to the fact that the storage space for data is finite and that the data processing time is much longer than the bunch-crossing time an advanced trigger system has to be used. The bunch crossing interval of 96 ns should be compared to the readout time for a detected event in the H1 detector which is about 1 ms. Thus the idea of a trigger system is to reject uninteresting events as early as possible in the read-out sequence and just keep those which are of potential interest. This is mainly done by requiring typical signatures for signal events on different levels and reject the rest as background. The trigger system at H1 consists of four different main triggers representing different levels of triggering. Each trigger level consists of several sub-triggers and different decision algorithms.

The main purpose of the **Level 1 (L1)** trigger is to make a fast decision for each bunch crossing. L1 consists of 192 trigger elements combined into 128 sub-triggers. If one of these sub-triggers accepts the event the event is taken to the next level in the trigger system. An important L1 sub-trigger element is the one that requires the energy deposited in the SPACAL to be large enough to be a scattered electron. An example of another trigger element is the one that requires the position of the scattering vertex to be within a

reasonable distance from the nominal interaction point. If the interaction vertex is outside the nominal interaction region the event is treated as background.

The **level 2 (L2)** and the **level 3 (L3)** triggers use selection criteria which depend on the sub-trigger used in the level 1 system. The level 2 trigger investigates correlations between different detector subsystems signals by using a neural network trigger and a topological trigger. The outcome of L2 is a reject or keep decision. If the events is accepted by L2, time consuming tasks are allowed to be performed by the readout system. In the mean time L3 perform further calculations for the event. In this analysis no explicit requirements were made on the L2 trigger elements, and in the 1997 data taking L3 was not implemented.

The **Level 4 (L4)** trigger is applied only after the complete detector has been read out and the full event information is available for analysis and decision. Due to the large number of events and the limited storage volume the number of events is pre-scaled by the L4 trigger, i.e. for processes with high cross-sections only a certain fraction of the events is kept. In the physics analysis a weighting factor has to be applied in order to compensate for the pre-scaling.

If the events also pass the L4 trigger they are divided into different event classes such as DIS and jet classes. Once classified, the full event information is finally stored and available for physics analysis. Events not belonging to any class are not stored to data summary tapes.

4.2.5 The Time-of-Flight System (ToF)

As part of the trigger elements in the L1 trigger system, Time-of-Flight (ToF) detectors are used to veto background events induced by beam-gas and beam-wall interactions outside the detector region. The ToF system consists of three veto detectors, two in the forward region (at +5.3m and +7.0m from the interaction vertex) and one in the backward region (at -3.2m from the interaction vertex). Each of the veto detectors consists of scintillator arrays which define time windows for the proton beam and the electron beam. That means that the scintillators register whether the particles hitting these detectors are in coincidence with the proton beam and the electron beam respectively. Particles originating from beam-gas or beam-pipe interactions are expected to fall into a different time window compared to particles created in the true beam-beam reaction, and in that way false events can be rejected.

4.2.6 Reconstruction of Kinematic Variables

To reconstruct the full kinematics of a DIS event several different methods can be used. The accuracy in the determination of the kinematic variables by the different methods depends on which kinematic region is covered. The kinematics can be fully determined from two independent variables. The most common method is the **electron method** where the energy and scattering angle of the scattered electron are measured. The variables defined by 4-momenta as in section 2.1 can be rewritten as a function of the electron scattering angle, θ_e, and the energy of the scattered electron, E'_e

$$y \approx y_e \equiv 1 - \frac{E'_e}{E_e} \sin \frac{\theta_e}{2} \tag{4.4}$$

$$Q^2 \approx Q^2_e \equiv 4 E_e E'_e \cos^2 \frac{\theta_e}{2} \tag{4.5}$$

$$x \approx \frac{Q^2}{4 E_e E_p y} \equiv \frac{E_e E'_e (1 + \cos\theta_e)}{E_p (2E_e - E'_e (1 - \cos\theta_e))} \tag{4.6}$$

where E_e and E_p are the energies of the electron and proton beam respectively and the '$\approx$' has been introduced because that the particles masses have been neglected.

An alternative way to extract the kinematics is to use the **hadronic method** where Q^2 and y are calculated from hadronic quantities

$$y \approx y_h \equiv \sum_{h,i} \frac{E_{h,i} - p_{zh,i}}{2E_e} \tag{4.7}$$

$$Q^2 \approx Q^2_h \equiv \frac{E_h^2 \sin {\theta_h}^2}{1 - y} = \frac{(\sum_{h,i} p_{th,i})^2}{1 - y} \tag{4.8}$$

where h means hadron and i denotes the ith particle in the hadronic final state. E_h and θ_h denotes the hadronic recoil jet energy and angle, which are related by

$$\tan \frac{\theta_h}{2} = \frac{\sum_{h,i} (E_{h,i} - p_{zh,i})}{E_{t,h}} \tag{4.9}$$

A third alternative is the **mixed method** in which a combination of y_h and Q^2_e is used.

With respect to resolutions of the DIS variables in the kinematic region in which this analysis is performed the electron method has turned out to give the best results. It is therefore consistently used in this analysis. However, the other methods will be used in section 6.2.2 in order to investigate the possibility to reduce detector migrations.

4.3 Detector Simulation and Reconstruction

The detector effects are estimated by letting the Monte Carlo events undergo a full simulation of the H1 detector. The simulation is performed by the GEANT [56] based program H1SIM [57], in which all the necessary acceptances and resolutions of the detector parts are implemented. After that, the simulated Monte Carlo events are reconstructed by the program H1REC, which is the same program used to reconstruct real data.

4.4 FSCOMB Objects

In order to improve the reconstruction of the hadronic final state the tracks and calorimeter clusters are combined by an algorithm that avoids double counting. Primary vertex tracks are extrapolated into the calorimeter and merged with calorimeter clusters which are summed up within a certain radius from the track. [58] These objects are referred to as FSCOMB objects.

Chapter 5

Event Selection and Control Distributions

Events from the 1997 data collection period, comprising a total integrated luminosity of 13.72 pb^{-1}, have been used in this analysis. This chapter describes how subsamples are selected from the data files. With the full inclusive forward jet selection applied, about 18000 events remain.

In section 5.1, the kinematic cuts, applied to restrict the physics phase space adequate to the selection of DIS events, are described. A second set of cuts concerns the selection of jets in different final state scenarios. The DIS and jet selection cuts are applied on both the data and the generated MC events, i.e. the selections are made on both the detector level and the hadron level. Cuts directly related to the performance of the different detector elements used for this analysis are described in section 5.2. These detector related cuts use restrictions on objects on the detector level to optimize the reconstruction of the desired events. In section 5.3.1 those parts of the SPACAL, not used in the analysis, due to inefficiency or dead cells, are listed and section 5.3.2 describes the triggers used and the trigger selection.

In section 5.4 a number of control distributions are presented. These plots illustrate the quality of the event simulation including the simulation of the detector performance. Control distributions of the DIS variables for different subsamples and jet quantities are presented. Finally, a section is devoted to a discussion around problems connected to the so-called p_t-balance.

To simplify the discussion in the following chapters, the **hadron level** and the **detector level** are defined already here. Hadron level events are generated directly from the Monte Carlo programs. These events include all final state particles produced in the Monte Carlo generated *ep*-collison, i.e. hadrons, leptons and photons, but they do not include QED ratiation. The events on detector level include in addition QED radiation, and have been subject to the full detector simulation of H1 (H1SIM). The final mesaurements are presented for data corrected for detector effects, i.e. the data have been corrected from the detector level to the hadron level by using the ratio of the hadron level and detector level Monte Carlo samples.

5.1 Physics Selection

The cuts presented in this section are applied to both generated Monte Carlo events, detector reconstructed Monte Carlo events and data, i.e. these cuts are applied on both the hadron level and the detector level and define the phase space of the analysis. In total three different selections are needed; the DIS selection, the forward jet selection and a three jet selection, including the forward jet.

5.1.1 DIS Selection

Electron Reconstruction Cuts

The scattered electron can be detected in either the SPACAL or in the LAr calorimeter. In this analysis only the SPACAL has been used, which means that the scattering angle of the electron, θ_e, is limited to the range

$$156^o < \theta_e < 175^o \ . \tag{5.1}$$

To suppress events in which an electron signal is mimicked by a particle from the hadronic final state, a minimum electron energy is required

$$E'_e > 10 \text{ GeV} \ . \tag{5.2}$$

For low energy deposition in the SPACAL, contributions from photoproduction (section 2.6) may become significant since the electron goes undetected into the beam pipe and a hadron may be misidentified as an electron in the SPACAL. Other sources of background arise from beam-gas and beam-wall interactions.

General DIS Reconstruction Cuts

Although the relation $Q^2 = xys$ means that only two variables are needed to determine the kinematics of an event completely, the DIS phase space used for the analysis is defined by applying three cuts to have a well defined phase space for which the detector acceptance is high and understood, and more efficiently cut out background from photoproduction.

In order to constrain the scattered electron within the acceptance of the SPACAL, and remove photoproduction events, one requires that

$$5 < Q^2 < 85 \text{ GeV}^2 \tag{5.3}$$

$$0.1 < y < 0.7 \tag{5.4}$$

Finally, in order to have a well defined region in x_{Bj},

$$0.0001 < x_{Bj} < 0.004 \tag{5.5}$$

is required. These restrictions are related to the cut in Q^2 and y by $Q^2 = xys$, although the restrictions in x_{Bj} are slightly harder compared to the former cuts.

5.1.2 Forward Jet Selection

The jets in this analysis are reconstructed in the Breit frame by the inclusive k_t algorithm (described in section 2.4.2). On the detector level, the algorithm is run over FSCOMB objects [58], which are the combination information from tracks and calorimeter clusters (see section 4.4).

The angular region close to the incoming proton direction is defined as the forward region. To select forward jets the pseudo rapidity of the jets, η_{jet}, is restricted to

$$1.735 < \eta_{\text{jet}} < 2.790 \tag{5.6}$$

where the upper (forward) limit ensures that the measured jet is inside the acceptance of the detector.

In order to avoid that jets are reconstructed from detector signals which does not originate from particles in the collisions, like electronic noise, a cut on the transverse momentum of the jet, $p_{t,\text{ jet}}$, is applied. The value of the cut is chosen small enough that the statistics is not severely reduced, but high enough that the influence of noise can be neglected, and also such that there is a correlation between the parton and hadron level jets. In this analysis the cut has been set to:

$$p_{t,\text{ jet}} > 3.5 \text{ GeV} \tag{5.7}$$

To favour BFKL dynamics, which predicts partons ordered in x, the available x-range should be chosen as large as possible. The two ends of the parton evolution ladder are defined by the reconstructed forward jet and the virtual photon vertex. In order to maximize the x-range, x_{jet}, defined as the fraction of the proton energy carried by the jet, should be much larger than x_{Bj}. The restriction is set to:

$$\frac{E_{\text{jet}}}{E_{\text{proton}}} \equiv x_{\text{jet}} > 0.035 \tag{5.8}$$

where E_{jet} and E_{proton} are the energies of the forward jet and the incoming proton respectively. Since the measurements are made in the small x region, where x_{Bj} extends down to $\sim 10^{-4}$, the cut fulfills the requirement that the difference between x_{jet} and x_{Bj} is large. The cut corresponds to $p_{t,\text{ jet}} > 3.5$ GeV for jets with $\eta_{\text{jet}} = 1.735$.

The contribution from events obeying DGLAP-dynamics, which means that the partons are ordered in virtuality, i.e. $p^2_{t,\text{forward jet}} < Q^2$, is suppressed by requiring the transverse momentum squared of the forward jet to be close to the virtuality of the photon, i.e. $r = \frac{p^2_{t,\text{jet}}}{Q^2} \sim 1$. This is realized by the cut

$$0.5 < \frac{p^2_{t,\text{jet}}}{Q^2} < 5.0 \tag{5.9}$$

where the upper value is determined by detector limitations, which will be discussed in section 6.2.1. This cut is only applied for the measurement of the single differential forward jet cross section, referred to as the inclusive forward jet sample. The forward jets fulfilling the cut are called Mueller jets [59, 60].

If more than one jet fulfills the forward requirements defined above, the most forward going jet is selected. This is the case for about 1% of the inclusive forward jet events.

5.1.3 2 + Forward Jet Selection

An alternative attempt to control the parton kinematics is based on the idea that, in addition to the forward jet, two more jets will be in the event. These di-jets are selected as the two highest p_t (hardest) jets in the event, with the forward jet excluded. To further increase the resolution in momentum and direction of the jets, the transverse momenta of the central jets and the forward jet are required to be

$$p_{t,\text{ jet}} > 6 \text{ GeV}. \tag{5.10}$$

The jets are ordered in rapidity according to

$$\eta_{fwd} > \eta_{jet_2} > \eta_{jet_1} > \eta_e \tag{5.11}$$

with η_e being the rapidity of the scattered electron. The variables $\Delta\eta_1$ and $\Delta\eta_2$ can be defined as the rapidity separation between the jets, according to:

$$\Delta\eta_1 = \eta_{jet_2} - \eta_{jet_1} \tag{5.12}$$

$$\Delta\eta_2 = \eta_{fwd} - \eta_{jet_2} \tag{5.13}$$

This provides a different method, to the one used in the inclusive forward jet analysis, and controls the parton dynamics in the reaction. If the di-jet system originates from the quarks q_1 and q_2 (see Fig. 5.1), the phase space for evolution in x between the di-jet system and the forward jet is increased by requiring that $\Delta\eta_1$ is small and that $\Delta\eta_2$ is large. The restriction $\Delta\eta_1 < 1$, favours small invariant masses of the di-jet system and thereby small values of x_g.

Since the forward jet is the only jet that is restricted in rapidity space, by the demand that it has to be close to the proton axis, the directions of the other jets are related to the forward jet through the $\Delta\eta$ requirements. When $\Delta\eta_2$ is small, it is therefore possible that one or both of the additional jets originate from gluon radiation close in rapidity space to the forward jet. With $\Delta\eta_1$ large, BFKL-like evolution may then occur between the two jets from the di-jet system, or, with both $\Delta\eta_1$ and $\Delta\eta_2$ small, even between the di-jet system and the hard scattering vertex. By studying the cross section for different $\Delta\eta$ values one can test theory and models for event topologies where the k_t ordering is broken at various locations along the evolution chain.

In the 2+forward jet selection the p_t^2/Q^2-cut is not applied on the forward jet due to detector effects, which will be discussed later, and because of the reduction in statistical precision. However, the x_{jet} cut is still applied in order to favour BFKL dynamics.

5.2 Detector Level Selection

The cuts described in this section are applied to experimental data and to Monte Carlo generated events, which have been passed through the detector simulation and reconstruction. Several cuts are applied to ensure a good reconstruction of the scattered electron and of the hadronic final state.

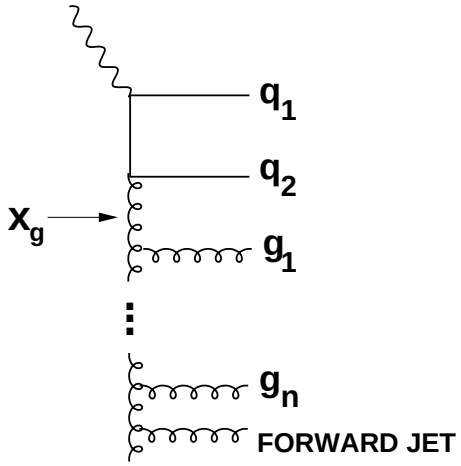

Figure 5.1: *Schematic diagram of an event giving a forward jet and a hard di-jet system. These may stem from the quarks (q_1 and q_2) in the hard scattering vertex or from the gluons in the parton ladder. x_g is the longitudinal momentum fraction of the proton carried by the propagating gluon, connecting to the hard di-jet system (in this case q_1 and q_2)*

Identification of the Scattered Electron

The following cuts are applied to ensure a well identified scattered electron:

To prevent hadrons from being misidentified as a scattered electron, one requires that the energy deposition is concentrated to the electromagnetic section of the SPACAL and that the hadronic region behind the electron cluster contains very little energy.

$$E_{\text{had}} < 0.5 \text{ GeV} \tag{5.14}$$

where E_{had} is the energy of the hadronic cluster as measured by the hadron SPACAL detector.

Photons produce similar clusters in the SPACAL to electrons, but do not give hits in the BDC, positioned in front of the SPACAL. In order to suppress fakes from combinations of hadron tracks with photon clusters, it is required that the radial distance, ΔR_{BDC}, between the BDC-track and the electron cluster in the SPACAL is less than 3.0 cm. Thus,

$$\Delta R_{\text{BDC}} < 3.0 \text{ cm}. \tag{5.15}$$

Scattered electrons which hit the SPACAL close to the edge of the detector may not deposit their full energy in the SPACAL and good energy measurement may thus suffer from transverse leakage. This is especially severe at the beam hole edge since most of the electrons are scattered at small angles. Hence, to obtain a good energy measurements one defines a "veto"-region close to the edge, in which the energy deposit is not allowed to exceed 1.0 GeV:

$$E_{\text{veto}} < 1.0 \text{ GeV} \tag{5.16}$$

where E_{veto} is the total energy deposit in the four veto layers, positioned in the SPACAL, closest to the beam pipe. They can clearly be seen in fig. 4.5.

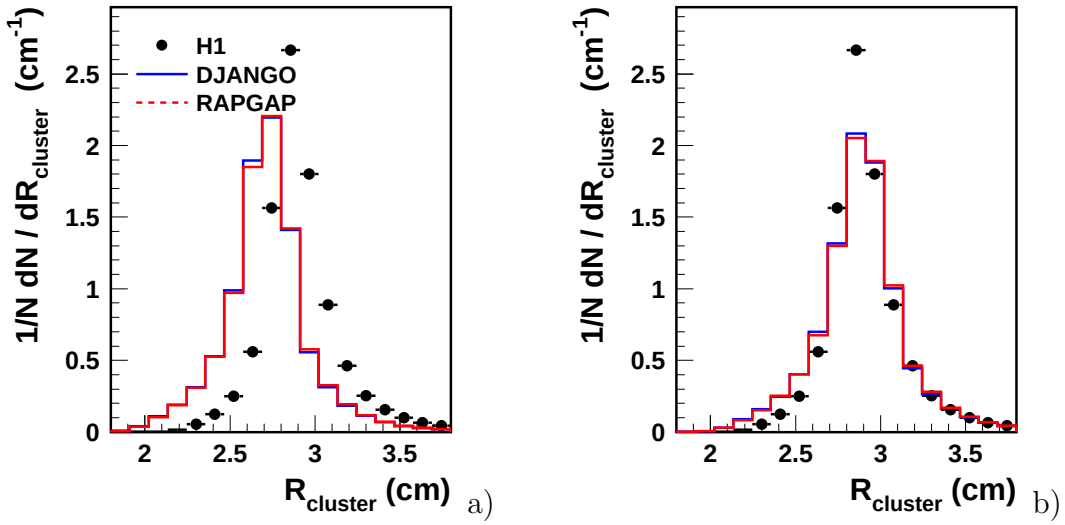

Figure 5.2: *The distributions of the electron cluster radius in the SPACAL, for data compared to detector simulated DJANGO and RAPGAP, events before (a) and after (b) the weighting factor has been applied to the Monte Carlo. The distributions are normalized to bin width and number of events.*

To reduce background from hadronic showers, the fact that hadronic showers have a broader spatial extension compared to electromagnetic showers is used. Thus it is required that the radius of the electron candidate cluster in the SPACAL is smaller than a specified value:

$$R_{\text{cluster}} < 3.5 \text{ cm}. \tag{5.17}$$

Before this cut is applied the reconstructed cluster in the simulated events is re-weighted by a factor of 1.065 due to a miss-estimate in the detector simulation [61]. Fig. 5.2 shows the R_{cluster} distribution for the DIS sample without the R_{cluster}-cut, before and after the weighting factor is applied. The agreement is still bad. However, the agreement around the cut value is clearly improved.

The Interaction Vertex

The collisions between the electrons and the protons are distributed in the z-direction around the nominal vertex position essentially due to the extension of the proton bunch. Thus, all collisions do not take place exactly at $z = 0$. Since the particle density in the bunches can normally be described by a Gaussian distribution, the frequency of collisions along the beam line also follows a Gaussian distribution around $z = 0$. Some of the beam particles will depart from the ideal beam orbit and at some stage collide with the beam-pipe. If this happens in the detector region the particles produced in the interaction with the beam pipe will give tracks in the detector. This is also true for interactions of the beam particles with the residual gas in the vacuum tube. The probability for such processes to occur is equally big around the full circumference of the HERA-ring, which means that the reconstructed collision vertex from such interactions will follow a flat distribution in z compared to Gaussian distribution for real events. Thus, by introducing a cut in z which

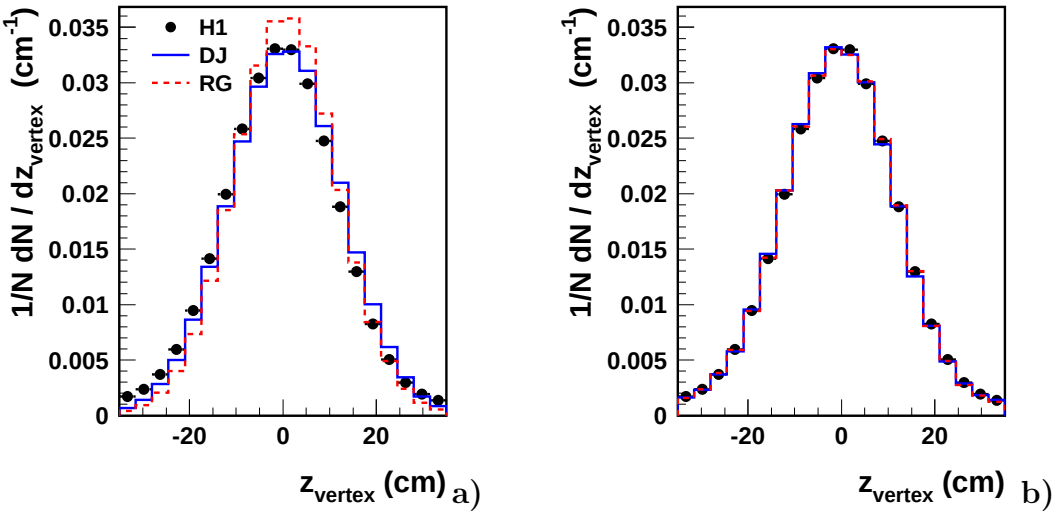

Figure 5.3: *The distributions of the z-vertex, for data compared to detector simulated DJANGO and RAPGAP events before (a) and after (b) weights have been applied to the simulated events. The distributions are normalized to bin width and number of events.*

defines the interaction region, a large fraction of the background events can be rejected. The cut which has been applied is:

$$|z_{\text{vertex}}| < 35 \text{ cm}. \tag{5.18}$$

After each new fill in HERA the beam orbits are optimized to give the highest possible luminosity. This means that the true interaction region can vary somewhat from run to run. This variation is not simulated in the reconstruction of the events, and therefore the reconstructed events have been re-weighted to describe the data. Fig. 5.3 shows the z-vertex position for data and detector simulated DJANGO and RAPGAP events, before and after the re-weighting.

The Final State $\sum_i(E_i - p_{z,i})$

Due to momentum conservation in ep-collisions it can be shown that $\sum_i(E_i - p_{z,i}) \approx 2E_e$, if the masses of the electron and proton are neglected. In the summation, i runs over all final state objects including the electron. In a real measurement the energy of the final state can only be determined to a certain degree of accuracy and therefore a cut in this variable must cover a certain region correlated to the detector performance. For the reconstructed $\sum_i(E_i - p_{z,i})$ it is required that:

$$35 < \sum_i (E_i - p_{z,i}) < 75 \text{ GeV} \tag{5.19}$$

since $2E_e = 55$ GeV at HERA energies. The purpose of this cut is to prevent events with badly reconstructed kinematics from being selected. The lower limit also removes background from photoproduction events in which the electron goes undetected in the beam-pipe. Fig. 5.4 shows the z-vertex position for data and detector simulated DJANGO and RAPGAP events, before and after the weighting.

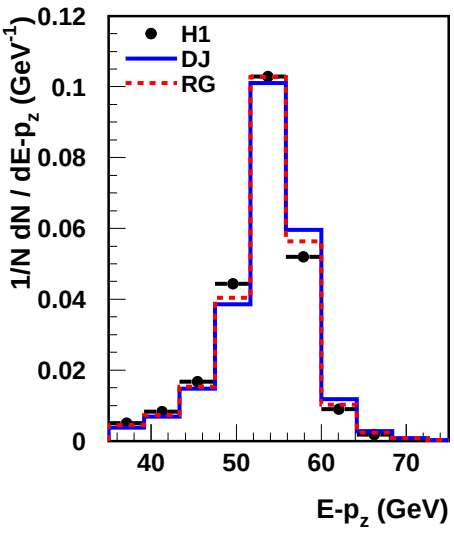

Figure 5.4: *The distribution of $E - p_z$, for data compared to detector simulated DJANGO and RAPGAP events. The distributions are normalized to bin width and number of events.*

5.3 Summary of Event Selection

Events are selected for three different measurements:

- The inclusive forward jet cross-section
- The triple differential forward jet cross-section
- The 2 + forward jet cross-section

The DIS sample is in all cases selected by applying the cuts shown in table 5.1. The forward jets are selected by the restrictions in table 5.2, where the p_t^2/Q^2-cut is applied for the inclusive forward jet cross-section only. 2+forward jet events are selected from events with 3 hard jets having $p_{t,\,\mathrm{jet}} > 6$ GeV, where one of the jets has to fulfill the "standard" requirements of an inclusive forward jet, table 5.3. The detector related cuts, applied to improve the quality of the data sample, are shown in table 5.4.

$5 < Q^2 < 85$ GeV^2
$0.1 < y < 0.7$
$0.0001 < x_{Bj} < 0.004$
$156^o < \theta_e < 175^o$
$E'_e > 10$ GeV

Table 5.1: *Cuts applied for the DIS selection.*

$1.735 < \eta_{\text{forward jet}} < 2.790$
$p_{t,\text{ forward jet}} > 3.5$ GeV
$x_{\text{forward jet}} > 0.035$
$0.5 < \frac{p^2_{t,\text{forward jet}}}{Q^2} < 5.0$

Table 5.2: *Additional requirements for the inclusive forward jet sample.*

$1.735 < \eta_{\text{forward jet}} < 2.790$
$p_{t,\text{ jets}} > 6$ GeV
$x_{\text{forward jet}} > 0.035$

Table 5.3: *Additional requirements for the 2+forward jet sample.*

5.3.1 Excluded SPACAL Regions

Due to dead cells and low efficiencies, the following regions of the SPACAL have not been used to tag the scattered electron during the data taking period used in this analysis [62].

$$\begin{array}{rrcrr}
-16.2 < x_{cog} < & 8.1 \text{ cm} & \wedge & -8.1 < y_{cog} < & 16.2 \text{ cm} \\
-25.0 < x_{cog} < & -20.5 \text{ cm} & \wedge & -37.5 < y_{cog} < & -33.0 \text{ cm} \\
-12.5 < x_{cog} < & -16.3 \text{ cm} & \wedge & -16.0 < y_{cog} < & -21.0 \text{ cm} \\
-31.5 < x_{cog} < & -25.5 \text{ cm} & \wedge & 33.1 < y_{cog} < & 39.1 \text{ cm} \\
-48.0 < x_{cog} < & -46.1 \text{ cm} & \wedge & -28.0 < y_{cog} < & -25.0 \text{ cm} \\
27.0 < x_{cog} < & 38.1 \text{ cm} & \wedge & -38.0 < y_{cog} < & -27.0 \text{ cm}
\end{array}$$

where (x_{cog}, y_{cog}) is the position of the electron cluster center of gravity.

5.3.2 Trigger Selection

The S0 and S3 L1 sub-triggers [63] have been used to select DIS events in the forward jet analysis. The combination of S0 and S3 gives trigger weights that are close to 1. The trigger requirements (expressed in the H1 trigger language) for S0 and S3 are

$$\begin{aligned}
S0 &= (SPCLe_IET > 2) \wedge (\text{BG Reduction}) \\
S3 &= (SPCLe_IET > 2) \wedge (SPCLe_ToF_E_2) \wedge (\text{BG Reduction})
\end{aligned}$$

where the requirement on the so-called Inclusive Electron Tagger, $SPCLe\_IET > 2$, means that the energy of a cluster in the SPACAL has to be larger than 5.7 GeV and $SPCLe\_ToF\_E\_2$ means that the total energy deposit in the SPACAL, within a certain time window, has to be larger than 12 GeV. Both triggers reduce the number of background events by using requirements on the time-of-flight measurement (BG Reduction). For an event produced in the interaction region the difference between the timing measurements in the forward and backward regions should be close to zero whereas for particles produced further away, but still inside the detector region, the difference increases with the distance.

$E_{\text{had}} < 0.5$ GeV
$\Delta R_{\text{BDC}} < 3.0$ cm
$E_{\text{veto}} < 1.0$ GeV
$R_{\text{cluster}} < 3.5$ cm
$\lvert z_{\text{vertex}} \rvert < 35$ cm
$35 < \sum_i (E_i - p_{z,i}) < 75$ GeV

Table 5.4: *Cuts applied on the detector level to select a clean DIS sample.*

The trigger efficiency, ϵ, is determined by using a so-called monitor trigger, which is independent of the requirements of the investigated trigger. This means that the investigated trigger and the monitor trigger should have no common requirements. The trigger efficiency is calculated bin by bin according to

$$\epsilon = \frac{N_{\text{true}\wedge\text{monitor}}}{N_{\text{monitor}}} \tag{5.20}$$

where $N_{\text{true}\wedge\text{monitor}}$ is the number of DIS events, selected according to the DIS selection, described in this chapter, accepted by both the true trigger and the monitor trigger, and N_{monitor} is the number of DIS events accepted by the monitor trigger. In this study the sub-triggers S67 and S77 are used as monitor triggers to study the efficiency of S0 and S3.

The trigger efficiencies are plotted separately in Fig. 5.5 and 5.6 as a function of E_e, θ_e, Q^2 , y and x_{Bj}. The efficiency is close to 100% in the full kinematic range for the S0 trigger. In the case of the S3 trigger the efficiency decreases at low energies of the scattered electron, due to the fact that the total energy deposit in the SPACAL is required to be larger than 12 GeV. This is also reflected in the other variables, mainly y.

5.4 Control Distributions

The sub-section shows various distributions related to the event selection. Compared to the experimental data are Monte Carlo generated events, which have undergone detector simulation and reconstruction. These plots provide information about how well the simulation of the detector performance is modeled. In this analysis events with initial and final state QED radiation on the hadron level, radiative events, have been generated by the DJANGO (CDM) and RAPGAP MC programs, and reconstructed in the detector simulation. These reconstructed events will later be used to estimate the resolution of variables and detector effects, which have to be corrected for.

5.4.1 DIS and Forward Jet Distributions

The control distributions for the DIS variables (x_{Bj}, y, Q^2, E'_e and θ_e) are shown in Fig. 5.7 for the inclusive DIS sample, and in Fig. 5.8 and 5.9 for events containing a forward jet before and after the restriction on p_t^2/Q^2 has been applied. The control distributions for the inclusive DIS sample are normalized to luminosity. Both the shape and cross-section

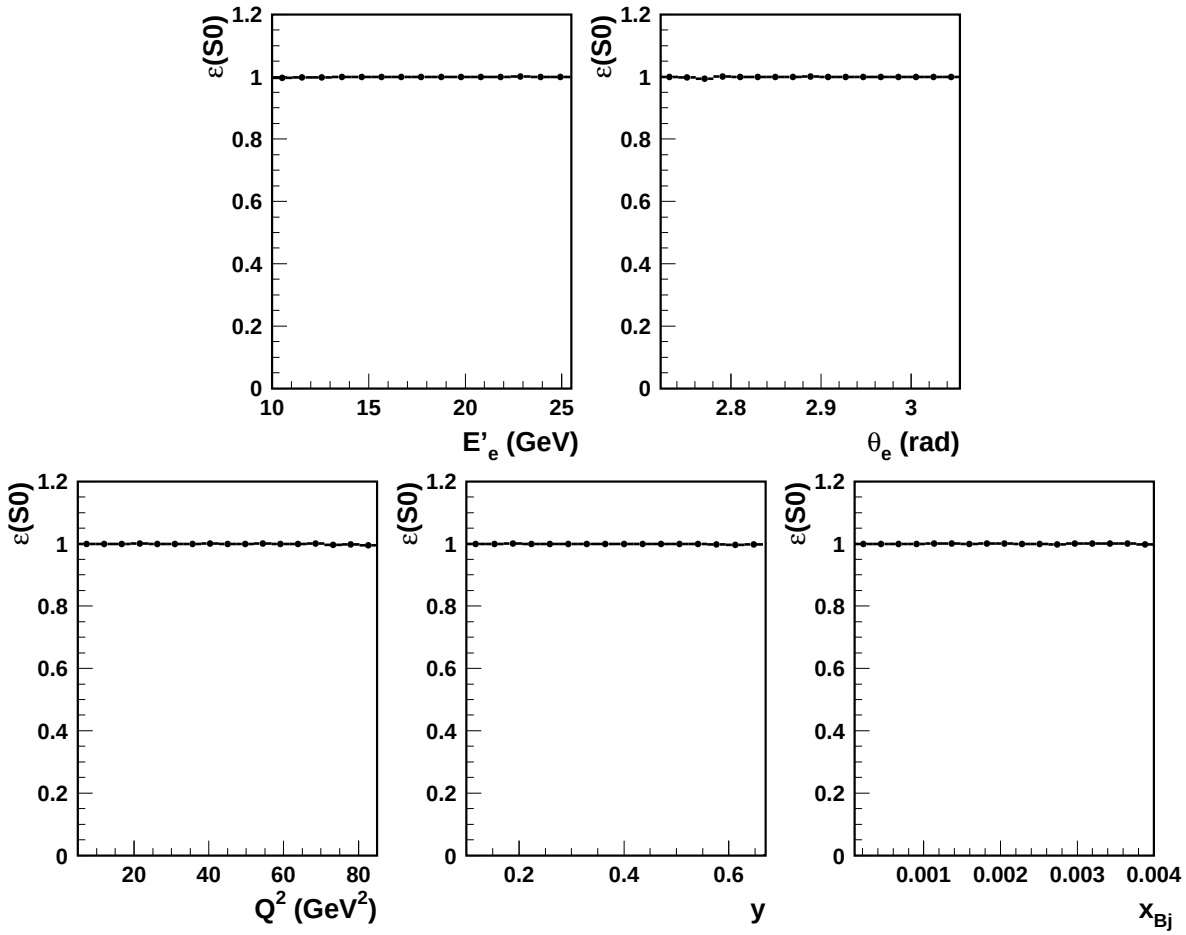

Figure 5.5: *Efficiencies for the S0 trigger measured as a function of the DIS variables.*

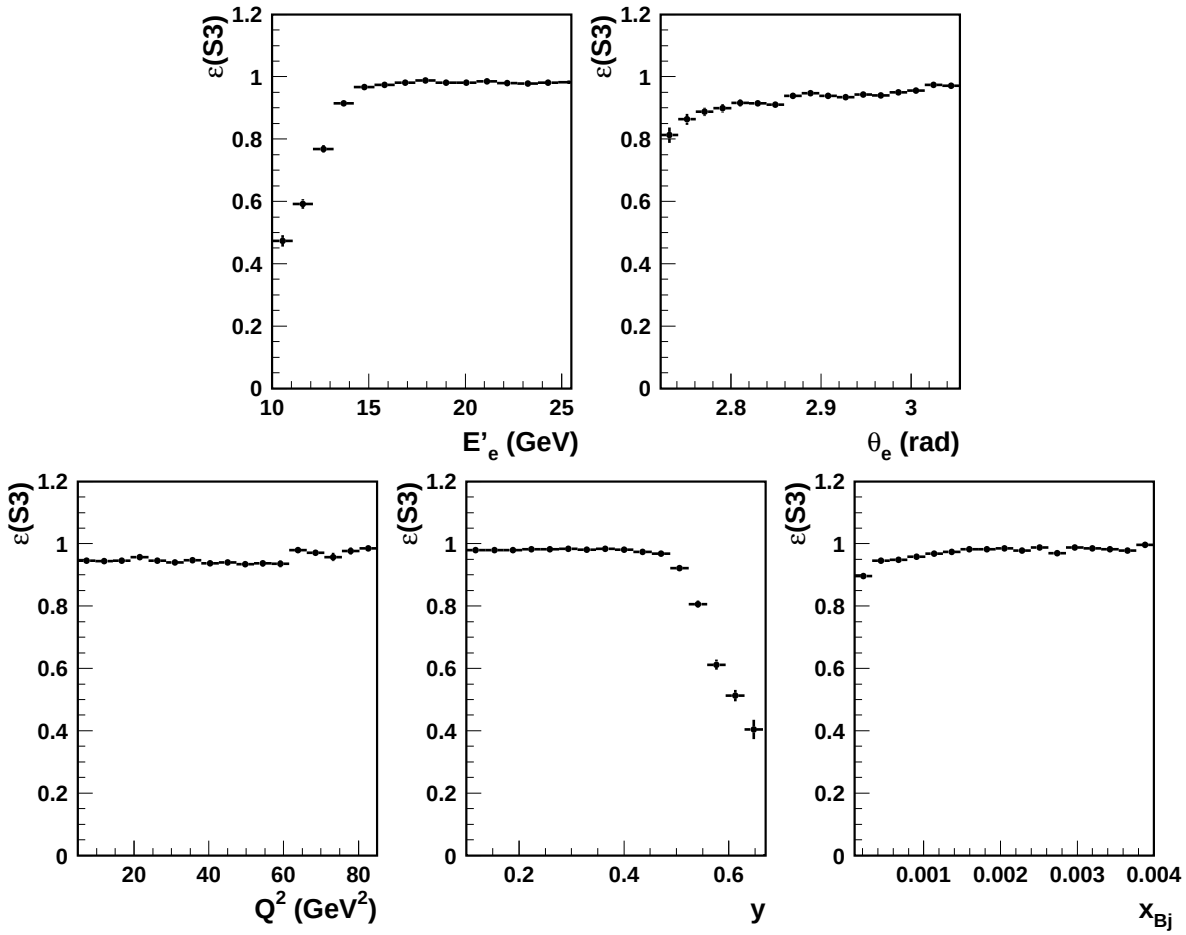

Figure 5.6: *Efficiencies for the S3 trigger measured as a function of the DIS variables.*

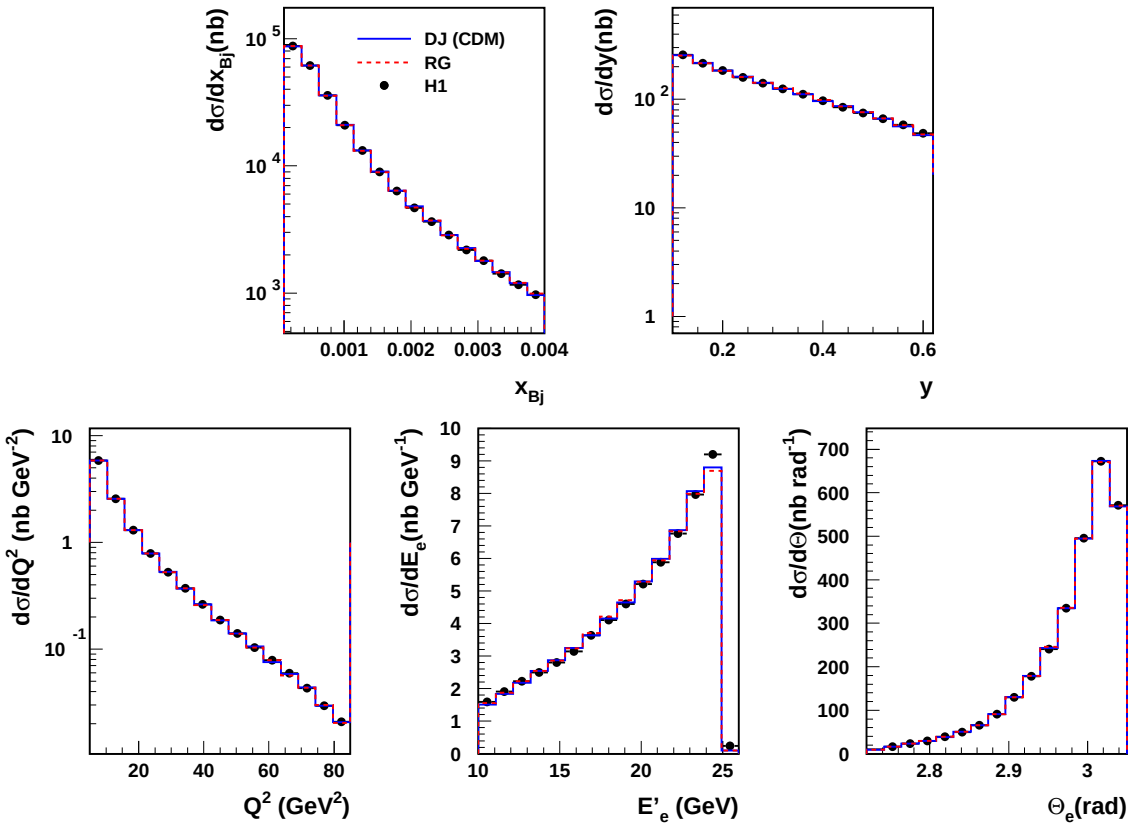

Figure 5.7: *Control distributions for the reconstruction of DIS kinematic variables from the inclusive DIS event sample.*

are described by the simulations. The control distributions for the forward jet events are normalized to the number of events since the forward jet cross-section is highly model dependent. In this case the data are better described in shape by the DJANGO Monte Carlo program than the RAPGAP generator.

For the same two forward jet samples the control distributions of the jet variables ($p_{t,\,\mathrm{jet}}$, E_{jet}, η_{jet}, ϕ_{jet} and $p^2_{t,\,\mathrm{jet}}/Q^2$) in the lab frame are shown in Fig. 5.10 and 5.11 without and with the $p^2_{t,\,\mathrm{jet}}/Q^2$-cut applied. For the sample without $p^2_{t,\,\mathrm{jet}}/Q^2$-cut the reconstructed RAPGAP events describe the data better in shape than the DJANGO events, while in the case with $p^2_{t,\,\mathrm{jet}}/Q^2$-cut the DJANGO events do slightly better, except for the $p_{t,\,\mathrm{jet}}$ and E_{jet} distributions.

The jet control distributions for the 2+forward jets are shown in Fig. 5.12.

5.4.2 The p_t-balance

According to momentum conservation the transverse momentum carried by the scattered electron should be balanced by the transverse momentum of the hadronic final state in the laboratory frame. The p_t-balance is, thus, defined as the transverse momentum of the

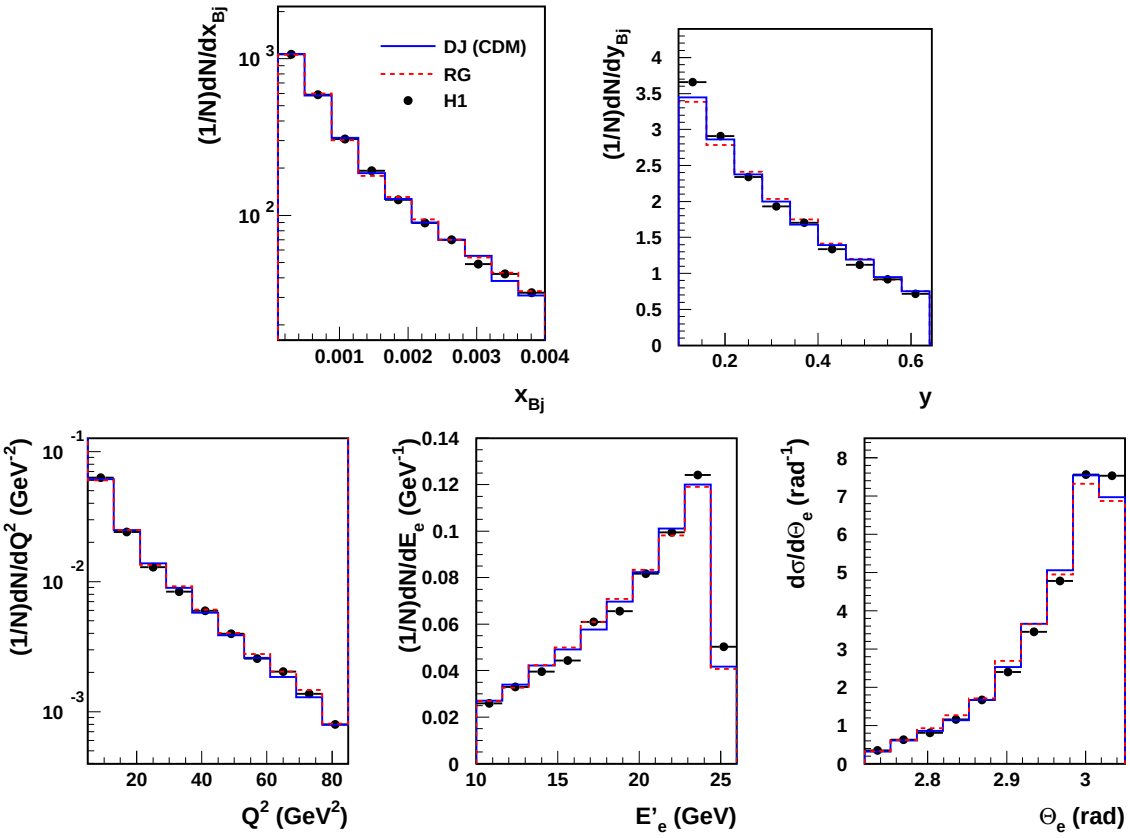

Figure 5.8: *Control distributions for the reconstruction of DIS kinematic variables for the forward jet sample without p_t^2/Q^2-cut.*

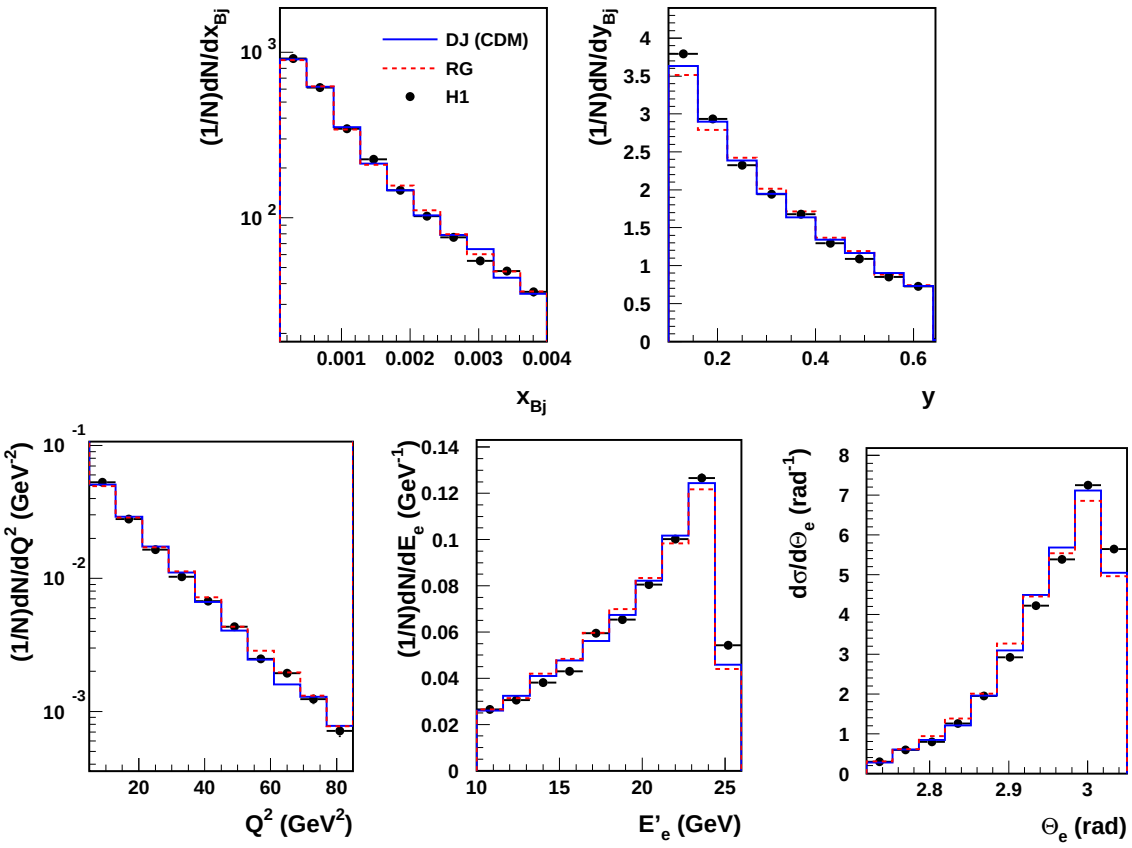

Figure 5.9: *Distributions of reconstructed kinematic quantities in the forward jet sample with the p_t^2/Q^2-cut applied. Data and the predictions of DJANGO and RAPGAP are shown.*

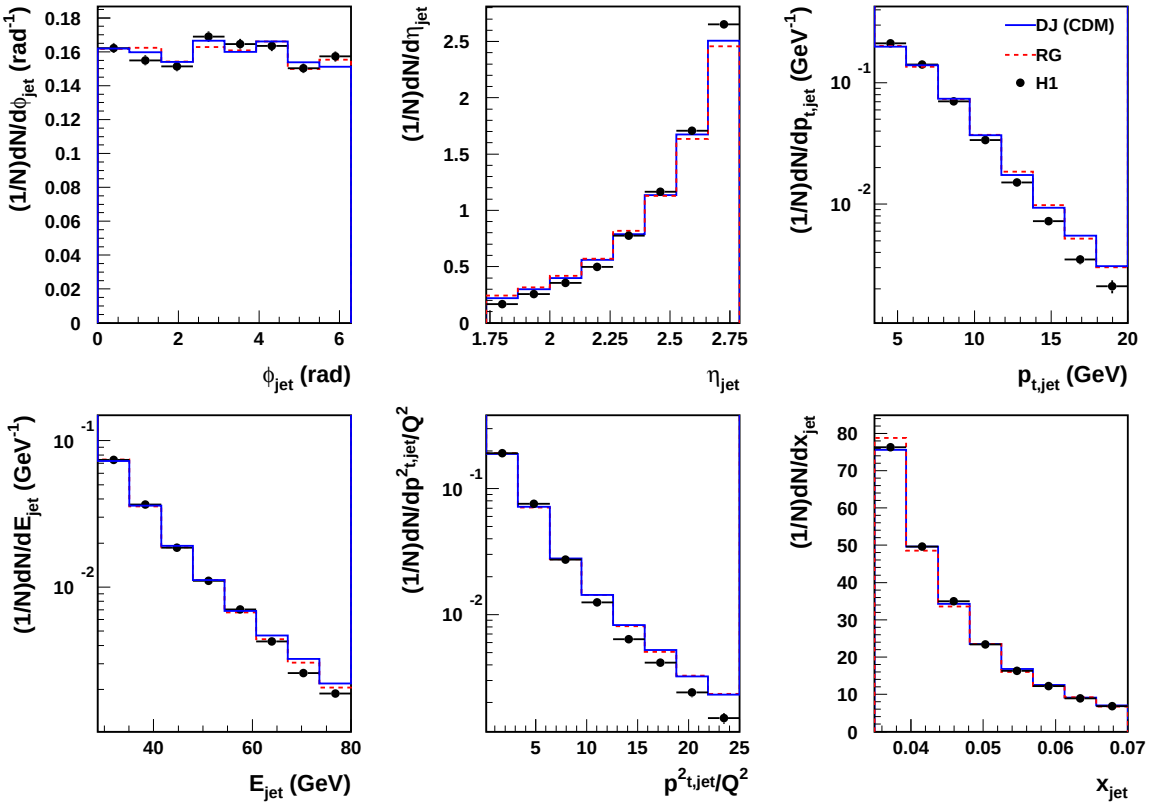

Figure 5.10: *Distributions of reconstructed kinematic jet quantities in the forward jet sample without the p_t^2/Q^2-cut applied. Data and the predictions of DJANGO and RAPGAP are shown.*

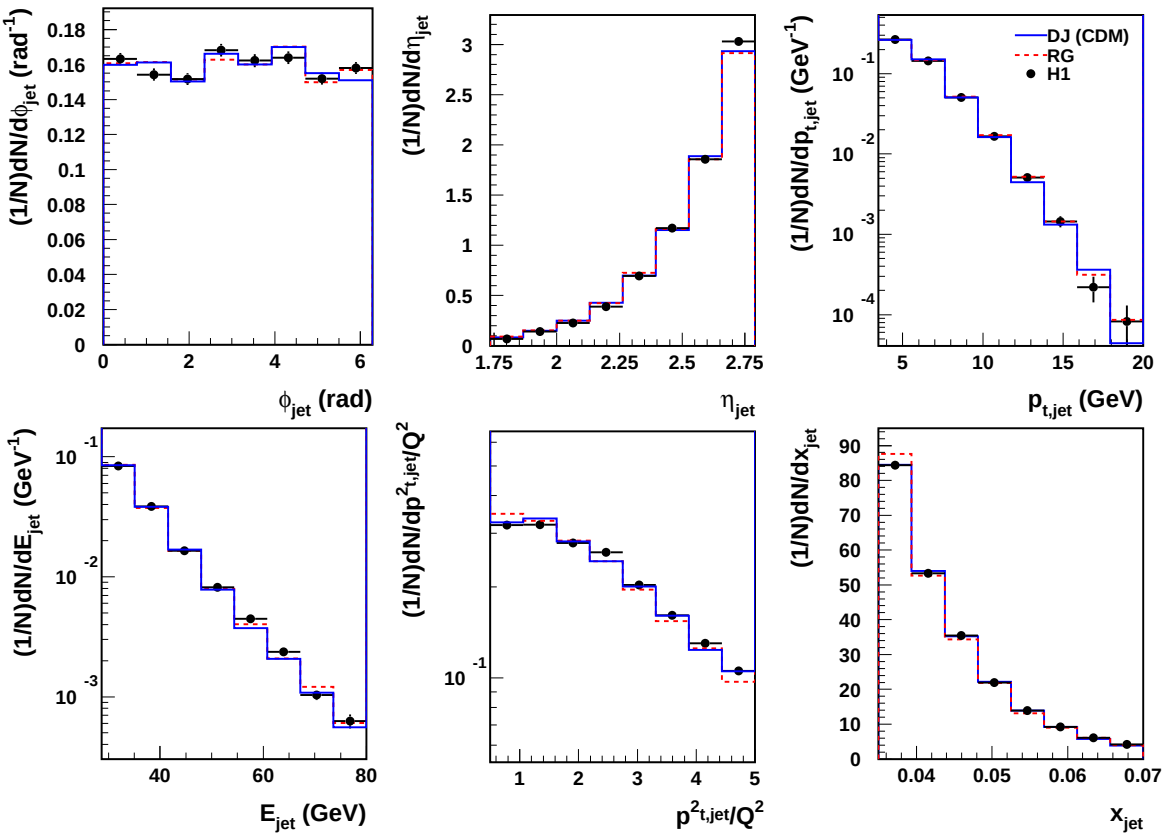

Figure 5.11: *Distributions of reconstructed kinematic jet quantities in the forward jet sample with the p_t^2/Q^2-cut applied. Data and the predictions of DJANGO and RAPGAP are shown.*

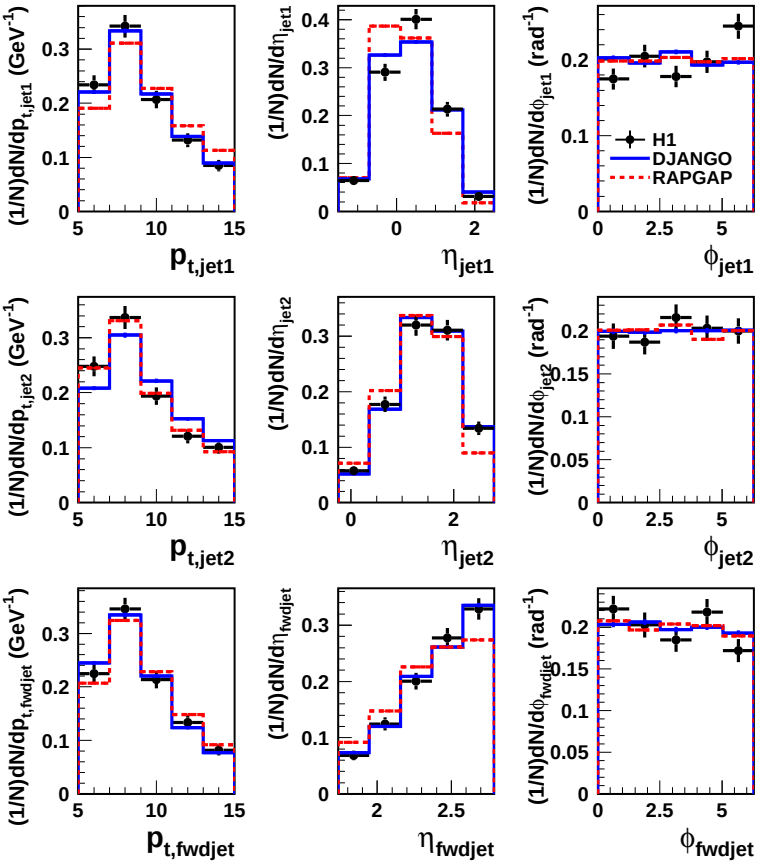

Figure 5.12: *Distributions of reconstructed kinematic jet quantities in the 2+forward jet sample. Data and the predictions of DJANGO and RAPGAP are shown. p_t is expressed in GeV.*

hadronic final state (hfs) divided by the transverse momentum of the electron

$$p_t\text{-balance} = \frac{p_{t,\text{hfs}}}{p_{t,e}} \tag{5.21}$$

where the transverse momentum p_t of the hadronic final state is calculated as

$$p^2_{t,\text{hfs}} = p^2_{x,\text{hfs}} + p^2_{y,\text{hfs}} = (\sum_i p_{x,i})^2 + (\sum_i p_{y,i})^2 \tag{5.22}$$

where the hfs momentum components p_x and p_y have been summed over all particles in the hfs, i.

The expected distribution of the p_t-balance should be peaked around unity. However, if there are systematic errors in the measurement of the hadronic final state the distribution could be shifted. The width of the distribution is determined by the measurement resolution and the solid angle covered by the detector. Although the aim is always to cover as much of 4π as possible it is unavoidable to include holes for detector support and for the beam pipe. To illustrate how the size of the beam pipe hole would influence the resolution in the p_t-balance determination, the p_t-balance has been plotted in Fig. 5.13 for six different scenarios for the angular coverage of the detector. As can be seen in (a) the backward beam-pipe opening, which is fixed to 0.07 rad in all plots (i.e. $\theta < 3.07$), has little influence on the resolution of the p_t-balance. This is also according to expectations since events in the Q^2-range 5 to 85 GeV do not contain hadrons along the incoming electron direction. However, as the beam hole in the forward direction is opened up, it is evident from Fig. 5.13 that the p_t-balance distribution becomes wider. For larger beam-pipe cuts there is a difference between the distribution obtained from events generated by DJANGO and the events generated in RAPGAP. This is a reflection of the fact that the CDM model generates more energy close to the proton beam direction [64] than RAPGAP, which leads to a model dependence such that one of the models will give a better description of the experimental data than the other for different conditions.

The actual cuts, corresponding to the full detector acceptance, have been applied in Fig. 5.14. Thus, objects outside the detector acceptance ($0.07 < \theta < 3.07$) are removed from the event before the p_t-balance is calculated. The results are shown for DIS events (a) and forward jet events (b). The effect of the beam-pipe cut is stronger for DJANGO than for RAPGAP, again due to the fact that the former produces more energy in the forward direction. The asymmetry in the distributions comes from the fact that the p_t-balance can not be negative but can be larger than 2.

In Figs. 5.14 ((c) and (d)) the p_t-balance distributions of Monte Carlo events on the detector level are compared to experimental data for inclusive DIS events and for forward jet events. It is observed that RAPGAP describes the DIS data quite well for the DIS events, whereas the description of the forward jet data is less convincing. DJANGO fails to reproduce the shape of the p_t-balance distributions for both samples. As the p_t-balance is model dependent it can not be used as a very good measure of the detector reconstruction quality. However, the fact that all studied distributions peak at 1, as expected, gives positive indications of the detector reconstruction quality.

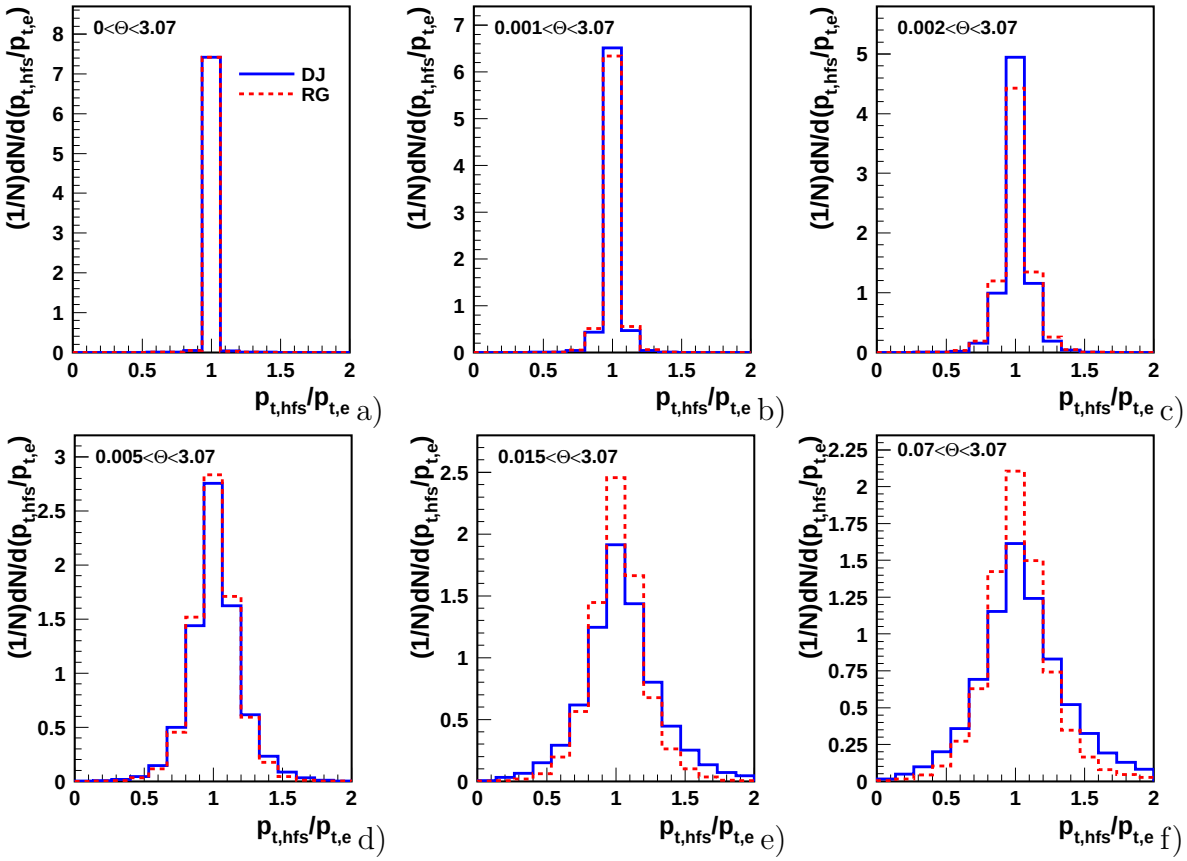

Figure 5.13: *The p_t-balance distributions for hadron level events, using different cuts on the polar angle (given in radians). The backward cut has been kept fixed to $\theta = 3.07$ rad in all plots. Distributions are plotted for the two generators, DJANGO (Full line) and RAPGAP(Dashed line), which have been used for the detector simulation. The distributions are normalized to the number of events.*

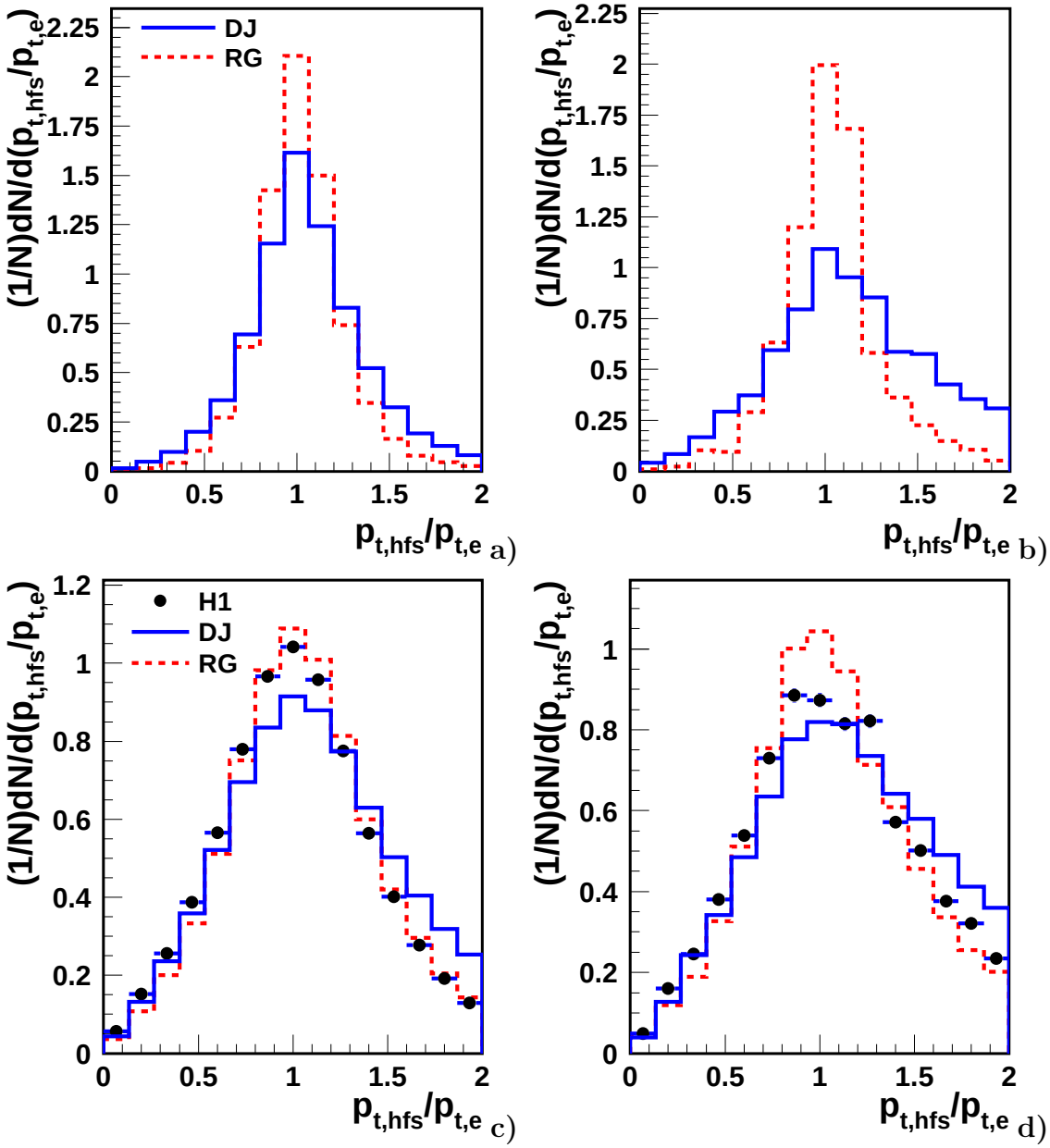

Figure 5.14: *The p_t-balance distributions on the hadron level (a and b) and the detector level (c and d), respectively, for DIS events (a and c) and forward jet events (b and d). On hadron level the distributions are plotted for DJANGO and RAPGAP, and on the detector level also for data. The distributions are normalized to the number of events.*

Chapter 6

Detector Effect Studies

In this chapter the events used to calculate the cross-sections are further studied. In section 6.1 the cross-sections, which are of interest for the analysis, are summarized, and in section 6.2 some detector effects are investigated in terms of purity (P) and stability (S). It is described how the purity and stability depend on the upper limit of the p_t^2/Q^2 cut. A toy model is constructed and studied to better understand variations of P and S.

In section 6.3 a special investigation of jet resolutions in the forward region is presented. Here the reconstruction of jets is studied by simulating single pion or single quark emissions at fixed angles and at fixed energy. The hadron level and the detector level jets are compared, and an alternative weighting scheme for the LAr calorimeter, originally calculated for pions, is tried for jets in the forward direction.

In section 6.4 the correction factors used to correct for detector effects are discussed.

Section 6.5 comprises another study of the jet reconstruction. It is shown that secondary scattering against one of the collimators close to the beam-pipe may have an effect at low transverse momenta, but for the jet samples used in this analysis the effect is well implemented in the detector simulation and thus taken care of in the correction of the data to the hadron level.

Finally, in section 6.6 the systematic errors of the measurement are presented.

6.1 The Cross-section Measurements

The following cross-sections are measured in this analysis.

Inclusive Forward Jet Cross-section, $\frac{d\sigma}{dx_{Bj}}$

The inclusive forward jet cross-section is measured as a function of x_{Bj}. The events for this sample are selected by the kinematic restrictions in table 5.1 and table 5.2.

Triple Differential Cross-section, $\frac{d\sigma^3}{dx_{Bj}dp_t^2dQ^2}$

For the triple differential cross-section the events have been selected according to the same kinematic cuts for the inclusive forward jet measurement, but instead of using the p_t^2/Q^2-cut the binning has been made in p_t^2 and Q^2 dividing the phase space into different regions of $r = p_t^2/Q^2$. Again the cross-section is studied as a function of x_{Bj}.

2+Forward Jet Cross-section, $\frac{d\sigma}{d\Delta\eta_2}$

The 2+forward jet cross-section is measured according to the principles explained in 5.1.3, where the relevant variables are also defined. The cross-section is measured as a function of the rapidity separation between the forward jet and the di-jet system, $\Delta\eta_2$, for two regions of the rapidity separations, $\Delta\eta_1$, between the central jets, $\Delta\eta_1 < 1$ and $\Delta\eta_1 > 1$. Again the phase space is restricted by the cuts in table 5.1 and table 5.2, but in this case the p_t^2/Q^2-cut is not used due to detector effects and statistical reasons.

6.2 Purity and Stability

Purity (P) and stability (S) are defined, according to H1 standards, as the number of MC events reconstructed (i.e. events on the detector level) and generated (i.e. events on the hadron level) in a bin divided by the number of reconstructed events for P, or number of generated events for S, in that bin:

$$P = \frac{N_{HAD\wedge DET}(\text{same bin})}{N_{DET}} \text{ (Calculated in bins of the detector variable)}$$

$$S = \frac{N_{HAD\wedge DET}(\text{same bin})}{N_{HAD}} \text{ (Calculated in bins of the hadron variable)}$$

Both quantities are calculated for events that have already passed the DIS selection. In addition a forward jet event is only added to the events in the numerator if the distance between the generated forward jet and the reconstructed forward jet in η-ϕ space is less than 1, i.e.

$$R = \sqrt{(\phi_{had} - \phi_{det})^2 + (\eta_{had} - \eta_{det})^2} < 1 \tag{6.1}$$

P (S) is thus a measurement of how large a fraction of the events that has migrated into (from) a specific bin by either bin-to-bin migration or migrations across the kinematic cuts defined in section 5.1. Obviously P and S should be close to, but not larger than, unity.

6.2.1 p_t^2/Q^2-cut Dependence

In Fig. 6.1 the purity and stability have been calculated using events generated by DJANGO both for different upper cuts on p_t^2/Q^2 and without any requirement on p_t^2/Q^2. It is seen that the P and S depend strongly on the upper limit of p_t^2/Q^2. The cut of $0.5 < p_t^2/Q^2 <$

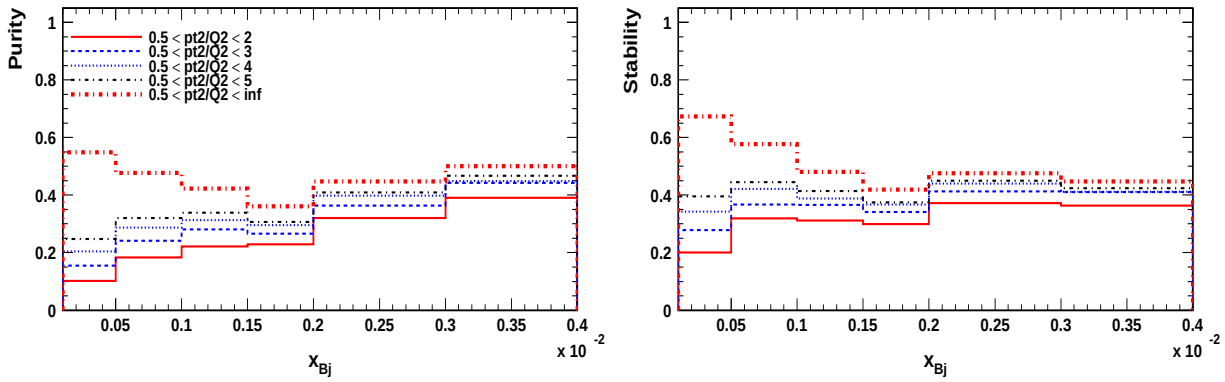

Figure 6.1: *Purity and stability, calculated from events generated by DJANGO, and fulfilling the forward jet selection cuts, as a function of* x_{Bj}.

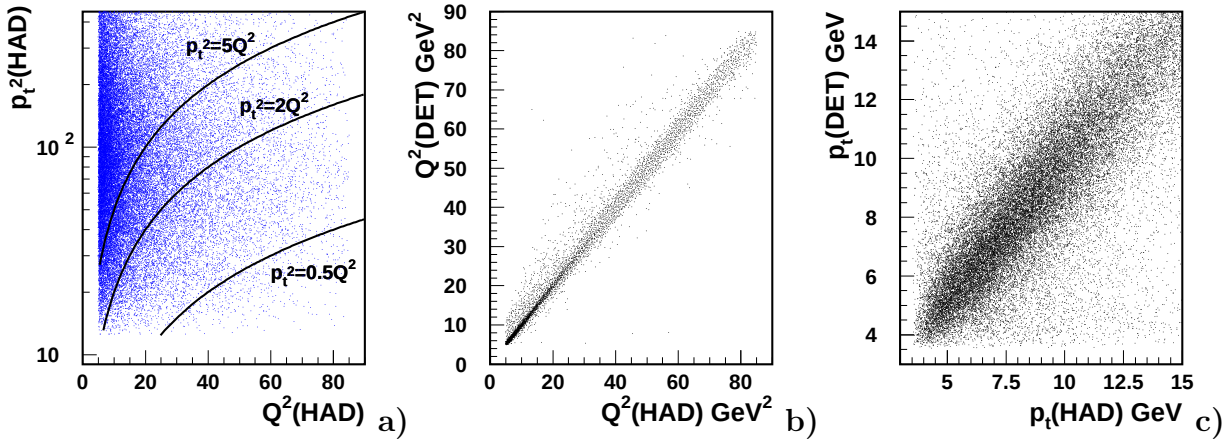

Figure 6.2: *Fig. a) shows the* $p_t^2 - Q^2$*-phase space and the cuts corresponding to* $0.5 < p_t^2/Q^2$, $p_t^2/Q^2 < 2$ *and* $p_t^2/Q^2 < 5$ *indicated by the 3 lines respectively. Figs. b) and c) show the correlation between the reconstructed (DET) and the generated (HAD)* Q^2 *and* p_t *values, respectively.*

2.0, which has been used in previous analyses, leads to values below 30% over a large x_{Bj} range and has therefore not been used in this analysis. Instead, in order to increase P and S to a reasonable level, the upper limit has been increased to 5. On one hand p_t^2/Q^2 should be as close to unity as possible to suppress the phase space for DGLAP. On the other hand P and S must have reasonable values.

The explanation for the behavior is that, as can be seen in Fig. 6.2a), changing the upper limit from 2 to 5 leaves a larger part of the p_t-phase space untouched, together with the fact that the resolution in the p_t measurement is much worse than that of the Q^2 determination. This is illustrated in the Figs. 6.2b) and c) where the hadron level quantity is plotted versus the detector level quantity.

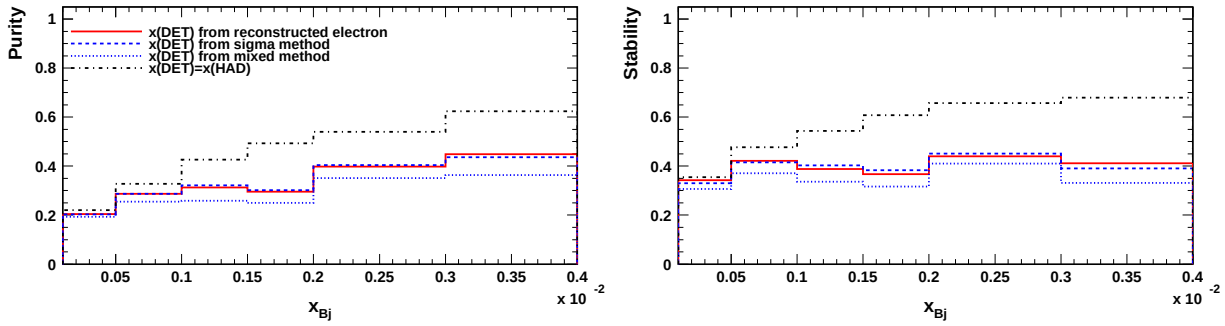

Figure 6.3: *Purity (P) and Stability (S) versus x_{Bj}, reconstructed with different kinematic methods, for forward jet events generated by DJANGO fulfilling the requirement* $0.5 < \frac{p_t^2}{Q^2} < 4$.

6.2.2 Reconstruction of x_{Bj}

The low values of P and S are partly due to to bin-to-bin migration in x_{Bj}. A test was made to see if one can improve P and S by changing the method used to reconstruct x_{Bj}. In Fig. 6.3 the purity and stability for the forward jet events with $0.5 < \frac{p_t^2}{Q^2} < 4$ is plotted as a function of x_{Bj} calculated by different kinematic reconstruction methods. The standard method is to use the measured scattered electron alone, but in some kinematic regions it can be more favorable to use either the sigma method or the mixed method, where combined clusters and tracks (FSCOMB objects) are used instead. These methods were discussed in section 4.2.6. To show the effects of bin to bin migrations in x_{Bj}, purity and stability are also plotted for the same events but with $x_{Bj(DET)}$ forced to be equal to $x_{Bj(HAD)}$ ($x_{Bj(DET)} = x_{Bj(HAD)}$), i.e. all bin to bin migration in x_{Bj} is avoided. As seen, the purity and stability can not be improved by using the sigma method or the mixed method. Further it is also observed that in the lowest x_{Bj} bin the low P and S can not be related to bin-to-bin migrations, but have to be explained completely by migrations across the kinematic limitations.

6.2.3 A Toy Model for Estimating P and S

In order to understand the behavior of P and S better a simple toy model was developed. The toy model uses the resolution, measured from MC events generated by DJANGO, for the various kinematic variables to simulate migrations between bins and across the selection cuts. In the toy model each variable is generated from some simple random number distribution or equally distributed random numbers approximating the true distributions of the variable. The toy model variable is then smeared by using random numbers, generated according to a Gaussian distribution with a width and shift equal to the resolution and shift of the true variable. The non-smeared and the smeared variables then correspond to being calculated on the hadron level and measured on the detector level, respectively, and are used to calculate purity and stability. The resolutions of the jet variables are measured for all events and forward jets fulfilling the selection criteria only, i.e. the resolutions for the variables are approximated with the average resolution within the analysis phase space. Furthermore, no correlations between the variables are implemented in the toy model.

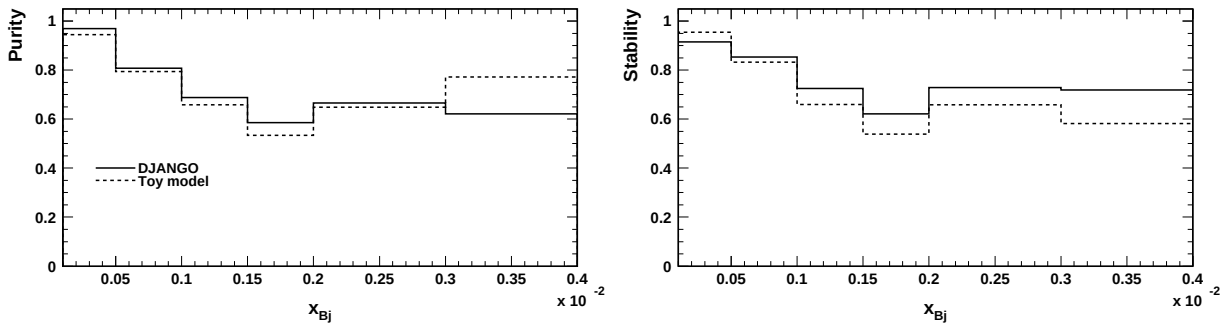

Figure 6.4: *Purity (P) and stability (S), for DIS events, generated by DJANGO and compared to a simple toy model.*

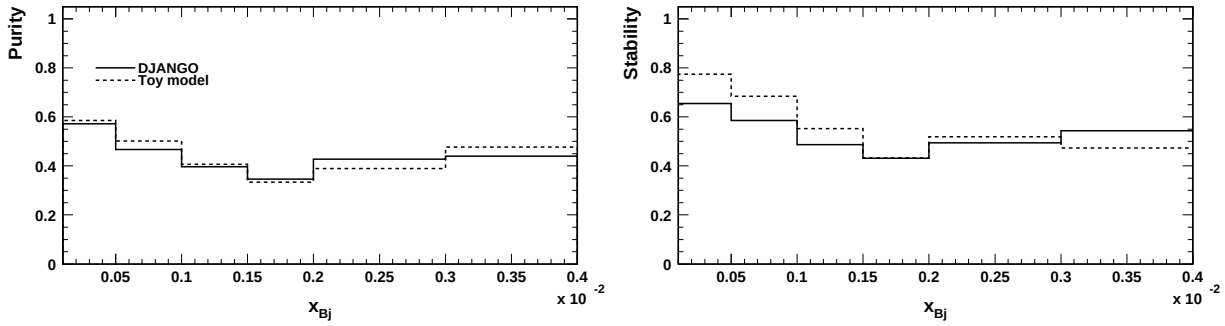

Figure 6.5: *Purity (P) and stability (S), for forward jet events without any p_t^2/Q^2-cut, generated by DJANGO and compared to a simple toy model.*

In Fig. 6.4-6.6 a comparison is made between P and S, calculated for different selection criteria, by DJANGO and the toy model. In Fig. 6.4 P and S are calculated for DIS events only. The first observation is that there is a reasonably good agreement between the toy model and DJANGO. From the figures and the definitions of P and S it can be concluded that bin to bin migrations in x_{Bj} are fully responsible for lowering P and S by up to 40%. A similar conclusion could already be drawn from Fig. 6.3 in section 6.2.2. By requiring that the events contain a forward jet but without any restrictions on p_t^2/Q^2, P and S are decreased to a level of 40-50% as can be seen in Fig. 6.5. Finally, in Fig. 6.6 the cut $0.5 < p_t^2/Q^2 < 5$ is also applied and one sees that the additional decrease in P and S is related to the p_t^2/Q^2-cut. This conclusion agrees with what was seen in Fig. 6.1. However at this point DJANGO and the toy model no longer agree at low x. This indicates that the shape of the distributions or the event population density over the phase space investigated is not well enough simulated in the toy model. Although the toy model is very simple the overall agreement between DJANGO and the toy model is surprisingly good.

6.2.4 Final P and S

In Fig. 6.7 the purity and stability calculations from forward jet events simulated by RAPGAP and DJANGO are compared as function of x_{Bj}. In Figs. 6.8 and 6.9 the corresponding P and S comparisons for the triple differential cross-section are shown. In this case the bin

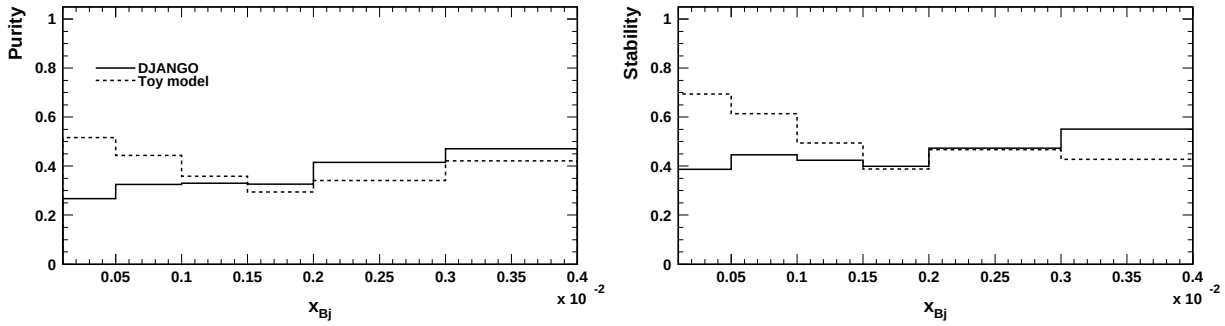

Figure 6.6: *Purity (P) and stability (S), for forward jet events, generated by DJANGO and compared to a simple toy model, with the* $0.5 < p_t^2/Q^2 < 5.0$ *cut applied.*

width in p_t^2 has been chosen twice as large as the resolution in p_t^2 in order to suppress the migrations and thus give reasonable values of P and S ($> 30\%$). The binning in Q^2 has been chosen to give equal statistics in each Q^2 bin. Finally in Fig. 6.10 P and S for the 2+forward cross-section are calculated by both RAPGAP and DJANGO. The conclusion from the figures is that the P and S in all cases are acceptable. This gives confidence in the measurement.

6.3 $p_{t,\,jet}$ Resolution Study

In order to better understand the limitations in the forward jet energy determination and to find out whether it would be possible to improve it, a systematic study was performed in which single pions and quarks, respectively, where generated in specific directions, listed in Table 6.1. The quark was allowed to hadronize and the resulting jet was reconstructed using the inclusive k_t-algorithm as in the analysis. The energy of the pions and quarks were generated at 30 GeV. In the case of single pions the jet should just be a single pion as long as no noise is clustered together with the pion into a jet. For consistency the jet algorithm was used for both the single quark and the single pion scenarios.

θ	η
7	2.794
10	2.436
15	2.028
20	1.735
25	1.506
30	1.317

Table 6.1: *The angles in which the pions and the single quark jets are simulated.*

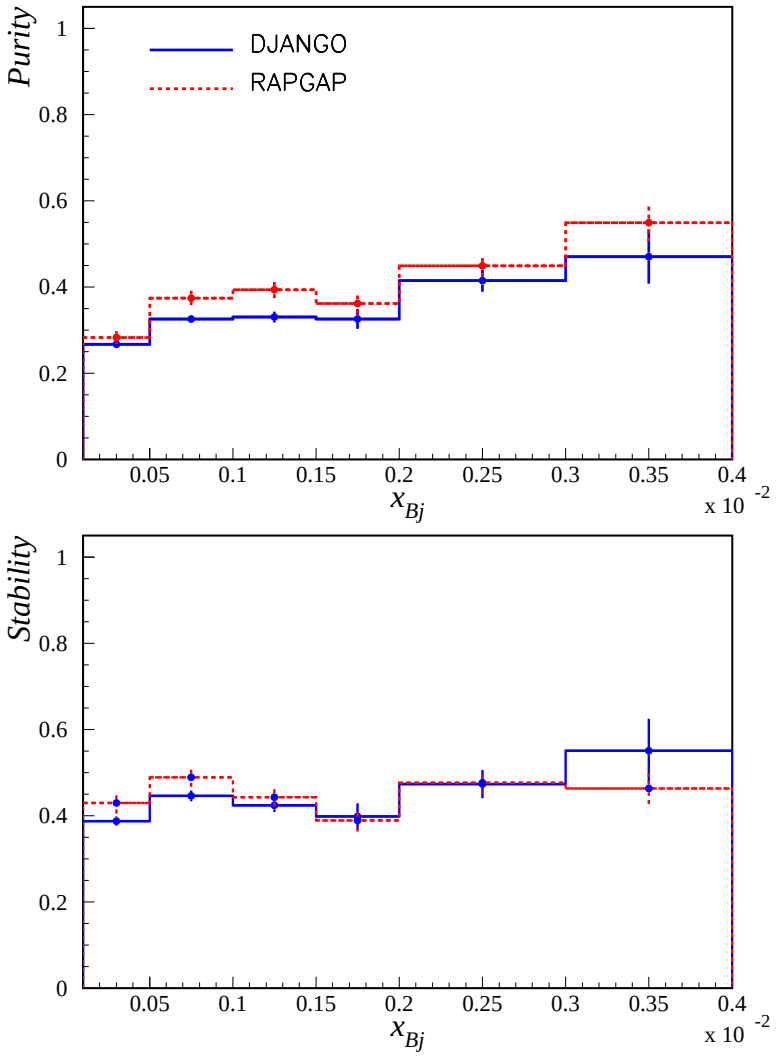

Figure 6.7: *Purity (P) and Stability (S) for forward jet events, with the p_t^2/Q^2-cut applied, as a function of x_{Bj}, calculated by RAPGAP (dashed line) and DJANGO (full line).*

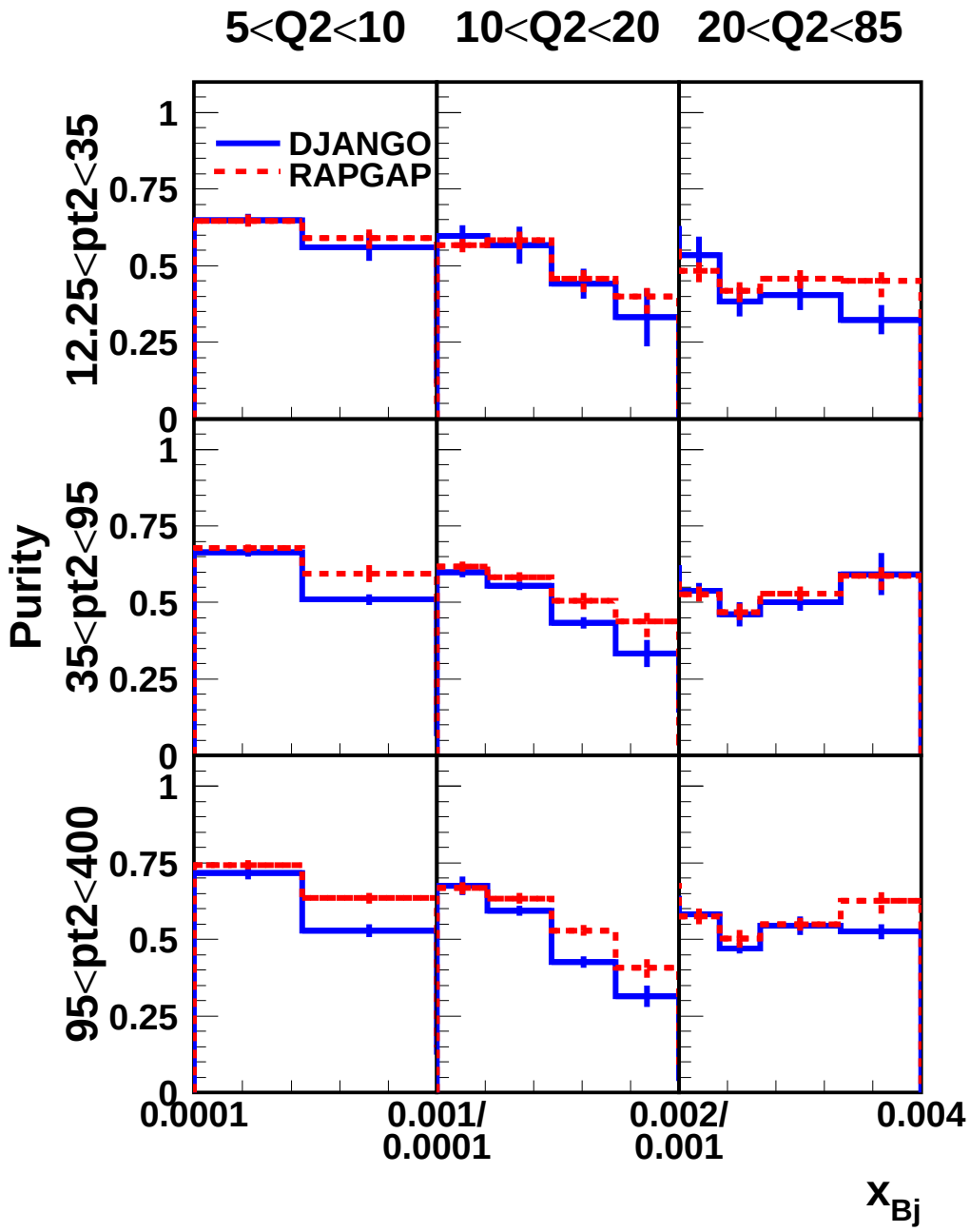

Figure 6.8: *Purity (P) for forward jet events as a function of x_{Bj}, as calculated by RAPGAP (dashed line) and DJANGO (full line), in bins of p_t^2 and Q^2.*

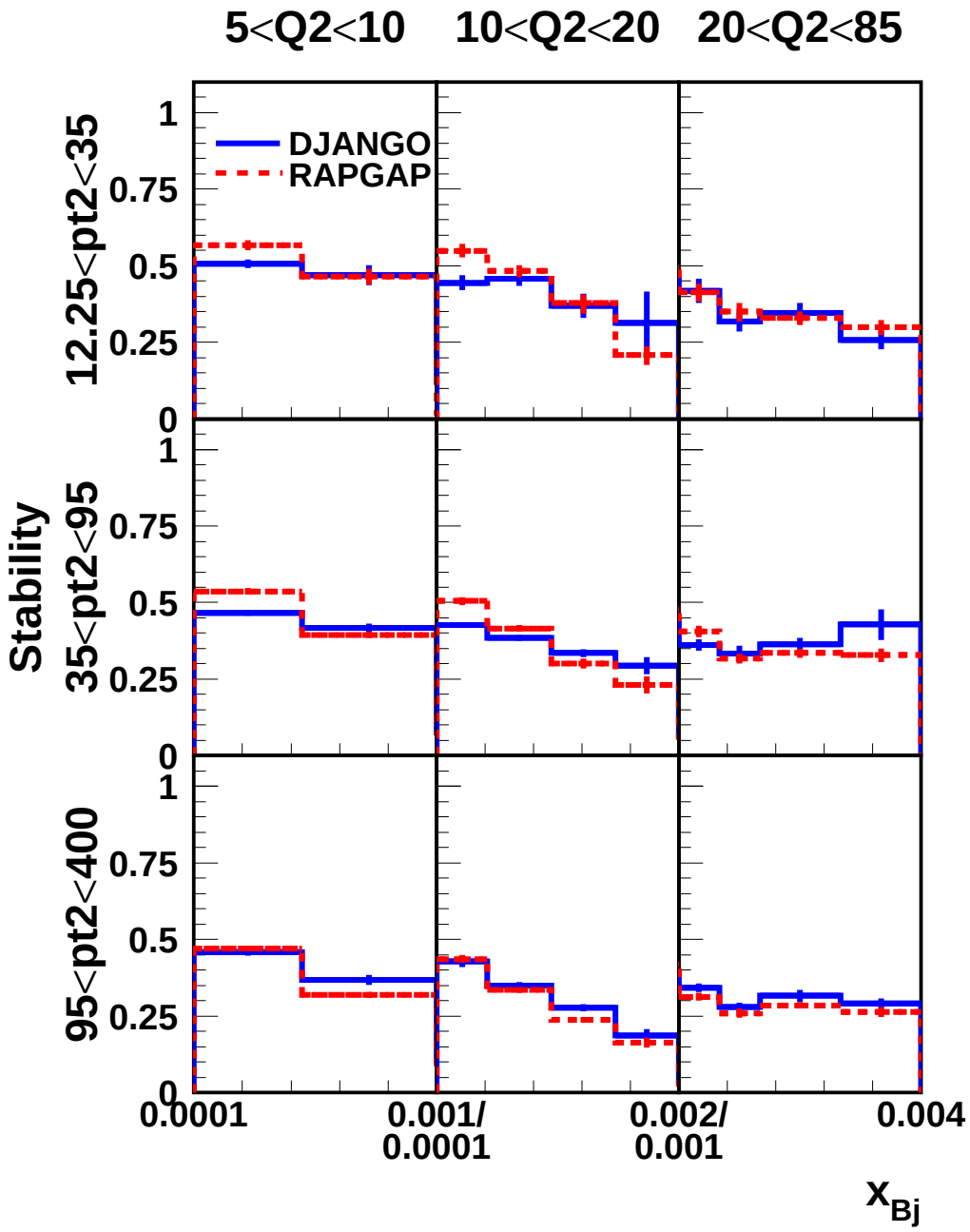

Figure 6.9: *Stability (S) for forward jet events as a function of x_{Bj} as calculated by RAPGAP (dashed line) and DJANGO (full line), in bins of p_t^2 and Q^2.*

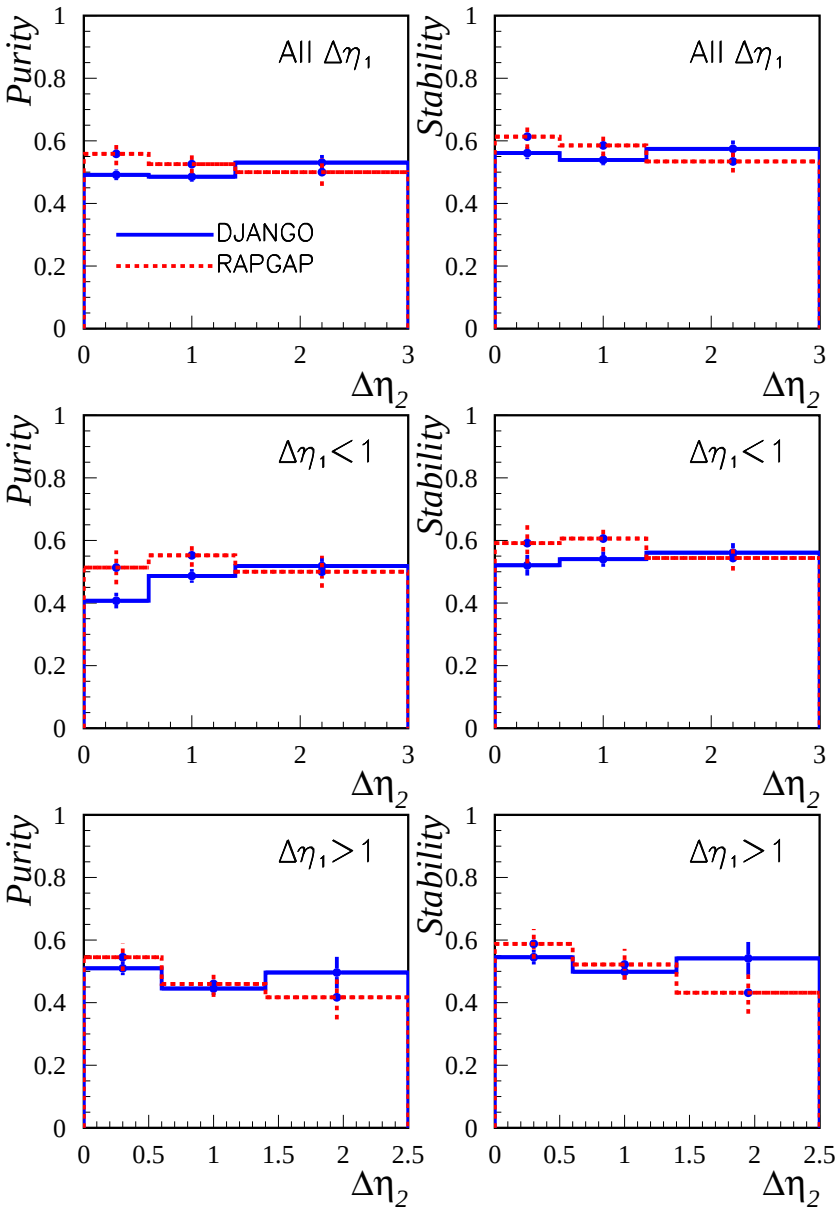

Figure 6.10: *Purity and Stability for the 2+forward jet events as a function of $\Delta\eta_2$ and for different $\Delta\eta_1$ choices, calculated by RAPGAP (dashed line) and DJANGO (full line).*

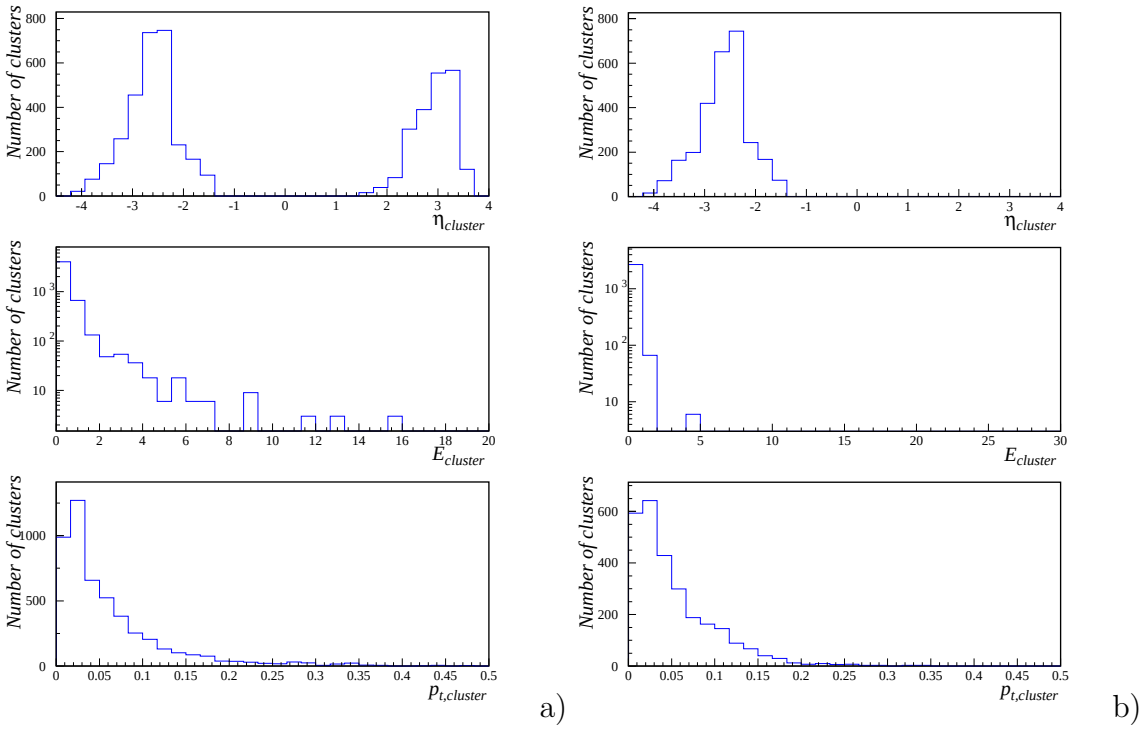

Figure 6.11: *Number of calorimeter clusters as a function of rapidity, energy (GeV) and transverse momentum (GeV) of the clusters from 2000 events generated with a single pion emitted in the beam direction. Thus, the detector is expected to be empty. The distributions are shown for events simulated with (a) and wihtout (b) the electronic noise of the LAr calorimeter.*

6.3.1 Single Pion Emission

As a start pions were generated in the beam direction only, which would leave the detector empty. Fig. 6.11a) shows the result and reveals that the detector contains a large number of clusters in the forward and backward regions. These clusters are mainly of low energy and low p_t, but one can also notice some clusters of very high energy. In order to investigate the clusters in the forward region, which could have great influence on this analysis, the same events were reconstructed again in the detector simulation but now with the electronic noise files of the LAr calorimeter empty. The results are shown in Fig. 6.11b). All the clusters in the forward region have disappeared and they can thus be related to electronic noise in the LAr. The fact that there are still clusters in the backward region is due to the fact that the SPACAL simulation is kept unchanged. In this analysis the noise in the backward direction may affect the reconstruction of the scattered electron only. However, this is avoided by the electron cuts and the detector level restrictions applied to improve the reconstruction of the scattered electron as described in chapter 5.

The jet energy distributions are shown in Fig. 6.12 for the different rapidity directions, normalized to the number of generated events. The detector level distributions are calculated using two different hadronic final state energy weighting schemes for the LAr calorimeter. The full line corresponds to the distribution which is obtained using the stan-

dard calibration scheme, while the dotted line shows the distribution as obtained using an alternative weighting scheme [65]. On the hadron level (dashed line) the distribution obviously has a sharp peak at 30 GeV, whereas on the detector level one gets a distribution given by the detector resolution. The standard scheme shows a significant shift towards lower energies with respect to the hadron level peak. The peak position from the alternative scheme, however, gives much better agreement. In both cases the distributions have a sharp peak at the lowest energies. This originates from the electronic noise clusters which are described above and shown in Fig. 6.11a). The improvement of the alternative weighting scheme can also be seen in the energy resolution plots, Fig. 6.13, where the resolutions on the detector level have been calculated for jets with energies above 10 GeV, to remove the noise clusters, and using the fixed 30 GeV pion energy on the hadron level as reference. The lower energy cut of the jets is chosen with respect to the dip visible between the true peak and the peak originating from the noise clusters at low energies in the energy distribution of the pions (Fig. 6.12).

Finally, the objects are required to have $p_t > 0.7$ GeV in order to be considered by the jet algorithm. The cut is chosen to be far from the p_t of the the noise clusters in Fig. 6.11, but also roughly corresponds to the cut $E_{jet} > 10$ GeV used above. From a comparison of the jet multiplicities on the detector level and the hadron level before and after the E_{jet} cut has been applied, it is proven that the noise reduction cut is well chosen. Figs. 6.14 and 6.15 shows the jet multiplicity with and without the p_t-restriction on the objects. Requiring $p_t > 0.7$ GeV gives a more or less perfect agreement between the detector level and the hadron level jet multiplicities. One has to keep in mind that the energy of the pions is fixed at 30 GeV, and in the real data analysis the cuts above have to be more carefully chosen if pions with smaller energies are to be considered.

6.3.2 Single Quark Emission

In this section single quark emissions with the same fixed angles (table 6.1) as the pion, is described. The quark is allowed to hadronize such that jets can be studied.

In Figs. 6.16-6.18 energy distributions, energy resolutions, and jet multiplicities are shown for the single quark jet events. Here the standard weighting scheme does a better job than in the one-pion case, while the alternative weighting scheme gives worse resolution and seems to shift the energy slightly towards higher energies. Again $E_{jet} > 10$ GeV is required in the resolution plots.

The jet multiplicity distribution, shown in Fig. 6.18, clearly shows that additional jets are reconstructed, leading to an unreasonable number of jets per emitted quark. This is the case not only on the detector level but also on the hadron level where one should expect one jet per event only. On the hadron level the only possible explanation would be that this is an effect of the jet reconstruction algorithm. The additional detector level jets at low energies can be expected to originate from the low energy noise clusters in the forward region, consistent with what was observed in the pion case. In order to verify this, the requirement $p_{t,\,\mathrm{jet}} > 3.5$ GeV, which corresponds to the momentum restriction used in the analysis, was introduced. This results in 1 jet per event on both the hadron level and the detector level, except in the most forward regions where, in some events, no jet is found,

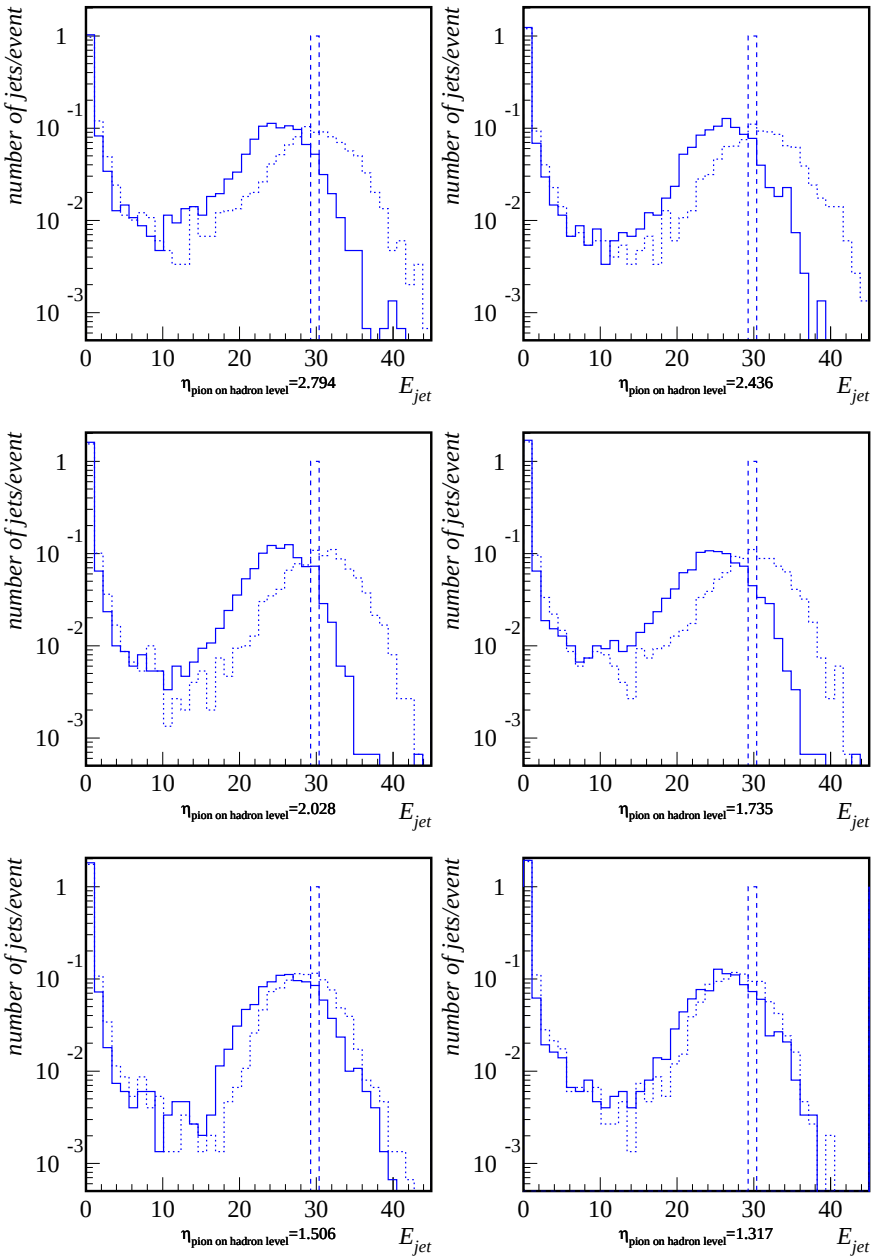

Figure 6.12: *Energy (GeV) distributions for single pions emitted in specific directions (see table 6.1) normalized to the number of events. The dashed line illustrates the hadron level, the full line the detector level with the standard hadronic final state (hfs) weighting scheme and the dotted line the detector level with alternative hfs weighting scheme.*

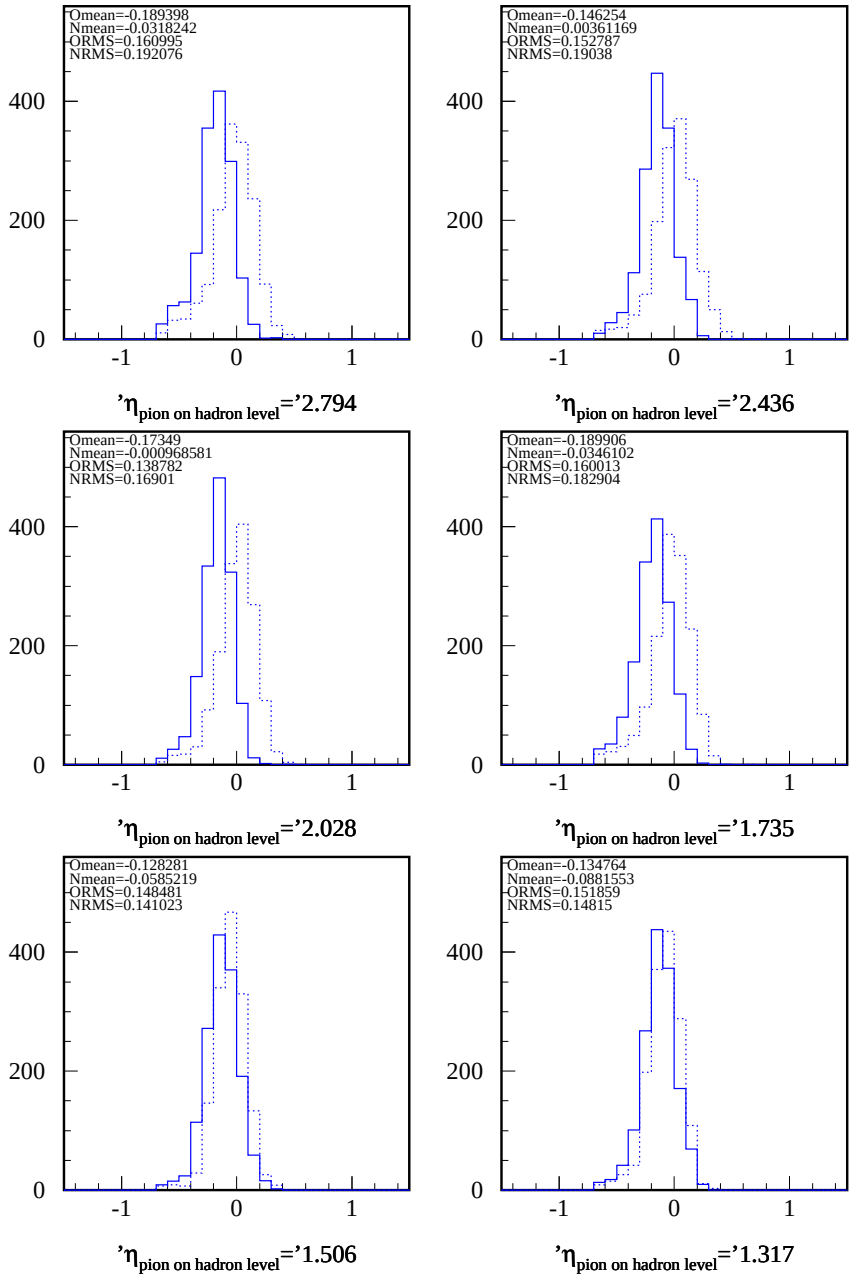

Figure 6.13: *Energy (GeV) resolutions for pions with* $E_{detectorlevel} > 10 GeV$ *and fixed* $E_{hadronlevel} = 30 GeV$*. The full line illustrates the detector level with standard hfs weighting scheme (Omean, ORMS) and the dotted line the detector level with alternative hfs weighting scheme (Nmean, NRMS).*

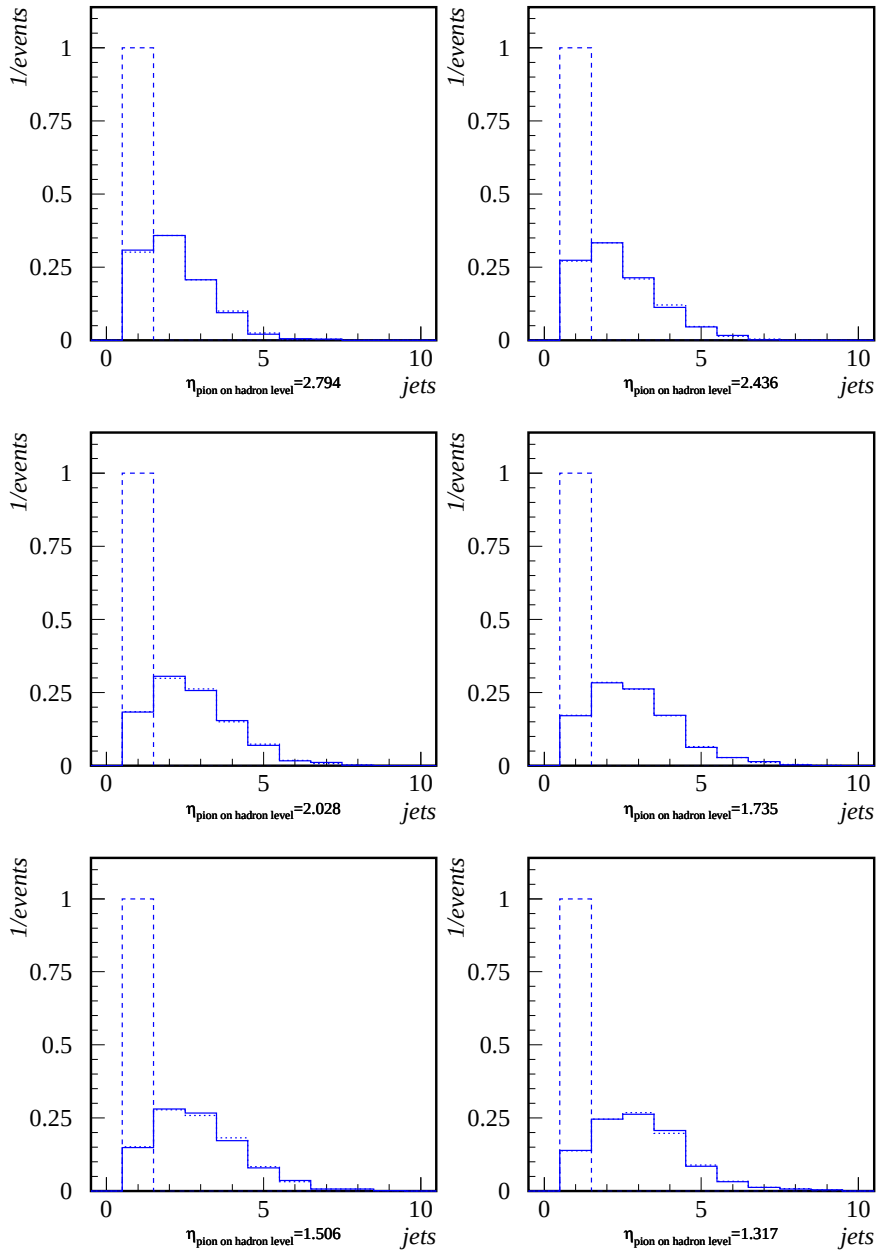

Figure 6.14: *Jet multiplicities for single pions without any p_t restrictions on the objects used by the jet algorithm. The dashed line illustrates the hadron level, the full line the detector level with the standard hadronic final state (hfs) weighting scheme and the dotted line the detector level with alternative hfs weighting scheme.*

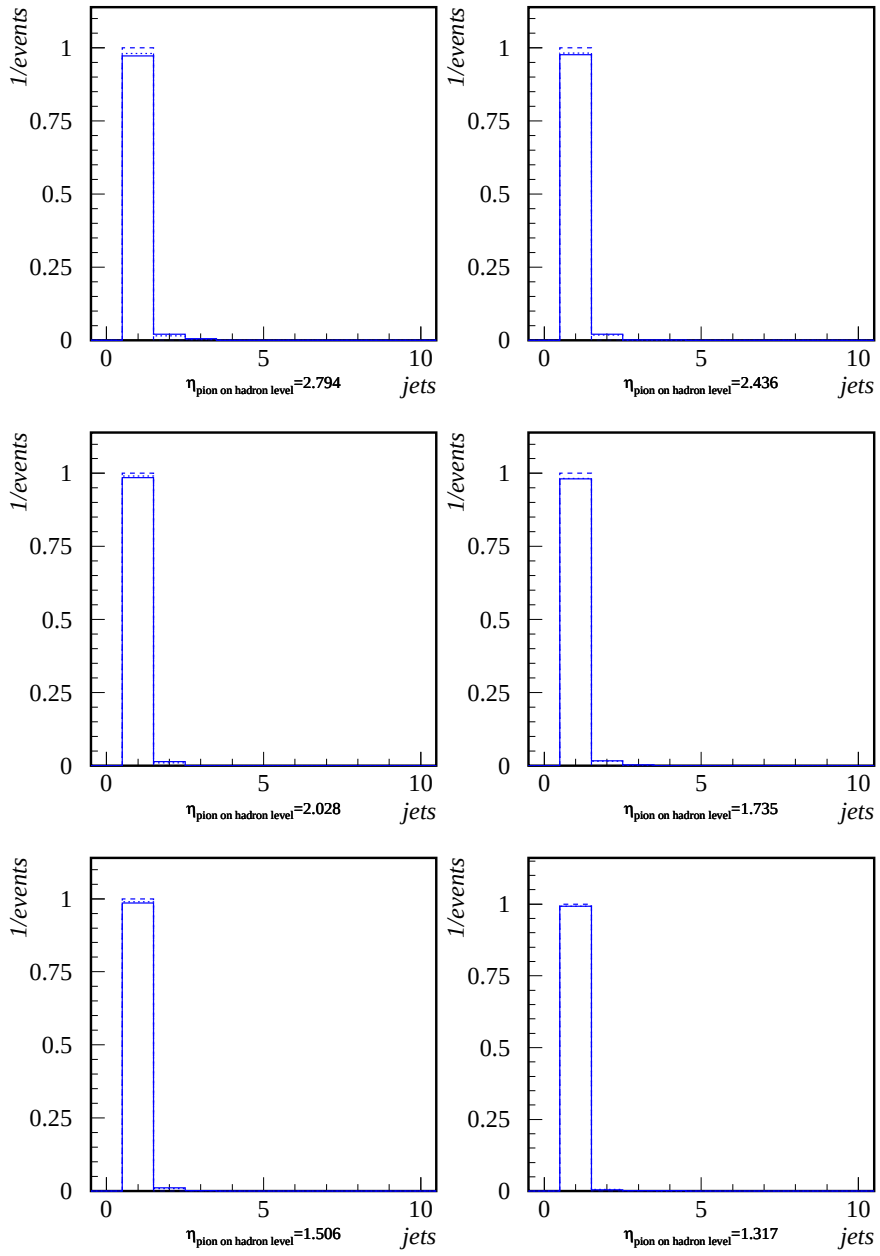

Figure 6.15: *Jet multiplicities for single pions with the requirement $p_t > 0.7 GeV$ for objects used by the jet algorithm. The dashed line illustrates the hadron level, the full line the detector level with the standard hadronic final state (hfs) weighting scheme, and the dotted line the detector level with alternative hfs weighting scheme.*

see Fig. 6.19. It is also found that the previous sharp rise at small energies in the energy distribution has disappeared. (Fig. 6.20, $\eta_{\text{quark on parton level}} = 2.794$)

As a last test, the requirement that objects used by the jet algorithm have $p_t > 0.7$ GeV was added. The cut again removes most of the 'background' clusters but may of course also remove low energy clusters in the jet. This would then lead to a decrease in the jet energy, which is also observed on the detector level (Fig. 6.21). Thus, requiring $p_t > 0.7$ GeV for the hadronic objects in addition to the p_t-cut of 3.5 GeV on the jet is not recommended.

The lack of jets in the lowest rapidity bin, in the plots where $p_{t,\text{ jet}} > 3.5$ GeV is required, is due to the implicit cut in energy at fixed η. On the hadron level this manifests itself as a sharp cut at $E_{\text{jet}} \approx 30$ GeV. (Fig. 6.20)

Concerning the alternative weighting scheme, which was developed for pions, the conclusion is that its use in jet physics is not recommended.

6.4 Correction Factors

The correction factors, C_i, are used to correct the data from the detector level to the non radiative hadron level bin by bin. This means that the data are corrected for detector effects and QED radiation effects. The correction factor for bin i is defined as

$$C_i = \frac{N_{\text{NRHAD},i}}{N_{\text{DET},i}} \tag{6.2}$$

where $N_{\text{NRHAD},i}$ is the number of events in bin i on non radiative hadron level (generated events) and $N_{\text{DET},i}$ is the number of events on the detector level (reconstructed events). For a perfect detector all the $C_i = 1$.

Correction factors are shown for the inclusive forward jet cross-section, $\frac{d\sigma}{dx_{Bj}}$, the triple differential cross-section, $\frac{d^3\sigma}{dx_{Bj}dp_t^2dQ^2}$ and the 2+forward jet cross-sections, $\frac{d\sigma}{d\Delta\eta_2}$ in Figs. 6.22-6.24.

The correction factors are calculated using DJANGO and RAPGAP, and the difference in the calculations between the two generators are used for the model dependent systematic error. For the final corrections of the data DJANGO has been used with the motivation that this model describes the data better than RAPGAP. Especially in terms of cross-section, as will be seen from the results presented in chapter 7, but also in terms of shape which is concluded from the control plots in section 5.4.1. The corretions are below 50% in all bins, which is fully acceptable.

6.5 Secondary Scattering Against Collimator

To further understand the jet reconstuction a comparison between jet rapidity distributions on the hadron and the detector level was made for Monte Carlo generated events, and on the detector level between uncorrected data and Monte Carlo generated events.

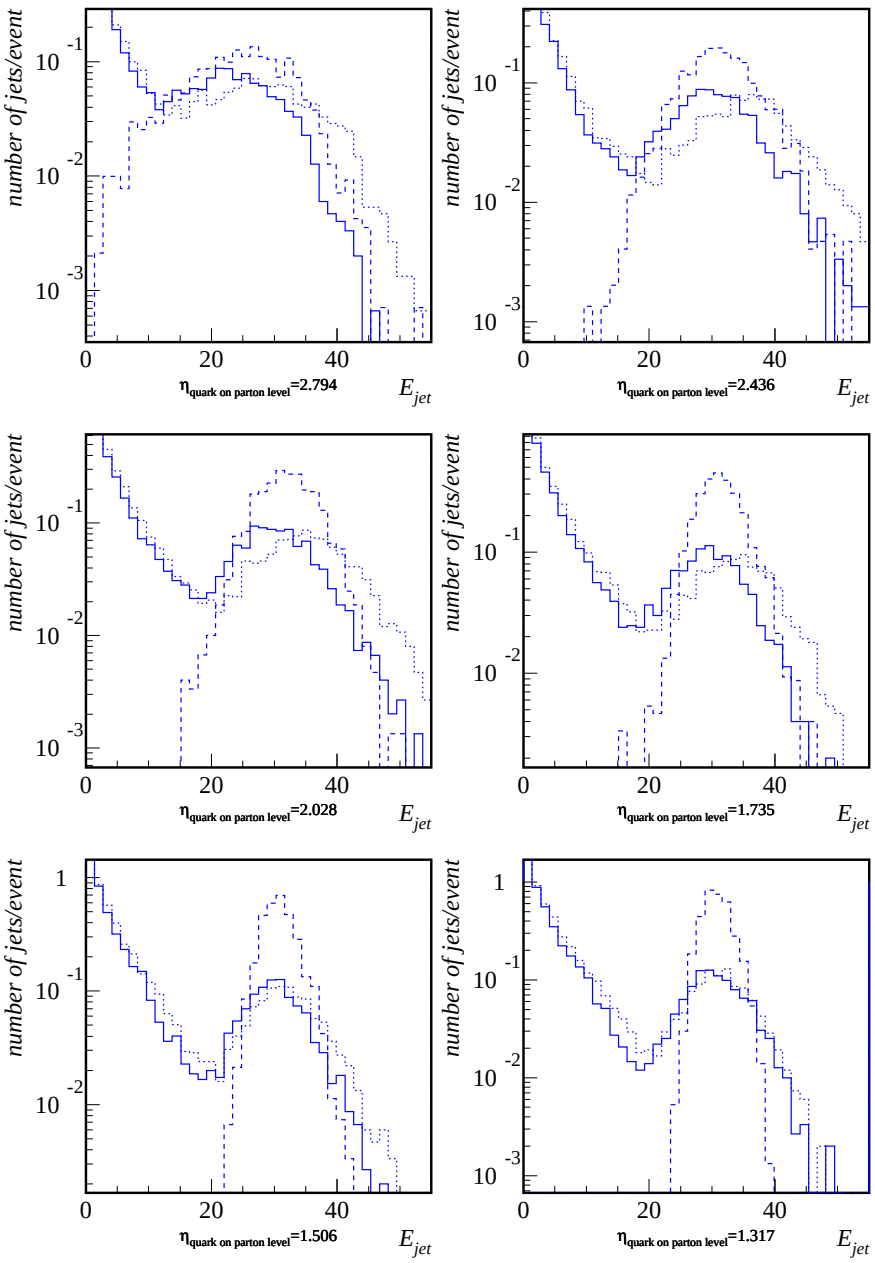

Figure 6.16: *Jet energy (GeV) distributions for single quark jets emitted in specific directions, normalized to the number of events. The distributions are shown for different values of the pseudorapidity of the emitted quark. The dashed line corresponds to the hadron level, the full line the detector level with the standard weighting scheme and the dotted line the detector level with an alternative weighting scheme.*

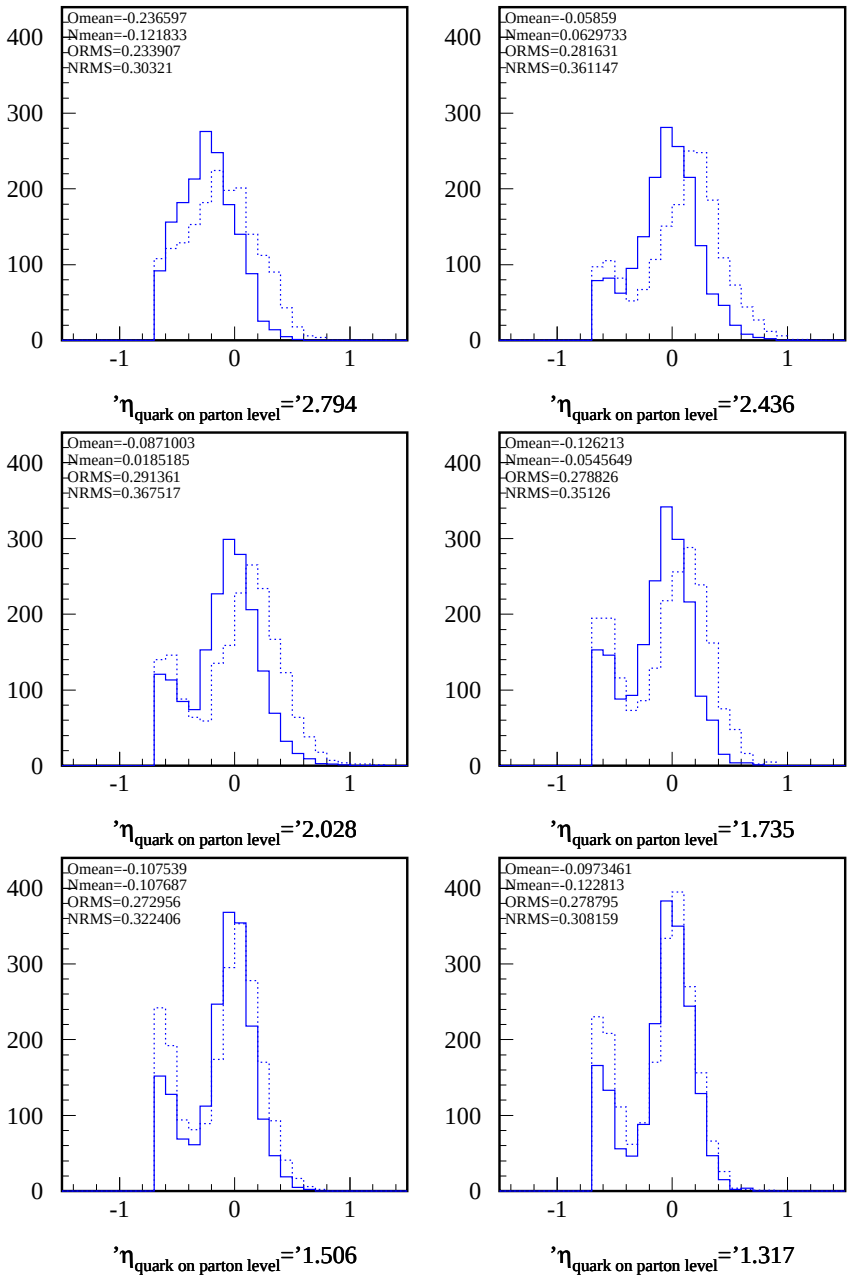

Figure 6.17: *Energy resolutions for single quark jets for different values of the pseudorapidity of the emitted quark. The full line corresponds to the detector level with the standard weighting scheme and the dotted line illustrates the detector level with an alternative weighting scheme. The y-axes give number of events.*

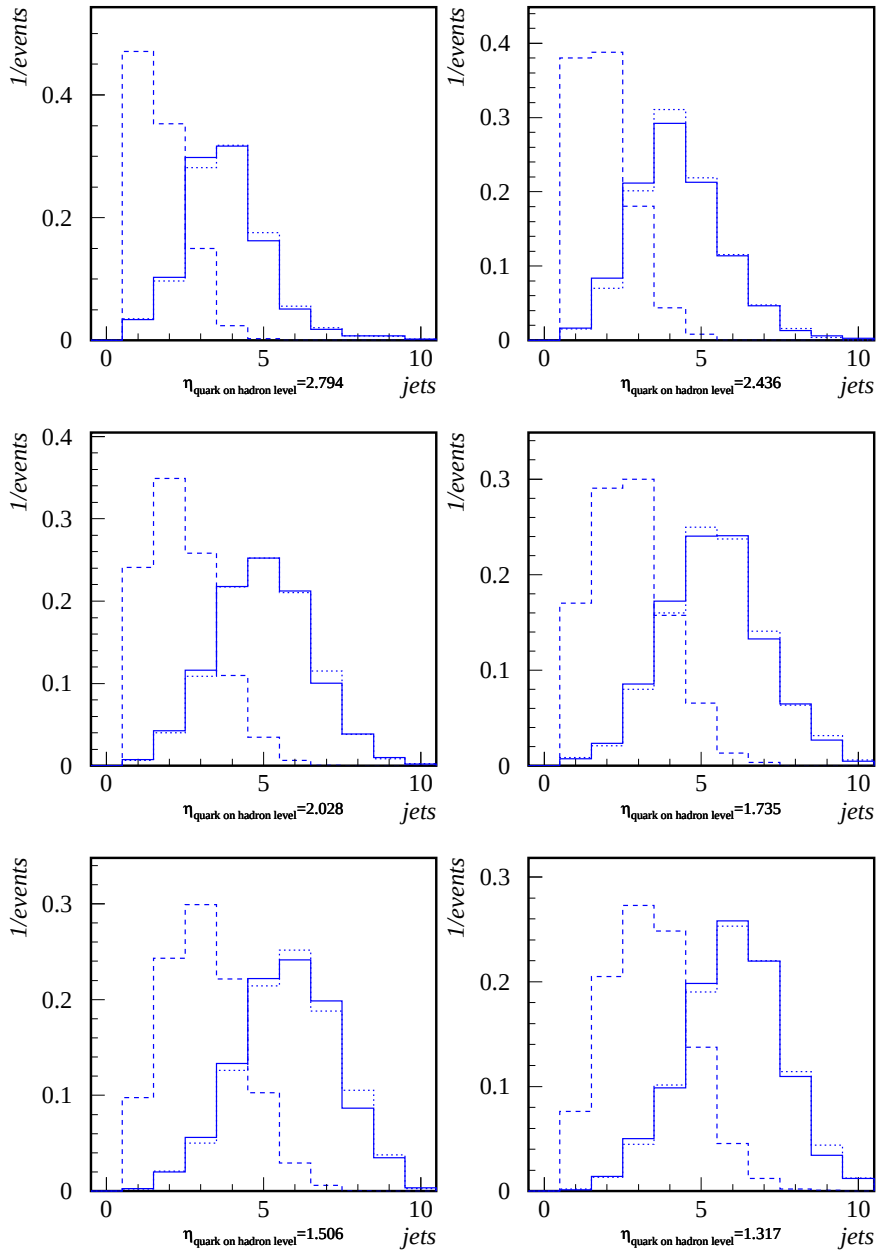

Figure 6.18: *Jet multiplicities for single quark jet events without any restriction on* $p_{t,\,jet}$*, shown for different values of the pseudorapidity of the emitted quark. The dashed line corresponds to the hadron level, the full line the detector level with the standard weighting scheme and the dotted line the detector level with an alternative weighting scheme.*

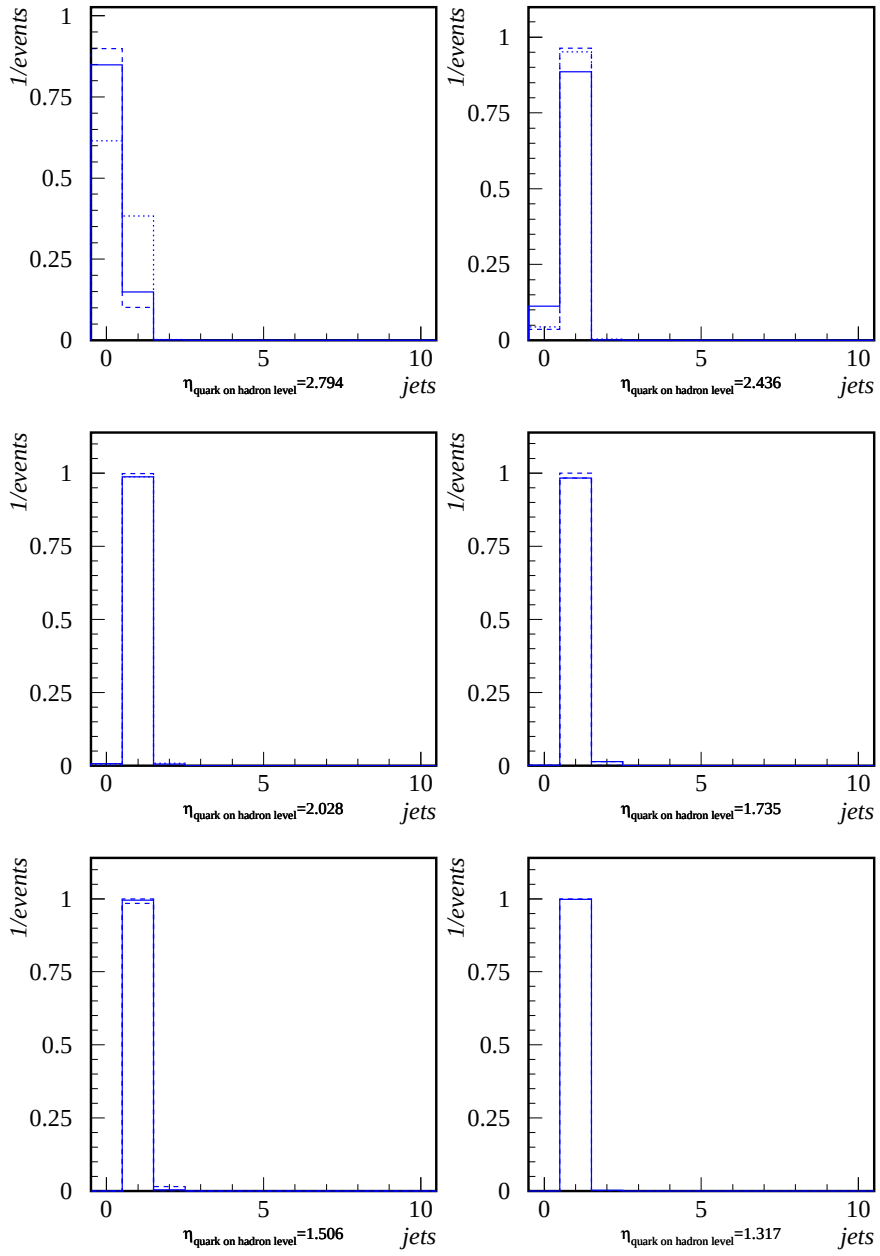

Figure 6.19: *Jet multiplicities for single quark jets with $p_t > 3.5$ GeV, shown for different values of the pseudorapidity of the emitted quark.. The dashed line corresponds to the hadron level, the full line the detector level with the standard weighting scheme, and the dotted line the detector level with and alternative weighting scheme.*

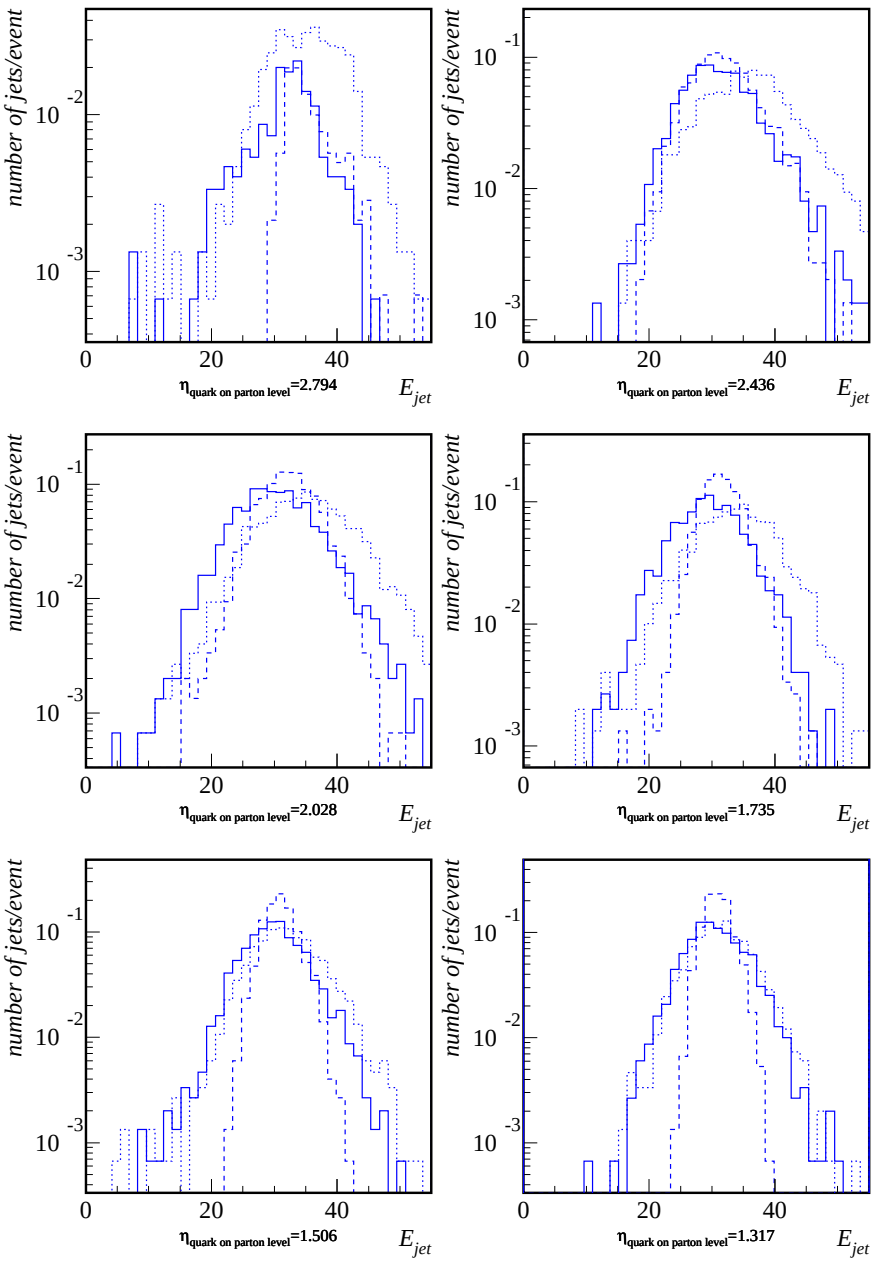

Figure 6.20: *Jet energies (GeV) distributions for single quark jets, emitted in specific directions, with $p_t > 3.5$ GeV normalized to the number of events. The distributions are shown for different values of the pseudorapidity of the emitted quark. The dashed line corresponds to the hadron level, the full line the detector level with the standard weighting scheme, and the dotted line the detector level with an alternative weighting scheme.*

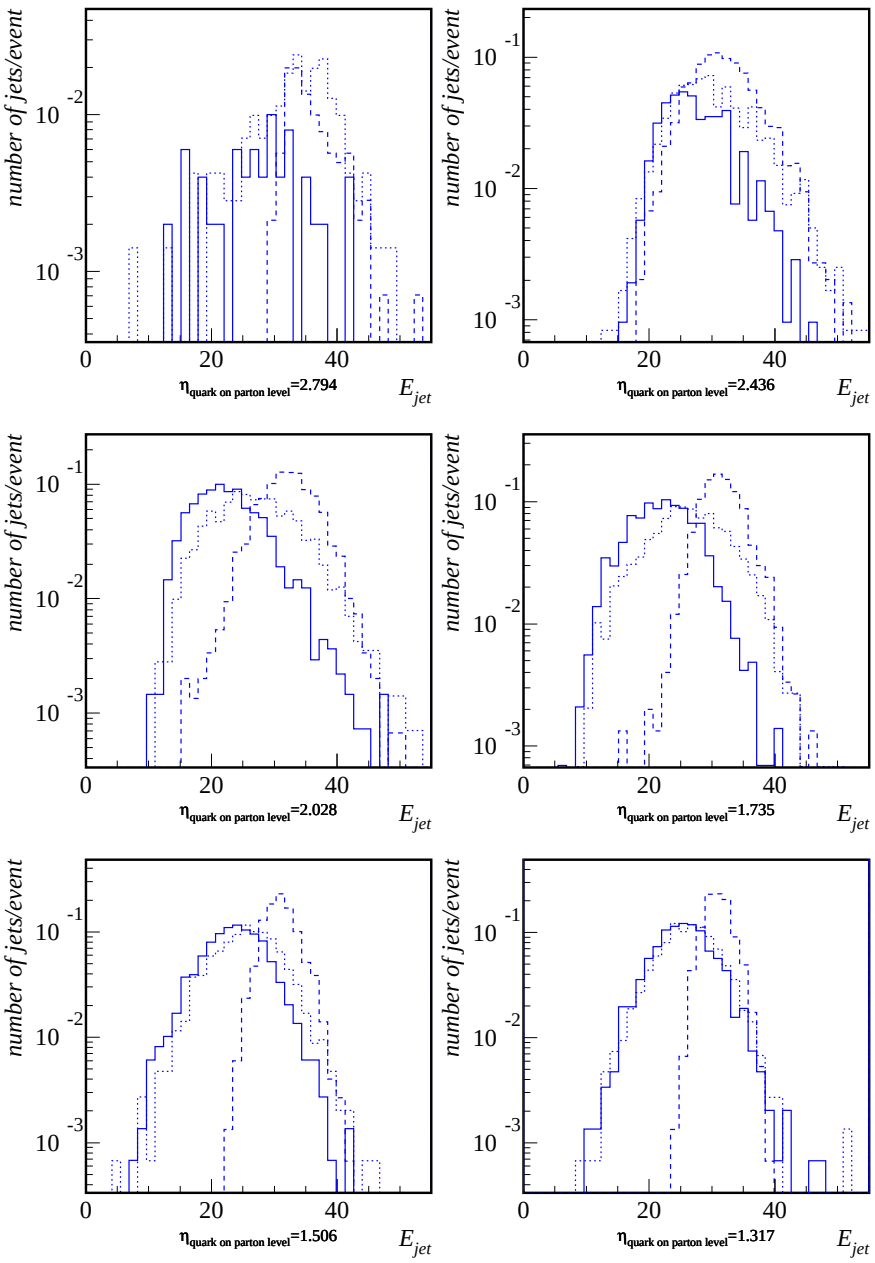

Figure 6.21: *Energies (GeV) distributions for single quark jets emitted in specific directions with* $p_{t,\ jet} > 3.5\ GeV$ *and with* $p_{t,objectsinjet} > 0.7\ GeV$. *The distributions are shown for different values of the pseudorapidity of the emitted quark. The dashed line corresponds to the hadron level, the full line the detector level with the standard weighting scheme, and the dotted line the detector level with an alternative weighting scheme.*

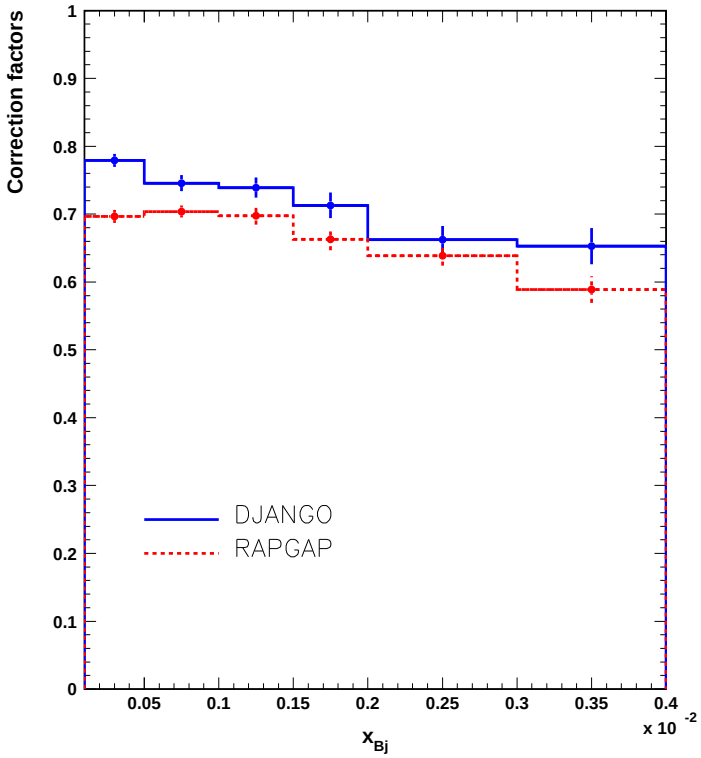

Figure 6.22: *Correction factors as a function of x_{Bj} for the inclusive forward jet cross-section. RAPGAP (dashed line) and DJANGO (full line).*

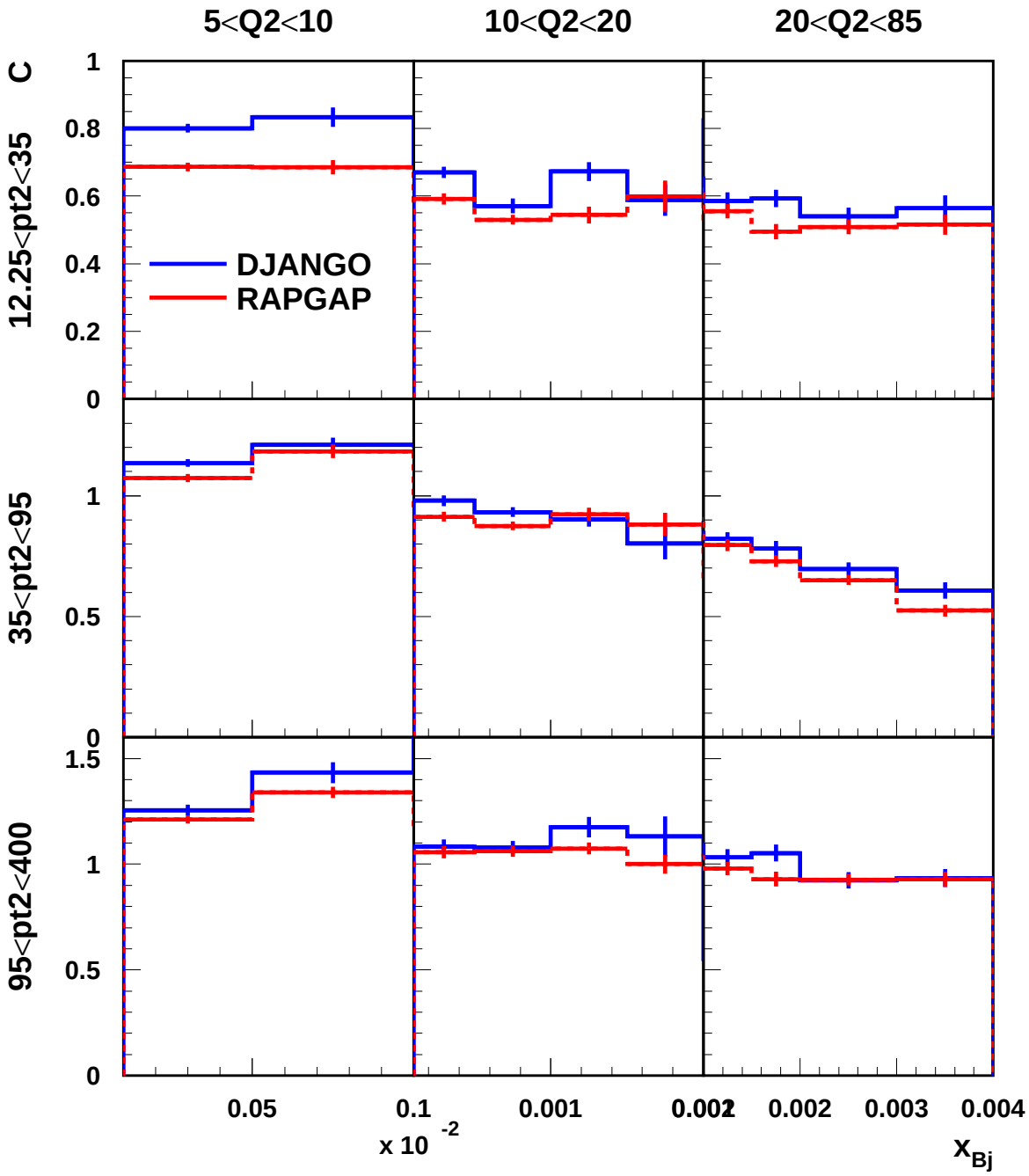

Figure 6.23: *Correction factors as a function of x_{Bj}, Q^2, p_t^2 for the triple differential forward jet cross-section. RAPGAP (dashed line) and DJANGO (full line).*

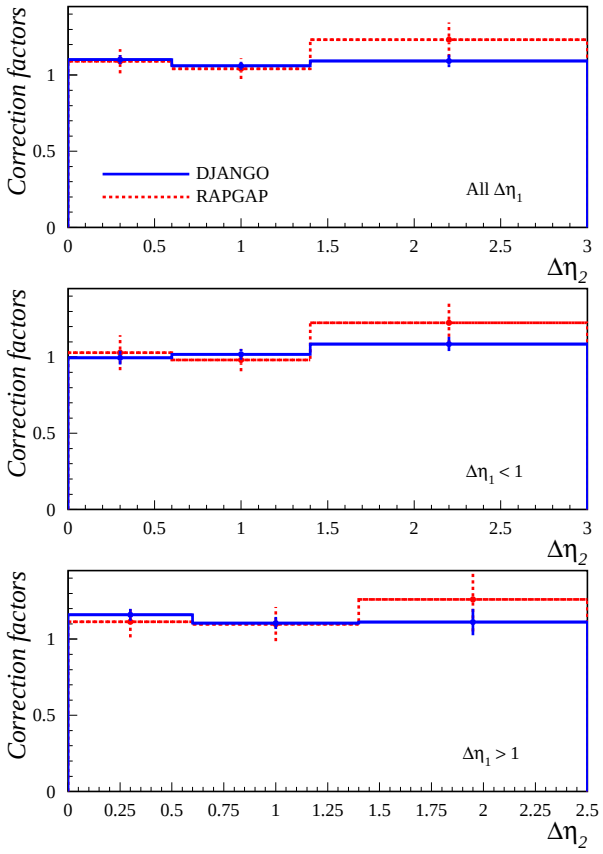

Figure 6.24: *Correction factors as a function of $\Delta\eta_2$ for the 2+forward jet cross-section with different $\Delta\eta_1$ choices. RAPGAP (dashed line) and DJANGO (full line).*

In Fig. 6.25a)-d) jet pseudo rapidity distributions for *all* jets in all events which have passed the DIS selection are shown for different minimum transverse momenta of the jets, $p_{\mathrm{t,\,jet}} > 0$ GeV, $p_{\mathrm{t,\,jet}} > 0.5$ GeV, $p_{\mathrm{t,\,jet}} > 3.5$ GeV and $p_{\mathrm{t,\,jet}} > 6$ GeV. These distributions are produced using DJANGO and are normalized to bin width and the total number of jet events in each distribution.

For low $p_{t,\,\mathrm{jet}}$ two significant differences between the hadron level and the detector level are seen. First, the detector level distribution has a huge peak at high rapidities ($\eta \approx 3.0$). This behaviour has already been explained in section 6.3 where effects from electronic noise in the LAr-calorimeter were discussed. In agreement with this study the peak is significantly reduced when $p_{t,\,\mathrm{jet}} > 3.5$ GeV is required (Fig.6.25c). The peak in the same region on the hadron level is explained from the large hadron production by the color string connecting to the proton remnant, in which a large amount of energy is available for increased particle production.

The other deviation is observed as a broader peak around $\eta_{lab} \approx 1.7$ in the detector level distribution and this behaviour is also most prominent for small $p_{t,\,\mathrm{jet}}$. The peak on the detector level is also of interest for the 2+forward jet scenario since one of the two cental jets is reconstructed in the region of this peak, as can be seen in Fig. 5.12. However, when requiring $p_{t,\,\mathrm{jet}} > 6$ GeV the difference between the hadron level and the detector level is significantly decreased (Fig.6.25d).

One typical event, contributing to the increased detector activity at $\eta_{lab} \approx 1.7$ is shown by an event display in the $y - z$ view in Fig. 6.26. A secondary scattering vertex is clearly visible. The reason for this effect is secondary scattering against one of the collimators, which provide shielding against synchrotron radiation, close to the beam pipe. Since the bump in the distribution is seen for detector reconstructed Monte Carlo events the effect is apparently included in the detector simulation, and is thus expected to be corrected for when correcting for detector effects (Eq. 6.2).

To verify that this expectation is true, a comparison between data and Monte Carlo distributions were made on the detector level in Fig. 6.27 for the same scenario as above. Data are here shown together with RAPGAP and DJANGO with ARIADNE on the detector level. Looking at RAPGAP one observers that both the effects from the collimator scattering and the noise in the forward region are well reproduced by the detector simulation for $p_{\mathrm{t,\,jet}} > 3.5$ GeV and $p_{\mathrm{t,\,jet}} > 6$ GeV, respectively. DJANGO however overshoots the data at high pseudorapidities. This is due to the well-known fact that ARIADNE (CDM) produces a higher energy flow close to the proton remnant than RAPGAP. This feature of CDM was already seen in the p_t-balance study in section 5.4.2, where ARIADNE, RAPGAP and data were compared. When producing the corresponding control plots on jet rapidities for the forward jet scenario, Fig. 6.28, and for the 2+forward jet scenario, Fig. 6.29, one sees that the agreement between data and MC is good. The excess of soft particles with low p_t in DJANGO is also gone.

Although these effects are taken into account when correcting the data from detector to the hadron level it is not clear if the tracks coming from the collimator scattering confuse the reconstruction of final state combined (FSCOMB) objects. For example should a calorimeter cluster related to a particle scattered in the collimator not be combined with a track from the primary vertex. Ultimately, all tracks and clusters produced from the collimator scattering should be removed from the list of particle candidates before the jet

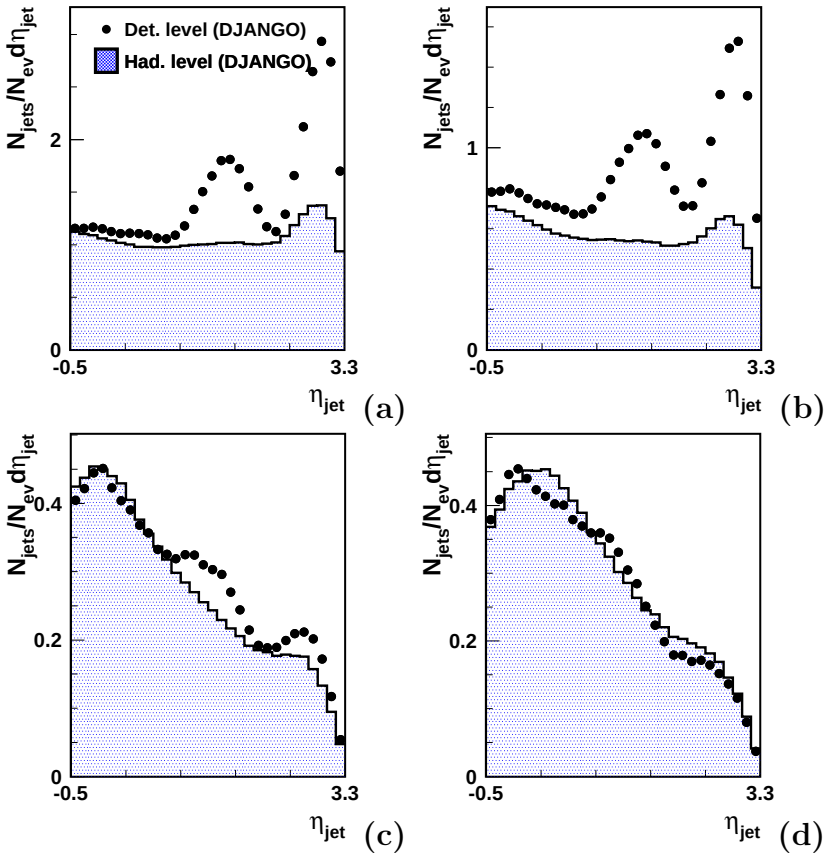

Figure 6.25: *Comparison between hadron and detector level distributions for all jets in DIS events generated by DJANGO. The plots show the pseudorapidity for jets with* $p_{t,\,jet} > 0$ *GeV (a),* $p_{t,\,jet} > 0.5$ *GeV (b),* $p_{t,\,jet} > 3.5$ *GeV (c) and* $p_{t,\,jet} > 6.0$ *GeV (d).*

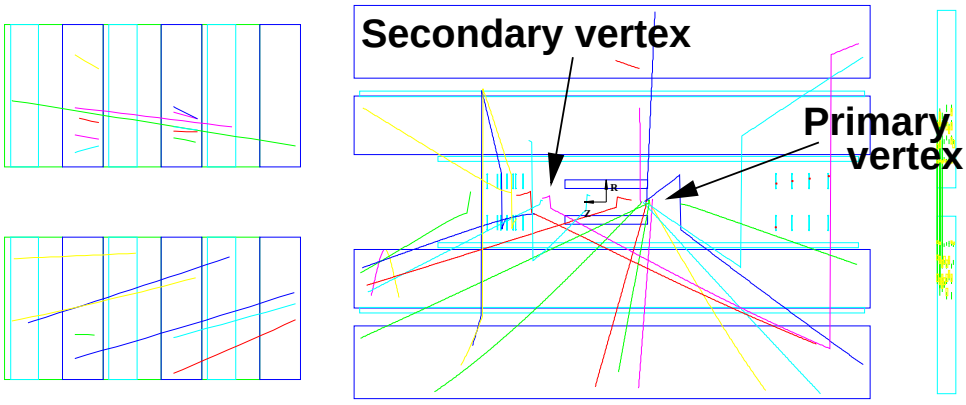

Figure 6.26: *One of the events where a secondary vertex is visible.*

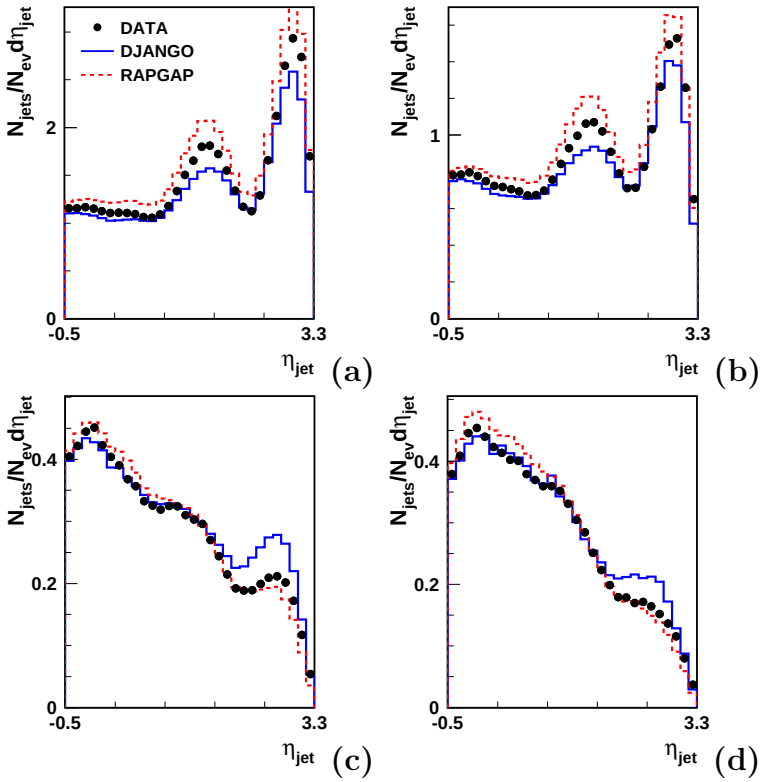

Figure 6.27: *Comparison between detector level distributions for all jets in DIS events. The plots show the pseudorapidity for jets with* $p_{t,\,jet} > 0$ *GeV (a),* $p_{t,\,jet} > 0.5$ *GeV (b),* $p_{t,\,jet} > 3.5$ *GeV (c) and* $p_{t,\,jet} > 6.0$ *GeV (d).*

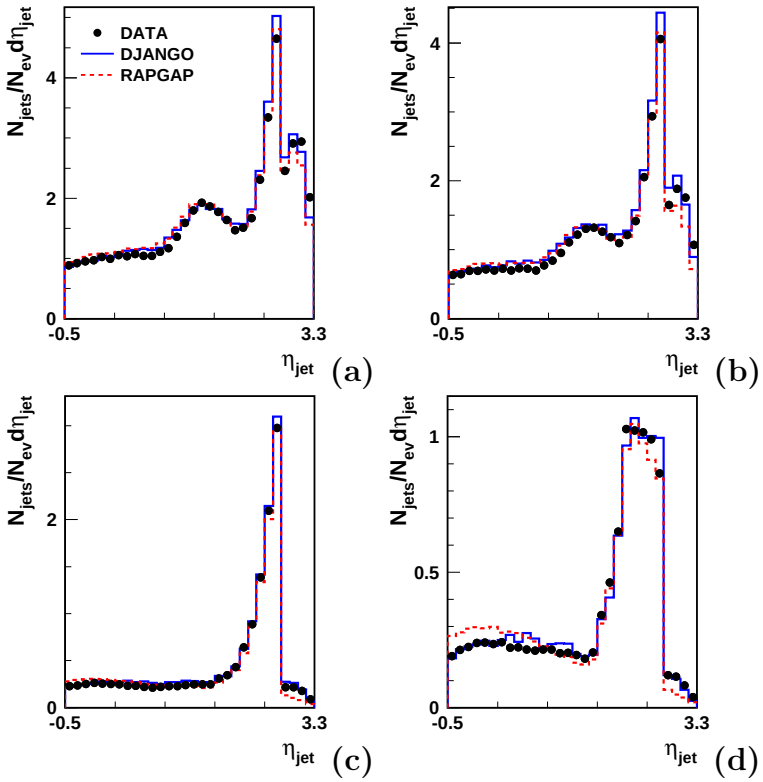

Figure 6.28: *Comparison between detector level distributions for all jets in all forward jet events (with p_t^2/Q^2-cut). The plots show the pseudorapidity for jets with $p_{t,\ jet} > 0$ GeV (a), $p_{t,\ jet} > 0.5$ GeV (b), $p_{t,\ jet} > 3.5$ GeV (c) and $p_{t,\ jet} > 6.0$ GeV (d)*

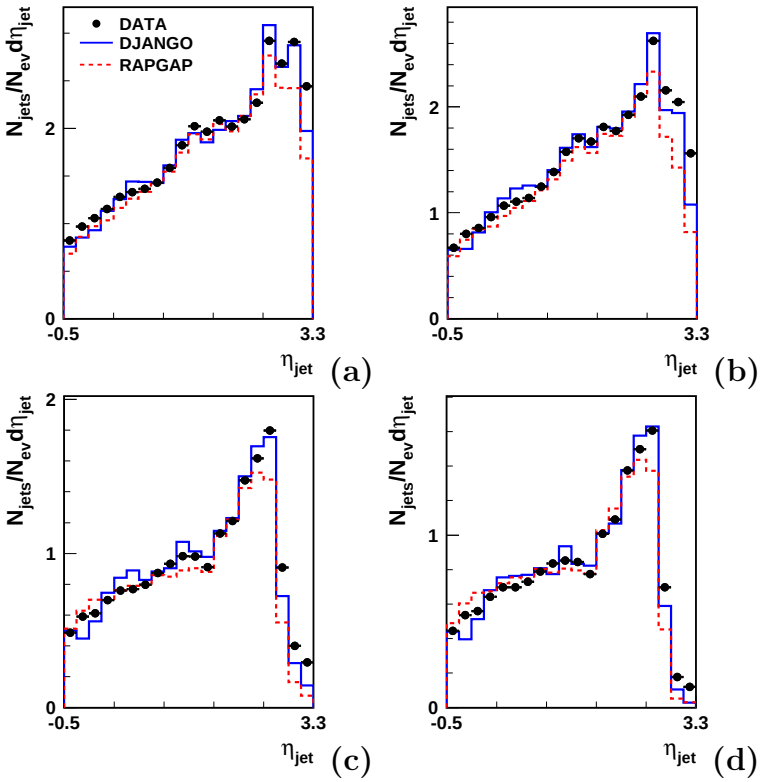

Figure 6.29: *Comparison between detector level distributions for all jets in 2+forward jet events. The plots show the pseudorapidity for jets with* $p_{t,\ jet} > 0$ *GeV (a),* $p_{t,\ jet} > 0.5$ *GeV (b),* $p_{t,\ jet} > 3.5$ *GeV (c) and* $p_{t,\ jet} > 6.0$ *GeV (d)*

algorithm is run. This possibility for improvement can be investigated in a future analysis. Already for the new object oriented-based analysis scheme a new FSCOMB (now called HADROOII) scheme exist.

6.6 Systematic Errors

Systematic errors have been estimated for the data. The total average systematic errors are 10%, 12% and 14% for the inclusive, triple and the 2+forward jet cross-section, respectively. A summary of the estimated systematic errors are shown in table 11.4.2. The following systematic errors are considered:

- The energy calibration of the hadronic calorimeter has been performed to a precision of $\pm$ 4%. In order to estimate the dependence of the measured forward jet cross-section on this uncertainty, the energy scale was changed within these limits and the influence on the forward jet cross-section was calculated using the DJANGO generator. The average systematic error is typically 8 % for the inclusive forward jet cross-section and the triple differential forward jet cross-section, and 13 % for the 2+forward cross-section.

- For the SPACAL electromagnetic calorimeter the energy scale is known to an accuracy of $\pm$ 1%. Changing the scale by this amount in the forward jet cross section calculations results in an average systematic error of typically 3% for the single and triple differential measurement, and 1% for the 2+forward jet measurement.

- The uncertainty in the measured scattering angle of the electron has been estimated to be $\pm$ 1 mrad. The systematic error from this uncertainty was calculated by shifting the electron angle by this amount in the DJANGO program before the events were subject to the event reconstruction (H1REC). The resulting systematic errors in the forward jet cross sections are typically 1%.

- The error from the model dependence has been taken as the difference between the correction factors calculated from the DJANGO and the RAPGAP Monte Carlo programs. Taking this variation into account yields a systematic error of around 5% in the inclusive cross-section, 8% for the triple differential cross-section and 6% in the 2+forward jet cross-section.

- The PHOJET [66,67] Monte Carlo generator was used in order to estimate the extent to which DIS forward jet events could be faked by photoproduction background. The contribution to the forward jet cross-section was calculated to be $\sim$ 1%.

- The normalization uncertainty of the luminosity measurement has been estimated to be 1.5%.

The systematic errors from the uncertainties in the energy scale of the LAr and the SPACAL, and the uncertainty in the measured scattering angle of the electron, are estimated for each data point, whereas the uncertainty in the luminosity measurement and the background from photoproduction were taken the same for all data points.

	$\frac{d\sigma}{dx_{Bj}}$	$\frac{d\sigma^3}{dx_{Bj}dp_t^2dQ^2}$	$\frac{d\sigma}{d\Delta\eta_2}$
Model dependence (DJANGO, RAPGAP)	± 5.1%	± 8.1%	± 6.4%
LAr hadronic energy scale(± 4%)	+6.9/-8.4%	+8.5/-7.3%	+13.3/-12.1%
SPACAL em energy scale (± 1%)	+3.9/-3.1%	+3.7/-3.0%	+1.1/-0.9%
Angle of scattered electron (± 1mrad)	+0.7/-0.6%	+1.1/-1.0%	+1.1/-1.3%
Photoproduction (PHOJET)	∼ 1%		
Luminosity	± 1.5%		
Total	∼ 10 %	∼ 12%	∼ 14%

Table 6.2: *The source of the systematic errors and their impacts on the forward jet cross-section measurements.*

Chapter 7

Results

The cross-sections are presented in the following order. First the inclusive cross-section as a function of x_{Bj} is presented, then the triple differential cross-section as a function of x_{Bj} in bins of p_t^2 and Q^2 follows. Finally 2+forward cross-sections are presented as a function of the rapidity separation between the most forward going central jet and the forward jet. In all three cases the experimental results are compared to the fixed order parton level calculations, corrected to the hadron level, and the QCD calculations including parton showers and hadronisation separately. A definition of the measured cross-sections, and the cuts used to select events can be found in section 6.1.

In the figures RAPGAP is denoted as RG-DIR and RG-DIR+RES, for the DGLAP direct and the DGLAP direct plus resolved photon contributions, respectively. CASCADE is labeled CASCADE set-1 and CASCADE set-2 for the two different PDFs described in chapter 3. The parton level calculations are denoted by LO or NLO. The data in the figures are marked with dots. The hatched band surrounding the data points represents the energy scale uncertainty, while the error bars are subdivided into the statistical error and the systematic errors other than those due to the energy scale uncertainty.

7.1 Inclusive Forward Jet Cross-section

Fig. 7.1a) shows the inclusive forward jet cross section as a function of x_{Bj} compared to the predictions of the LO($O(\alpha_s)$) and NLO($O(\alpha_s^2)$) di-jet calculations from DISENT, which have been corrected for hadronizations effects ($1+\delta_{\rm HAD}$) (see chapter 3). In Fig. 7.1b) and c) data are compared to the various QCD calculations with parton showers and hadronisation.

From the figures it is obvious that the DGLAP model with direct photon interactions alone (RG-DIR) and the NLO di-jet calculation give similar predictions and both fall below the data particularly in the low x_{Bj} region. The somewhat improved agreement at higher x_{Bj} can be understood from the fact that the range in the longitudinal momentum fraction, carried by the gluon propagator, which is available for higher order emissions is decreased.

From Fig. 7.1a) it can be observed that, at small x_{Bj}, the NLO di-jet calculations are significantly larger than the LO contribution. This reflects the fact that, in this case, the LO scenarios are suppressed by kinematics, i.e. there is almost no contribution from

forward jets. The NLO contribution opens the phase space for forward jets and improves the description considerably. However the NLO di-jet calculations are still a factor of 2 below the data at low x_{Bj}, indicating that nature produces higher order emissions. The description of the data by the DGLAP-model is significantly improved if contributions from resolved virtual photon interactions are included (RG-DIR+RES), due to the fact that the transverse momentum ordering is broken. However, there is still a discrepancy in the lowest x_{Bj}-bin, where a possible BFKL signal would be expected to show up most prominently. The CDM model, which is not based on standard evolution equations, but gives emissions that are non-ordered in transverse momentum, shows a similar behaviour as the RG DIR+RES model.

The CCFM-model (both set-1 and set-2) predicts a somewhat different shape for the x_{Bj} distribution, which results in a comparatively poor description of the data, but still better than the NLO di-jet prediction.

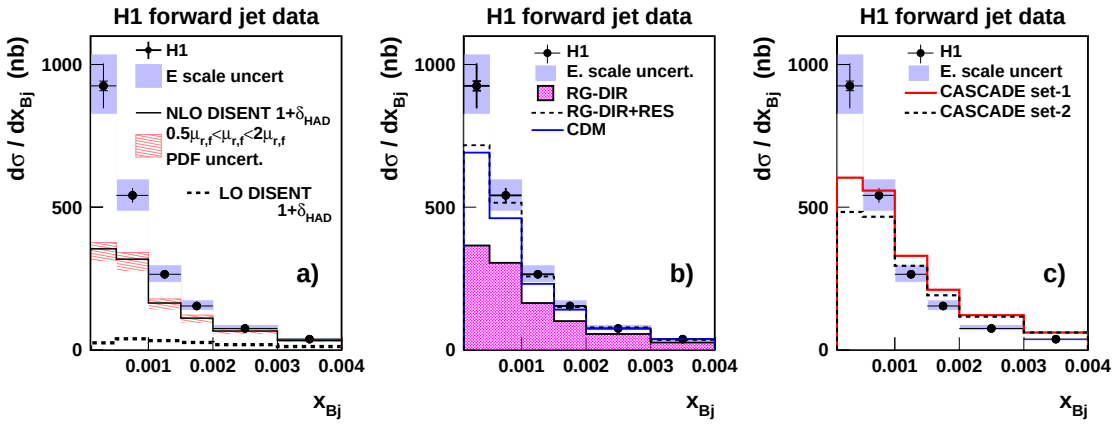

Figure 7.1: *Forward jet cross-sections on hadron level as a function of x_{Bj}. The systematic errors from the uncertainty of the energy scales in the detectors are shown by the band following the data points. The statistical errors are shown by the inner error bars, while the full error bars represent the systematic errors, not already included in the error band, added in quadrature to the statistical errors. The data are compared to LO and NLO di-jet calculations from DISENT (a) and to QCD Monte Carlo models (b and c). The band following the NLO di-jet calculations illustrates the theoretical uncertainties in the calculations, estimated as described in section 3.1. The LO and NLO calculations have been corrected for hadronisation effects.*

7.2 Triple Differential Forward Jet Cross-section

The triple differential cross section $\frac{d^3\sigma}{dx_{Bj}dQ^2dp^2_{t,\,\mathrm{jet}}}$ is shown in Figs. 7.2-7.4 for three regions in Q^2 and $p^2_{t,\,\mathrm{jet}}$ as a function of x_{Bj}. Fig. 7.2 presents the cross section compared to LO and NLO di-jet calculations, including theoretical errors, represented by error bands. As for earlier spectra, the NLO calculations are corrected to the hadron level. In Figs. 7.3 and 7.4 the data are also confronted with QCD models using parton showers and color

string hadronisation. Inside each figure the possible values of $r = p_t^2/Q^2$ are written, as are the average values.

7.2.1 Comparison to LO and NLO Di-jet Calculations

From Fig. 7.2 it can be observed that the NLO di-jet calculations in general undershoot the data. As was the case for the single differential cross section the NLO di-jet calculations are closer to the data at higher x_{Bj} (also higher Q^2 due to kinematics). The NLO di-jet calculations are also closer to the data for harder forward jets, and in the highest p_t^2-bin the difference between data and NLO di-jet is, in several x_{Bj}-bins, covered by the large uncertainty of the NLO di-jet calculations. This is consistent with the results from a previous measurement on inclusive jet production [68]. A possible explanation is that jets with high p_t remove a large fraction of the energy from the parton ladder, leaving a limited energy available for additional emissions. Thus, the parton ladder is shorter and more similar to the diagrams covered by the NLO di-jet calculations. To summarize, the worst (best) description by NLO di-jet is at low (high) x_{Bj}, Q^2 and p_t^2. For high p_t one can also see that the LO contribution becomes more important, indicating that the phase space starts to open up for LO, making the prediction of NLO di-jet stronger.

7.2.2 Comparison to QCD models with Parton Showers and Hadronisation

The overall behaviour of the inclusive cross-section as a function of x_{Bj} (Fig. 7.1) is reflected in the triple differential cross-section. The comparisons between data and Monte Carlo have below been separated into three sections representing the different kinematic regions of interest. However, these regions overlap. As already observed in the single differential measurement the CCFM model predicts a somewhat harder x_{Bj} distribution than seen in the data. This is true for the full kinematic range and leads to the poor description of the data seen in Fig. 7.4.

$p_{t,\,\mathrm{jet}}^2 \sim Q^2$ ($r \sim 1$)

This is the region where events with parton emissions ordered in p_t are suppressed, and thus parton dynamics beyond DGLAP are expected to be manifested. In this kinematic region the data are well described by the DGLAP resolved (RG-DIR+RES) model, as observed in Fig. 7.3b) and f) whereas the CDM model, like for the inclusive measurement, gives a somewhat lower, cross-section at low x_{Bj}.

$p_{t,\,\mathrm{jet}}^2 < Q^2$ ($r < 1$)

The predictions of the DGLAP direct photon interactions (RG-DIR) are closest to the data in the kinematic region covered by Fig. 7.3c), where Q^2 might become larger than $p_{t,\,\mathrm{jet}}^2$. However, the choice of data-bins allows $p_{t,\,\mathrm{jet}}^2$ to be of the same order or even greater than Q^2, so emissions non-ordered in virtuality are expected to contribute as well. This could explain why the direct model (RG-DIR) does not give agreement with data except in the highest x_{Bj}-bin, where non-ordered emission are expected to be less important. The CDM and DGLAP resolved model (RG-DIR+RES) reproduce the data very well in this region.

$p^2_{t,\,\mathrm{jet}} > Q^2$ $(r > 1)$

This is the kinematic region where $p^2_{t,\,\mathrm{jet}}$ is larger than Q^2, which is typical for processes where the virtual photon is resolved. As expected the DGLAP resolved model (RG-DIR+RES) provides a good overall description of the data, again similar to the CDM model. However, in the regions where r is highest and x_{Bj} small, CDM shows a tendency to overshoot the data. DGLAP direct (RG-DIR) gives cross sections which are too low (see Fig. 7.3d), g) and h)).

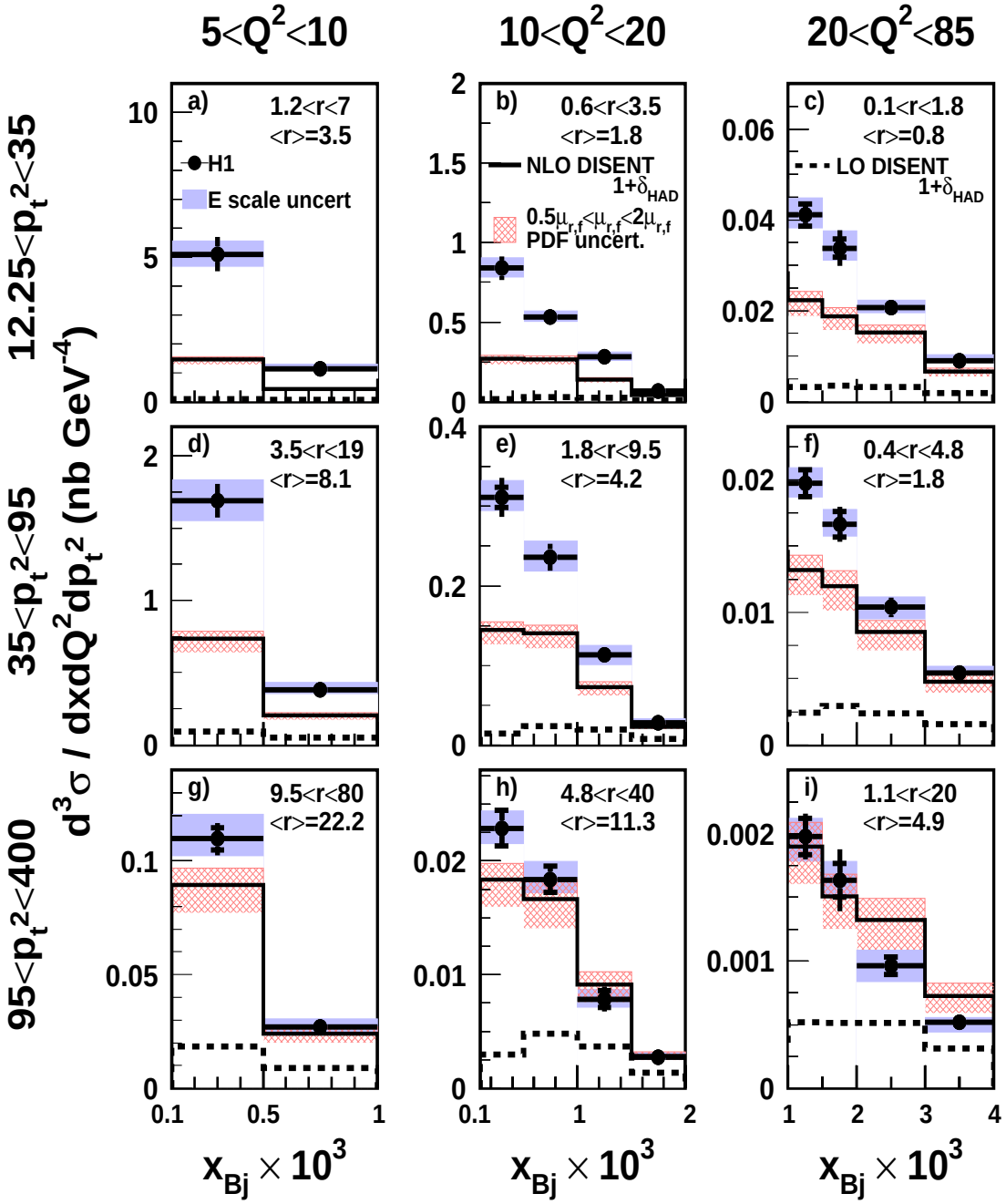

Figure 7.2: *Forward jet cross-sections on hadron level as a function of x_{Bj}, in bins of Q^2 and $p^2_{t,\,jet}$. The systematic errors from the uncertainty of the energy scales in the detectors are shown by the band following the data points. The statistical errors are shown by the inner error bars, while the full error bars represent the systematic errors, not already included in the error band, added in quadrature to the statistical errors. The data are compared to LO and NLO di-jet calculations from DISENT. In each bin the coverage in and the average value of $r = p^2_{t,\,jet}/Q^2$ is shown. These calculations have been corrected for hadronisation effects. The band following the NLO di-jet calculations illustrates the theoretical uncertainties in the calculations, estimated as described in section 3.1.*

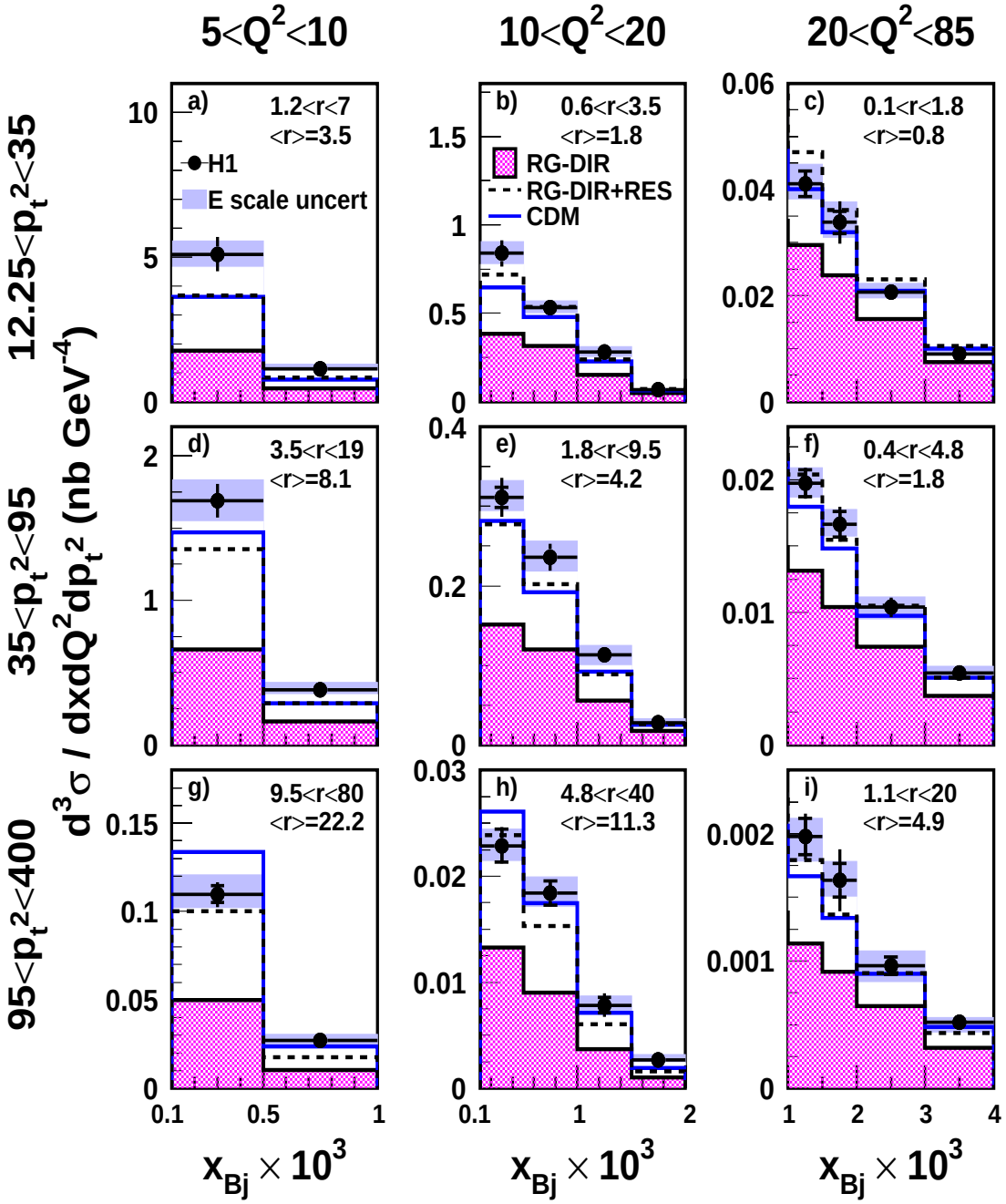

Figure 7.3: *Forward jet cross-sections on hadron level as a function of x_{Bj}, in bins of Q^2 and $p^2_{t,\,jet}$. The systematic errors from the uncertainty of the energy scales in the detectors are shown by the band following the data points. The statistical errors are shown by the inner error bars, while the full error bars represent the systematic errors, not already included in the error band, added in quadrature to the statistical errors. In each bin the coverage in and the average value of $r = p^2_{t,\,jet}/Q^2$ is shown. The data are compared to the prediction of RAPGAP DIR, RAPGAP DIR+RES and CDM.*

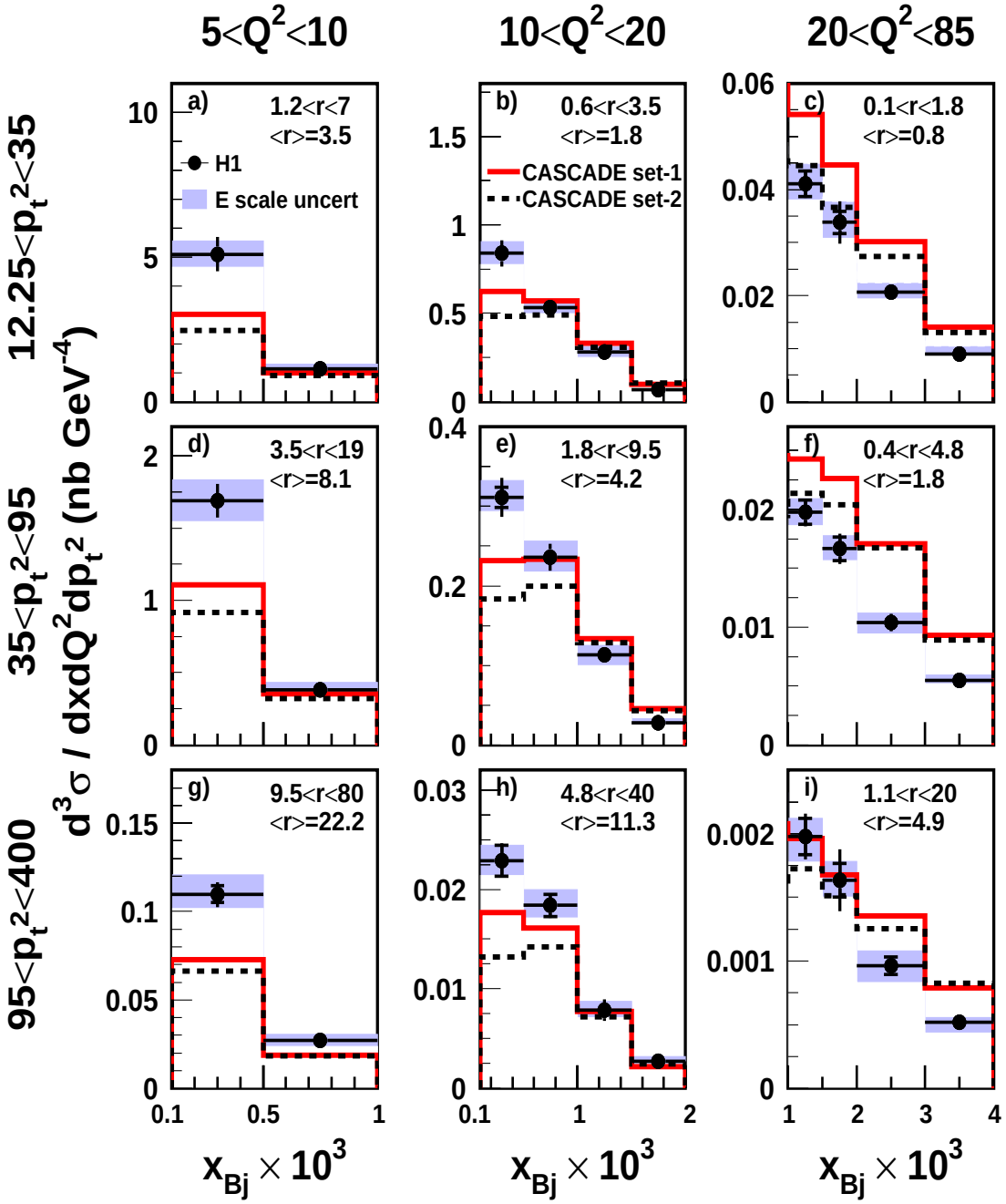

Figure 7.4: *Forward jet cross-sections on hadron level as a function of x_{Bj}, in bins of Q^2 and $p^2_{t,\,jet}$. The systematic errors from the uncertainty of the energy scales in the detectors are shown by the band following the data points. The statistical errors are shown by the inner error bars, while the full error bars represent the systematic errors, not already included in the error band, added in quadrature to the statistical errors. In each bin the coverage in and the average value of $r = p^2_{t,\,jet}/Q^2$ is shown. The data are compared to the predictions of CASCADE.*

7.3 2+Forward Jet Cross-section

In this section, reconstruction of two jets in the central region of the detector is required in addition to the forward jet. The selection is described in detail in section 5.1.3. The same settings of the QCD calculations with parton showers and hadronisation were used as in the previous studies, while the NLO 3-jet cross sections were calculated by using NLOJET++, since this not is possible with DISENT.

As seen in the results, when requiring $\Delta\eta_1 < 1$ the cross-section falls at low $\Delta\eta_2$ since then the parton ladder is expected to be very short, which means that the probability for 3-jet events becomes small compared to high $\Delta\eta_2$.

7.3.1 Comparison to NLO 3-jet Calculations

As seen in Fig. 7.5 NLOJET++ provides a reasonable description of the data, taking into account the large uncertainties of the NLO prediction. There is good agreement when the two additional hard jets are emitted in the central region ($\Delta\eta_2$ large). However, if the additional hard jets are shifted to the forward region ($\Delta\eta_2$ small), the data are less well described by NLOJET++, which can be an indication that the more forward the additional jets go, the higher the probability is that one of them, or even both, do not actually originate from quarks but from additional radiated gluons. For gluon induced processes, which dominate at small x, events where two of the three selected jets originate from gluons are produced by NLOJET++ only in the real emission corrections to the three-jet final state. This effectively means that these kinematic configurations are only produced to leading order (α_s^3). The most extreme case, where all three reconstructed jets are produced by gluons, is not considered by NLOJET++. This results in a depletion of the theoretical cross section in the small $\Delta\eta_2$ region, which is more pronounced when $\Delta\eta_1$ is also small, i.e. when all three jets are in the forward region. Consequently a significant deviation between data and NLOJET++ can be observed for such events (see the lowest bin in Fig. 7.5b). NNLO calculations, currently not available, might improve the description of the data in this domain since virtual corrections to the production of two gluons could increase the cross section for such final states, and additional gluon emissions would enhance the probability that one of the soft radiated gluons produces a jet that fulfills the transverse momentum requirement applied in this analysis.

7.3.2 Comparison to QCD Models with Parton Showers and Hadronisation

Radiation that breaks the k_t-ordering may occur at different locations along the evolution chain, depending on the values of $\Delta\eta_1$ and $\Delta\eta_2$. Since one may get events where one or both jets from the di-jet system are produced by gluon radiation, it is noteworthy that CDM provides the best description of the data, while the other models fail in most of the bins (Fig. 7.6). The 2+forward jet sample differentiates CDM and the DGLAP-resolved model, in contrast to the more inclusive forward jet samples where CDM and RG-DIR+RES give similar predictions. The conclusion is that additional breaking of the k_t ordering is needed compared to what is included in the resolved photon model.

The DGLAP models give cross sections that are too low except when both $\Delta\eta_1$ and $\Delta\eta_2$ are large. For this last topology all models agree with the data, indicating that the available phase space is exhausted and that little freedom is left for dynamical variations.

For the 2+forward jet sample CCFM does not describe the shape of the η-distributions well (Fig. 7.7).

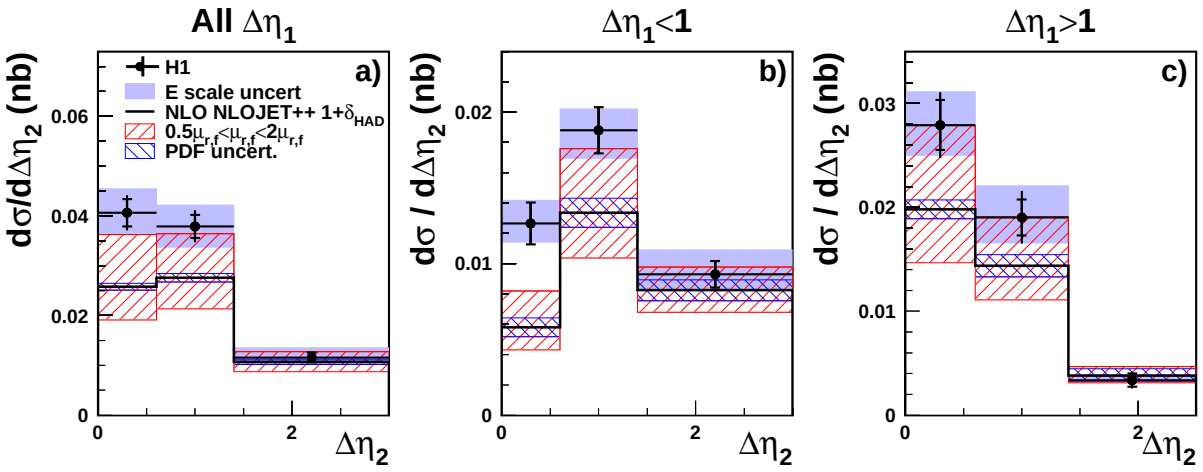

Figure 7.5: *2+forward jet cross-sections as a function of the rapidity separation between the forward jet and the most forward-going additional jet, $\Delta\eta_2$. Results are shown for the full sample and for two ranges of the separation between the two additional jets, $\Delta\eta_1 < 1$ and $\Delta\eta_1 > 1$. The systematic errors from the uncertainty of the energy scales in the detectors are shown by the band following the data points. The statistical errors are shown by the inner error bars, while the full error bars represent the systematic errors, not already included in the error band, added in quadrature to the statistical errors. The data are compared to the LO and NLO predictions of three-jet final state calculations by NLOJET++ $(1+\delta_{HAD})$. The band around the fixed order calculations illustrates the theoretical uncertainties in the calculations.*

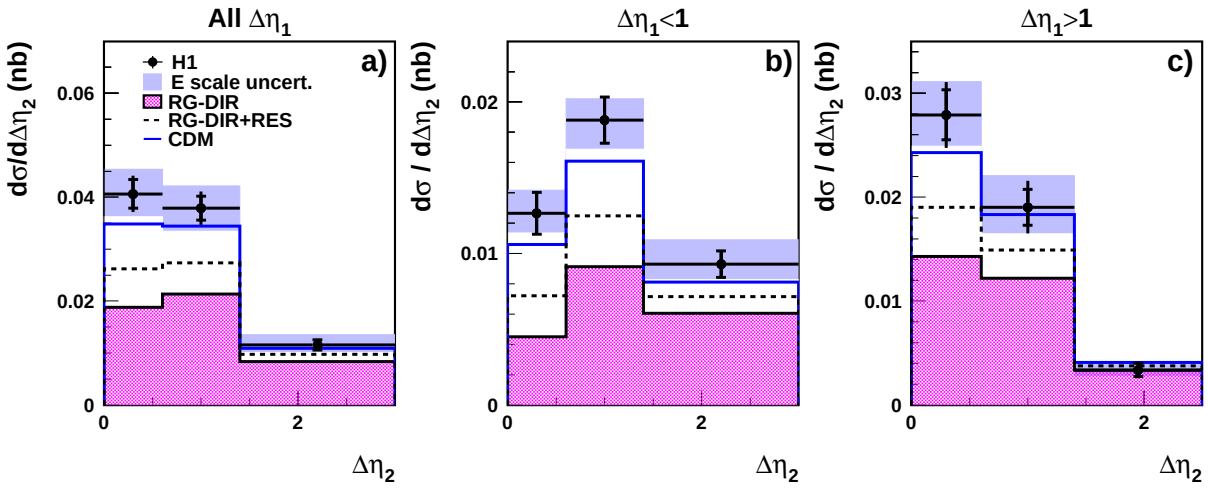

Figure 7.6: *2+forward jet cross-sections a function of the rapidity separation between the forward jet and the most forward-going additional jet, $\Delta\eta_2$. Results are shown for the full sample and for two ranges of the separation between the two additional jets, $\Delta\eta_1 < 1$ and $\Delta\eta_1 > 1$. The systematic errors from the uncertainty of the energy scales in the detectors are shown by the band following the data points. The statistical errors are shown by the inner error bars, while the full error bars represent the systematic errors, not already included in the error band, added in quadrature to the statistical errors. The data are compared to the predictions of RAPGAP DIR, RAPGAP DIR+RES and CDM.*

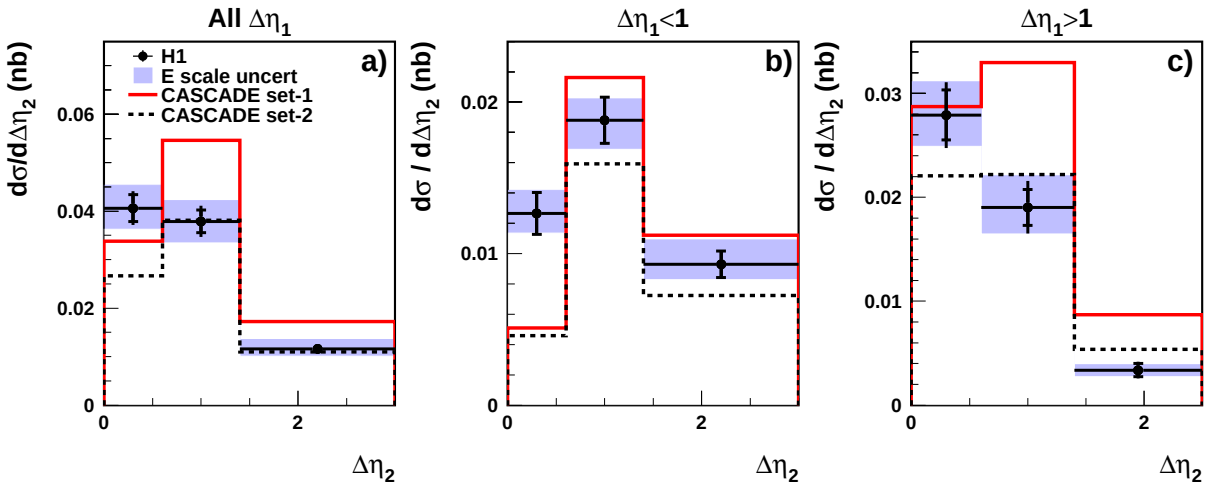

Figure 7.7: *2+forward jet cross-sections as a function of the rapidity separation between the forward jet and the most forward-going additional jet, $\Delta\eta_2$. Results are shown for the full sample and for two ranges of the separation between the two additional jets, $\Delta\eta_1 < 1$ and $\Delta\eta_1 > 1$. The systematic errors from the uncertainty of the energy scales in the detectors are shown by the band following the data points. The statistical errors are shown by the inner error bars, while the full error bars represent the systematic errors, not already included in the error band, added in quadrature to the statistical errors. The data are compared to the predictions of CASCADE.*

Chapter 8

Summary

An investigation of DIS events containing a jet in the forward direction has been performed using data collected in 1997, comprising an integrated luminosity of 13.72 pb^{-1}. Various constraints have been applied, which suppress contributions to the parton evolution described by the DGLAP equations and thus enhance the sensitivity to new parton dynamics. Several observables involving forward jet events have been studied and compared to the predictions of fixed order parton level calculations and QCD calculations including parton showers and hadronisation.

In order to obtain the best possible results several detector studies were performed. For example were the possible effects, from electronic noise in the forward region of the LAr-calorimeter and scattering against a collimator close to the primary vertex investigated. It was shown that requiring the transverse momentum of the forward jet to be larger than 3.5 GeV reduces the effects in the final results from both sources. The influence of these background sources are well implemented in the detector simulation. Purity and stability were shown to be larger than 40% in most bins and the corrections from the detector to the hadron level were in most cases below 20%.

Although, this measurement of the parton dynamics is of higher accuracy compared to earlier measuements [2, 3], the conclusions are similar. Also a recently published measurements on forward π^0 production in H1 [69] and the measurement of forward jet production in ZEUS [70] are consistent within the overlapping kinematical range. A more detailed comparison between the H1 and ZEUS results can be found in [71] where premilinary results on the forward jet measurement, reported in this thesis, and the ZEUS forward jet measurement were presented together.

The results on inclusive forward jet production show that NLO di-jet calculations and interactions with pointlike photons give cross sections which are consistently below the data at small values of x_{Bj}. Scattering against partons inside the virtual photon and the colour dipole model come closest to the data. Parton evolution with no ordering in p_t of the emissions as described by the CCFM model, studied with the different parameterizations of the unintegrated gluon density, does not reproduce the shape of the distribution. This proves that the forward jet cross section is sensitive to the details of the unintegrated gluon density and that these measurements can be used to further constrain the unintegrated parton density.

In order to further investigate the details of the parton dynamics, the total forward jet sample was subdivided into bins of Q^2 and $p^2_{t,\,\mathrm{jet}}$ such that kinematic regions were defined in which different evolution dynamics were expected to dominate. In this measurement the NLO di-jet calculations are closer to describing the data for high $p^2_{t,\,\mathrm{jet}}$ where the number of emissions are expected to be fewer. For the NLO di-jet calculations the large scale uncertainty could account for the deviations at high $p_{t,\,\mathrm{jet}}$. In general the NLO di-jet calculations from DISENT describe the data for high values of x_{Bj}, Q^2 and p^2_t, but fail for lower values of these variables.

In the region expected to include more DGLAP like dynamics, $Q^2 > p^2_{t,\,\mathrm{jet}}$, the DGLAP direct is closer to the data compared to other regions in $p^2_{t,jet}$ and Q^2. In this region and in the region where contributions from resolved processes are expected to become important ($p^2_{t,\,\mathrm{jet}} > Q^2$) the DGLAP resolved model and CDM give good agreement with data. The cross sections predicted by the DGLAP direct model are consistently too low. In the non-DGLAP like region ($Q^2 \sim p^2_{t,\,\mathrm{jet}}$) the CDM and DGLAP resolved model again reproduce the data best. The CCFM model in most cases fails to describe the shapes of the distributions.

The study of events with a reconstructed central di-jet system in addition to the forward jet reveals reasonably good agreement with CDM both in the region where the BFKL evolution is expected to dominate as well as in the more DGLAP like region. The DGLAP models (direct and resolved) both predicts too low a cross-section. For the first time, this gives evidence for parton dynamics in which the breaking of the k_t-ordering provided by the resolved photon model is not enough. The predictions by NLOJET++ give good agreement with the data only if the additional jets are emitted in the central region.

The fact that CCFM does not describes the shape of the spectra indicates that the forward jet cross-section can be used to improve the unintegrated parton density.

The results of this research suggest that a more complete description of the radiation pattern at small x_{Bj} requires the introduction of terms beyond those present in the collinear DGLAP approximation. It is observed that higher order parton emissions with significant transverse momentum contribute noticeably to the cross section. Calculations which include these processes, such as CDM and the resolved photon model, provide a better description of the data. A feature of these models compared to simple direct DGLAP evolution is that they break the ordering in transverse momentum. The similar behaviour of CDM and the DGLAP resolved model indicates that the energy stored in the evolution ladder does not allow for enough emissions to give a significant separation of the models. However, in the more exclusive mesurement of 2+forward jet events a clear differentiation of the models is obtained for the first time.

Part 2

Forward Jet Production in Diffractive Scattering

Chapter 9

Introduction to Forward Jet Production in Diffraction

As has been discussed already, cross sections in non-diffractive DIS can be factorized into a partonic cross section, describing the hard subprocess between the virtual photon and a parton in the proton, together with a parton density function, giving the probability to find a parton in the proton with a certain momentum fraction, x, in case the resolution power of the photon is Q^2. Diffractive scattering is characterized by a lack of hadronic activity in a region close to the proton direction (rapidity gap), which can be explained by the absence of color exchange in the interaction.

The understanding of diffraction is still fairly poor and the availible models differ significantly in their descriptions of the exchange of a colour singlet object. Theoretically this can be described by either of the following scenarios; by introducing a colorless pseudoparticle (the Pomeron), by the exchange of two gluons (the 2-gluon exchange model) or by adding soft color interactions to the hard exchange, where the soft color interactions contribute very little to the momentum transfer, but cause a rearrangement of the string topology (the SCI model).

In the resolved pomeron model, factorization has to be valid in order for the model to describe the data, whereas the 2-gluon exchange model will work even in the case of non-factorization, since this is a pertubatively calculable process at LO 2- or 3-jet (α_s^2/α_s^3) accuracy. An investigation of forward jet production in diffractive scattering is expected to provide a sensitive test of the factorization theorem.

The selected jet is produced at forward angles in the event, and well away from the electron side of the collision. Thus, in diffraction it is likely that the forward jet is the object closest to the rapidity gap. In such way, the scale of the diffractive scattering, and also the Pomeron remnant are expected to be relevant for the measurement. The measurement may therefore, to a larger extent compared to e.g. diffractive di-jet measurements, target a kinematic region for which the factorization ansatz may not be valid.

The diffractive analysis is performed on data from the 1999 and 2000 years, for which data were collected with higher luminosity compared to the data used in the forward jet analyses presented in part 1. For these, and later runs, the proton energy at HERA was incresed from 820 GeV to 920 GeV. Also, the diffractive analysis is performed with help of

the comparatively new object oriented analysis scheme (H1OO). For simplicity the measurements are presented as a ratio between the diffractive and non-diffractive cross-section. This gives a cancellation of uncertainties, and a more direct information on differences between the parton dynamics in the diffractive and non-diffractive events.

Chapter 10

Diffractive Scattering

Already in the first running years of HERA the H1 and ZEUS collaborations observed electron-proton scattering events with no activity in the forward region [72, 73]. These events could not be explained by the standard DIS models, which had been successful in describing the F_2 distributions. The events were called rapidity gap events, due to the gap in rapidity between the proton system, Y, and the obsevered hadronic system, X, (see Fig. 10.1), and it was found that they constitute about 10% of the total inelastic cross-section [74]. The difference between a normal DIS event and a rapidity gap event is illustrated in Fig. 10.1, where data are compared to MC generated events. The plot shows the number of events as a function of the rapidity of the most forward going particle in the event, η_{max}. In normal DIS the most forward going particle is expected to be close to the proton remnant, which corresponds to the distribution given by the MC events generated by RAPGAP with inclusive DIS. In the case of rapidity gap events, η_{max} extends towards lower rapidities as seen from the experimental data in Fig. 10.1. Scatterings resulting in large rapidity gaps are also referred to as diffractive scattering due to the analogy to diffraction in optics, since the t-dependence of elastic processes at fixed s is similar to the classical diffraction pattern from the scattering of light off an opaque sphere.

10.1 Theory

Theoretically diffractive scattering is described by an absence of colour flow somewhere in the exchange mechanism between the interacting particles, i.e. an exchange of a colorless object (color singlet state) is taking place. This is in contrast to non-diffractive scattering where an exchanged gluon is forming a colour string between the interacting particles, which breaks up and fragments into hadrons. In diffractive ep scattering the absence of color flow close to the proton may mean that the proton is not part of the normal fragmentation process, and therefore may remain intact. In such case the proton will essentially proceed unscattered in the beam pipe due to its high initial momentum. A schematic diagram of such an event is drawn in Fig. 10.1a).

The color singlet exchange can be described by introducing a pseudo-particle called the **pomeron** (denoted $\mathbb{P}$). In deep inelastic ep-collisions, where the high energy gives a large resolving power, the pomeron is assumed to be a hadron like object, and is assigned

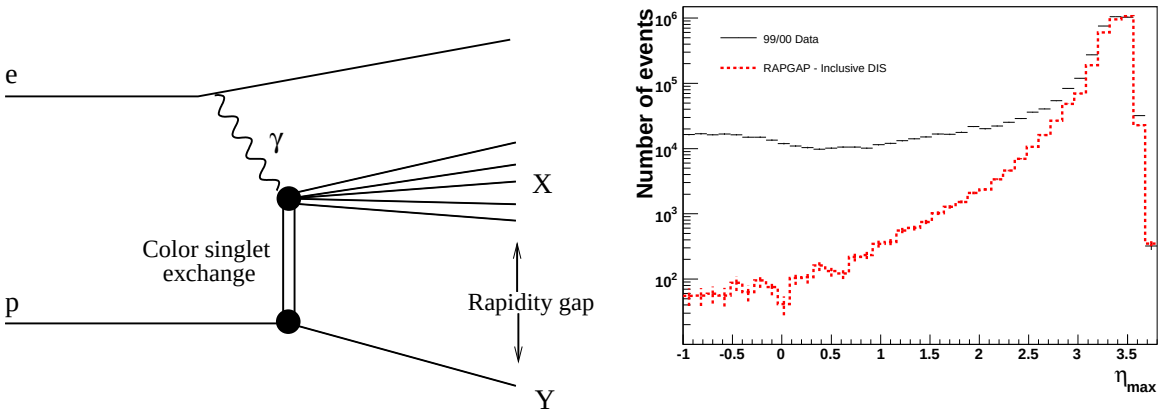

Figure 10.1: *a) Schematic diagram of diffractive scattering. The upper black dot which illustrates the fragmention into the system X includes higher order QCD reactions. b) Detector level distributions of data and Monte Carlo generated DIS events, showing the most forward going hadron activity, η_{max}, in events for which the inclusive DIS selection (eq. 5.1 and 5.4) have been applied. The Monte Carlo (RAPGAP) distribution has been rescaled to describe the peak in the data.*

a parton density function. However, other color singlet exchange models also exist. Two of these, the 2-gluon exchange model and the soft color interaction model, are discussed in section 10.1.4 and section 10.1.5, respectively.

In diffraction it may also happen that enough energy is transferred to the proton such that it breaks up and fragments to a hadronic state with a mass larger than the proton rest mass. This is referred to as **proton dissociation**.

10.1.1 Diffractive Kinematics and the Diffractive Stucture Function

The diffractive kinematics is described by a set of variables, which are introduced below. The hadronic final state is divided into two subsystems, X and Y, separated by the rapidity gap. The invariant masses for these systems are

$$M_X^2 = P_X^2$$
$$M_Y^2 = P_Y^2$$

where P_X and P_Y denote the four-momenta of the systems, respectively. If no proton dissociation is involved M_Y equals the proton rest mass.

Furthermore, the four-momentum transfered by the color-singlet system, t, i.e. the rest mass of the pomeron, is given by

$$t = (P_p - P_Y)^2. \tag{10.1}$$

In DIS two more quantities can be defined, $x_{I\!P}$ and β. In analogy to x_{Bj} in the lowest order inclusive DIS, the fraction of proton momentum carried by the exchanged color singlet

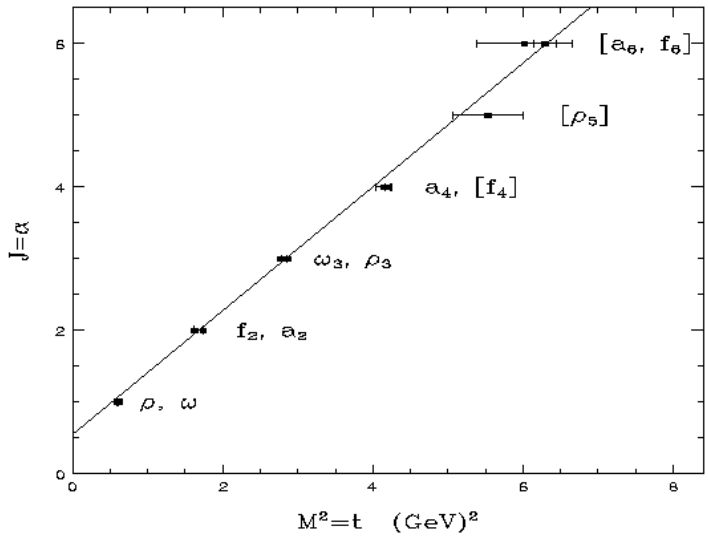

Figure 10.2: *Chew-Frautschi plot showing the correlation between the spin and the mass of some mesons [77].*

object, $x_{\mathbb{P}}$, is defined by

$$x_{\mathbb{P}} = \frac{q \cdot (P_p - P_Y)}{q \cdot P_p} \approx \frac{Q^2 + M_X^2}{Q^2 + W^2} \tag{10.2}$$

where the approximation is valid if the mass of the proton and the color singlet object are neglected.

Finally, β is defined as

$$\beta = \frac{x_{Bj}}{x_{\mathbb{P}}} \tag{10.3}$$

and can be interpreted as the fractional momentum of the pomeron carried by the struck parton inside the pomeron.

10.1.2 Regge Phenomenology

The pomeron-based model in diffraction was developed before QCD was invented. Then, the total cross-section of soft hadron-hadron interactions was described by the exchange of mesons. For a complete description, contributions from several different mesons has to be taken into account. This can be done by using Regge theory [75, 76], which implies that the mass squared, $M^2 = t$, and the angular momentum, α, of the contributing mesons are linearly correlated, i.e. the mesons follow a so-called Regge trajectory

$$\alpha(t) = \alpha(0) + \frac{d\alpha(t)}{dt} t \tag{10.4}$$

In the beginning of the 1960's Chew and Frautschi verified this [77], as illustrated by the Chew-Frautschi plot in Fig. 10.2.

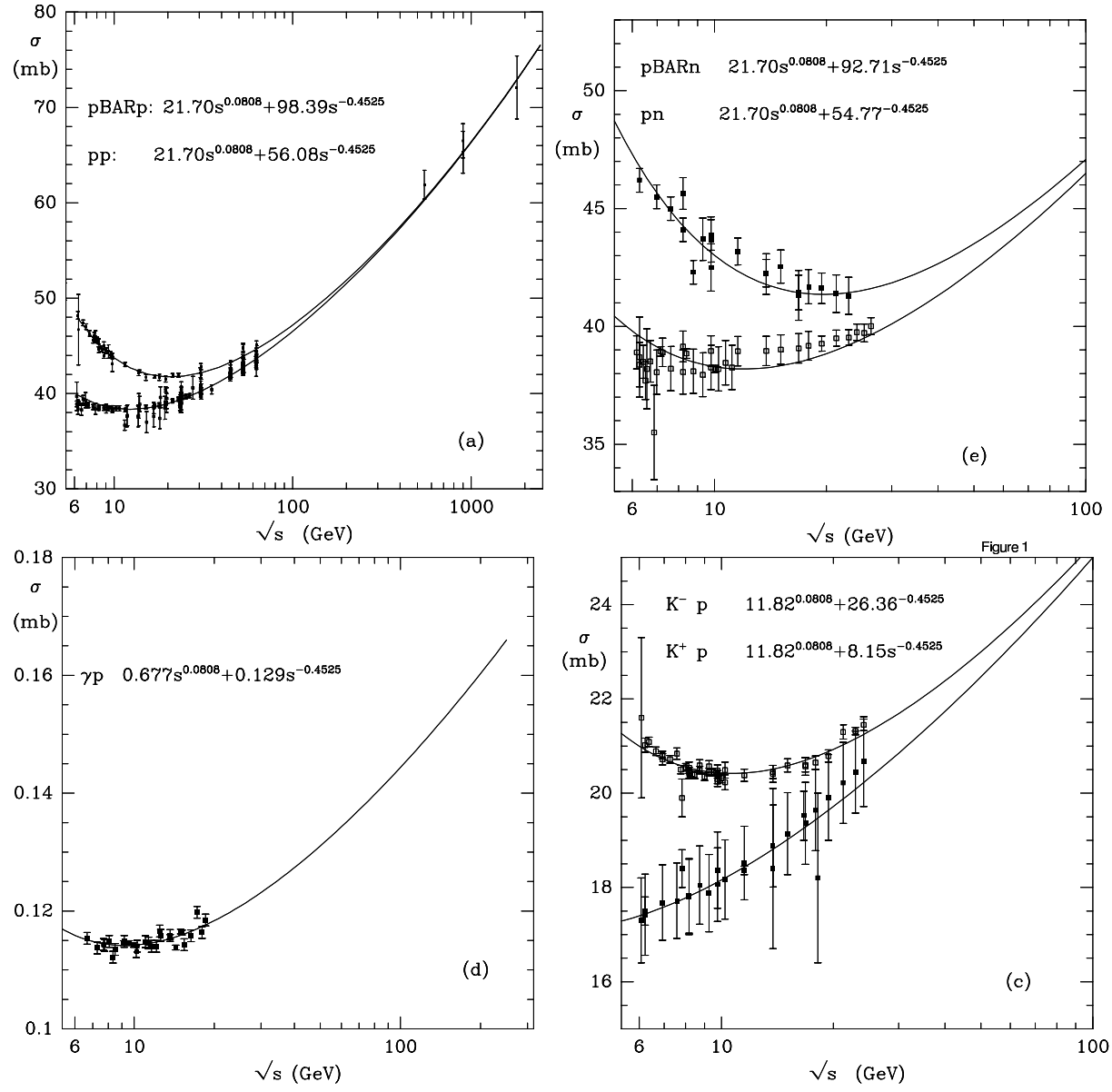

Figure 10.3: *Data with fits, according to Eq. 10.6, for the total cross-sections of different reactions [79].*

Furthermore, one can show (by using the optical theorem) [78], that the total cross-section can be expressed as

$$\sigma \propto s^{\alpha(0)-1} \tag{10.5}$$

Experimental data on total cross-sections for pp, $p\bar{p}$, pn, $p\bar{n}$, γp, K^-p and K^+p may be described by a parametrisation containing two terms according to:

$$\sigma = X^{AB} * s^{\epsilon} + Y^{AB} * s^{-\eta} \tag{10.6}$$

Here A and B denotes the interacting particles and X, Y, ϵ and η are determined from fits. A selection of measurements and fits are shown in Fig. 10.3 [79].

It is interesting to point out two things. First, the value of the fitted parameter η in Fig. 10.3 ($\eta = 1 - \alpha(0) = 0.4525$) agrees well with the intercept of the meson trajetory with the y-axis in the Chew-Frautschi plot, Fig. 10.2. That means that for low s the mesons on the Regge trajectory in Fig. 10.2 provide the dominating exchange. Second, the fitted parameters ϵ and η are universal constants, i.e. they are the same for all reactions.

The fact that two different terms are needed to describe the cross-section can be interpreted such that two different exchange trajectories contribute to the scattering. The second exchange (corresponding to the first term in Eq. 10.6) is the already mentioned pomeron. The corresponding trajectory has been determined, by making fits to cross-sections of diffractive data [80, 81], to be

$$\alpha(t) = 1.1 + 0.25t \tag{10.7}$$

However, so far no physics candidates on the pomeron trajectory have been observed. An expected candidate would, according to theoretical predictions, carry the quantum numbers of vacuum. That is partly experimentally reflected by the fact that the fitted parameters for the pomeron term in Fig. 10.3 are the same for e.g. pp and $\bar{p}p$ scattering, meaning that the pomeron does not distinguish between particles and anti-particles. Possible candidates are glueballs, but no clear evidence for their existence has been seen.

In Fig. 10.4 the meson trajectory, referred to as the Reggeon, and the pomeron trajectory are shown. The figure also shows yet another trajectory, the so-called pion trajectory.

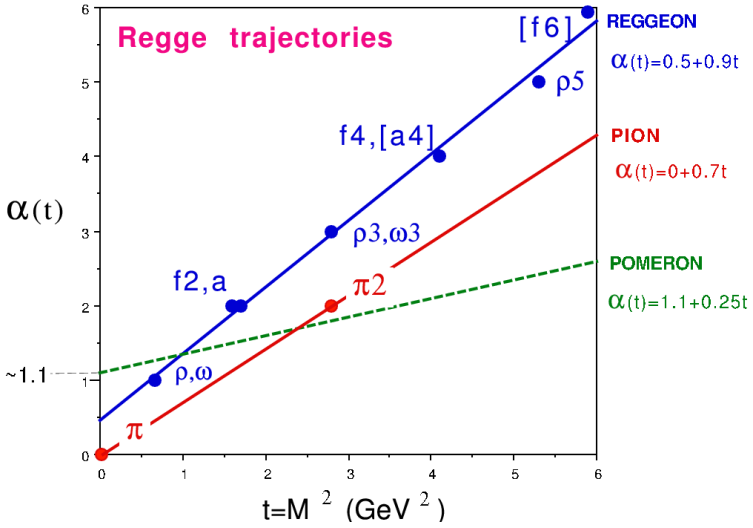

Figure 10.4: *The meson, pomeron and pion trajectories [82].*

10.1.3 The Resolved Pomeron

If the pomeron can be interpreted as an object with a hadron like substructure, a structure function, $F_2^{\mathbb{P}}$, can be defined for the pomeron and, by using the factorization theorem. The diffractive structure function, $F_2^{D(4)}$, can be factorized into $F_2^{\mathbb{P}}(\beta, Q^2)$, giving the probability of having a parton, which carries a fraction β of the pomeron momentum, if

measured with a resolution given by Q^2, and a universal flux factor $f_{I\!P}(x_{I\!P}, t)$, which gives the probability of creating a pomeron inside the proton with a momentum fraction $x_{I\!P}$, providing a momentum transfer t, i.e.

$$F_2^{D(4)}(\beta, Q^2, x_{I\!P}, t) = f_{I\!P}(x_{I\!P}, t) F_2^{I\!P}(\beta, Q^2) \tag{10.8}$$

where the number "4" in the notation of $F^{D(4)}$ refers to the number of parameters. For $F^{D(3)}$ the dependence on t has been integrated.

The pomeron flux factor, $f_{I\!P}(x_{I\!P}, t)$, is identical to a "pomeron density function" for which several different parametrisations exist. Some of these are described in [83–88]. As for the parton density function $f_{I\!P}$ has to be determined from experimental fits.

In the case of a meson exchange $F_2^{I\!P}$ is being replaced by the structure function of the mesons (Reggeon). Finally, the diffractive cross-section contains terms for both pomeron and meson exchanges, which means a more correct description of F_2^D is given by:

$$F_2^{D(4)}(\beta, Q^2, x_{I\!P}, t) = f_{I\!P}(x_{I\!P}, t) F_2^{I\!P}(\beta, Q^2) + f_{I\!R}(x_{I\!R}, t) F_2^{I\!R}(\beta, Q^2) \tag{10.9}$$

where $f_{I\!R}(x_{I\!R}, t)$ and $F_2^{I\!R}(\beta, Q^2)$ are the flux factor and the structure function of the Reggeon exchange, respectively.

The resolved pomeron and reggeon model is implemented in the RAPGAP Monte Carlo program.

10.1.4 The Soft Color Interaction Model

The soft color interaction model (SCI) [89] for diffraction is leaving the model of scattering against a preformed color singlet object (the pomeron) behind, and is based on normal DIS reactions. SCI includes instead non-pertubative soft color interactions in the scattering which may change the color structure in the event, but not the momentum of the involved partons. In the end this results in rapidity gaps in the fragmentation processes, in which color strings break up (explained in section 2.4.1).

Fig. 10.5a), b) and c) illustrate the appearance of rapidity gaps in the SCI further. In Fig. 10.5a) a normal DIS event, with the color strings (dashed lines) drawn according to the conventional Lund string connection model [28, 29] between partons, is shown. When the color strings fragment, hadrons will be created over the full rapidity range. Fig. 10.5b) and c) show how the color flow can be rearranged by the exchange of soft gluons between the partons such that an abscence of color flow occurs.

The SCI model has only one free parameter, R, which gives the probability for soft color interactions to occur. R is determined by making fits to measurements of the diffractive structure function.

In a modified version of the SCI model [90], R is exponentially suppressed by the difference in area, ΔA, between the new and the old configuraion, where the area for a string configuration between two partons, i and j, is given by the Lund Area Law according to $A_{ij} = (p_i + p_j)^2 + (m_i + m_j)^2 = 2(p_i p_j + m_i m_j)$. R is modified by a factor of $1 - e^{-b\Delta A}$, where also b is a free parameter.

The SCI models are implemented in the LEPTO [91] Monte Carlo program. The model for DIS events in this program is similar to what is used in RAPGAP, i.e. the DIS events are generated by using a leading order matrix element and DGLAP based parton showers.

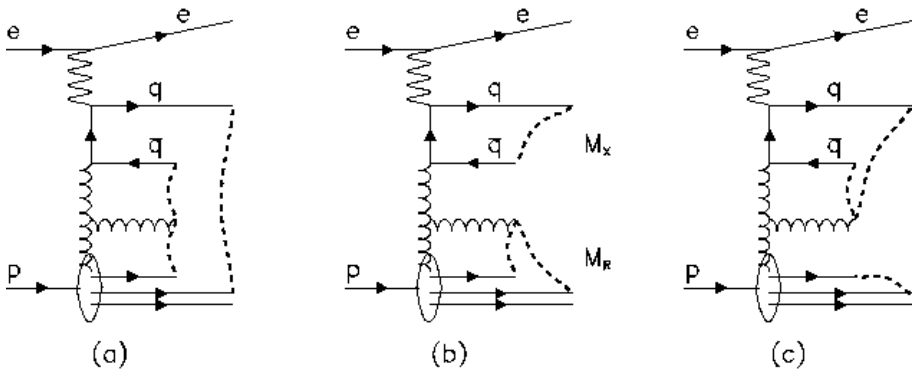

Figure 10.5: *a) A normal DIS event with string stretching without any soft color interactions involved. b,c) Color flow in case of soft color interactions (not drawn) in the events, according to the SCI-model. The stretching of the color strings change and result in gaps in the color flow. The color strings are indicated by dashed lines. [89]*

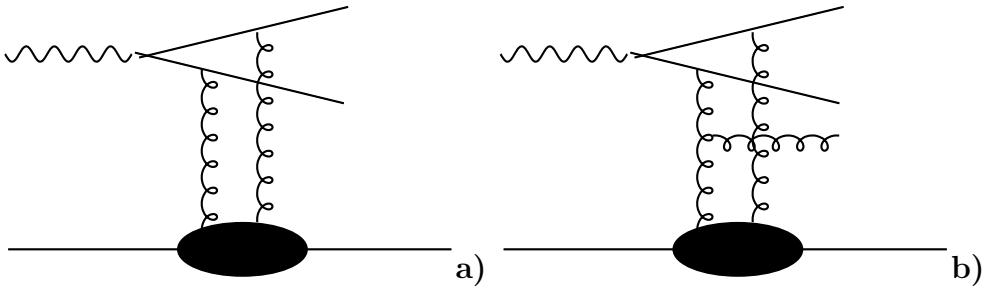

Figure 10.6: *Diagrams of a) two jet production and of b) three jet production the in 2-gluon exchange model.*

10.1.5 The 2-gluon Exchange Model

Another model for color singlet exchange in diffraction is the 2-gluon exchange model. The two most simple configurations have been theoretically calculated. The first one is $\gamma p \rightarrow q\bar{q}p$ [92], as shown in Fig. 10.6a), and the second one is $\gamma p \rightarrow q\bar{q}gp$ [93], as illustrated in Fig. 10.6b). In these calculations the involved partons are hard. This makes the model pertubatively calculable and independent of the factorization theorem. The calculations are made at LO 2-jet (α_s^2) and 3-jet (α_s^3) accuracy, respectively.

Events with the 2-gluon exchange model can be calculated by the RAPGAP Monte Carlo program.

Chapter 11

Diffractive Forward Jet Analysis - Experimental method

Below follows a summary of the diffractive forward jet analysis. After a description of the phase space and detector level selections, control distributions, corrections, purity and stability are discussed.

The sub-detectors which are specifically used to select diffractive events, i.e. the forward muon detector and the proton remnant tagger, are briefly described below together with the corresponding detector requirement used. A general description of the H1 detector has already been given in chapter 4.

It should be pointed out already here that the diffractive analysis described in the following is still in an initial state. In order to prepare the data for a publication, still several things have to be understood in more detail and preferably data from the last running years of HERA should be used in order to increase the statistics and benefit from the proton tag by the forward detectors. With the significantly higher statistics from the years 2001 and on, an unbiased sample of diffractive events can be obtained from a proton tag in the Forward Proton Spectrometer (FPS) and the Very Forward Proton Spectometer. The current analysis is performed on 99/00 data.

11.1 DIS and Forward Jet Selection

With a few exceptions, which are listed below, the DIS and forward jet event selections are identical to the cuts described in Chapter 5 and summarized in Eqs. 5.1, 5.2 and 5.4. The following cuts differ:

- The statistics is increased slightly by changing $E_{\text{electron, min}}$ from 10 to 9 GeV and Q^2_{max} from 85 to 100 GeV^2.
- Due to the small diffractive forward jet phase space a cut on p_t^2/Q^2 is not statistically affordable. Thus, this cut is not applied.
- Due to the higher proton energy, 920 GeV compared to 820 GeV, the x_{jet}-cut is lowered to $x_{\text{jet}} > 0.03$ in order to still match the $p_t > 3.5$ GeV cut.

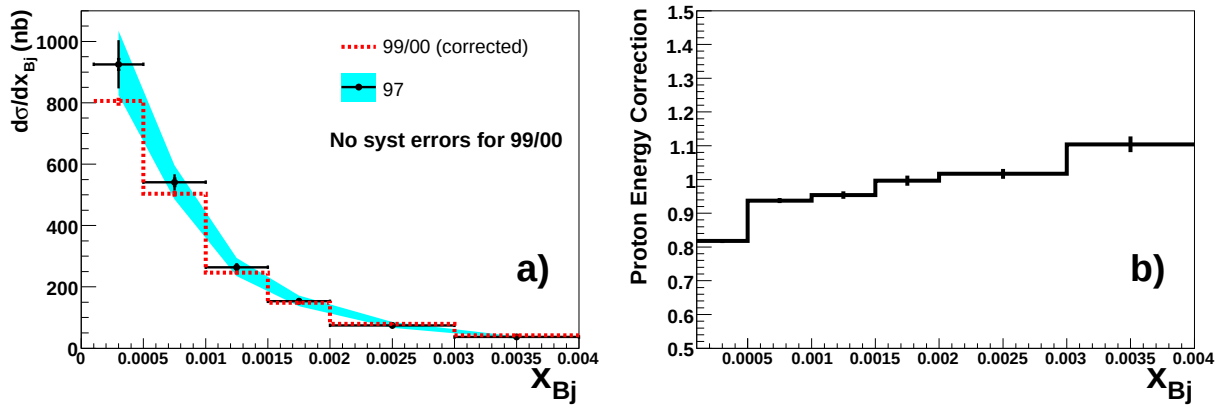

Figure 11.1: *a) Reproduction of the single differential forward jet cross-section for the 1997 data, and the proton energy corrections applied to the 99/00 data.*

11.1.1 Cross-check against the 1997 Forward Jet Analysis Results

As a cross-check, the 1997 forward jet analysis data were repeated using the 99/00 data and the H1 object oriented analysis program. The same selection as described in Chapter 5 and corrections for detector effects were applied. The reproduction is shown in Fig. 11.1a) and 11.2 for single and triple differential cross-sections, respectively, where the 97-data are shown with both statistical and systematic errors, while the 99/00 data only include the statistical errors. As seen the old data are in good agreement with the newer data. The corrections for the difference in proton energy, applied to the 99/00 data, were estimated by running RAPGAP with the two different proton energies. The correction factors, which are the ratio between the two different results from RAPGAP, are shown in Fig. 11.1b) for the single differential cross-section. The general behavior of this correction for the triple differential cross-section is the same.

11.2 The Monte Carlo Sample

Monte Carlo events are generated with the RAPGAP Monte Carlo program and detector simulated using the H1SIM program. In addition to non-diffractive events, RAPGAP generates diffractive events of the following three kinds:

- Diffractive events with pomeron exchange, with light quarks (u,d,s) contributing to the pomeron structure.
- Diffractive events with pomeron exchange, with charm quarks (c) contributing to the pomeron structure
- Diffractive events with reggeon exchange, with u-,d-,s-,c- quarks contributing to the reggeon structure.

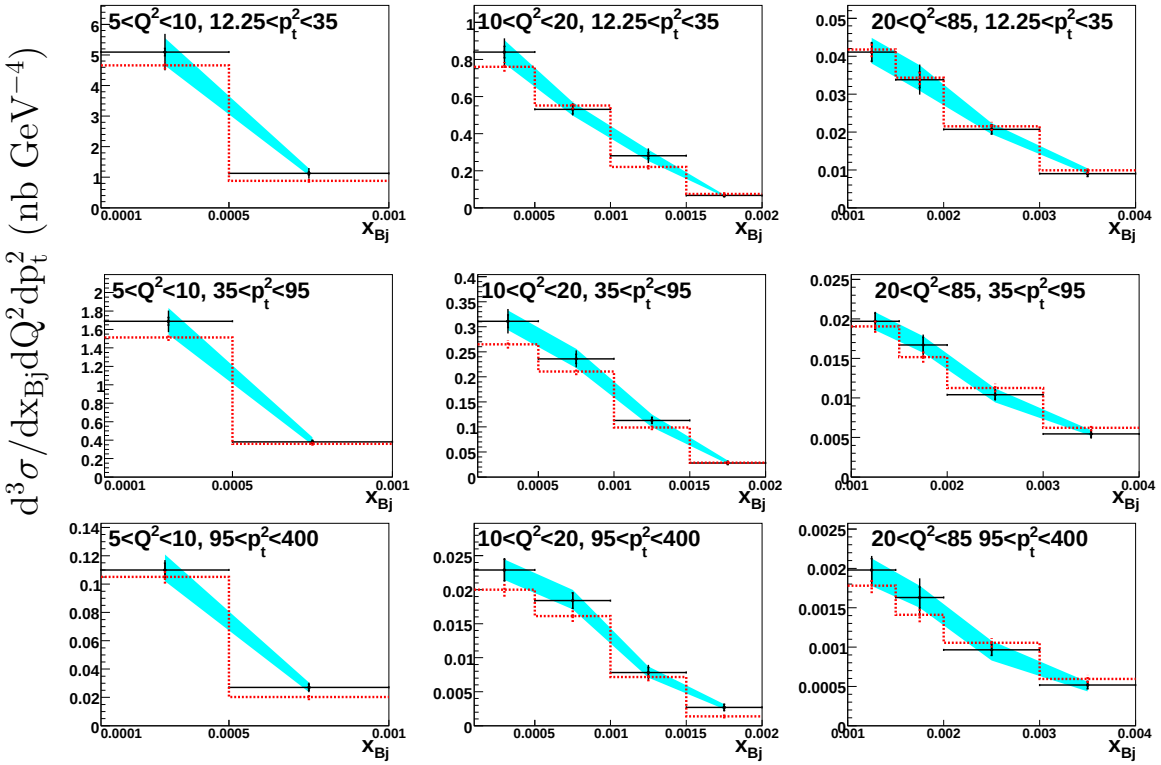

Figure 11.2: *Comparison between 97 and 99/00 triple differential forward jet cross-sections. The 99/00 data is shown without systematic errors and is corrected for the higher proton energy.*

The contribution from these events is added to the non-diffractive Monte Carlo contribution in order to describe the diffractive data. The same cuts as for the real data are applied to the detector level Monte Carlo events. Since inclusive measurements, e.g. F_2, do not exclude contributions from diffraction, such contributions are to some extent already accounted for in the "non-diffractive" PDFs (which are extracted from fits to the data). This results in some double counting when adding contributions from non-diffractive and diffractive Monte Carlo events. In order to avoid double counting of events in the overlapping parts of the phase-space the non-diffractive Monte Carlo events are used in the region:

$$x_{\mathbb{P}} > 0.2 \quad \text{OR} \quad M_Y > 5 \text{ GeV} \tag{11.1}$$

while the diffractive Monte Carlo events are used in the region

$$x_{\mathbb{P}} < 0.2, \quad 0.8 < M_Y < 1.2 \text{ GeV} \tag{11.2}$$

These requirements are applied on the hadron level variables.

11.3 Selection of Diffractive Events

The selection of diffractive events in the H1 detector can be done either by tagging on the scattered proton, which can be detected in one of the forward proton detectors, or by requiring a large rapidity gap (LRG). A recent H1 publication [80], in which the diffractive structure function was measured, shows that the two methods give consistent results for such an inclusive measurent.

The proton tag method has the advantage that the sample will be unbiased, but has the disadvantage that the acceptance of the detectors are low, which will result in a small statistical sample. The LRG method has the advantage to give a large statistical sample, but does not provide an unambigous selection of diffractive events.

The possibility to tag the scattered proton in the forward proton spectrometer for the present analysis of forward jet production was found to give too low statistics. Thus, instead the LRG method is used.

11.3.1 Tagging the Forward Proton Spectrometer

In the forward proton spectrometer (FPS), scattered protons are detected by four different scintilliator detectors, positioned in a distance of 63, 80, 81 and 90 meters from the interaction point in the proton direction.

However, the FPS, suffers from very small acceptance and was active only for half of the luminosity period during 1999-2000. Forward jet events, which are selected by applying the cuts described in section 11.1, and using the trigger elements for the horizontal layers (positioned at 63 and 80 meters) of the FPS, only gives 87 coincidences between the two

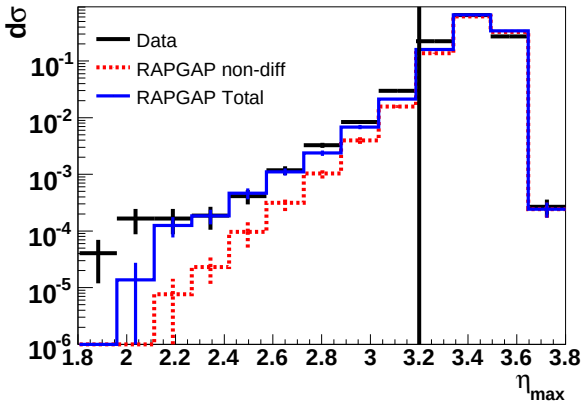

Figure 11.3: *The η_{max} distributions on detector level for data and Monte Carlo generated forward jet events. The vertical line indicate where the η_{max}-cut is applied.*

trigger elements [1], and about 600 hits for the single trigger elements respectivly. The small number of coincidences compared to the large number of single hits indicates that events from beam gas interactions constitute a serious background [94].

11.3.2 The Large Rapidity Gap Method

In order to select diffractive rapidity gap events on the detector level, the following veto cuts are applied to the data and the detector simulated Monte Carlo events.

The η_{max} - cut

The hadronic activity, which is most forward in the LAr calorimeter in an event, is required to have a rapidity, η_{max}, which fulfills:

$$\eta_{max} < 3.2 \tag{11.3}$$

In order to avoid event rejections due to noise in the calorimeter only objects with an energy larger than 400 MeV are considered. In Fig. 11.3 the η_{max} distribution is shown for data, non-diffractive Monte Carlo events and the sum of the diffractive and non-diffractive Monte Carlo sample. The vertical line in the figure illustrates where the selection cut is applied, according to Eq. 11.3. The agreement between the Monte Carlo and data gives confidence in the detector description, which is important when correcting for detector effects.

The Forward Muon Detector (FMD)

The forward muon detector is placed in the proton direction outside the main detector. It consists of a toroidal magnet with 3 drift chamber planes on either side, Fig. 11.4. Each

[1] trigger elements 164 resp. 165

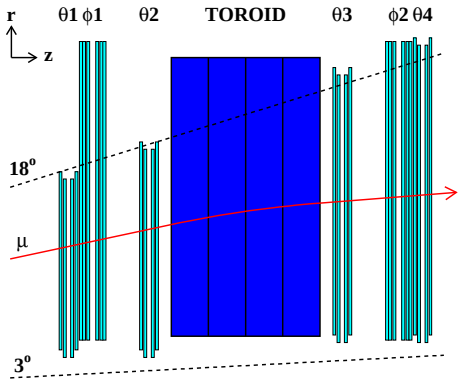

Figure 11.4: *Schematic figure of the forward muon detector. θ and ϕ indicate the layers which are designed to measure the polar and the azimuthal angles, respectively. Due to high background from synchrotron radiation, the layers behind the toroid are not used as veto layers in the analysis.*

of the planes have double layers, with the two layers displaced by half the width of the drift cells, in order to reduce left-right ambiguites. The primary task of this detector is to determine the momenta of forward going muons, but the FMD is also used as a veto detector to select diffractive events. In case particles in non-diffractive events are produced at small angles, they may scatter against dead material in the beam-pipe and create showers in the FMD. For the reconstruction of muon tracks these events clearly constitute a background, whereas in a diffractive analysis they destroy the rapidity gap and will signal a non-diffractive event. Thus, from scattering of particles against dead material, the FMD has a veto sensitivy to particle production also outside its constructed range ($3^o < \theta < 18^o$).

Rapidiy gap events are tagged by allowing at most one hit in the first two double layers, and one additional hit pair in the third double layer, i.e.

$$N_{\mathrm{FMD},1-2} < 2 \quad \text{AND} \quad N_{\mathrm{FMD},1-3} < 3 \tag{11.4}$$

In Fig. 11.5a) and b) it is clearly seen that for more than 1 hit in the first 2 layers and more than 2 hits in the first 3 layers, there is almost no diffractive events but only non-diffractive events. Thus, the events to the right of the vertical lines are cut away to select diffractive events.

The noise in the FMD is not included in the detector simulation, but can be estimated by using so-called randomly triggered data events. These events are not related to any physics trigger but collected at constant rate, giving events which are supposed to be empty, which is the case for the majority of collisions at HERA. In the actual analysis these events are removed by the physics triggers. The noise is estimated by requiring such events to fulfill

$$N_{\mathrm{FMD},1-2} > 1 \quad \text{AND} \quad N_{\mathrm{FMD},1-3} > 2 \quad \text{AND} \quad \eta_{max} < 3.2 \tag{11.5}$$

i.e. the FMD cuts are reversed in order to only select events which would fail the diffractive selection due to the FMD requirement. The LAr calorimeter noise is already implemented

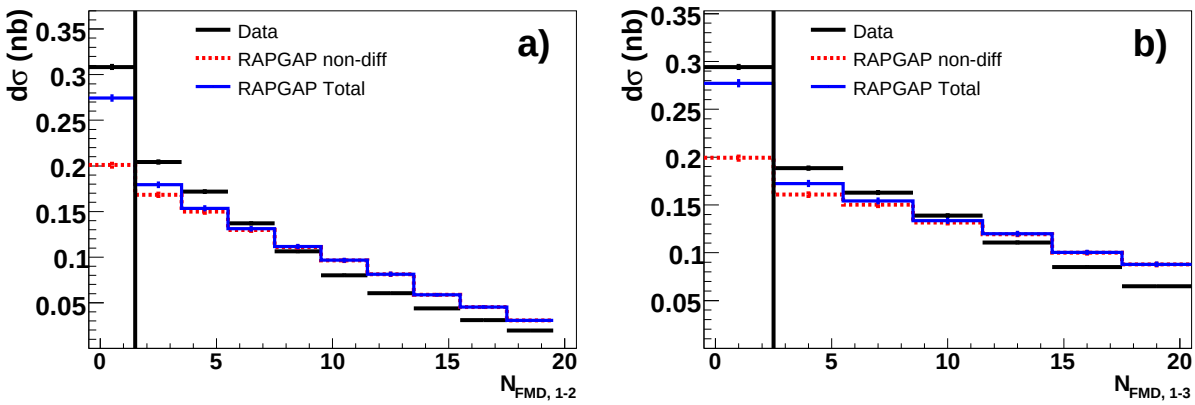

Figure 11.5: *The distribution of the total number of hits in the first two (a) and three (b) layers in the FMD. The thick black vertical lines illustrate the where the cuts are applied. The distributions are shown for forward jet events, for which the data are normalized to luminosity and the Monte Carlo distributions are scaled to the data.*

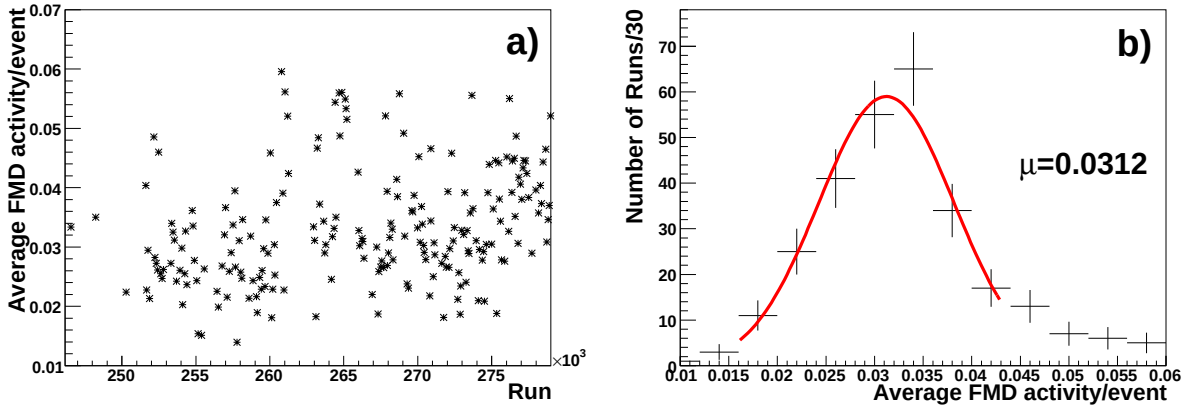

Figure 11.6: *a) shows the average activity in the FMD for random triggered events fulfilling the requirements of Eq. 11.5 as a function of run number. b) shows a Gaussian distribution fitted to the same noise activity.*

in the detector simulation and therefore the η_{max}-cut is kept as in the diffractive selection, in order not to double count events, which otherwise would have been rejected due to noise in the LAr calorimeter. Fig. 11.6a) shows the number of events with activity in the FMD normalized to the total number of events as a function of run number. Fig. 11.6b) shows a Gaussian distribution fitted to the FMD activity for the random triggered events, giving an estimated noise of 3.1%. This is in agreement with earlier studies at H1 [95]. Thus, the diffractive data are corrected by multiplying the number of events with $C_{\mathrm{FMD}} = 1.031$.

The Proton Remnant Tagger (PRT)

The proton remnant tagger (PRT) is situated in the forward direction, 24 meters from the interaction vertex. It consists of 7 double layer scintillator counters surrounding the beam pipe, and covering a rapidity region of $6 < \eta < 7.5$. The detector arrangement is sketched

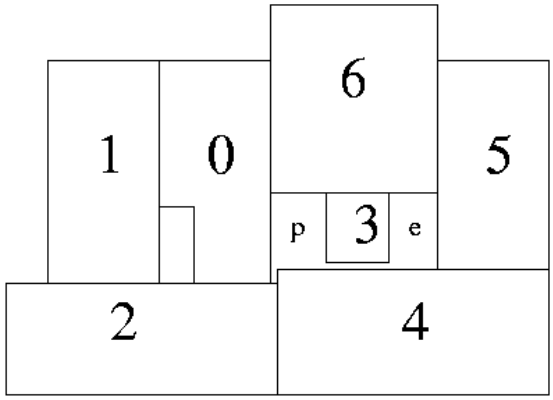

Figure 11.7: The location of the scintillator detectors of the PRT (p and e denotes the proton and the electron beam, respectively).

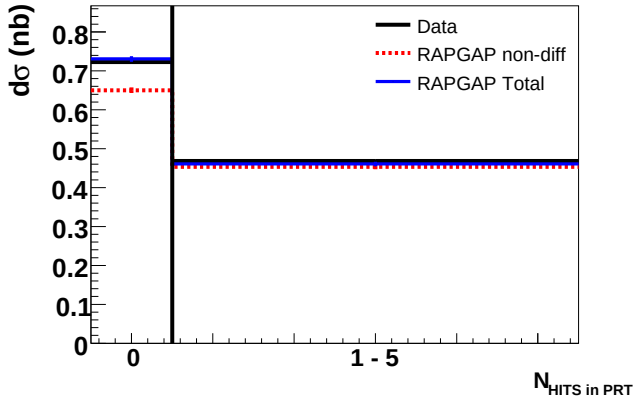

Figure 11.8: *The total number of hits in the layers 0-4 of the proton remnant tagger. All events contributing to the right bin are rejected.*

in Fig. 11.7, where the beam-pipes are denoted by p and e. The layers denoted 5 and 6 layers are known to be too noisy and are therefore excluded in the analysis.

To further reject events with some activity in the forward region also the PRT is used as a veto detector. The requirement is that a diffractive event should not have any hits in layers 0-4 of the detector, $N_{\text{PRT, 0-4}}$, i.e.

$$N_{\text{PRT, 0-4}} < 1 \tag{11.6}$$

The activity in the proton remnant tagger is shown in Fig. 11.8. As seen in the figure, the non-diffractive events are suppressed and the diffractive events are favoured below the cut, indicated by the vertical line, compared to above the cut. The noise in the PRT is overestimated in the detector simulations. Therefore, for the Monte Carlo files the activity in the PRT has been randomly reduced after the detector simulation, in order to obtain a better description of the data.

11.3.3 Phase Space Cuts for Diffractive Events

The diffractive phase space is defined by two cuts. In order to suppress contributions from non-diffractive events, one requires that

$$x_{\mathbb{P}} < 0.05. \tag{11.7}$$

Events with high mass proton dissociation are rejected by the requirement

$$M_Y < 1.6 \text{ GeV} \tag{11.8}$$

on hadron level events.

The variables are defined in Section 10.1.1.

11.4 Control Distributions

In order to verify that detector effects are correctly reproduced by the detector simulation various control distributions have been produced. Distributions are shown for the non-diffractive forward jet sample in Fig. 11.9 and for the diffractive forward jet sample in Fig. 11.10. Due to the limited statistics of the final diffractive forward jet sample, already in the control distributions the same bin widths as for the final measurement, are used. These are optimized to obtain similar number of events in each bin.

The figures show shape comparisons between the data and the Monte Carlo distributions, i.e. the data are normalized to luminosity, while the number of Monte Carlo events are scaled to the data. It should be noted, that since the final results are shown as a ratio between the the diffractive and non-diffractive contributions, the measured absolute cross-sections are of minor importance.

Furthermore, as seen in the previous non-diffractive forward jet analysis the shape of the distributions are well described by non-diffractive events alone (chapter 5). Thus, for this sample only the non-diffractive Monte Carlo sample is used, while for the diffractive sample shown in Fig. 11.10, the diffrative and the non-diffractive events are normalised to luminosity and summed as described in section 11.2. The description of all variables are improved by reweighting the Monte Carlo events to fit the Q^2 distribution.

The background from non-diffractive forward jet events is separatly shown in Fig. 11.10 and it is less than 20% of the diffractive forward jet sample. The correction for this background is included in the detector corrections.

11.4.1 Corrections of the Data

The measured ratio between diffractive and non-diffractive events is corrected to the non-radiative hadron level, seperately for both detector effects ($C_{\text{DET, non-diff fj}}$ resp. $C_{\text{DET, diff fj}}$) and QED radiation ($C_{\text{QED, non-diff fj}}$ resp. $C_{\text{QED, diff fj}}$). The diffractive data are also corrected for the noise contribution in the FMD (C_{FMD}) which is not included into the detector

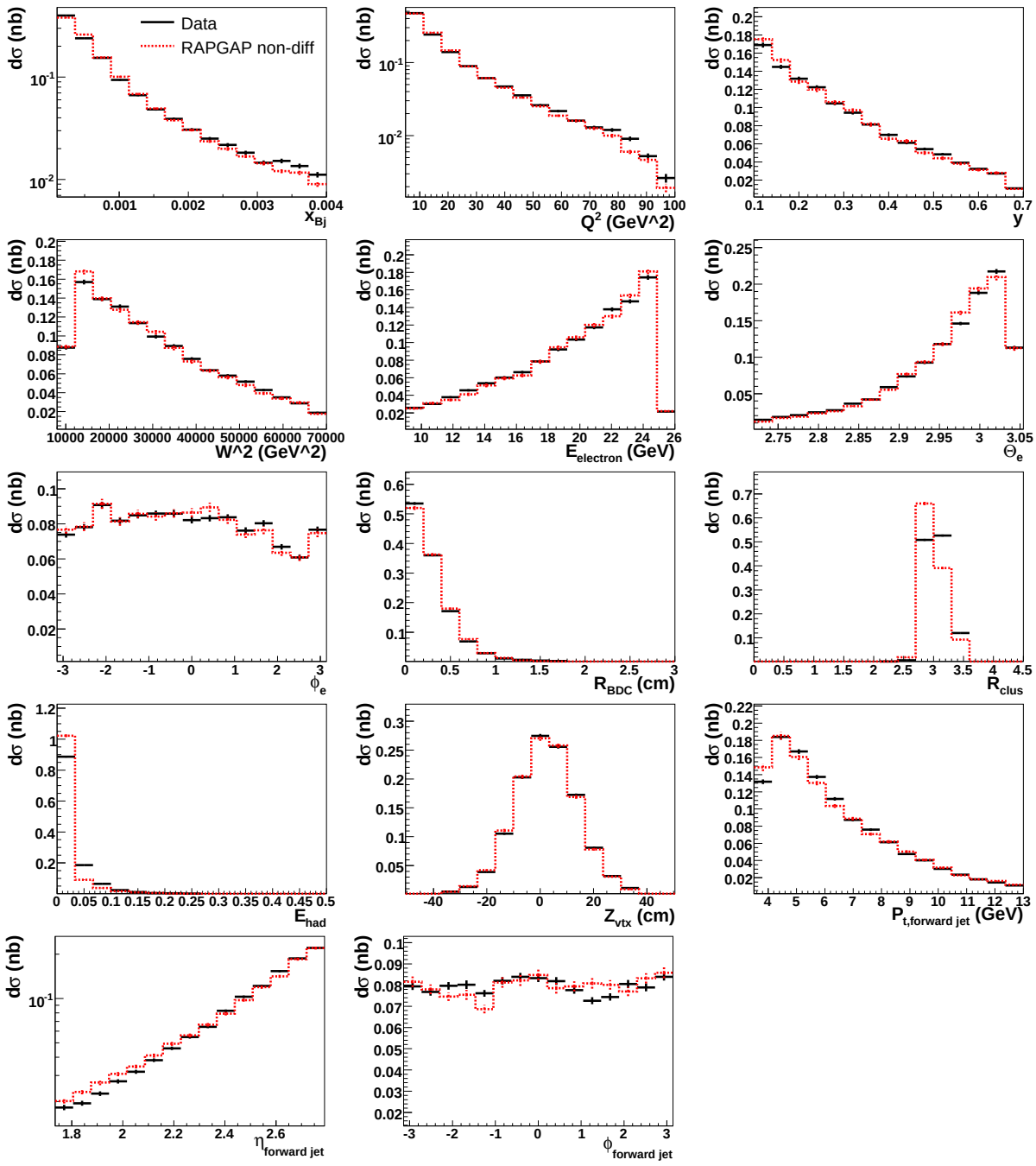

Figure 11.9: *Control distributions for events in the non-diffractive forward jet sample. In order to improve the description of the data, the Monte Carlo events have been reweighted to the data such that a better agreement with the Q^2 distribution is obtained.*

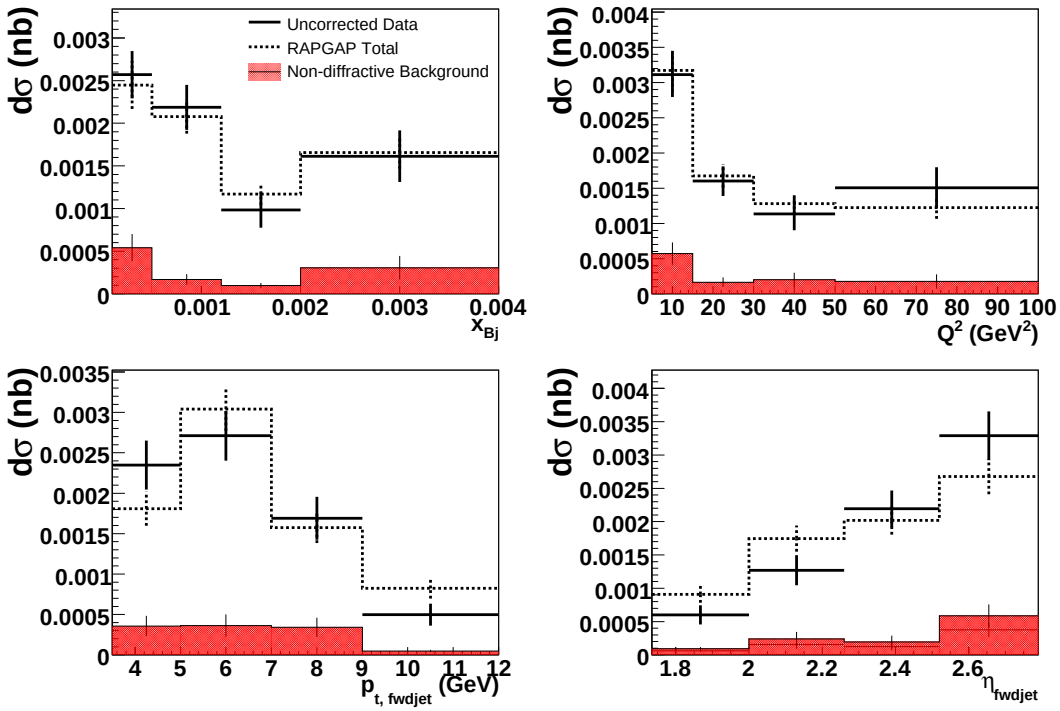

Figure 11.10: *Control distributions for events in the diffractive forward jet sample. In order to improve the description of the data, the Monte Carlo events have been reweighted to the data such that a better agreement with the Q^2 distribution is obtained.*

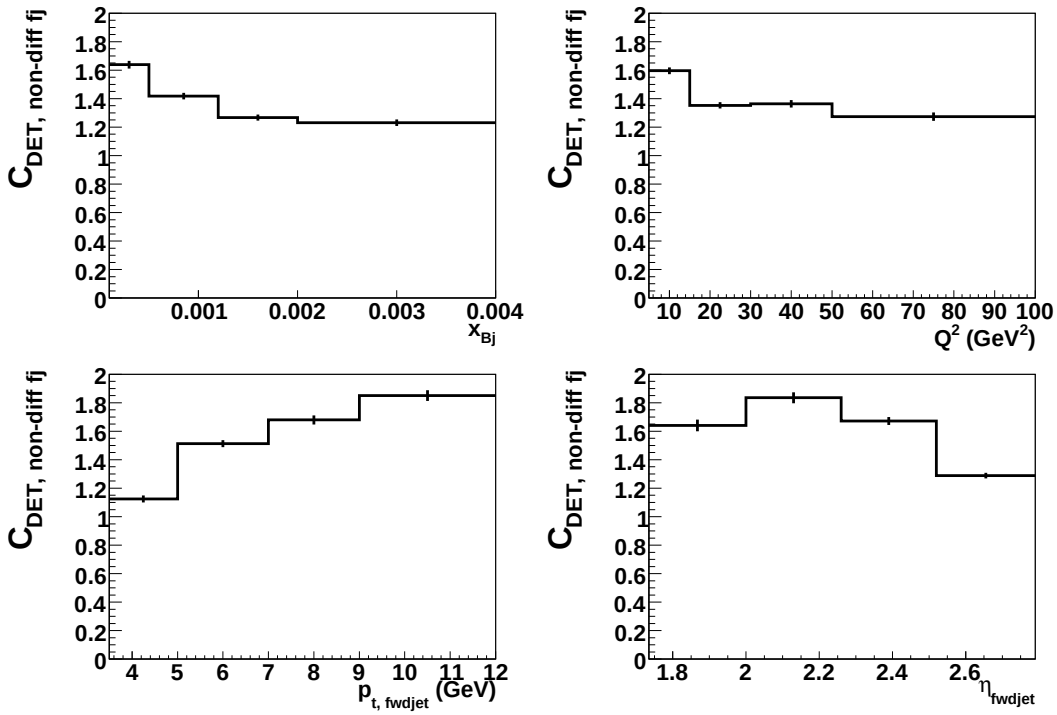

Figure 11.11: *Detector correction factors applied to the non-diffractive forward jet data for the various kinematic variables.*

simulation. Thus, the total correction for the ratio between non-diffractive and diffractive forward jets are given by

$$C_{\text{ratio}} = \frac{C_{\text{DET, diff fj}} * C_{\text{QED, diff fj}} * C_{FMD}}{C_{\text{DET, non-diff fj}} * C_{\text{QED, non-diff fj}}} \tag{11.9}$$

The separate and total correction factors are shown in Figs. 11.11-11.15. Although the separate corrections are usually not larger than, or around, a factor of 2, the contributions from each is such that the total corrections become large.

11.4.2 Systematic Errors

Since a cancellation between the diffractive and non-diffractive systematic errors is expected for the measurement of the ratio between diffractive and non-diffractive events, only the systematic errors from non-diffractive contributions have been estimated. Thus, the systematic errors for the ratio are overestimated. The systematic errors which have been used here are the uncertainty in the absolute energy scale of the LAr calorimeter, the uncertainty of the absolute energy scale of the electromagnetic calorimeter in the SPACAL, and the uncertainty in the measured angle of the scattered electron. Their impact on the ratio is shown in table 11.1. A more detailed study of the systematic errors will be needed for the presentation of the final results.

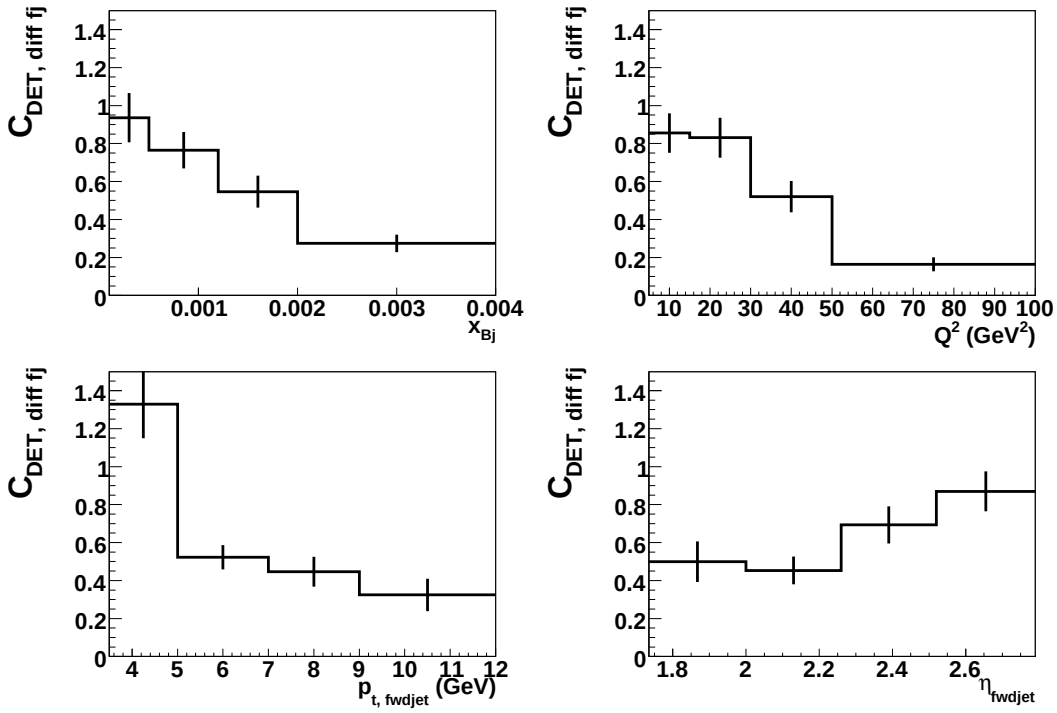

Figure 11.12: *Detector correction factors applied to the diffractive forward jet data for the various kinematic variables.*

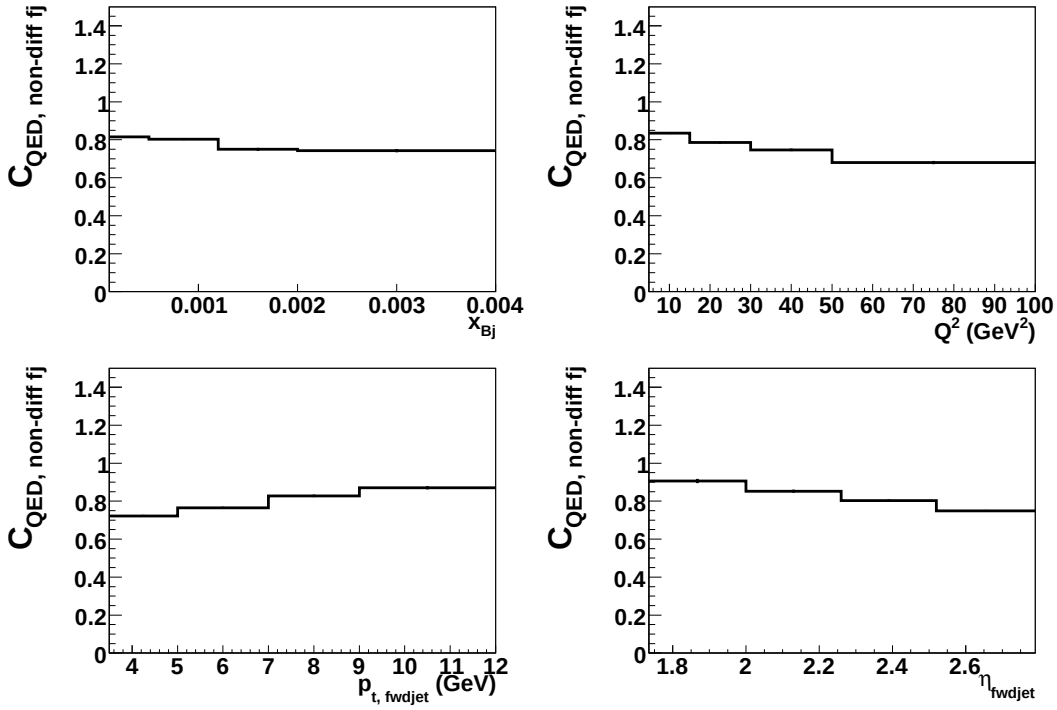

Figure 11.13: *QED correction factors applied to the non-diffractive forward jet data for the various kinematic variables.*

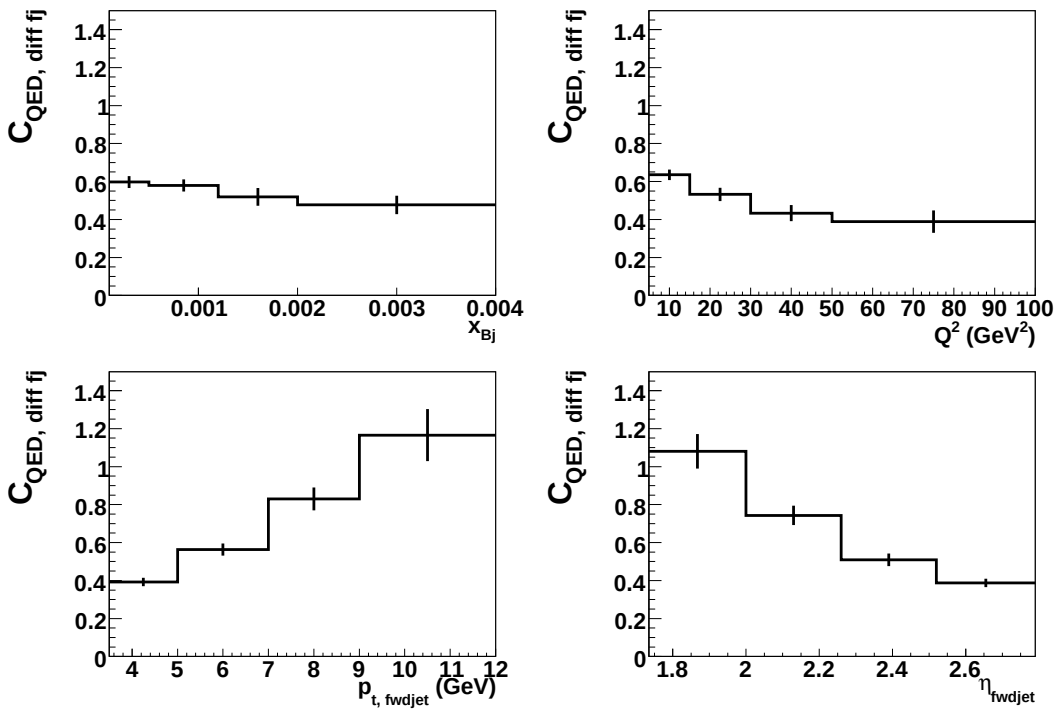

Figure 11.14: *QED correction factors applied to the diffractive forward jet data for the various kinematic variables.*

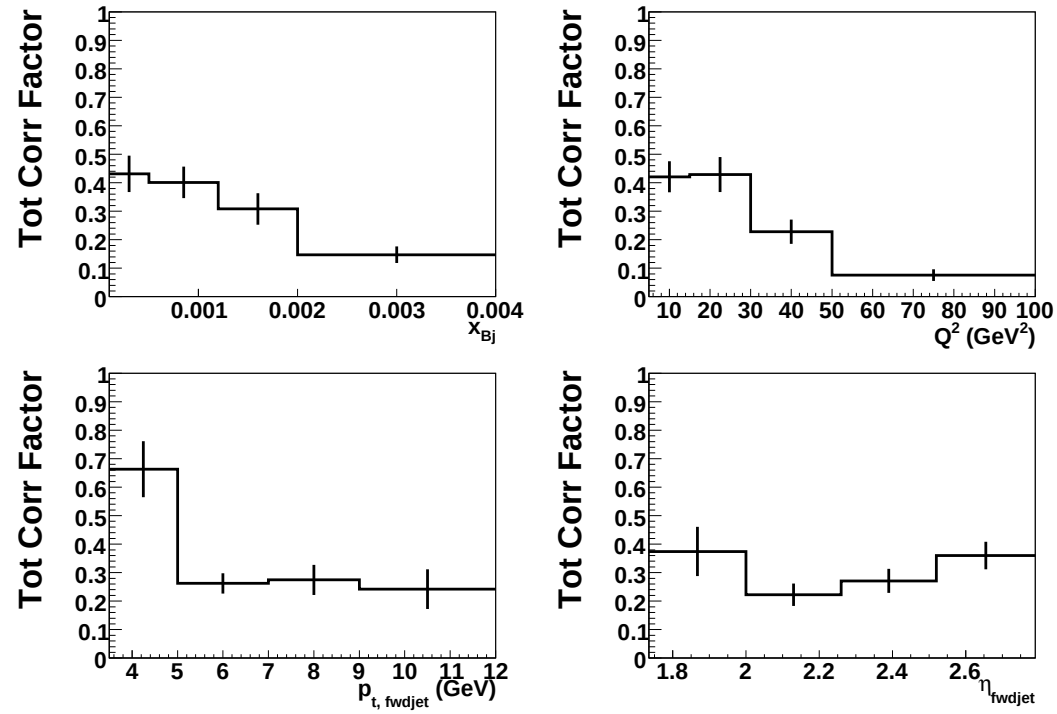

Figure 11.15: *Total correction factors (Eq. 11.9) applied to the data for the various kinematic variables.*

Source	Influence on result
LAr hadronic energy scale($\pm$ 4%)	10-15 %
SPACAL em energy scale ($\pm$ 1%)	$\sim$ 4 %
Angle of scattered electron ($\pm$ 1mrad)	$<$ 1%
Total	$\sim$ 11 %

Table 11.1: *Systematic errors and their impact on the measurement.*

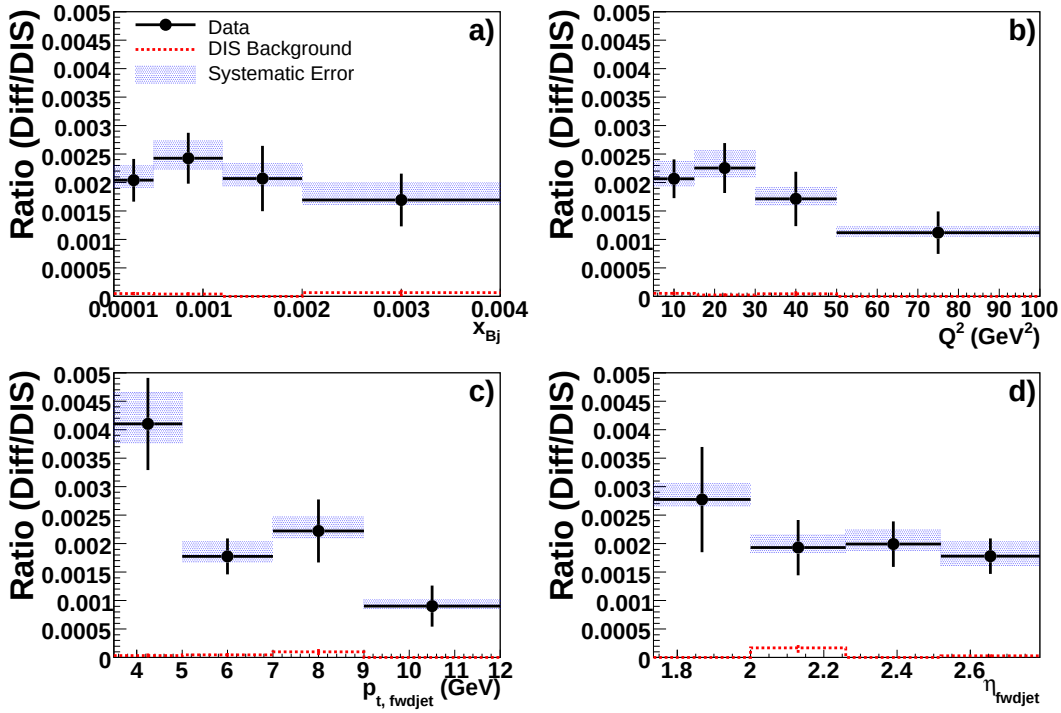

Figure 11.16: *The data on hadron level with systematic and statistical errors. The dashed lines show the background ratio from non-diffractive DIS events, estimated by using RAPGAP.*

11.4.3 Corrected Data

The ratio of diffractive over normal DIS events for corrected data are shown in Fig. 11.16, with systematic errors indicated by the shaded band. This is the result of the measurement, giving a ratio of about 0.2%. In this figure the background ratio from hadron level non-diffractive events (estimated by using RAPGAP) are also shown. As seen in the figure, the background from non-diffractive events to diffractive DIS events is neglible on the hadron level, indicating that the diffractive hadron level selection is effective and thus the non-diffractive background appearing in the detector level distributions (Fig. 11.10) has been corrected for in going to the hadron level.

11.4.4 Purity and Stability

The purity and stability for the forward jet sample are both around 60% for the non-diffractive forward jet sample from 99/00 data. This is significantly better than for the 1997 measurement. The reasons for this are:

- As already discussed, the p_t^2/Q^2-cut is not applied due to reasons of statistics. (See study in section 6.2.1)
- In H1OO, which is used for the 99/00 sample, a different combinatorial scheme of tracks and clusters are used, giving a better resolution of the jet quantities compared to the FSCOMB objects used in the former analysis package of the 97 sample [96].
- Due to larger (fewer) bins, there are to some extent less migrations between bins.

Applying the diffractive selection on DIS events without any forward jet requirement also gives high purity and stability. However, as soon as the diffractive selection is applied on top of the forward jet selection, the purity and stability decreases drastically to below 30%.

Chapter 12

Diffractive Forward Jet Events - Results

In this chapter the data on the ratio between diffractive and non-diffractive forward jet cross-sections are compared to the resolved Pomeron model, the 2-gluon exchange calculation and the SCI model. The non-diffractive Monte Carlo events are generated according to the standard LO ME complemented with DGLAP based parton showers. Contributions from meson exchange are neglible and not shown in the figures.

In each figure, the data, corrected for detector effects and QED radiation, is represented by black dots, with bars indicating the statistical errors. The shaded band around the data points illustrates the systematic uncertainty.

For the resolved pomeron model and the 2-gluon exchange calculation, contributions from charm quark production is included, giving, an additional $\sim 25\%$ diffractive forward jet cross-section.

12.1 Comparison to Monte Carlo Predictions

12.1.1 The Resolved Pomeron Model

In Fig. 12.1 a comparison to the resolved pomeron model is made. Diffractive Monte Carlo events have been generated by RAPGAP using 3 different parton distributions obtained from NLO fits to the diffractive structure function data [97]:

Fit 1 assumes that the pomeron only consists of quarks.

Fit 2 assumes that the pomeron consists of both quarks and gluons. In this fit the momentum fraction of the pomeron carried by the gluon is assumed to be flat.

Fit 3 assumes contribution from both quarks and gluons. In this fit a more detailed expression of the gluon momentum distributions is used, which assumes that the momentum fraction of the pomeron carried by the gluon is peaked at higher values.

As seen in the figures the resolved pomeron, Fit 2, is in best agreement with data for x_{Bj} and Q^2. For the $p_{t,\,\mathrm{fwdjet}}$ and η_{fwdjet}, Fit 1 gives the best description. The general result for Fit 3 is that the extra momentum on the gluons, results in too high a forward jet rate.

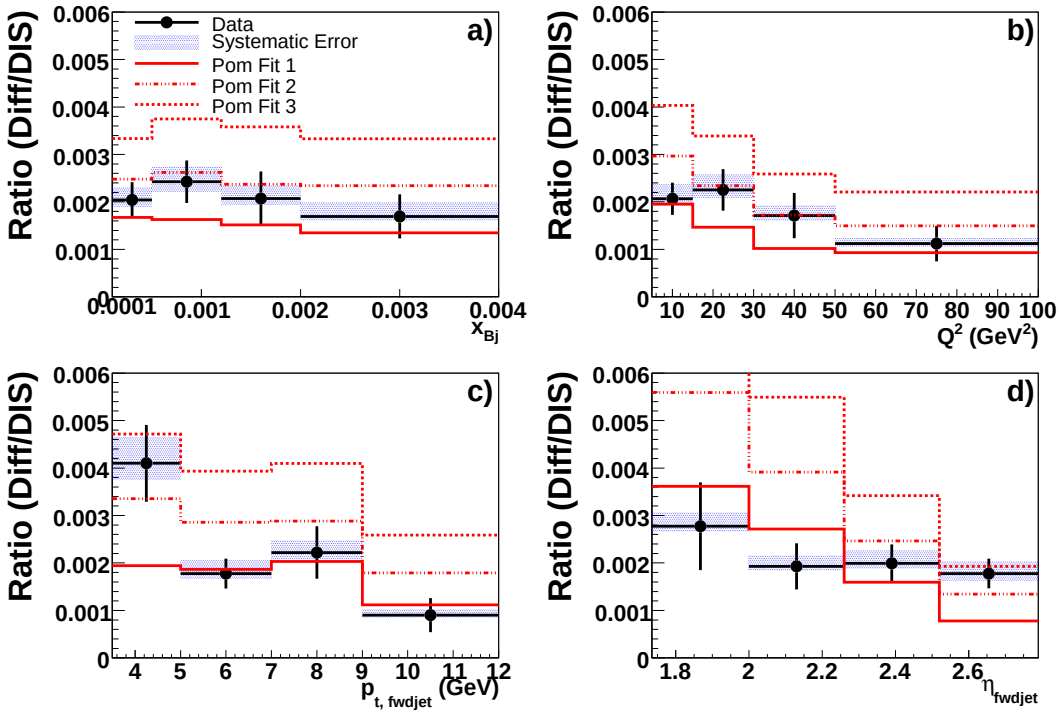

Figure 12.1: *The ratio of diffractive to non-diffractive forward jet cross-sections as a function of a) x_{Bj}, b) Q^2, c) $p_{t,\,fwdjet}$ and d) η_{fwdjet}. Data, with statistical (bars) and systematic (band) errors, are compared to the predictions of the resolved pomeron model.*

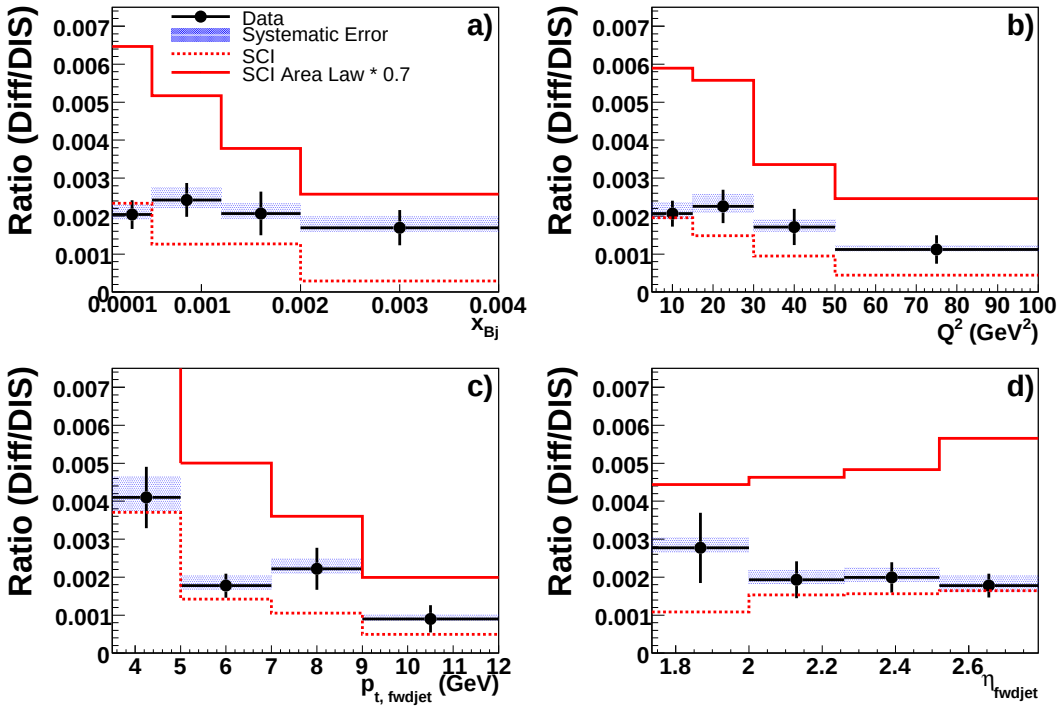

Figure 12.2: *The ratio of diffractive to non-diffractive forward jet cross-sections as a function of a) x_{Bj}, b) Q^2, c) $p_{t,\ fwdjet}$ and d) η_{fwdjet}. Data, with statistical (bars) and systematic (band) errors, are compared to the predictions of the SCI model. The SCI model with the area law supression is scaled by a factor of 0.7.*

12.1.2 The SCI Model

In Fig. 12.2 the data are compared to predictions from the SCI model, with and without the supression from the area law (see section 10.1.4). The latter has been scaled by a factor of 0.7 in order to keep the ranges on the y-axes reasonable. The SCI model without the area law supression is close to describing the jet variables within the statistical errors, but fails for the inclusive variables, where the prediction undershoots the data. Including the corrections from the area law give predictions which are more than a factor of two above the data.

12.1.3 The 2-gluon Exchange Model

The predictions from the 2-gluon exchange calculations for $\gamma p \rightarrow q\bar{q}gp$ are shown in Fig. 12.3. The contribution from the $\gamma p \rightarrow q\bar{q}p$ calculation gives a neglible contribution, and is therefore not shown in the figure. The additional gluon emission in $\gamma p \rightarrow q\bar{q}gp$ increases the diffractive forward jet production significantly. As seen in the figure, the predictions are strongly depending on the p_t-cut made on the quarks and the emitted gluon in the calculation. In the figure, the results from the 2g-model is shown for $p_t > 0.5$ Gev, $p_t > 0.8$ Gev, $p_t > 1.0$ Gev and $p_t > 1.5$ GeV. The p_t-cut of 0.8 GeV gives the best description of the data points. A more detailed adjustment of the cut is possible.

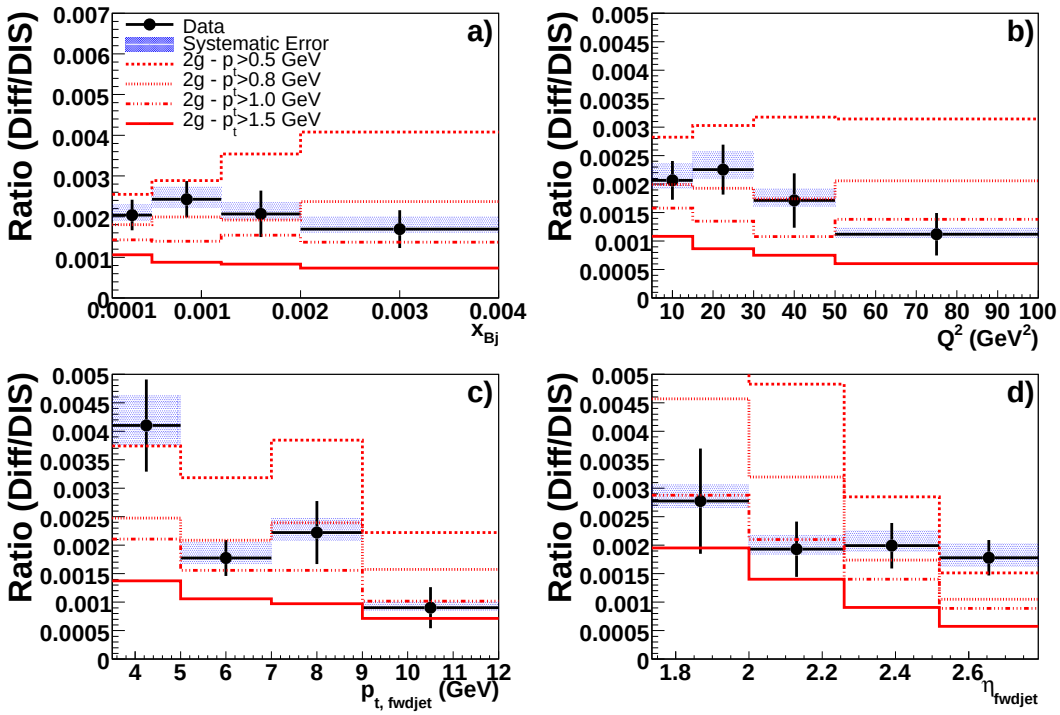

Figure 12.3: *The ratio of diffractive to non-diffractive forward jet cross-sections as a function of a) x_{Bj}, b) Q^2, c) $p_{t,\ fwdjet}$ and d) η_{fwdjet}. Data, with statistical (bars) and systematic (band) errors, are compared to the predictions of the 2-gluon exchange model with the $\gamma p \rightarrow q\bar{q}gp$ calculations. Different p_t-cuts on the emitted partons have been applied in the calculations.*

The p_t-cut is applied in order to avoid singularities in the calculations, and looking at the difference between the result of $p_t > 0.5$ GeV and the other three predictions in the x_{Bj} distributions, the requiriment of $p_t > 0.5$ GeV may be close to the limit where physical calculations are reliable.

For technical reasons, the 2-gluon model events have been generated together with the GRV derivative unintegrated PDF [34].

12.2 Conclusions

The measured cross-section ratios between diffractive and non-diffractive forward jet production are around 0.2%, which is much smaller than for example the corresponding ratio of di-jet cross-sections in the same diffractive kinematic range.

For x_{Bj}, Q^2 and η_{fwdjet} the cross-section ratio is, within the statistical errors, close to beeing flat, which leads to the conclusion that the underlying parton dynamics are similar in diffractive and non-diffractive events. The statistical errors are however large and future large statistics analyses should be able to test this more accurately.

The fact that the resolved pomeron model describes the measurement well for x_{Bj} and Q^2, but also to some extent for $p_{t,\,\mathrm{fwdjet}}$ implies that the factorization theorem should be valid.

Futhermore, by tuning the p_t-cut in the 2-gluon exchange calculation, the study shows possibilities for also this model to describe the data.

Chapter 13

Forward Jets in Diffraction - Summary

An attempt to measure forward jets in diffraction using 99/00 data has been made by applying a LRG selection on top of the old forward jet selection. This leads to a small diffractive forward jet phase space, i.e. the ratio between diffractive and non-diffractive forward jet events is small, around 0.2%.

Although the statistical errors are large, the results from the the resolved pomeron model indicates that the factorization theorem holds for events with a forward jet in the final state. Also the 2-gluon exchange model seems to have the prospect to describe the data.

It should be noted that the 2-gluon exchange model is a pertubative calculation with essentially only one free parameter. The resolved pomeron model, on the other hand is a phenomenological model with several free parameters, using diffractive parton density functions, which are obtained from fits to the diffractive structure funtion.

While the non-diffractive part of the measurement is well under control, and the newer data reproduce the published measurement, more work is needed for the diffractive forward jets. In the continuation of this analysis several details have to be studied in more detail, such as the low purity and stability, and large correction factors. Also, by going to newer data, the number of available events will increase, and the possibility to replace the LRG selection by a diffractive selection based on tagging the scattered proton will increase. An attempt to use proton tagging in the FPS on the data sample from 99/00 gave an unacceptable small diffractive forward jet sample. It was shown that the opportunity to use the FPS together with the forward jet requirement was not possible for the 99/00 data sample.

Acknowledgement

I would especially like to thank Leif Jönsson for supervision and invaluable support. Leif always gives his PhD-students highest priority, and has been of great help on both the analysis part and with writing the thesis. Hannes Jung for supervision during the stay in Lund, and for continuing to supervise me also after his employment in Lund ended. He is appreciated for always having time for feedback and help, and for comments on the thesis. I would like to thank my room-mates and friends Magnus Hansson and Sakar Osman for the useful and profound discussions we have every single day. Leif, Hannes, Magnus and Sakar; I enjoy working with you. Martin Karlsson is acknowledged for his help to get me started in the analysis work. Stephen Maxfield and Dave Milstedt for a lot of valuable comments on the PhD thesis. The H1 collaborators at DESY, especially the members of the HaQ and the Diffractive groups. Pierre van Mechelen is appreciated for beeing an excellent referee for the published paper on forward jet production. I also would like to thank the theorists in Lund for productive discussions on the forward jet analysis.

I express my gratidude to all the happy people at the Department of Experimental High Energy Physics in Lund, for jokes and discussions at the regular day lunches, making it fun to come to work also on the rainy days. I give extra creds to the thesis inspector, Anders Oskarsson, for feedback on the thesis.

I also thank Rickard du Rietz for help on latex and perl, and Henrik Ekstrand for the design of the cover of this thesis.

Last, but not least, I am grateful to my family for always supporting me.

Bibliography

[1] A. Aktas et al., *Eur. Phys. J.* **C46** (2006) 27.

[2] C. Adloff et al., *Phys. Lett.* **B462** (1999) 440.

[3] C. Adloff et al., *Nucl. Phys.* **B538** (1999) 3.

[4] F. Halzen, A. D. Martin, Quarks and Leptons, 1984, ISBN 0-471-88741-2.

[5] M. Kuhlen, QCD at HERA, The Hadronic Final State in Deep Inelastic Scattering, 1999, ISBN 3-540-65118-7.

[6] R. Devenish, A. Cooper-Sarkar, Deep Inelastic Scattering, 2004, ISBN 0-19-850671-6.

[7] S. Aid et al., *Nucl. Phys.* **B470** (1996) 3.

[8] S. Catani, M. H. Seymour, *Acta Phys. Polon.* **B28** (1997) 863.

[9] Z. Nagy, Z. Trocsanyi, *Phys. Rev. Lett.* **87** (2001) 082001.

[10] V. Gribov, L. Lipatov, *Sov. J. Nucl. Phys.* **15** (1972) 438 and 675.

[11] L. Lipatov, *Sov. J. Nucl. Phys.* **20** (1975) 94.

[12] G. Altarelli, G. Parisi, *Nucl. Phys.* **B 126** (1977) 298.

[13] Y. Dokshitzer, *Sov. Phys. JETP* **46** (1977) 641.

[14] E. A. Kuraev, L. N. Lipatov, V. S. Fadin, *Sov. Phys. JETP* **45** (1977) 199.

[15] E. A. Kuraev, L. N. Lipatov, V. S. Fadin, *Sov. Phys. JETP* **44** (1976) 443.

[16] I. I. Balitsky, L. N. Lipatov, *Sov. J. Nucl. Phys.* **28** (1978) 822.

[17] M. Ciafaloni, *Nucl. Phys.* **B296** (1988) 49.

[18] S. Catani, F. Fiorani, G. Marchesini, *Phys. Lett.* **B 234** (1990) 339.

[19] S. Catani, F. Fiorani, G. Marchesini, *Nucl. Phys.* **B336** (1990) 18.

[20] S. Catani, M. Ciafaloni, F. Hautmann, *Nucl. Phys.* **B366** (1991) 135.

[21] G. Marchesini, *Nucl. Phys.* **B 445** (1995) 49.

[22] G. Gustafson, *Phys. Lett.* **B175** (1986) 453.

[23] G. Gustafson, U. Pettersson, *Nucl. Phys.* **B306** (1988) 746.

[24] B. Andersson, G. Gustafson, L. Lonnblad, *Nucl. Phys.* **B339** (1990) 393.

[25] L. Lonnblad, *Z. Phys.* **C65** (1995) 285.

[26] A. H. Mueller, *Nucl. Phys.* **B415** (1994) 373.

[27] L. Lonnblad, , talk at the 10th International Workshop on Photon-Photon Collisions - PHOTON '95, Sheffield, UK, 8 - 13 Apr 1995.

[28] B. Andersson, G. Gustafson, G. Ingelman, T. Sjostrand, *Phys. Rept.* **97** (1983) 31.

[29] B. Andersson, The Lund Model, 1998, ISBN 0-521-42094-6.

[30] S. Catani, Y. L. Dokshitzer, B. R. Webber, *Phys. Lett.* **B285** (1992) 291.

[31] S. Catani, Y. L. Dokshitzer, M. H. Seymour, B. R. Webber, *Nucl. Phys.* **B406** (1993) 187.

[32] M. Karlsson, A Study of Parton Dynamics from Deep Inelastic Scattering Events Containing a Jet in the Forward Direction, 2002, PhD thesis.

[33] L. Lonnblad, *Comput. Phys. Commun.* **71** (1992) 15.

[34] H. Jung, *Comp. Phys. Commun.* **86** (1995) 147.

[35] H. Jung, *Comput. Phys. Commun.* **143** (2002) 100.

[36] H. Jung, CCFM prediction on forward jets and F2: Parton level predictions and a new hadron level Monte Carlo generator CASCADE, 1998, hep-ph/9908497.

[37] H. Jung, G. P. Salam, *Eur. Phys. J.* **C19** (2001) 351.

[38] M. Hansson, H. Jung, Status of CCFM: Un-integrated gluon densities, 2003, hep-ph/0309009.

[39] A. Kwiatkowski, H. Spiesberger, H. J. Mohring, *Comp. Phys. Commun.* **69** (1992) 155.

[40] K. Charchula, G. A. Schuler, H. Spiesberger, *Comput. Phys. Commun.* **81** (1994) 381.

[41] T. Sjostrand, *Comput. Phys. Commun.* **39** (1986) 347.

[42] T. Sjostrand, *Comput. Phys. Commun.* **82** (1994) 74.

[43] S. Catani, M. H. Seymour, *Nucl. Phys.* **B485** (1997) 291.

[44] E. W. N. Glover, *Nucl. Phys. Proc. Suppl.* **116** (2003) 3.

[45] E. W. N. Glover, Overview of NNLO QCD corrections, 2001, hep-ph/0106069.

[46] M. A. Kimber, A. D. Martin, M. G. Ryskin, *Phys. Rev.* **D63** (2001) 114027.

[47] J. Pumplin et al., *JHEP* **07** (2002) 012.

[48] J. Pumplin et al., *Phys. Rev.* **D65** (2002) 014013.

[49] H. Jung, Un-integrated uPDFs in CCFM, 2004, hep-ph/0411287.

[50] H. Jung, , prepared for 12th International Workshop on Deep Inelastic Scattering (DIS 2004), Strbske Pleso, Slovakia, 14-18 Apr 2004.

[51] G. A. Schuler, T. Sjostrand, *Phys. Lett.* **B376** (1996) 193.

[52] N. H. Brook, I. O. Skillicorn, *Phys. Lett.* **B497** (2001) 55.

[53] C. Adloff et al., *Nucl. Phys.* **B485** (1997) 3.

[54] C. Adloff et al., *Eur. Phys. J.* **C12** (2000) 595.

[55] C. Adloff et al., *Eur. Phys. J.* **C19** (2001) 289.

[56] R. Brun, R. Hagelberg, M. Hansroul, J. C. Lassalle, , cERN-DD-78-2-REV.

[57] H. Collaboration, Guide to the Simulation program H1SIM, H1 Softwarenote 3, (1989).

[58] C. Adloff et al., *Z. Phys.* **C74** (1997) 221.

[59] A. H. Mueller, *Nucl. Phys. Proc. Suppl.* **18C** (1991) 125.

[60] A. H. Mueller, *J. Phys.* **G17** (1991) 1443.

[61] A. Meyer, Measurement of the structure function F2(x,Q2) of the proton at low Q2 with the H1 detector at HERA using the new detector components SPACAL and BDC, 1997, PhD thesis.

[62] T. Schorner, Messung inklusiver Jet-Wirkungsquerschnitte in tiefunelastischer ep-Streuung mit dem H1-Detektor bei HERA, 2001, PhD thesis.

[63] H1 trigger web page.

[64] Discussion with Leif Lönnblad, 2004.

[65] J. Marks, H1, 2003.

[66] R. Engel, *Z. Phys.* **C66** (1995) 203.

[67] R. Engel, J. Ranft, *Phys. Rev.* **D54** (1996) 4244.

[68] C. Adloff et al., *Phys. Lett.* **B542** (2002) 193.

[69] A. Aktas et al., *Eur. Phys. J.* **C36** (2004) 441.

[70] S. Chekanov et al., *Phys. Lett.* **B632** (2006) 13.

[71] A. Knutsson, Studies of forward jets in DIS, Prepared for 12th International Workshop on Deep Inelastic Scattering (DIS 2004), Strbske Pleso, Slovakia, 14-18 Apr 2004.

[72] T. Ahmed et al., *Nucl. Phys.* **B429** (1994) 477.

[73] M. Derrick et al., *Phys. Lett.* **B315** (1993) 481.

[74] T. Ahmed et al., *Nucl. Phys.* **B429** (1994) 477.

[75] T. Regge, *Nuovo Cim.* **14** (1959) 951.

[76] T. Regge, *Nuovo Cim.* **18** (1960) 947.

[77] G. F. Chew, S. C. Frautschi, *Phys. Rev. Lett.* **8** (1962) 41.

[78] F. J.R, R. D.A., Quantum Chromo Dynamics and the Pomeron, 1997, iSBN0-521-56880-3.

[79] A. Donnachie, P. V. Landshoff, *Phys. Lett.* **B296** (1992) 227.

[80] A. Aktas et al., *Eur. Phys. J.* **C48** (2006) 715.

[81] A. Aktas et al., Diffractive deep-inelastic scattering with a leading proton at HERA, 2006, hep-ex/0606003.

[82] K. Borras, QCD and collider physics II Lecture, SoSe 24/5-2006, University Hamburg, Diffaction.

[83] P. Bruni, G. Ingelman, *Phys. Lett.* **B311** (1993) 317.

[84] P. Bruni, G. Ingelman, , presented at Europhysics Conference on High Energy Physics, Marseille, France, 22-28 Jul 1993.

[85] P. . Bruni, G. Ingelman, A. Solano, , to appear in Proc. of Workshop on Physics at HERA, Hamburg, Germany, Oct 29-30, 1991.

[86] A. Donnachie, P. V. Landshoff, *Nucl. Phys.* **B244** (1984) 322.

[87] K. H. Streng, HARD QCD SCATTERINGS IN DIFFRACTIVE REACTIONS AT HERA, CERN-TH-4949.

[88] E. L. Berger, J. C. Collins, D. E. Soper, G. Sterman, *Nucl. Phys.* **B286** (1987) 704.

[89] A. Edin, G. Ingelman, J. Rathsman, *Phys. Lett.* **B366** (1996) 371.

[90] J. Rathsman, *Phys. Lett.* **B452** (1999) 364.

[91] G. Ingelman, A. Edin, J. Rathsman, *Comput. Phys. Commun.* **101** (1997) 108.

[92] J. Bartels, H. Lotter, M. Wusthoff, *Phys. Lett.* **B379** (1996) 239.

[93] J. Bartels, H. Jung, M. Wusthoff, *Eur. Phys. J.* **C11** (1999) 111.

[94] Discussion with Mikhail Kapichine, November 2006.

[95] H1 diffractive working group web-page.

[96] M. Hansson, HaQ-meeting Presentation, 21/3-2006.

[97] C. Adloff et al., *Z. Phys.* **C76** (1997) 613.

Publication:

Forward Jet Production in Deep Inelastic Scattering at HERA

Eur. Phys. J. C 46, 27-42 (2006)

Eur. Phys. J. C 46, 27–42 (2006)
Digital Object Identifier (DOI) 10.1140/epjc/s2005-02471-x

THE EUROPEAN PHYSICAL JOURNAL C

Forward jet production in deep inelastic scattering at HERA

The H1 Collaboration

A. Aktas[10], V. Andreev[26], T. Anthonis[4], S. Aplin[10], A. Asmone[34], A. Astvatsatourov[4], A. Babaev[25], S. Backovic[31], J. Bähr[39], A. Baghdasaryan[38], P. Baranov[26], E. Barrelet[30], W. Bartel[10], S. Baudrand[28], S. Baumgartner[40], J. Becker[41], M. Beckingham[10], O. Behnke[13], O. Behrendt[7], A. Belousov[26], Ch. Berger[1], N. Berger[40], J.C. Bizot[28], M.-O. Boenig[7], V. Boudry[29], J. Bracinik[27], G. Brandt[13], V. Brisson[28], D. Bruncko[16], F.W. Büsser[11], A. Bunyatyan[12,38], G. Buschhorn[27], L. Bystritskaya[25], A.J. Campbell[10], S. Caron[1], F. Cassol-Brunner[22], K. Cerny[33], V. Cerny[16,47], V. Chekelian[27], J.G. Contreras[23], J.A. Coughlan[5], B.E. Cox[21], G. Cozzika[9], J. Cvach[32], J.B. Dainton[18], W.D. Dau[15], K. Daum[37,43], Y. de Boer[25], B. Delcourt[28], A. De Roeck[10,45], K. Desch[11], E.A. De Wolf[4], C. Diaconu[22], V. Dodonov[12], A. Dubak[31,46], G. Eckerlin[10], V. Efremenko[25], S. Egli[36], R. Eichler[36], F. Eisele[13], M. Ellerbrock[13], E. Elsen[10], W. Erdmann[40], S. Essenov[25], A. Falkewicz[6], P.J.W. Faulkner[3], L. Favart[4], A. Fedotov[25], R. Felst[10], J. Ferencei[16], L. Finke[11], M. Fleischer[10], P. Fleischmann[10], G. Flucke[10], A. Fomenko[26], I. Foresti[41], G. Franke[10], T. Frisson[29], E. Gabathuler[18], E. Garutti[10], J. Gayler[10], C. Gerlich[13], S. Ghazaryan[38], S. Ginzburgskaya[25], A. Glazov[10], I. Glushkov[39], L. Goerlich[6], M. Goettlich[10], N. Gogitidze[26], S. Gorbounov[39], C. Goyon[22], C. Grab[40], T. Greenshaw[18], M. Gregori[19], B.R. Grell[10], G. Grindhammer[27], C. Gwilliam[21], D. Haidt[10], L. Hajduk[6], M. Hansson[20], G. Heinzelmann[11], R.C.W. Henderson[17], H. Henschel[39], O. Henshaw[3], G. Herrera[24], M. Hildebrandt[36], K.H. Hiller[39], D. Hoffmann[22], R. Horisberger[36], A. Hovhannisyan[38], T. Hreus[16], S. Hussain[19], M. Ibbotson[21], M. Ismail[21], M. Jacquet[28], L. Janauschek[27], X. Janssen[10], V. Jemanov[11], L. Jönsson[20], D.P. Johnson[4], A.W. Jung[14], H. Jung[20,10], M. Kapichine[8], J. Katzy[10], I.R. Kenyon[3], C. Kiesling[27], M. Klein[39], C. Kleinwort[10], T. Klimkovich[10], T. Kluge[10], G. Knies[10], A. Knutsson[20], V. Korbel[10], P. Kostka[39], K. Krastev[10], J. Kretzschmar[39], A. Kropivnitskaya[25], K. Krüger[14], J. Kückens[10], M.P.J. Landon[19], W. Lange[39], T. Laštovička[39,33], G. Laštovička-Medin[31], P. Laycock[18], A. Lebedev[26], G. Leibenguth[40], V. Lendermann[14], S. Levonian[10], L. Lindfeld[41], K. Lipka[39], A. Liptaj[27], B. List[40], J. List[11], E. Lobodzinska[39,6], N. Loktionova[26], R. Lopez-Fernandez[10], V. Lubimov[25], A.-I. Lucaci-Timoce[10], H. Lueders[11], D. Lüke[7,10], T. Lux[11], L. Lytkin[12], A. Makankine[8], N. Malden[21], E. Malinovski[26], S. Mangano[40], P. Marage[4], R. Marshall[21], M. Martisikova[10], H.-U. Martyn[1], S.J. Maxfield[18], D. Meer[40], A. Mehta[18], K. Meier[14], A.B. Meyer[11], H. Meyer[37], J. Meyer[10], S. Mikocki[6], I. Milcewicz-Mika[6], D. Milstead[18], D. Mladenov[35], A. Mohamed[18], F. Moreau[29], A. Morozov[8], J.V. Morris[5], M.U. Mozer[13], K. Müller[41], P. Murín[16,44], K. Nankov[35], B. Naroska[11], Th. Naumann[39], P.R. Newman[3], C. Niebuhr[10], A. Nikiforov[27], D. Nikitin[8], G. Nowak[6], M. Nozicka[33], R. Oganezov[38], B. Olivier[3], J.E. Olsson[10], S. Osman[20], D. Ozerov[25], V. Palichik[8], I. Panagoulias[10], T. Papadopoulou[10], C. Pascaud[28], G.D. Patel[18], M. Peez[29], E. Perez[9], D. Perez-Astudillo[23], A. Perieanu[10], A. Petrukhin[25], D. Pitzl[10], R. Plačakytė[27], B. Portheault[28], B. Povh[12], P. Prideaux[18], A.J. Rahmat[18], N. Raicevic[31], P. Reimer[32], A. Rimmer[18], C. Risler[10], E. Rizvi[19], P. Robmann[41], B. Roland[4], R. Roosen[4], A. Rostovtsev[25], Z. Rurikova[27], S. Rusakov[26], F. Salvaire[11], D.P.C. Sankey[5], E. Sauvan[22], S. Schätzel[10], F.-P. Schilling[10], S. Schmidt[10], S. Schmitt[10], C. Schmitz[41], L. Schoeffel[9], A. Schöning[40], H.-C. Schultz-Coulon[14], K. Sedlák[32], F. Sefkow[10], R.N. Shaw-West[3], I. Sheviakov[26], L.N. Shtarkov[26], T. Sloan[17], P. Smirnov[26], Y. Soloviev[26], D. South[10], V. Spaskov[8], A. Specka[29], B. Stella[34], J. Stiewe[14], I. Strauch[10], U. Straumann[41], V. Tchoulakov[8], G. Thompson[19], P.D. Thompson[3], F. Tomasz[14], D. Traynor[19], P. Truöl[41], I. Tsakov[35], G. Tsipolitis[10,42], I. Tsurin[10], J. Turnau[6], E. Tzamariudaki[27], M. Urban[41], A. Usik[26], D. Utkin[25], S. Valkár[33], A. Valkárová[33], C. Vallée[22], P. Van Mechelen[4], A. Vargas Trevino[7], Y. Vazdik[26], C. Veelken[18], A. Vest[1], S. Vinokurova[10], V. Volchinski[38], B. Vujicic[27], K. Wacker[7], J. Wagner[10], G. Weber[11], R. Weber[40], D. Wegener[7], C. Werner[13], M. Wessels[10], B. Wessling[10], C. Wigmore[3], Ch. Wissing[7], R. Wolf[13], E. Wünsch[10], S. Xella[41], W. Yan[10], V. Yeganov[38], J. Žáček[33], J. Zálešák[32], Z. Zhang[28], A. Zhelezov[25], A. Zhokin[25], Y.C. Zhu[10], J. Zimmermann[27], T. Zimmermann[40], H. Zohrabyan[38], F. Zomer[28]

[1] I. Physikalisches Institut der RWTH, Aachen, Germany[a]
[2] III. Physikalisches Institut der RWTH, Aachen, Germany[a]
[3] School of Physics and Astronomy, University of Birmingham, Birmingham, UK[b]
[4] Inter-University Institute for High Energies ULB-VUB, Brussels; Universiteit Antwerpen, Antwerpen; Belgium[c]
[5] Rutherford Appleton Laboratory, Chilton, Didcot, UK[b]
[6] Institute for Nuclear Physics, Cracow, Poland[d]
[7] Institut für Physik, Universität Dortmund, Dortmund, Germany[a]
[8] Joint Institute for Nuclear Research, Dubna, Russia
[9] CEA, DSM/DAPNIA, CE-Saclay, Gif-sur-Yvette, France

[10] DESY, Hamburg, Germany
[11] Institut für Experimentalphysik, Universität Hamburg, Hamburg, Germany[a]
[12] Max-Planck-Institut für Kernphysik, Heidelberg, Germany
[13] Physikalisches Institut, Universität Heidelberg, Heidelberg, Germany[a]
[14] Kirchhoff-Institut für Physik, Universität Heidelberg, Heidelberg, Germany[a]
[15] Institut für Experimentelle und Angewandte Physik, Universität Kiel, Kiel, Germany
[16] Institute of Experimental Physics, Slovak Academy of Sciences, Košice, Slovak Republic[f]
[17] Department of Physics, University of Lancaster, Lancaster, UK[b]
[18] Department of Physics, University of Liverpool, Liverpool, UK[b]
[19] Queen Mary and Westfield College, London, UK[b]
[20] Physics Department, University of Lund, Lund, Sweden[g]
[21] Physics Department, University of Manchester, Manchester, UK[b]
[22] CPPM, CNRS/IN2P3, Univ. Mediterranee, Marseille, France
[23] Departamento de Fisica Aplicada, CINVESTAV, Mérida, Yucatán, México[k]
[24] Departamento de Fisica, CINVESTAV, México[k]
[25] Institute for Theoretical and Experimental Physics, Moscow, Russia[l]
[26] Lebedev Physical Institute, Moscow, Russia[e]
[27] Max-Planck-Institut für Physik, München, Germany
[28] LAL, Université de Paris-Sud, IN2P3-CNRS, Orsay, France
[29] LLR, Ecole Polytechnique, IN2P3-CNRS, Palaiseau, France
[30] LPNHE, Universités Paris VI and VII, IN2P3-CNRS, Paris, France
[31] Faculty of Science, University of Montenegro, Podgorica, Serbia and Montenegro[e]
[32] Institute of Physics, Academy of Sciences of the Czech Republic, Praha, Czech Republic[e,i]
[33] Faculty of Mathematics and Physics, Charles University, Praha, Czech Republic[e,i]
[34] Dipartimento di Fisica Università di Roma Tre and INFN Roma 3, Roma, Italy
[35] Institute for Nuclear Research and Nuclear Energy, Sofia, Bulgaria[e]
[36] Paul Scherrer Institut, Villigen, Switzerland
[37] Fachbereich C, Universität Wuppertal, Wuppertal, Germany
[38] Yerevan Physics Institute, Yerevan, Armenia
[39] DESY, Zeuthen, Germany
[40] Institut für Teilchenphysik, ETH, Zürich, Switzerland[j]
[41] Physik-Institut der Universität Zürich, Zürich, Switzerland[j]

[42] Also at Physics Department, National Technical University, Zografou Campus, 15773 Athens, Greece
[43] Also at Rechenzentrum, Universität Wuppertal, Wuppertal, Germany
[44] Also at University of P.J. Šafárik, Košice, Slovak Republic
[45] Also at CERN, Geneva, Switzerland
[46] Also at Max-Planck-Institut für Physik, München, Germany
[47] Also at Comenius University, Bratislava, Slovak Republic

Received: 30 August 2005 / Revised version: 10 December 2005 /
Published online: 14 February 2006 – © Springer-Verlag / Società Italiana di Fisica 2006

Abstract. The production of forward jets has been measured in deep inelastic ep collisions at HERA. The results are presented in terms of single differential cross sections as a function of the Bjorken scaling variable (x_{Bj}) and as triple differential cross sections $d^3\sigma/dx_{Bj}dQ^2dp^2_{t,\mathrm{jet}}$, where Q^2 is the four momentum transfer squared and $p^2_{t,\mathrm{jet}}$ is the squared transverse momentum of the forward jet. Also cross sections for events with a di-jet system in addition to the forward jet are measured as a function of the rapidity separation between the forward jet and the two additional jets. The measurements are compared with next-to-leading order QCD calculations and with the predictions of various QCD-based models.

[a] Supported by the Bundesministerium für Bildung und Forschung, FRG, under contract numbers 05 H1 1GUA /1, 05 H1 1PAA /1, 05 H1 1PAB /9, 05 H1 1PEA /6, 05 H1 1VHA /7 and 05 H1 1VHB /5
[b] Supported by the UK Particle Physics and Astronomy Research Council, and formerly by the UK Science and Engineering Research Council
[c] Supported by FNRS-FWO-Vlaanderen, IISN-IIKW and IWT and by Interuniversity Attraction Poles Programme, Belgian Science Policy
[d] Partially Supported by the Polish State Committee for Scientific Research, SPUB/DESY/P003/DZ 118/2003/2005
[e] Supported by the Deutsche Forschungsgemeinschaft
[f] Supported by VEGA SR grant no. 2/4067/ 24
[g] Supported by the Swedish Natural Science Research Council
[i] Supported by the Ministry of Education of the Czech Republic under the projects LC527 and INGO-1P05LA259
[j] Supported by the Swiss National Science Foundation
[k] Supported by CONACYT, México, grant 400073-F

1 Introduction

The hadronic final state in deep inelastic scattering offers a rich field of research for QCD phenomena. This includes studies of hard parton emissions which result in well defined jets, perturbative effects responsible for multiple gluon emissions and the non-perturbative hadronisation process.

HERA has extended the available region in the Bjorken scaling variable, x_{Bj}, down to values of $x_{Bj} \simeq 10^{-4}$, for values of the four momentum transfer squared, Q^2, larger than a few GeV^2, where perturbative calculations in QCD are expected to be valid. At these low x_{Bj} values, a parton in the proton can induce a QCD cascade, consisting of several subsequent parton emissions, before eventually an interaction with the virtual photon takes place (Fig. 1). QCD calculations based on "direct" interactions between a point-like photon and a parton from an evolution chain, as given by the DGLAP scheme [1–5], are successful in reproducing the strong rise of $F_2(x_{Bj}, Q^2)$ with decreasing x_{Bj} over a large Q^2 range [6–9]. The DGLAP evolution resums leading $\log(Q^2)$ terms. This approximation, however, may become inadequate for small x_{Bj}, where $\log(1/x)$ terms become important in the evolution equation. In this region the BFKL scheme [10–12] is expected to describe the data better, since this evolution equation sums up terms in $\log(1/x)$. Since the inclusive F_2 measurements are strongly dominated by lowest order processes, signatures for BFKL-dynamics have to be searched for in specific studies of the hadronic final state.

Significant deviations from the simple leading order (LO) DGLAP approach are observed in the fractional rate of di-jet events [13–15], inclusive jet production [16,17], transverse energy flow [18,19] and p_t spectra of charged particles [20]. Extending the calculations from LO to next-to-leading order (NLO) accuracy accounts for some of the deviations observed in jet production, but at low x_{Bj} and low Q^2 the description of the measurements is still unsatisfactory. Next-to-next-to-leading order (NNLO) calculations do not exist so far and therefore higher order contributions can only be approximated by phenomenological QCD based models, based on LO matrix element calculations together with parton shower evolution. Ascribing partonic structure to the virtual photon and thus considering so called resolved photon processes, including parton showers from both the photon and the proton side, results in an improved description of the data including particle production in the forward region (the angular region close to the proton beam direction) [13,21–26]. The colour dipole model (CDM) [27,28], which assumes gluon emissions to originate from independently radiating colour dipoles, is in fairly good agreement with the measurements. This suggests that different parton dynamics, not included in the DGLAP approximation, are responsible for the observed deviations.

The large phase space available at low x_{Bj} makes the production of forward jets a particularly interesting process for the study of parton dynamics [29,30], since jets emitted close to the proton direction lie well away in rapidity from the photon end of the evolution ladder (Fig. 1). Here a new measurement of forward jet production is presented using data collected in 1997 with the H1 detector, comprising an integrated luminosity of 13.7 pb^{-1}. The enlarged statistics allows to study more differential distributions than previously presented [31,32], and new observables compared to other measurements [33]. The proton energy is 820 GeV and the positron energy is 27.6 GeV which correspond to a centre-of-mass-energy of $\sqrt{s} \approx 300$ GeV.

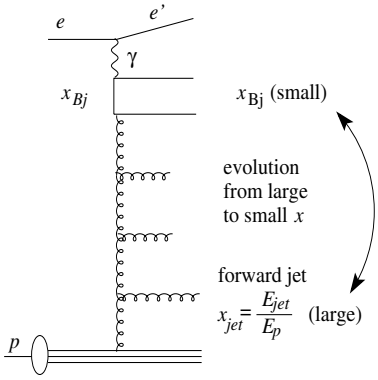

Fig. 1. Schematic diagram of ep scattering with a forward jet taking a fraction $x_{\rm jet} = E_{\rm jet}/E_p$ of the proton momentum. The evolution in the longitudinal momentum fraction, x, from large $x_{\rm jet}$ to small x_{Bj} is indicated

Measurements are presented in regions of phase space where the DGLAP approximation might be insufficient to describe the parton dynamics. In inclusive forward jet production this is expected to be the case when the transverse momentum squared of the jet and the photon virtuality are of similar order. More exclusive final states, like those containing a di-jet system in addition to the forward jet (called '2+forward jet'), provide a further handle to control the parton dynamics. The forward jet measurements are compared to LO and NLO di- and three-jet calculations, and different phenomenological QCD based models. This measurement is complementary to a similar measurement of π^o-production in the forward direction, which has been presented in [26].

2 QCD based models and theoretical calculations

The conventional description of the parton cascade is given by the DGLAP evolution equations. The basic assumption is that the leading contribution comes from cascades with strong ordering in the virtualities of the parton propagators in the evolution chain, with the largest virtualities reached in the hard scattering with the photon. This implies strong ordering of the transverse momenta of the emitted partons (k_t). Since their virtualities and transverse momenta squared are small compared to the

[1] Partly Supported by Russian Foundation for Basic Research, grants no. 03-02-17291 and 04-02-16445

hard scale, Q^2, the propagators can be treated as massless and assumed to be collinear with the incoming proton (collinear approach). The interaction is assumed to take place with a point-like photon (DGLAP direct) and the hard subprocess is at the photon vertex.

If the transverse momenta of the partons emitted in the hard scattering process are larger than the virtuality of the photon, then the partonic structure of the virtual photon might be resolved and the interaction take place with one of the partons in the photon. In this case a partonic structure is assigned to the photon and a photon parton density function is convoluted with the matrix element, which within the DGLAP model means that two evolution ladders are introduced, one from the photon side and one from the proton side of the hard subprocess. This is called the resolved photon model (DGLAP resolved) and is described in [22,23].

The BFKL ansatz predicts strong ordering in the longitudinal momentum fraction of the parton propagators but no ordering in their virtualities. This means that the virtualities and the transverse momenta of the propagators can take any kinematically allowed value at each splitting. One consequence of this is that the matrix element must be taken off mass-shell and convoluted with parton distributions which take the transverse momenta of the propagators into account (unintegrated parton densities).

The CCFM equation [34–37] provides a bridge between the DGLAP and BFKL descriptions by resumming both $\log(Q^2)$ and $\log(1/x)$ terms in the relevant limits, and is expected to be valid in a wider x range. The CCFM equation leads to parton emissions ordered in angle. An unintegrated gluon density is used as input to calculations based on this model.

A different approach to the parton evolution is given by the colour dipole model (CDM), in which the emissions are generated by colour dipoles, spanned between the partons in the cascade. Since the dipoles radiate independently there is no ordering in the transverse momenta of the emissions and the behaviour of the parton showers is in that sense similar to that in the BFKL case.

The measurements performed here are compared to several QCD based models:

- The RAPGAP [38] Monte Carlo program, which uses LO matrix elements supplemented with initial and final state parton showers generated according to the DGLAP evolution scheme for the description of DIS processes (RG-DIR). It can be interfaced to HERACLES [39], which simulates QED-radiative effects. RAPGAP also offers the possibility to include contributions from processes with resolved transverse virtual photons (RG-DIR+RES). In order to accommodate the contributions from both direct and resolved photon processes the renormalisation scale is set to $Q^2 + \hat{p}_t^2$, where $\hat{p}_t$ is the transverse momentum of both partons in the centre-of-mass of the hard subsystem.
- The DJANGO [40] program with the CDM as implemented in ARIADNE [41]. Parameters of ARIADNE are tuned using the CTEQ6M [42] parton density functions and the data sets [20,43,19].
- The CASCADE Monte Carlo program [44,45], which is based on the CCFM formalism [34–37]. Two different versions of the unintegrated gluon density are used, J2003-set-1 and set-2 [46]. The difference between these two sets is that in set-1 only singular terms are included in the splitting function, whereas set-2 also takes the non-singular terms into account. These unintegrated gluon densities are determined from fits to the $F_2(x, Q^2)$ data obtained by H1 and ZEUS in 1994 and 1996/97. The renormalisation scale used in CASCADE is $\mu_r^2 = p_{t,q}^2 + 4m^2$, where $p_{t,q}$ is the transverse momentum of one of the quarks in the ep centre-of-mass and m is the quark mass. The factorisation scale is given by $\mu_f^2 = \hat{s} + Q_t^2$, where $\hat{s}$ is the invariant mass squared of the $q\overline{q}$-pair and Q_t is the transverse momentum of this system.

Simulated events from the RAPGAP (RG-DIR) and DJANGO Monte Carlo programs are processed through the detailed H1 detector simulation [47] in order to test the understanding of the detector and to extract correction factors.

The forward jet cross sections are compared to LO (α_s) and NLO (α_s^2) calculations of di-jet production via direct photon interactions as obtained from the DISENT program [48,49] . Since the jet search is performed in the Breit frame the selected events always contain at least one jet in addition to the forward jet, such that comparisons with the DISENT predictions are adequate. The renormalisation scale μ_r^2 is given by the average p_t^2 of the di-jets from the matrix element ($p_{t,\text{di-jets}}^2$), while the factorisation scale μ_f^2 is given by the average p_t^2 of all forward jets in the selected sample[1] ($\langle p_{t,\text{jet}}^2 \rangle$). The calculations are corrected for hadronisation effects, which are estimated using CASCADE together with the KMR parton density function [50]. The KMR parton density function takes only the matrix element and one additional emission into account and should therefore be suitable for correcting the NLO di-jet calculations. The correction factors for hadronisation effects ($1 + \delta_{\text{HAD}}$) are determined by calculating the ratio bin-wise between the hadron and parton level cross sections, obtained using the same jet algorithm and kinematic restrictions. For the single and triple differential cross sections the hadronisation corrections are of the order of 10% or less over the full kinematic range investigated.

In the analysis of events with two jets in addition to the forward jet, the measured cross sections are compared to the predictions of NLOJET++ [51]. This program provides perturbative calculations of cross sections for three-jet production in DIS at NLO (α_s^3) accuracy. In NLOJET++, where the factorisation scale can be defined for each event, μ_r^2 and μ_f^2 are set to the average p_t^2 of the forward jet and the two hardest jets in the event. The NLOJET++ calculations are corrected to hadron level using CASCADE together with the unintegrated gluon

[1] For the triple differential forward jet cross section, $d^3\sigma/dx_{Bj}dQ^2dp_{t,\text{jet}}^2$, this means different factorisation scales for the three different $p_{t,\text{jet}}$ bins.

Table 1. The renormalisation (μ_r^2) and factorisation (μ_f^2) scales, and the parton density functions used in the different programs. The average squared transverse momentum of the forward jet, $\langle p_{t,\mathrm{jet}}^2 \rangle$, is 45 GeV^2 for the single differential forward jet cross section, and 24, 55 and 183 GeV^2 for the three different p_t^2-bins in the triple differential cross sections

	CASCADE	RG-DIR/RES	DISENT	NLOJET++
μ_r^2	$p_{t,q}^2 + 4m^2$	$Q^2 + \hat{p}_t^2$	$p_{t,\text{di-jets}}^2$	$(p_{t,\text{jet1}}^2 + p_{t,\text{jet2}}^2 + p_{t,\text{fwdjet}}^2)/3$
μ_f^2	$\hat{s} + Q_t^2$	$Q^2 + \hat{p}_t^2$	$\langle p_{t,\text{jet}}^2 \rangle$	$(p_{t,\text{jet1}}^2 + p_{t,\text{jet2}}^2 + p_{t,\text{fwdjet}}^2)/3$
proton PDF	J2003 set-1 &-2	CTEQ6L [42]	CTEQ6M	CTEQ6M
photon PDF	–	SaS1D [54] (RES only)	–	–

density J2003 set-2 [46]. The hadronisation effects for the '2+forward jet' cross sections vary between 30% and 50%.

The NLO calculations by DISENT and NLOJET++ are performed using the CTEQ6M [42] parametrisation of the parton distributions in the proton. The uncertainty in the NLO calculations originating from the PDF uncertainty is estimated by using the CTEQ eigenvector sets according to [42]. The scale uncertainty for these calculations is estimated by simultaneously changing the renormalisation and factorisation scales (μ_r^2, μ_f^2) by a factor of 4 up and 1/4 down. In CASCADE the renormalisation scale μ_r^2 is changed by the same factors and in each case the unintegrated gluon density is adjusted such that the prediction of CASCADE describes the inclusive F_2 data [52,53]. The forward jet cross section is then calculated to estimate the upper and lower limit of the scale uncertainty. The resulting uncertainty in the cross section prediction is less than 10% at the smallest x_{Bj} and decreases for higher x_{Bj} (these errors are not shown in the figures). The parton densities and the scales used in the QCD calculations are given in Table 1.

In [55] next-to-leading order calculations of the forward jet cross section are presented, in which the contributions from direct and resolved virtual photons are taken into account in a consistent way. The inclusion of NLO contributions from the resolved part corresponds to an additional gluon emission in a direct process and thus may constitute an approximation of the NNLO direct cross section.

3 The H1 detector

A detailed description of the H1 detector can be found in [56–58]. The detector elements important for this analysis are described below. The coordinate system of H1 is defined such that the positive z axis is in the direction of the incident proton beam. The polar angles are defined with respect to the proton beam direction.

The interaction vertex is determined with the central tracking detector consisting of two concentric drift chambers (CJC) and two concentric z drift chambers (CIZ and COZ). The kinematic variables x and Q^2 are determined from a measurement of the scattered electron in the lead-scintillating fibre calorimeter (SpaCal) and the backward drift chamber (BDC), covering the polar angular range $153^\circ < \theta < 177^\circ$.

The SpaCal has an electromagnetic section with an energy resolution of $7\%/\sqrt{E/GeV} \oplus 1\%$, which together with a hadronic section represents a total of two interaction lengths. Identification of the scattered electron is improved using the BDC, situated in front of the SpaCal. The scattering angle of the electron is determined from the measured impact position in the BDC and the reconstructed primary interaction vertex.

The hadronic final state is reconstructed with the Liquid Argon calorimeter (LAr), the central tracking detector and the SpaCal. The LAr calorimeter is of a sandwich type with liquid argon as the active material. It covers the range $4^\circ < \theta < 154^\circ$. In test beam measurements pion induced hadronic energies were reconstructed with a resolution of about $50\%/\sqrt{E/\mathrm{GeV}} \oplus 2\%$ [59]. The measurement of charged particle momenta provided by the central tracking detector is performed in a solenoidal magnetic field of 1.15 T with a precision of $\sigma_p/p^2 = 0.003$ GeV^{-1}.

The luminosity is determined from the rate of Bethe-Heitler events ($e + p \to e + \gamma + p$) with a precision of 1.5%.

The scattered electron is triggered by its energy deposition in the SpaCal. For events used in this analysis, with the electron energy required to be above 10 GeV, the trigger efficiency is essentially 100%.

4 Experimental strategy and phase space definition

Differences between the various approaches to the modelling of the parton cascade dynamics are most prominent in the region close to the proton remnant direction, i.e. away from the photon side of the ladder. This can be understood from the fact that the strong ordering in virtuality of the DGLAP description gives the softest k_t-emissions closest to the proton whereas in the BFKL model the emissions can be arbitrarily hard in this region, as long as they are kinematically allowed.

In most of the HERA kinematic range the DGLAP approximation is valid. A method to suppress contributions from DGLAP like events is to select events with a jet close to the proton direction (a forward jet) with the additional constraint that the squared transverse momentum of this jet, $p_{t,\mathrm{jet}}^2$, is approximately equal to the virtuality of the photon propagator, Q^2 (see Fig. 1). This will suppress con-

tributions with strong ordering in virtuality as is the case in DGLAP evolution. If, at the same time, the forward jet is required to take a large fraction of the proton momentum, $x_{\rm jet} \equiv E_{\rm jet}/E_p$, such that $x_{\rm jet} \gg x_{Bj}$, the phase space for an evolution with ordering in the longitudinal momentum fraction, as described by BFKL, is favoured. By requiring $x_{\rm jet} \gg x_{Bj}$ contributions from zeroth order processes are also suppressed. Based on calculations in the leading log approximation of the BFKL kernel, the cross section for DIS events at low x_{Bj} and large Q^2 with a forward jet [29,30] is expected to rise more rapidly with decreasing x_{Bj} than expected from DGLAP based calculations.

DIS events are selected by requiring a scattered electron in the backward SpaCal calorimeter and a matching track in the backward drift chamber (BDC), applying the following cuts:

$$\begin{gathered} E'_e > 10 \text{ GeV} \\ 156^\circ < \theta_e < 175^\circ \\ 0.1 < y < 0.7 \\ 0.0001 < x_{Bj} < 0.004 \\ 5 \text{ GeV}^2 < Q^2 < 85 \text{ GeV}^2 \end{gathered}$$

where E'_e is the energy of the scattered electron, θ_e its polar angle, and y is the inelasticity variable. The lower cut on Q^2 and and the upper on y reduce the background from photoproduction.

Massless jets are defined using the k_t-jet algorithm [60, 61] with combined calorimeter and track information [62] as input. The jet algoritm is applied in the Breit-frame with the p_t-recombination scheme and the distance parameter is set to one. The selection further requires the reconstruction of at least one jet in the laboratory frame, satisfying the cuts below:

$$\begin{gathered} p_{t,\rm jet} > 3.5 \text{ GeV} \\ 7^\circ < \theta_{\rm jet} < 20^\circ \\ x_{\rm jet} > 0.035 \end{gathered}$$

where the $p_{t,\rm jet}$- and $\theta_{\rm jet}$-cuts are applied in the laboratory frame. If there is more than one jet fulfilling these requirements the most forward is chosen. For the single differential cross section measurement an additional cut $0.5 < r = p^2_{t,\rm jet}/Q^2 < 5$ is applied.

Data are presented as single differential cross-sections as a function of x_{Bj} ($d\sigma/dx_{Bj}$), and triple differential cross-sections as a function of x_{Bj} in bins of Q^2 and $p^2_{t,\rm jet}$ ($d^3\sigma/dx_{Bj}dQ^2dp^2_{t,\rm jet}$). Another event sample, called the '2+forward jet' sample, is selected by requiring that, in addition to the forward jet, at least two more jets are found. Out of these, the two with the highest transverse momenta are chosen. This provides further constraints on the kinematics at the expense of reducing the data sample.

For the '2+forward jet' sample the p_t is required to be larger than 6 GeV for all 3 jets. The other cuts on the forward jet are kept the same as specified above, and no $p^2_{t,\rm jet}/Q^2$-cut is applied. The two additional jets are required to lie in pseudorapidity, $\eta = -\ln\tan(\theta/2)$, between the electron and the forward jet, $\eta_e < \eta_{\rm jet1} < \eta_{\rm jet2} < \eta_{fwd\,\rm jet}$.

The final numbers of events used for the single and the triple differential forward jet cross section are 17316 and 23992, respectively. The number of selected '2+forward jet' events is 854.

5 Correction factors and systematic uncertainties

The RAPGAP and DJANGO programs, together with a simulation of the H1 detector, are used to correct the data for acceptances, inefficiencies, and bin to bin migrations due to the finite detector resolutions. The shapes of the distributions of the DIS kinematic variables and the jet variables for the forward jet sample, as defined in Sect. 4, are compared to the predictions from RAPGAP and DJANGO. This is done by reweighting the Monte Carlo x_{Bj} distributions to give the best possible agreement with data and by studying how well the distributions of the other kinematic variables are described. The distributions are reproduced equally well by the predictions of RAPGAP and DJANGO after the detector simulation. In Fig. 2 detector level distributions are shown for x_{Bj}, $E_{\rm jet}$ and $p^2_{t,\rm jet}/Q^2$ for the forward jet samples, with and without the $p^2_{t,\rm jet}/Q^2$-cut applied. These distributions are normalised to the number of events and thus give a shape comparison to investigate the understanding of the detector, independently of the normalisation of the physics models.

The hadron level cross sections are extracted by applying correction factors to the data in order to take detector effects into account. The correction factors are calculated as the ratio of the CDM Monte Carlo prediction at the hadron and detector levels, in a bin-by-bin procedure. These factors correct the data from detector level to non-radiative hadron level, i.e. the data are also corrected for QED radiative effects. RAPGAP and CDM give similar values over the full kinematic range covered in this investigation. The correction factors are generally between 0.7 and 1.2 but in a few kinematic bins they reach values of 0.5 or 1.4 due to limited resolution of the jet quantities. The variations in the correction factors between the two Monte Carlo models are included in the systematic error.

The purity and acceptance[2] are found to be larger than 30% in all bins. For the '2+forward jet' analysis they are larger than 40% in all bins.

The systematic errors are estimated for each data point separately as the quadratic sum of the individual errors described below. The following systematic errors are considered:

- The hadronic energy scale uncertainty is determined to be 4%. In order to estimate the related un-

[2] The purity (acceptance) is obtained from the same Monte Carlo simulations as used for the correction factors and is defined as the number of simulated events which originate from a bin and are reconstructed in it divided by the number of reconstructed (generated) events in that bin.

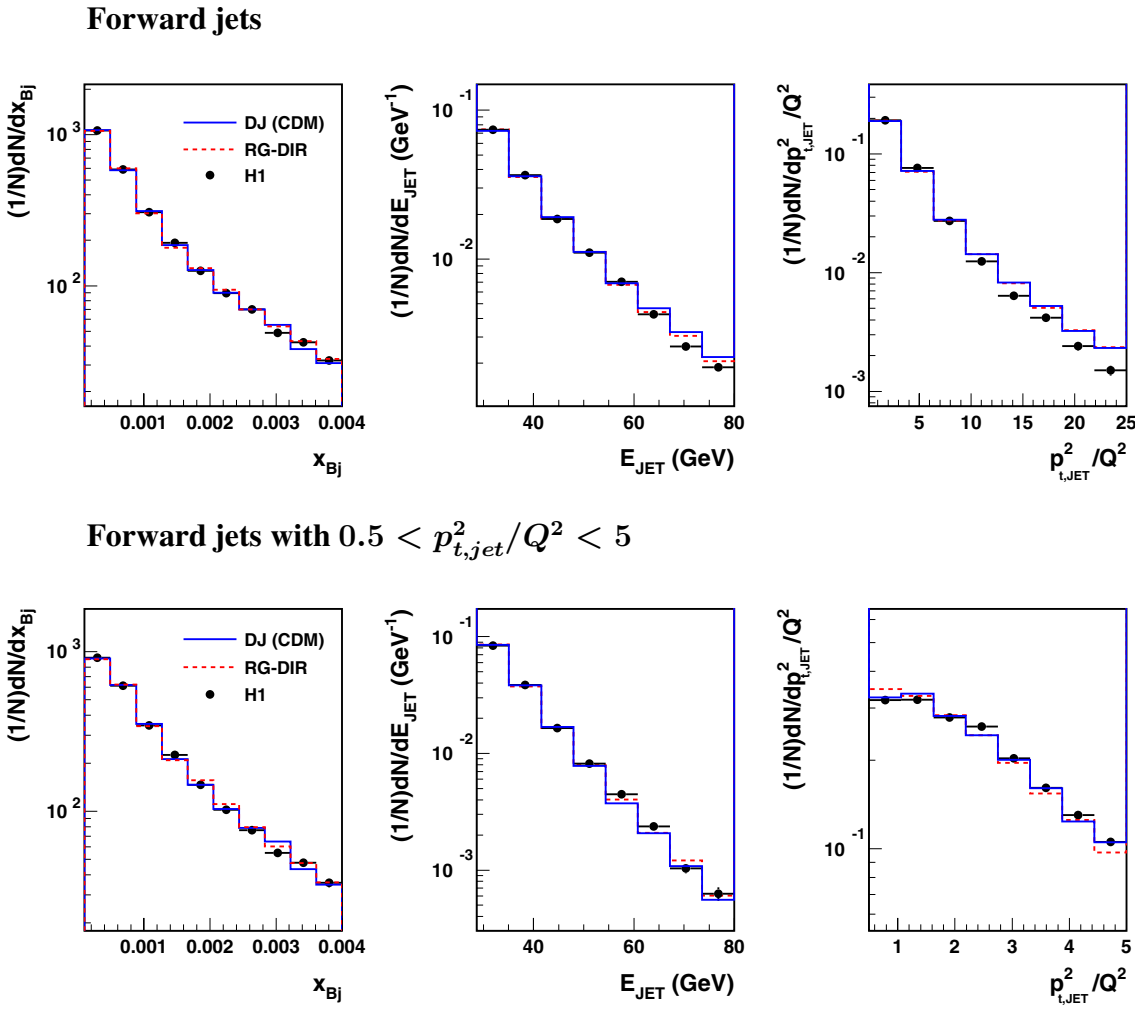

Fig. 2. Control plots for the forward jet selection. The sample with no $p^2_{t,\mathrm{jet}}/Q^2$-cut applied (upper) and the sample with the $0.5 < p^2_{t,\mathrm{jet}}/Q^2 < 5$-cut applied (lower) are shown. The distributions are at detector level and normalised to unity. All variables are measured in the laboratory frame. Comparisons are made to the predictions of the DJANGO (full line) and RAPGAP (dashed line) Monte Carlo programs, after reweighting of the Monte Carlo samples (see text)

certainty of the measured forward jet cross section, the reconstructed hadronic energies in the DJANGO/ARIADNE simulation were increased and decreased by this amount. The average resulting error is typically 8% for both the single differential forward jet cross section and the triple differential forward jet cross section, and 13% for the '2+forward jet' cross section.

– The electromagnetic energy scale as measured in the SpaCal is known to an accuracy of 1%. Changing the scale by this amount in the forward jet cross section calculations using DJANGO/ARIADNE results in an average systematic error of typically 3% for the single and triple differential measurement, and 1% for the '2+forward jet' measurement.
– The uncertainty on the measured scattering angle of the electron is estimated to be 1 mrad, which contributes typically 1% to the error in the forward and '2+forward jet' cross section.
– The error from the model dependence is taken as the difference between the correction factors calculated from the DJANGO/ARIADNE and the RG-DIR Monte Carlo programs. Taking this variation into account yields a systematic error of about 5% for the single differential forward jet cross section, 8% for the triple differential case and 13% in the '2+forward jet' cross section.
– The PHOJET [63,64] Monte Carlo generator was used in order to estimate the extent to which DIS forward jet events could be faked by photoproduction ($Q^2 \sim 0$ GeV^2) background. The influence on the measurement is found to be negligible. The error attributed to this source of uncertainty is taken to be 1%.
– The uncertainty of the luminosity measurement is estimated to be 1.5%.

The averages of these sums are 10%, 12% and 14% for the single differential, triple differential and the '2+forward jet' cross section, respectively. In the figures the

Table 2. Single differential forward jet cross sections in bins of x_{Bj}. The statistical error ($\Delta_{\rm Stat}$), the error from the uncertainty of the calorimetric energy scales ($\Delta_{\rm Syst1}$) and from the other systematic errors ($\Delta_{\rm Syst2}$) are specified. The correction factors ($1+\delta_{HAD}$) for the hadronisation effects are also given

x_{Bj}	$d\sigma/dx_{Bj}$ (nb)	$\Delta_{\rm Stat}$ (nb)	$\Delta_{\rm Syst1}$ (nb)	$\Delta_{\rm Syst2}$ (nb)	Had. corr. factor
0.0001-0.0005	925	± 17	$^{+110}_{-100}$	$^{+77}_{-77}$	0.87
0.0005-0.001	541	± 12	$^{+54}_{-55}$	$^{+23}_{-24}$	0.96
0.001-0.0015	264	± 8	$^{+30}_{-28}$	$^{+11}_{-11}$	0.97
0.0015-0.002	153	± 6	$^{+19}_{-16}$	$^{+8}_{-8}$	1.03
0.002-0.003	74.5	± 3.0	$^{+10.7}_{-8.0}$	$^{+1.9}_{-1.8}$	1.06
0.003-0.004	36.7	± 2.0	$^{+2.1}_{-5.7}$	$^{+2.4}_{-2.4}$	1.04

systematic errors due to the energy scale uncertainty of the calorimeters ($\Delta_{\rm Syst1}$) are shown separately as bands around the data points, whereas the other systematic errors ($\Delta_{\rm Syst2}$) are included in the error bars together with the statistical errors. The errors are given separately in the tables.

6 Results

6.1 Single differential cross section

The measurement of the single differential forward jet cross section is presented at the hadron level in the phase space region defined in Sect. 4. The phase space for DGLAP evolution is suppressed by the additional requirement $0.5 < p^2_{t,\rm jet}/Q^2 < 5$ as discussed in Sect. 4.

The measured single differential forward jet cross sections are listed in Table 2. In Fig. 3a they are compared with LO (α_s) and NLO (α_s^2) calculations from DISENT. The calculations are multiplied by $(1+\delta_{\rm HAD})$ to correct to the hadron level. The uncertainty from the factorisation and renormalisation scales, and the uncertainty in the PDF parametrisation, are added in quadrature to give the total theoretical error, which is shown as a band around the histogram presenting the theoretical prediction. In Fig. 3b and c the data are compared to the various QCD based models.

In Fig. 3a it can be observed that, at small x_{Bj}, the NLO di-jet calculations from DISENT are significantly larger than the LO contribution. This reflects the fact that the contribution from forward jets in the LO scenario is suppressed by kinematics. For small x_{Bj} the NLO contribution is an order of magnitude larger than the LO contribution. The NLO contribution opens up the phase space for forward jets and improves the description of the data considerably. However, the NLO di-jet predictions are still a factor of 2 below the data at low x_{Bj}, which is an indication that still higher order corrections in α_S are needed. If the renormalisation and factorisation scales are set to Q^2 instead of p_t^2, the NLO prediction increases by about 35% at low x_{Bj} but the scale uncertainties are significantly larger (not shown). The somewhat improved agreement at higher x_{Bj} can be understood from the fact that the range in the longitudinal momentum fraction which is available for higher order emissions decreases.

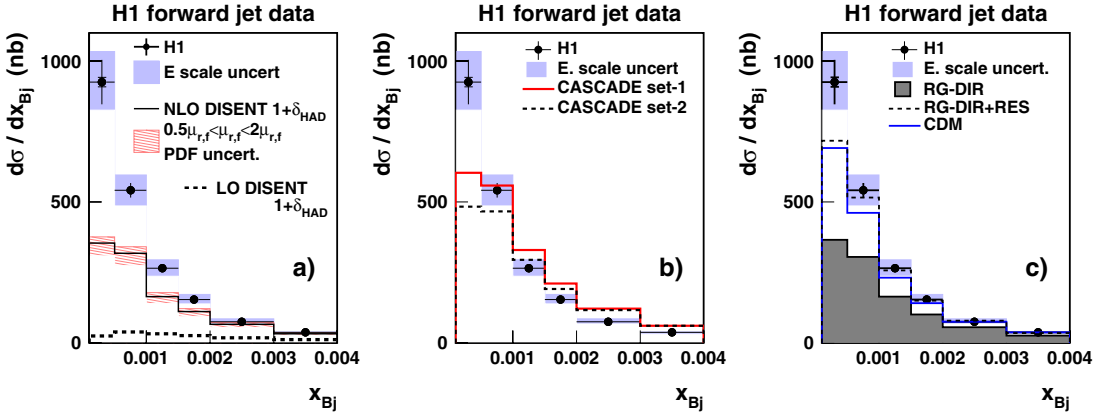

Fig. 3. The hadron level cross section for forward jet production as a function of x_{Bj} compared to NLO predictions from DISENT (**a**) and to QCD Monte Carlo models (**b** and **c**). The shaded band around the data points shows the error from the uncertainties in the calorimetric energy scales. The inner error bars show the statistical errors. The outer error bars represent the statistical errors added in quadrature to the systematic uncertainties not already included in the error band. The hatched band around the NLO calculations illustrates the theoretical uncertainties in the calculations, estimated as described in the text. The dashed line in **a** shows the LO contribution

From Fig. 3b it is seen that the CCFM model (both set-1 and set-2) predicts a somewhat harder x_{Bj} distribution, which results in a comparatively poor description of the data.

Figure 3c shows that the DGLAP model with direct photon interactions alone (RG-DIR) gives results similar to the NLO di-jet calculations and falls below the data, particularly in the low x_{Bj} region. The description of the data by the DGLAP model is significantly improved if contributions from resolved virtual photon interactions are included (RG-DIR+RES). However, there is still a discrepancy in the lowest x_{Bj}-bin, where a possible BFKL signal would be expected to show up most prominently. The CDM model, which gives emissions that are non-ordered in transverse momentum, shows a behaviour similar to the RG DIR+RES model. Analytic calculations where resolved photon contributions are included to NLO order [55] again give similar agreement with the data as the RG DIR+RES model [22].

6.2 Triple differential cross sections

In this section data are presented as triple differential forward jet cross sections. The total forward jet event sample is subdivided into bins of Q^2 and $p^2_{t,\mathrm{jet}}$. The triple differential cross section $d\sigma/dx_{Bj}dQ^2dp^2_{t,\mathrm{jet}}$ versus x_{Bj} is shown in Figs. 4–6 for three regions in Q^2 and $p^2_{t,\mathrm{jet}}$. Figure 4 presents the cross section compared to NLO (α_s^2) calculations, including theoretical errors, represented by error bands. In Fig. 5 and 6 comparisons to QCD Monte Carlo models are shown. The same parton density functions and scales are used as in the measurement of the single differential cross section. The cross section values are listed in Table 3.

From Fig. 4 it can be observed that the NLO calculations in general undershoot the data but similarly to the single differential cross section the NLO calculations get closer to the data at higher x_{Bj} and so too, due to the kinematics, at higher Q^2. The NLO calculations also give a better description of data for harder forward jets. In the highest $p^2_{t,\mathrm{jet}}$-bin the difference between data and NLO is less than the (large) uncertainty in the NLO calculations in several x_{Bj}-bins. This is consistent with the results from a previous measurement on inclusive jet production [17]. A possible explanation is that jets with high p_t remove a large fraction of the energy from the parton ladder, leaving limited energy available for additional emissions. Thus, the parton ladder is shorter and more like the NLO configuration. For high $p_{t,\mathrm{jet}}$ the phase space for LO starts to open up, which also makes the NLO prediction more reliable. In contrast, at low x_{Bj} and low $p_{t,\mathrm{jet}}$, higher order corrections might still be needed to describe the data.

The comparisons between data and QCD based models are discussed in three different kinematic regions as specified below. These regions are however not strictly separated, but overlap. In all three regions the CDM and DGLAP resolved (RG-DIR+RES) models give very similar predictions (see Fig. 6) indicating that a breaking of the ordering of the virtuality is necessary to describe the data. As already observed in the single differential measurement the CCFM model predicts a somewhat harder x_{Bj} distribution than seen in the data. This is true for the full kinematic range and leads to the poor description of the data as seen in Fig. 5.

$p^2_{t,\mathrm{jet}} \sim Q^2$ $(r \sim 1)$

In this region events with parton emissions ordered in p_t are suppressed, and thus parton dynamics beyond DGLAP may show up. The data are best described by the DGLAP resolved model (RG-DIR+RES) as observed in Fig. 6b and f.

$p^2_{t,\mathrm{jet}} < Q^2$ $(r < 1)$

The region where Q^2 might become larger than $p^2_{t,\mathrm{jet}}$ is dominated by direct photon interactions. However, since r can take values up to 1.8 in the most DGLAP-like bin (Fig. 6c), events with $p^2_{t,\mathrm{jet}}$ of the same order or even greater than Q^2 are also contributing. This gives an admixture of events with emissions non-ordered in virtuality. This may explain why the DGLAP direct model (RG-DIR), although closer to the data in this region than in others, does not give good agreement with the data except for the highest x_{Bj}-bin. The CDM and DGLAP resolved model (RG-DIR+RES) reproduce the data very well in this region.

$p^2_{t,\mathrm{jet}} > Q^2$ $(r > 1)$

The kinematic region where $p^2_{t,\mathrm{jet}}$ is larger than Q^2 is typical for processes where the virtual photon is resolved. As expected the DGLAP resolved model (RG-DIR+RES) provides a good overall description of the data, again similar to the CDM model. However, it can be noted that in the regions where r is the highest and x_{Bj} small, CDM shows a tendency to overshoot the data. DGLAP direct (RG-DIR) gives cross sections which are too low (see Fig. 6 d, g and h).

6.3 Events with reconstructed di-jets in addition to the forward jet

Complementary to the analyses reported in Sects. 6.1 and 6.2, where the ratio $p^2_{t,\mathrm{jet}}/Q^2$ has been used to isolate regions where a possible BFKL signal is enhanced, another method is used to control the evolution kinematics in the analysis reported here. By requiring the reconstruction of the two hardest jets in the event in addition to the forward jet, different kinematic regions can be investigated by applying cuts on the jet momenta and their rapidity separation as described in more detail in Sect. 4.

In this scenario it is demanded that all jets have transverse momenta larger than 6 GeV. By applying the same $p_{t,\mathrm{jet}}$-cut to all three jets, evolution with strong k_t-ordering

Table 3. Triple differential cross sections in bins of Q^2, p_t^2 and x_{Bj}. The statistical error ($\Delta_{\rm Stat}$), the error from the uncertainty of the calorimetric energy scales ($\Delta_{\rm Syst1}$) and from the other systematic errors ($\Delta_{\rm Syst2}$) are specified

Q^2 (GeV^2)	p_t^2 (GeV^2)	x_{Bj}	$d^3\sigma/dx_{Bj}dQ^2dp_t^2$ (nb GeV^{-4})	$\Delta_{\rm Stat}$ (nb GeV^{-4})	$\Delta_{\rm Syst1}$ (nb GeV^{-4})	$\Delta_{\rm Syst2}$ (nb GeV^{-4})
5-10	12.25-35	0.0001-0.0005	5.10	$\pm$ 0.12	$^{+0.46}_{-0.44}$	$^{+0.58}_{-0.59}$
		0.0005-0.001	1.13	$\pm$ 0.05	$^{+0.16}_{-0.07}$	$^{+0.17}_{-0.17}$
	35-95	0.0001-0.0005	1.70	$\pm$ 0.04	$^{+0.14}_{-0.14}$	$^{+0.11}_{-0.11}$
		0.0005-0.001	$3.81\cdot10^{-1}$	$\pm 0.18\cdot10^{-1}$	$^{+0.51\cdot10^{-1}}_{-0.33\cdot10^{-1}}$	$^{+0.13\cdot10^{-1}}_{-0.10\cdot10^{-1}}$
	95-400	0.0001-0.0005	$1.11\cdot10^{-1}$	$\pm 0.05\cdot10^{-1}$	$^{+0.11\cdot10^{-1}}_{-0.08\cdot10^{-1}}$	$^{+0.05\cdot10^{-1}}_{-0.05\cdot10^{-1}}$
		0.0005-0.001	$2.71\cdot10^{-2}$	$\pm 0.22\cdot10^{-2}$	$^{+0.35\cdot10^{-2}}_{-0.33\cdot10^{-2}}$	$^{+0.26\cdot10^{-2}}_{-0.26\cdot10^{-2}}$
10-20	12.25-35	0.0001-0.0005	$8.40\cdot10^{-1}$	$\pm 0.31\cdot10^{-1}$	$^{+0.64\cdot10^{-1}}_{-0.62\cdot10^{-1}}$	$^{+0.67\cdot10^{-1}}_{-0.66\cdot10^{-1}}$
		0.0005-0.001	$5.31\cdot10^{-1}$	$\pm 0.24\cdot10^{-1}$	$^{+0.39\cdot10^{-1}}_{-0.34\cdot10^{-1}}$	$^{+0.22\cdot10^{-1}}_{-0.22\cdot10^{-1}}$
		0.001-0.0015	$2.81\cdot10^{-1}$	$\pm 0.16\cdot10^{-1}$	$^{+0.32\cdot10^{-1}}_{-0.29\cdot10^{-1}}$	$^{+0.36\cdot10^{-1}}_{-0.37\cdot10^{-1}}$
		0.0015-0.002	$6.67\cdot10^{-2}$	$\pm 0.73\cdot10^{-2}$	$^{+0.38\cdot10^{-2}}_{-0.65\cdot10^{-2}}$	$^{+0.09\cdot10^{-2}}_{-0.08\cdot10^{-2}}$
	35-95	0.0001-0.0005	$3.11\cdot10^{-1}$	$\pm 0.13\cdot10^{-1}$	$^{+0.21\cdot10^{-1}}_{-0.17\cdot10^{-1}}$	$^{+0.21\cdot10^{-1}}_{-0.21\cdot10^{-1}}$
		0.0005-0.001	$2.36\cdot10^{-1}$	$\pm 0.09\cdot10^{-1}$	$^{+0.20\cdot10^{-1}}_{-0.18\cdot10^{-1}}$	$^{+0.14\cdot10^{-1}}_{-0.15\cdot10^{-1}}$
		0.001-0.0015	$1.13\cdot10^{-1}$	$\pm 0.06\cdot10^{-1}$	$^{+0.12\cdot10^{-1}}_{-0.13\cdot10^{-1}}$	$^{+0.03\cdot10^{-1}}_{-0.03\cdot10^{-1}}$
		0.0015-0.002	$2.81\cdot10^{-2}$	$\pm 0.33\cdot10^{-2}$	$^{+0.50\cdot10^{-2}}_{-0.19\cdot10^{-2}}$	$^{+0.27\cdot10^{-2}}_{-0.22\cdot10^{-2}}$
	95-400	0.0001-0.0005	$2.29\cdot10^{-2}$	$\pm 0.16\cdot10^{-2}$	$^{+0.15\cdot10^{-2}}_{-0.15\cdot10^{-2}}$	$^{+0.08\cdot10^{-2}}_{-0.07\cdot10^{-2}}$
		0.0005-0.001	$1.84\cdot10^{-2}$	$\pm 0.11\cdot10^{-2}$	$^{+0.16\cdot10^{-2}}_{-0.13\cdot10^{-2}}$	$^{+0.04\cdot10^{-2}}_{-0.05\cdot10^{-2}}$
		0.001-0.0015	$7.83\cdot10^{-3}$	$\pm 0.74\cdot10^{-3}$	$^{+0.87\cdot10^{-3}}_{-0.75\cdot10^{-3}}$	$^{+0.83\cdot10^{-3}}_{-0.79\cdot10^{-3}}$
		0.0015-0.002	$2.70\cdot10^{-3}$	$\pm 0.45\cdot10^{-3}$	$^{+0.46\cdot10^{-3}}_{-0.27\cdot10^{-3}}$	$^{+0.35\cdot10^{-3}}_{-0.39\cdot10^{-3}}$
20-85	12.25-35	0.001-0.0015	$4.11\cdot10^{-2}$	$\pm 0.24\cdot10^{-2}$	$^{+0.37\cdot10^{-2}}_{-0.30\cdot10^{-2}}$	$^{+0.12\cdot10^{-2}}_{-0.12\cdot10^{-2}}$
		0.0015-0.002	$3.38\cdot10^{-2}$	$\pm 0.21\cdot10^{-2}$	$^{+0.38\cdot10^{-2}}_{-0.29\cdot10^{-2}}$	$^{+0.34\cdot10^{-2}}_{-0.34\cdot10^{-2}}$
		0.002-0.003	$2.07\cdot10^{-2}$	$\pm 0.12\cdot10^{-2}$	$^{+0.16\cdot10^{-2}}_{-0.13\cdot10^{-2}}$	$^{+0.06\cdot10^{-2}}_{-0.07\cdot10^{-2}}$
		0.003-0.004	$9.03\cdot10^{-3}$	$\pm 0.79\cdot10^{-3}$	$^{+1.37\cdot10^{-3}}_{-0.12\cdot10^{-3}}$	$^{+0.44\cdot10^{-3}}_{-0.44\cdot10^{-3}}$
	35-95	0.001-0.0015	$1.97\cdot10^{-2}$	$\pm 0.10\cdot10^{-2}$	$^{+0.11\cdot10^{-2}}_{-0.11\cdot10^{-2}}$	$^{+0.06\cdot10^{-2}}_{-0.05\cdot10^{-2}}$
		0.0015-0.002	$1.67\cdot10^{-2}$	$\pm 0.10\cdot10^{-2}$	$^{+0.11\cdot10^{-2}}_{-0.10\cdot10^{-2}}$	$^{+0.09\cdot10^{-2}}_{-0.09\cdot10^{-2}}$
		0.002-0.003	$1.04\cdot10^{-2}$	$\pm 0.06\cdot10^{-2}$	$^{+0.08\cdot10^{-2}}_{-0.10\cdot10^{-2}}$	$^{+0.05\cdot10^{-2}}_{-0.05\cdot10^{-2}}$
		0.003-0.004	$5.45\cdot10^{-3}$	$\pm 0.39\cdot10^{-3}$	$^{+0.46\cdot10^{-3}}_{-0.24\cdot10^{-3}}$	$^{+0.46\cdot10^{-3}}_{-0.46\cdot10^{-3}}$
	95-400	0.001-0.0015	$1.98\cdot10^{-3}$	$\pm 0.14\cdot10^{-3}$	$^{+0.15\cdot10^{-3}}_{-0.20\cdot10^{-3}}$	$^{+0.11\cdot10^{-3}}_{-0.11\cdot10^{-3}}$
		0.0015-0.002	$1.63\cdot10^{-3}$	$\pm 0.13\cdot10^{-3}$	$^{+0.15\cdot10^{-3}}_{-0.13\cdot10^{-3}}$	$^{+0.20\cdot10^{-3}}_{-0.20\cdot10^{-3}}$
		0.002-0.003	$9.64\cdot10^{-4}$	$\pm 0.70\cdot10^{-4}$	$^{+1.15\cdot10^{-4}}_{-1.35\cdot10^{-4}}$	$^{+0.07\cdot10^{-4}}_{-0.07\cdot10^{-4}}$
		0.003-0.004	$5.17\cdot10^{-4}$	$\pm 0.49\cdot10^{-4}$	$^{+0.41\cdot10^{-4}}_{-0.81\cdot10^{-4}}$	$^{+0.06\cdot10^{-4}}_{-0.03\cdot10^{-4}}$

is not favoured. Decreasing the $p_{t,\rm jet}$-cut is not possible in this analysis due to detector resolutions. The jets are ordered in rapidity according to $\eta_{fwd\,\rm jet} > \eta_{\rm jet_2} > \eta_{\rm jet_1} > \eta_e$ with η_e being the rapidity of the scattered electron. The cross section is measured in two intervals of $\Delta\eta_1 = \eta_{\rm jet_2} - \eta_{\rm jet_1}$. If the di-jet system originates from the quarks q_1 and q_2 (see Fig. 7), the phase space for evolution in x between the di-jet system and the forward jet is increased by requiring that $\Delta\eta_1$ is small and that $\Delta\eta_2 = \eta_{fwd\,\rm jet} - \eta_{\rm jet_2}$ is large. $\Delta\eta_1 < 1$ favours small invariant masses of the di-jet system and thereby small values of x_g (see Fig. 7). With $\Delta\eta_2$ large, x_g carries only a small fraction of the total propagating momentum, leaving the rest for additional radiation. It should be kept in mind, however, that only the forward jet is explicitely restricted in rapidity space, by the demand that it has to be close to the proton axis. The directions of the other jets are related to the forward jet through the $\Delta\eta$ requirements. When $\Delta\eta_2$ is small, it is therefore possible that one or both of the additional jets originate from gluon radiation close in rapidity space to the forward jet. With $\Delta\eta_1$ large, BFKL-like evolution may then occur between the two jets from the di-jet system, or, with both $\Delta\eta_1$ and $\Delta\eta_2$ small, even between the di-jet system and the hard scattering vertex. By studying the cross section for different $\Delta\eta$ values one can test theory and models for event topologies where the k_t ordering is broken at varying locations along the evolution chain.

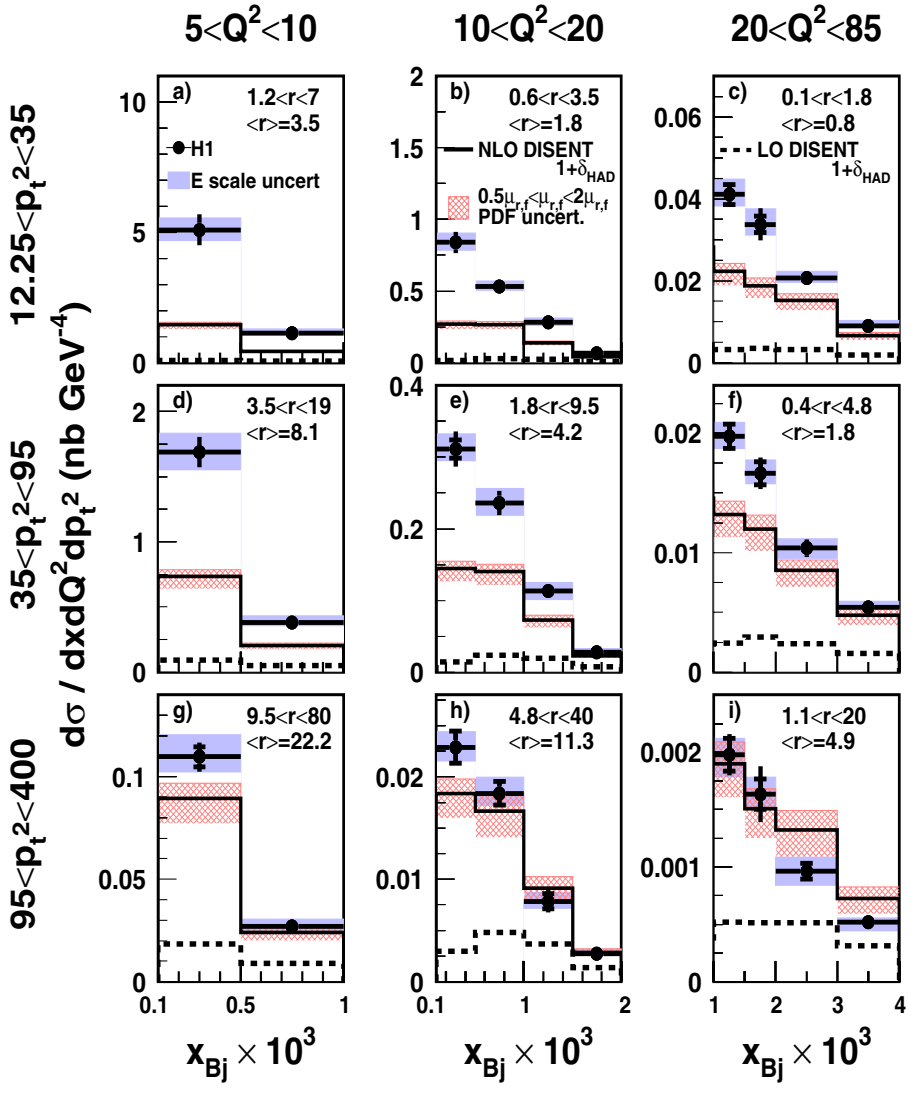

Fig. 4. The hadron level triple differential cross section for forward jet production as a function of x_{Bj}, in bins of Q^2 (GeV^2) and $p^2_{t,\mathrm{jet}}$ (GeV^2). The data are compared to the prediction of NLO (full line) and LO (dashed line) calculations from DISENT. Both calculations are corrected for hadronisation effects. The band around the data points illustrates the error due to the uncertainties in the calorimetric energy scales. The inner error bars show the statistical errors. The outer error bars represent the statistical errors added in quadrature to the systematic uncertainties not already included in the error band. The band around the NLO calculations illustrates the theoretical uncertainties in the calculations. In each bin the range in and the average value of $r = p^2_{t,\mathrm{jet}}/Q^2$ is shown

The cross sections for events containing a di-jet system in addition to the forward jet are presented as a function of $\Delta\eta_2$ in Figs. 8–10 for all '2+forward jet' events , and for the requirements $\Delta\eta_1 < 1$ and $\Delta\eta_1 > 1$, respectively. The measured cross sections are given in Table 4. For the $\Delta\eta_1 < 1$ region the cross section falls at low $\Delta\eta_2$ since the phase space becomes smaller when the 3 jets are forced to be close together. Figure 8 gives a comparison of data to

Table 4. '2+forward jet' cross sections in bins of $\Delta\eta_2$ for all $\Delta\eta_1$, $\Delta\eta_1 < 1$ and $\Delta\eta_1 > 1$. The statistical error (Δ_{Stat}), the error from the uncertainty of the calorimetric energy scales (Δ_{Syst1}) and from the other systematic errors (Δ_{Syst2}) are specified. The correction factors $(1+\delta_{HAD})$ for the hadronisation effects are also given

$\Delta\eta_1$	$\Delta\eta_2$	$d\sigma/d\Delta\eta_2$ (pb)	Δ_{Stat} (pb)	Δ_{Syst1} (pb)	Δ_{Syst2} (pb)	Had. corr. factor
	0.0–0.6	40.6	±2.7	$^{+4.8}_{-4.4}$	$^{+2.1}_{-2.2}$	0.72
All $\Delta\eta_1$	0.6–1.4	37.9	±2.2	$^{+4.3}_{-4.4}$	$^{+2.2}_{-2.2}$	0.60
	1.4–3.0	11.6	±1.0	$^{+2.0}_{-1.5}$	$^{+0.2}_{-0.2}$	0.55
	0.0–0.6	12.7	±1.3	$^{+1.5}_{-1.3}$	$^{+0.3}_{-0.4}$	0.74
$\Delta\eta_1 < 1$	0.6–1.4	18.8	±1.5	$^{+1.4}_{-1.9}$	$^{+0.4}_{-0.4}$	0.61
	1.4–3.0	9.3	±0.9	$^{+1.6}_{-1.0}$	$^{+0.3}_{-0.3}$	0.59
	0.0–0.6	27.9	±2.4	$^{+3.2}_{-3.0}$	$^{+2.1}_{-2.1}$	0.71
$\Delta\eta_1 > 1$	0.6–1.4	19.0	±1.7	$^{+3.0}_{-2.6}$	$^{+1.8}_{-1.9}$	0.60
	1.4–2.5	3.4	±0.6	$^{+0.5}_{-0.6}$	$^{+0.5}_{-0.5}$	0.50

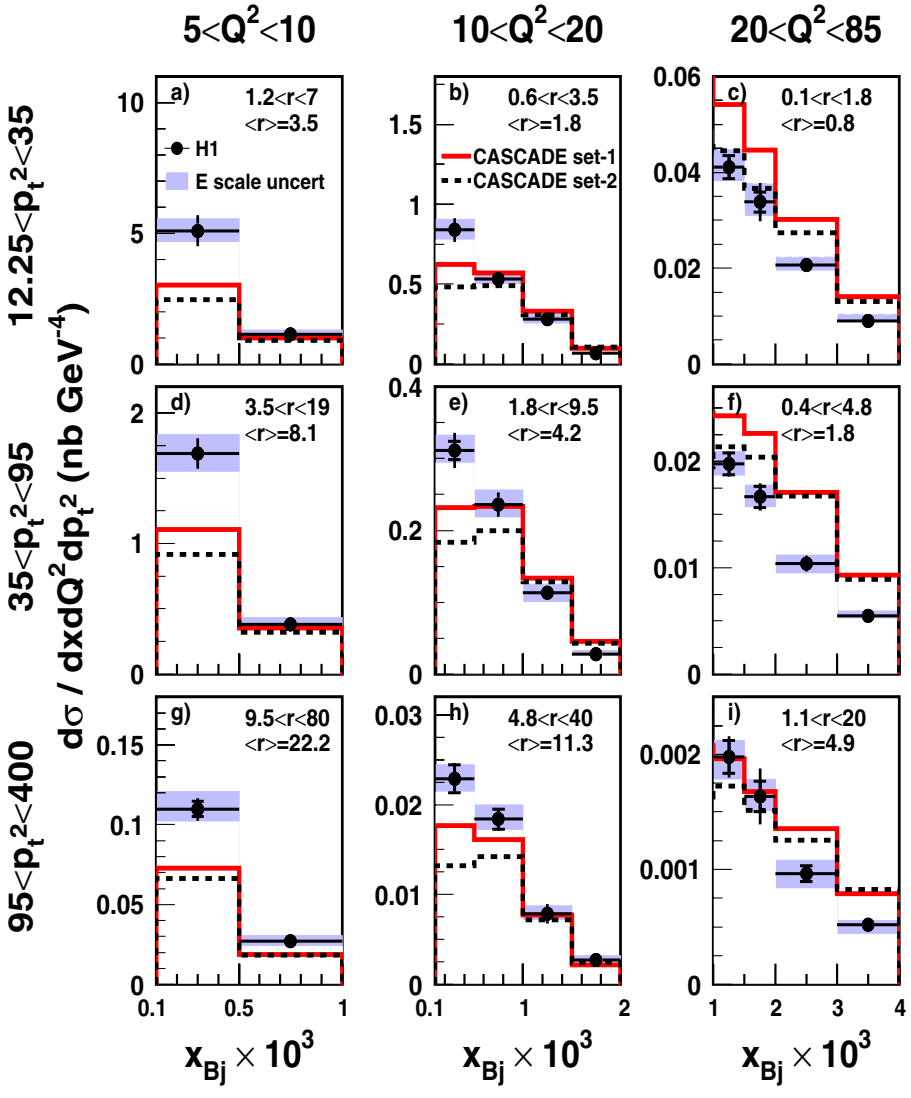

Fig. 5. The hadron level triple differential cross section for forward jet production as a function of x_{Bj}, in bins of Q^2 (GeV^2) and $p^2_{t,\mathrm{jet}}$ (GeV^2). The data are compared to the predictions of CASCADE. The band around the data points illustrates the error due to the uncertainties in the calorimetric energy scales. The inner error bars show the statistical errors. The outer error bars represent the statistical errors added in quadrature to the systematic uncertainties not already included in the error band. In each bin the range in and the average value of $r = p^2_{t,\mathrm{jet}}/Q^2$ is shown

NLO (α_s^3) predictions with theoretical error contributions included as bands. In Figs. 9 and 10 comparisons to QCD based models are presented.

In this investigation the same settings of the QCD based models are used as in Sects. 6.1 and 6.2, while the NLO three-jet cross sections are calculated using NLOJET++.

From Fig. 8 it is observed that NLOJET++ provides a reasonable description of the data, taking into account the large uncertainties of the NLO prediction. A good agreement is seen when the two additional hard jets are emitted in the central region ($\Delta\eta_2$ large). It is interesting to note that a fixed order calculation (α_s^3), including the $\log(1/x)$-term to the first order in α_s, is able to describe these data well. However, the more the additional hard jets are shifted to the forward region ($\Delta\eta_2$ small), the less well are the data described by NLOJET++. This is an indication that the more forward the additional jets go, the higher the probability is that one of them, or even both, do not actually originate from quarks but from additional radiated gluons. For gluon induced processes, which dominate at small x, NLOJET++ calculates the NLO contribution to final states containing one gluon jet and two jets from the di-quarks, i.e. it accounts for the emission of one gluon in addition to the three jets. Thus, events where two of the three selected jets originate from gluons are produced by NLOJET++ only in the real emission corrections to the three-jet final state, which effectively means that these kinematic configurations are only produced to leading order (α_s^3). The most extreme case, where all three reconstructed jets are produced by gluons, is not considered by NLOJET++. This results in a depletion of the theoretical cross section in the small $\Delta\eta_2$ region, which is more pronounced when $\Delta\eta_1$ is also small, i.e. when all three jets are in the forward region. Consequently a significant deviation between data and NLOJET++ can be observed for such events (see the lowest bin in Fig. 8b). Accounting for still higher orders in α_s might improve the description of the data in this domain since virtual corrections to the production of two gluons could increase the cross section for such final states, and additional gluon emissions would enhance the probability that one of the soft radiated glu-

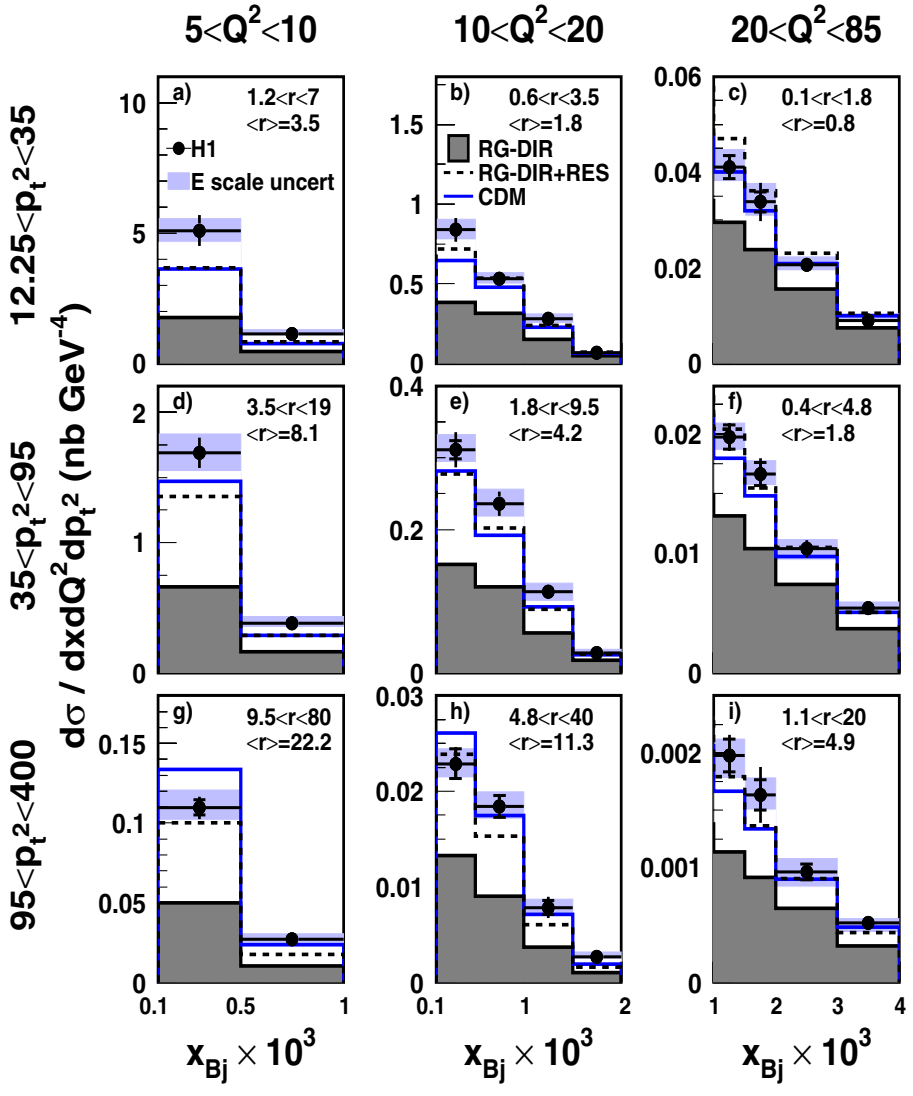

Fig. 6. The hadron level triple differential cross section for forward jet production as a function of x_{Bj}, in bins of Q^2 (GeV^2) and $p^2_{t,\mathrm{jet}}$ (GeV^2). The data are compared to the prediction of RAPGAP DIR, RAPGAP DIR+RES and CDM. The band around the data points illustrates the error due to the uncertainties in the calorimetric energy scales. The inner error bars show the statistical errors. The outer error bars represent the statistical errors added in quadrature to the systematic uncertainties not already included in the error band. In each bin the range in and the average value of $r = p^2_{t,\mathrm{jet}}/Q^2$ is shown

ons produces a jet that fulfills the transverse momentum requirement applied in this analysis.

For the '2+forward jet' sample CCFM is not describing well the shape of the η-distributions (Fig. 9a, b and c).

As explained above, evolution with strong k_t-ordering is disfavoured in this study. Radiation that is non-ordered in k_t may occur at different locations along the evolution chain, depending on the values of $\Delta\eta_1$ and $\Delta\eta_2$. As can be seen from Fig. 10, the colour dipole model gives good agreement in all cases, whereas the DGLAP models give cross sections that are too low except when both $\Delta\eta_1$ and $\Delta\eta_2$ are large. For this last topology all models and the NLO calculation agree with the data, indicating that the available phase space is exhausted and that little freedom is left for dynamical variations.

If one or both jets from the di-jet system are produced by gluon radiation, which, intuitively, is increasingly probable the more forward these jets go, it necessarily means that the k_t ordering is broken. In this context it is noteworthy that CDM provides the best description of the data while the other models, including the DGLAP-

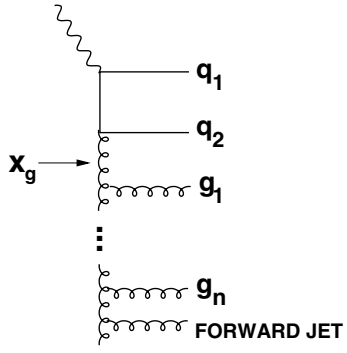

Fig. 7. A schematic diagram of an event giving a forward jet and two additional hard jets. These may stem from the quarks (q_1 and q_2) in the hard scattering vertex or from gluons in the parton ladder. x_g is the longitudinal momentum fraction carried by the gluon, connecting to the hard di-jet system (in this case q_1 and q_2)

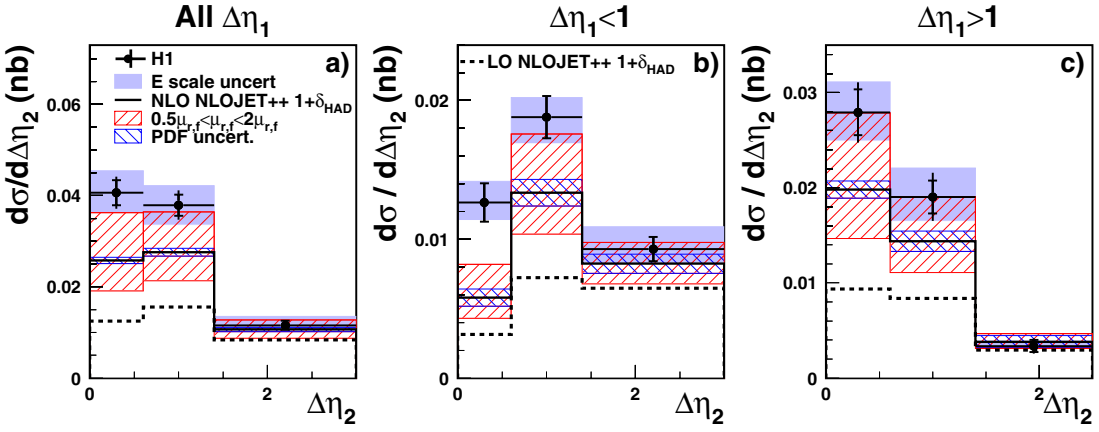

Fig. 8. The cross section for events with a reconstructed high transverse momentum di-jet system and a forward jet as a function of the rapidity separation between the forward jet and the most forward-going additional jet, $\Delta\eta_2$. Results are shown for the full sample and for two ranges of the separation between the two additional jets, $\Delta\eta_1 < 1$ and $\Delta\eta_1 > 1$. The data are compared to the LO and NLO predictions of three-jet final state calculations by NLOJET++ $(1 + \delta_{\mathrm{HAD}})$. The band around the data points illustrates the error due to the uncertainties in the calorimetric energy scales. The inner error bars show the statistical errors. The outer error bars represent the statistical errors added in quadrature to the systematic uncertainties not already included in the error band. The band around the NLO calculations illustrates the theoretical uncertainties in the calculations

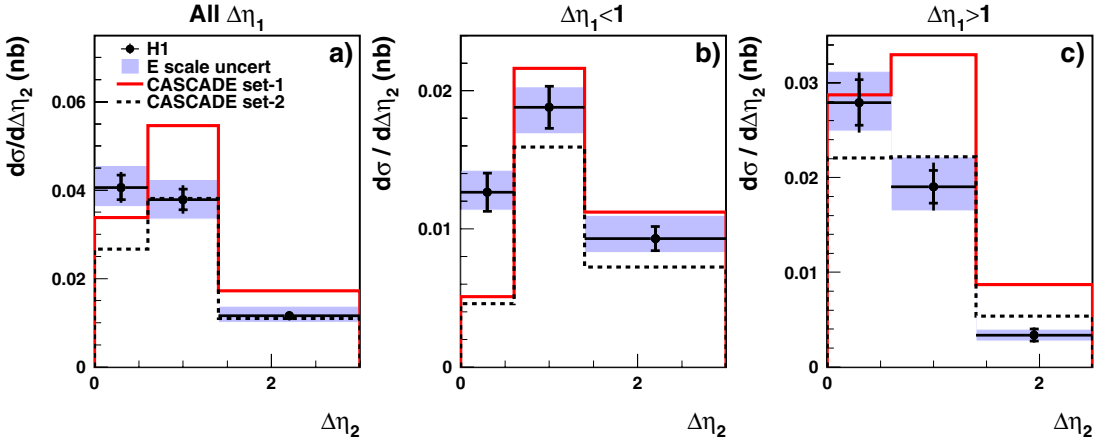

Fig. 9. The cross section for events with a reconstructed high transverse momentum di-jet system and a forward jet as a function of the rapidity separation between the forward jet and the most forward-going additional jet, $\Delta\eta_2$. Results are shown for the full sample and for two ranges of the separation between the two additional jets, $\Delta\eta_1 < 1$ and $\Delta\eta_1 > 1$. The data are compared to the predictions of CASCADE. The band around the data points illustrates the error due to the uncertainties in the calorimetric energy scales. The inner error bars show the statistical errors. The outer error bars represent the statistical errors added in quadrature to the systematic uncertainties not already included in the error band

resolved model, fail in most of the bins. The '2+forward jet' sample differentiates CDM and the DGLAP-resolved model, in contrast to the more inclusive samples where CDM and RG-DIR+RES give the same predictions. The conclusion is that additional breaking of the k_t ordering is needed compared to what is included in the resolved photon model.

7 Summary

An investigation of DIS events containing a jet in the forward direction is presented. Various constraints are applied, which suppress contributions to the parton evolution described by the DGLAP equations and enhance the sensitivity to BFKL-like parton dynamics. Several observables involving forward jet events are studied and compared to the predictions of NLO calculations and QCD based models.

Leading order (α_s) calculations of the single differential forward jet cross section, $d\sigma/dx_{Bj}$, are well below the measurements, which is expected since forward jet production is kinematically suppressed in LO. For this reason the NLO corrections are quite large and improve the description of the data considerably, although the predictions remain low at small values of x_{Bj}. Further higher order corrections might still improve the description of the data in this kinematic domain. Predictions based on the DGLAP

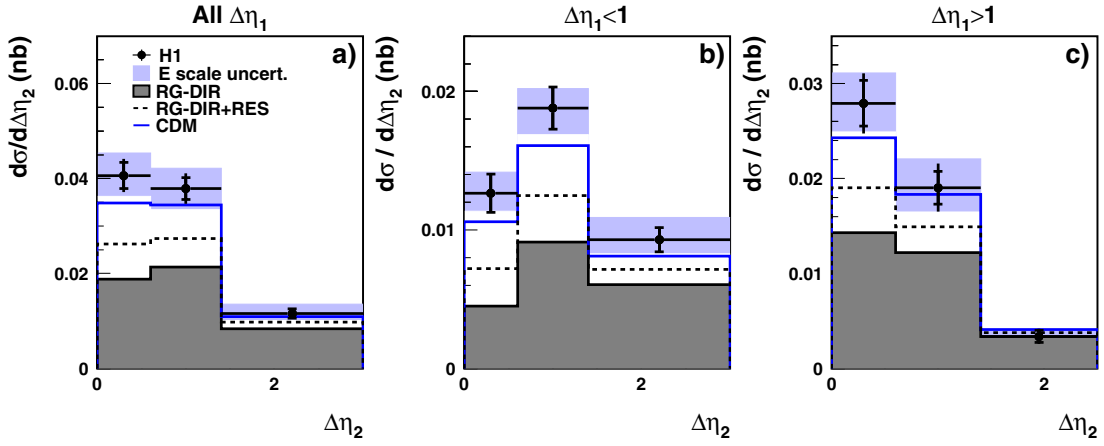

Fig. 10. The cross section for events with a reconstructed high transverse momentum di-jet system and a forward jet as a function of the rapidity separation between the forward jet and the most forward-going additional jet, $\Delta\eta_2$. Results are shown for the full sample and for two ranges of the separation between the two additional jets, $\Delta\eta_1 < 1$ and $\Delta\eta_1 > 1$. The data are compared to the predictions of RAPGAP DIR, RAPGAP DIR+RES and CDM. The band around the data points illustrates the error due to the uncertainties in the calorimetric energy scales. The inner error bars show the statistical errors. The outer error bars represent the statistical errors added in quadrature to the systematic uncertainties not already included in the error band

direct model also underestimate the data at low x_{Bj}. The DGLAP resolved photon model (RG-DIR+RES) and the colour dipole model (CDM) come closest to the data.

The total forward jet sample is subdivided into bins of Q^2 and $p^2_{t,\mathrm{jet}}$ such that kinematic regions are defined in which the effects of different evolution dynamics are enhanced. In the most DGLAP enhanced region ($Q^2 \gg p^2_{t,\mathrm{jet}}$) and in the region where contributions from resolved processes are expected to become important ($p^2_{t,\mathrm{jet}} \gg Q^2$), the measured triple differential forward jet cross sections are well described by the CDM and the DGLAP resolved model (RG-DIR+RES). In the BFKL region ($Q^2 \sim p^2_{t,\mathrm{jet}}$) the CDM and DGLAP resolved model (RG-DIR+RES) again reproduce the data best. A general observation is that the DGLAP resolved model and CDM tend to fall below the data at low x_{Bj}, Q^2 and p^2_t. The cross sections predicted by the DGLAP direct model (RG-DIR) are consistently too low in all regions and especially at low x_{Bj}.

The NLO di-jet calculations from DISENT describe the data for the largest values of x_{Bj} at high values of Q^2 and p^2_t, but fail for low values of these variables.

The measured cross section for events with a reconstructed di-jet system in addition to the forward jet are in good agreement with the predictions of NLOJET++ if the additional jets are emitted in the central region. A deviation is observed for event topologies where all three jets are forced towards the forward direction. The data are best described by the CDM. The DGLAP resolved model (RG-DIR+RES) is below the data as is, to an even greater extent, the DGLAP direct model (RG-DIR). This result gives the first evidence for parton dynamics in which there is additional breaking of the k_t-ordering compared to that provided by the resolved photon model.

The CCFM model, as implemented in CASCADE, with two different parametrisations of the unintegrated gluon density, fails to describe the shape of both the single and triple differential cross sections, as well as the '2+forward jet' cross section. This might be caused by the parametrisation of the unintegrated gluon density and/or the missing contributions from splittings into quark pairs.

The observations made here demonstrate that an accurate description of the radiation pattern at small x_{Bj} requires the introduction of terms beyond those included in the DGLAP direct approximation (RG-DIR). Higher order parton emissions with breaking of the transverse momentum ordering contribute noticeably to the cross section. Calculations which include such processes, such as CDM and the resolved photon model, provide a better description of the data. The similar behaviour of CDM and the DGLAP resolved model (RG-DIR+RES), which describe the data best, indicates that the inclusive forward jet measurements do not give a significant separation of the models. However, in the more exclusive measurement of '2+forward jet' events a clear differentiation of the models is obtained since, in contrast to CDM, the DGLAP resolved model (RG-DIR+RES) fails to describe the data.

Acknowledgements. We are grateful to the HERA machine group whose outstanding efforts have made and continue to make this experiment possible. We thank the engineers and technicians for their work in constructing and maintaining the H1 detector, our funding agencies for financial support, the DESY technical staff for continual assistance and the DESY directorate for hospitality which they extend to the non-DESY members of the collaboration. J. Bartels, G. Gustafson and L. Lönnblad are acknowledged for valuable discussions concerning the interpretation of the results.

References

1. V. N. Gribov, L. N. Lipatov, Sov. J. Nucl. Phys. **15** (1972) 675 [Yad. Fiz. **15** (1972) 1218].

2. V. N. Gribov, L. N. Lipatov, Sov. J. Nucl. Phys. **15** (1972) 438 [Yad. Fiz. **15** (1972) 781].
3. L. N. Lipatov, Sov. J. Nucl. Phys. **20** (1975) 94 [Yad. Fiz. **20** (1974) 181].
4. G. Altarelli, G. Parisi, Nucl. Phys. B **126** (1977) 298.
5. Y. L. Dokshitzer, Sov. Phys. JETP **46** (1977) 641 [Zh. Eksp. Teor. Fiz. **73** (1977) 1216].
6. C. Adloff et al. [H1 Collaboration], Eur. Phys. J. C **13** (2000) 609 [hep-ex/9908059].
7. C. Adloff et al. [H1 Collaboration], Eur. Phys. J. C **21** (2001) 33 [hep-ex/0012053].
8. S. Chekanov et al. [ZEUS Collaboration], Eur. Phys. J. C **21** (2001) 443 [hep-ex/0105090].
9. S. Chekanov et al. [ZEUS Collaboration], Phys. Rev. D **70** (2004) 052001 [hep-ex/0401003].
10. E. A. Kuraev, L. N. Lipatov, V. S. Fadin, Sov. Phys. JETP **44** (1976) 443 [Zh. Eksp. Teor. Fiz. **71** (1976) 840].
11. E. A. Kuraev, L. N. Lipatov, V. S. Fadin, Sov. Phys. JETP **45** (1977) 199 [Zh. Eksp. Teor. Fiz. **72** (1977) 377].
12. I. I. Balitsky, L. N. Lipatov, Sov. J. Nucl. Phys. **28** (1978) 822 [Yad. Fiz. **28** (1978) 1597].
13. C. Adloff et al. [H1 Collaboration], Eur. Phys. J. C **13** (2000) 397 [hep-ex/9812024].
14. C. Adloff et al. [H1 Collaboration], Eur. Phys. J. C **13** (2000) 415 [hep-ex/9806029].
15. S. Chekanov et al. [ZEUS Collaboration], Eur. Phys. J. C **23** (2002) 13 [hep-ex/0109029].
16. C. Adloff et al. [H1 Collaboration], Phys. Lett. B **415** (1997) 418 [hep-ex/9709017].
17. C. Adloff et al. [H1 Collaboration], Phys. Lett. B **542** (2002) 193 [hep-ex/0206029].
18. S. Aid et al. [H1 Collaboration], Phys. Lett. B **356** (1995) 118 [hep-ex/9506012].
19. C. Adloff et al. [H1 Collaboration], Eur. Phys. J. C **12** (2000) 595 [hep-ex/9907027].
20. C. Adloff et al. [H1 Collaboration], Nucl. Phys. B **485** (1997) 3 [hep-ex/9610006].
21. J. Breitweg et al. [ZEUS Collaboration], Phys. Lett. B **479** (2000) 37 [hep-ex/0002010].
22. H. Jung, L. Jönsson, H. Küster, "Resolved photon processes in DIS and small x dynamics," [hep-ph/9805396].
23. H. Jung, L. Jönsson, H. Küster, Eur. Phys. J. C **9** (1999) 383 [hep-ph/9903306].
24. A. Aktas et al. [H1 Collaboration], Eur. Phys. J. C **37** (2004) 141 [hep-ex/0401010].
25. C. Adloff et al. [H1 Collaboration], Phys. Lett. B **462** (1999) 440 [hep-ex/9907030].
26. A. Aktas et al. [H1 Collaboration], Eur. Phys. J. C **36** (2004) 441 [hep-ex/0404009].
27. B. Andersson, G. Gustafson, L. Lönnblad, U. Pettersson, Z. Phys. C **43** (1989) 625.
28. L. Lönnblad, Z. Phys. C **65** (1995) 285.
29. A. H. Mueller, Nucl. Phys. Proc. Suppl. **18C**, 125 (1991).
30. A. H. Mueller, J. Phys. G **17** (1991) 1443.
31. C. Adloff et al. [H1 Collaboration], Nucl. Phys. B **538** (1999) 3 [hep-ex/9809028].
32. J. Breitweg et al. [ZEUS Collaboration], Eur. Phys. J. C **6** (1999) 239 [hep-ex/9805016].
33. S. Chekanov et al. [ZEUS Collaboration], hep-ex/0502029.
34. M. Ciafaloni, Nucl. Phys. B **296** (1988) 49.
35. S. Catani, F. Fiorani, G. Marchesini, Phys. Lett. B **234** (1990) 339.
36. S. Catani, F. Fiorani, G. Marchesini, Nucl. Phys. B **336** (1990) 18.
37. G. Marchesini, Nucl. Phys. B **445** (1995) 49 [hep-ph/9412327].
38. H. Jung, Comput. Phys. Commun. **86** (1995) 147.
39. A. Kwiatkowski, H. Spiesberger, H. J. Möhring, Comput. Phys. Commun. **69** (1992) 155.
40. K. Charchula, G. A. Schuler, H. Spiesberger, Comput. Phys. Commun. **81** (1994) 381.
41. L. Lönnblad, Comput. Phys. Commun. **71** (1992) 15.
42. J. Pumplin et al. JHEP **0207** (2002) 012 [hep-ph/0201195].
43. C. Adloff et al. [H1 Collaboration], Eur. Phys. J. C **19** (2001) 289 [hep-ex/0010054].
44. H. Jung, G. P. Salam, Eur. Phys. J. C **19** (2001) 351 [hep-ph/0012143].
45. H. Jung, Comput. Phys. Commun. **143** (2002) 100 [hep-ph/0109102].
46. M. Hansson, H. Jung, "Status of CCFM: Un-integrated gluon densities", [hep-ph/0309009].
47. R. Brun, R. Hagelberg, M. Hansroul, J. C. Lassalle, CERN-DD-78-2-REV
48. S. Catani, M. H. Seymour, Phys. Lett. B **378** (1996) 287 [hep-ph/9602277].
49. S. Catani, M. H. Seymour, Nucl. Phys. B **485** (1997) 291 [Erratum-ibid. B **510** (1997) 503] [hep-ph/9605323].
50. M. A. Kimber, A. D. Martin, M. G. Ryskin, Phys. Rev. D **63** (2001) 114027 [hep-ph/0101348].
51. Z. Nagy, Z. Trocsanyi, Phys. Rev. Lett. **87** (2001) 082001 [hep-ph/0104315].
52. H. Jung, "Un-integrated PDFs in CCFM", hep-ph/0411287.
53. H. Jung, Proceedings of the 12th International Workshop on Deep Inelastic Scattering (DIS 2004), Strbske Pleso, Slovakia, April 14-18, 2004, Eds. D. Bruncko, J. Ferencei, P. Strizenec, Inst. Exp. Phys. SAS, 2004, Kosice, Vol 1, p.299.
54. G. A. Schuler, T. Sjöstrand, Phys. Lett. B **376** (1996) 193 [hep-ph/9601282].
55. G. Kramer, B. Pötter, Phys. Lett. B **453** (1999) 295 [hep-ph/9901314].
56. I. Abt et al. [H1 Collaboration], Nucl. Instrum. Meth. A **386** (1997) 348.
57. I. Abt et al. [H1 Collaboration], Nucl. Instrum. Meth. A **386** (1997) 310.
58. R. D. Appuhn et al. [H1 SPACAL Group], Nucl. Instrum. Meth. A **386** (1997) 397.
59. B. Andrieu et al. [H1 Calorimeter Group Collaboration], Nucl. Instrum. Meth. A **336** (1993) 499.
60. S. Catani, Y. L. Dokshitzer, M. H. Seymour, B. R. Webber, Nucl. Phys. B **406** (1993) 187.
61. S. Catani, Y. L. Dokshitzer, B. R. Webber, Phys. Lett. B **285** (1992) 291.
62. C. Adloff et al. [H1 Collaboration], Z. Phys. C **74** (1997) 221 [hep-ex/9702003].
63. R. Engel, J. Ranft, Phys. Rev. D **54** (1996) 4244 [hep-ph/9509373].
64. R. Engel, Z. Phys. C **66** (1995) 203.